VNIVERSITAT DE VALÈNCIA

Departamento de Astronomía y Astrofísica

General relativistic collapse of rotating stellar cores

TESIS DOCTORAL PRESENTADA POR

Pablo Cerdá Durán

2006

Dr. José Antonio Font Roda, profesor de la Universidad de Valencia,

CERTIFICA:

Que la presente memoria, "General relativistic collapse of rotating stellar cores", ha sido realizada bajo su dirección, por Pablo Cerdá Durán, y que constituye su tesis doctoral para optar al grado de Doctor en Física.

Y para que quede constancia y tenga los efectos que corresponda, firma el presente certificado en Burjassot, a 3 de Julio de 2006 .

Firmado: José Antonio Font Roda

a Laura

Agradecimientos

En primer lugar, quiero dar las gracias a mi director, ya que sin él nunca habría podido terminar esta tesis. Su apoyo científico, y en muchos casos moral, a hecho que fuera un placer estar bajo su dirección. Ha sabido mantener la presión adecuada para que diera lo mejor de mi mismo, y me ha enseñado a ser pragmático cuando hacía falta. Tampoco me olvido del papel que ha tenido su ayuda en la redacción de esta tesis, en un idioma, el inglés, que gracias a él conozco un poco mejor.

Quisiera agradecer a José María Ibáñez, por haberme supervisado en los primeros momentos de la tesis, por la multitud de buenas ideas y mejores consejos que me ha dado, por sus "discusiones de café", y por alguna que otra paella. Quiero agradecerle su firme apoyo a la investigación, y la especial consideración que ha tenido siempre con los investigadores más jóvenes.

Ich möchte Harald Dimmelmeier für seine wertwolle hilfe danken. Er bot mir freundlich seinen numerischen Code an, der die Grundlage meiner Arbeit ist. Ich danke ihm auch, weil ich zu Hause fühlte, als ich in München war.

Quiero agradecer a Guillaume Faye, por haberme guiado pacientemente por las profundidades y entresijos de la relatividad general, y mostrarme la belleza de los desarrollos post-Newtonianos. También por todas las discusiones, científicas o no, que he tenido con él, casi siempre disfrutando de una buena comida.

A Vicent Quilis por sus interesantes propuestas científicas, por sus *masclets*, y por estar siempre dispuesto a tomar un café. También por su ayuda numérica y por el considerable esfuerzo que ha hecho en la mejora de los recursos computacionales del departamento, sin los cuales las simulaciones de esta tesis habrían sido del todo imposibles. A José Pons por estar siempre dispue-

sto a ayudar y discutir sobre lo que fuera, lo que ha enriquecido siempre mi trabajo.

Quisiera dar las gracias también a Manolo y Luis, por hacer más llevaderos estos años, por su ayuda numérica y por haberse portado siempre como buenos amigos. También a Arturo, Guillermo, Emilio, Alicia, Carlos, Toni y en general a toda la gente con la que, por una razón u otra, he compartido despacho durante los años que he pasado en el DAA.

Quiero dar las gracias a Diego por dirigirme el trabajo de investigación, y por, en largas discusiones frente a la pizarra, enseñarme el modo de abordar cualquier problema científico. A Chema, por su guia en el proceso de presentación de la tesis. A Pepe, por sus conversaciones durante la comida. A Ramón por su *filologia recreativa*. A Joan Ferrando y Juan Antonio Morales por solventar algunas de mis dudas sobre relatividad. A Enric por su ayuda informática. A Manel, a Feli y a Reme por su eficiencia y por estar siempre al tanto de todos los asuntos administrativos. Y en general a todos los miembros del departamento, ya sean PDI, PAS o cualquier otra cosa.

Gracias a mis padres por apoyarme siempre en lo que hago, y por la educación que me han dado, que me ha hecho como soy, y cuya consecuencia directa es esta tesis.

Gracias a Laura, por estar siempre a mi lado y animarme a seguir adelante, y sobre todo por hacerme feliz.

Resumen

Introducción

La astronomía de ondas gravitatorias

A comienzos del siglo veinte, la teoría de Einstein de la relatividad general revolucionó nuestra manera de entender el mundo físico con un nuevo paradigma que no sólo describía la gravitación sino el espacio-tiempo en si mismo. Actualmente esta teoría está profundamente arraigada, y es la base de los modelos más realistas en cosmología y astrofísica. Sin embargo, todas sus predicciones no han podido todavía ser confirmadas por las observaciones. Una de estas predicciones es la existencia de ondas gravitatorias. En el amanecer de un nuevo siglo está emergiendo una nueva rama de la astronomía, la astronomía de ondas gravitatorias, dedicada al estudio de objetos astrofísicos y cosmológicos mediante la detección de las ondas gravitatorias emitidas por estos.

Para que un objeto astrofísico emita ondas gravitatorias observables desde la Tierra, éste debe ser un objeto compacto con fuertes campos gravitatorios que además tengan variaciones temporales. El estudio de las ondas gravitatorias emitidas es una herramienta excelente para observar las partes más recónditas de dichos objetos astrofísicos. Por ejemplo, se podrá observar el colapso de núcleo estelares en la formación de supernovas o el vecindario de agujeros negros rodeados de discos de acrecimiento. Estas regiones son invisibles a cualquier otra observación del espectro electromagnético. También se podrán detectar las perturbaciones del espacio tiempo producidas por el choque de dos agujeros negros, que de otra manera serían invisibles. Además será posible

realizar observaciones complementarias de fuentes conocidas de radiación electromagnética, como escenarios que involucren estrellas de neutrones o enanas blancas. Estas observaciones nos ayudarán a constreñir mejor los parámetros de estos sistemas (masa, momento angular, tamaño, ecuación de estado de la materia nuclear, etc). Para impulsar el crecimiento de esta nueva rama de la astronomía es indispensable un desarrollo en paralelo de detectores y modelado de fuentes.

A lo largo de las dos últimas décadas han sido diseñados un gran número de detectores de ondas gravitatorias. Se han construido gigantescas instalaciones con detectores basados en interferometría láser en Europa (VIRGO, EGO), EE.UU. (LIGO) y Japón (TAMA), para detectar ondas gravitatorias en el rango de los kHz, y extensiones de estos interferómetros ya están planeadas (Advanced LIGO en EE.UU., LCGT en Japón y EURO en Europa). También interferómetros en el espacio (la colaboración ESA/NASA llamada LISA) para observar fuentes emitiendo en el rango de los mHz. Por otro lado, el modelado de fuentes es necesario para establecer que objetos astrofísicos y cosmológicos serán detectables en términos de amplitud de la señal y rango de frecuencias, y reperrcute en el diseño de los actuales y futuros detectores. Pero los modelos teóricos no sólo son útiles para el diseño del detector, sino también son una parte esencial del proceso de detección. El bajo nivel señal/ruido de los detectores convierte la detección en un reto, que sólo podrá ser superado si se usan técnicas específicas como el filtrado por reconocimiento de patrones (*matched filtering*). En estas técnicas, las plantillas de ondas gravitatorias proporcionadas por el modelado de fuentes, son cruciales para ayudar en el análisis de datos. Además, se necesitan modelos teóricos para interpretar dichas ondas y extraer su contenido físico, que es al fin y al cabo la meta final de la astronomía de ondas gravitatorias.

Uno de los escenarios astrofísicos más interesantes donde buscar ondas gravitatorias es el colapso gravitatorio de los núcleos de hierro en estrellas masivas ($M \geq 8M_{\odot}$). El objeto resultante, una proto-estrella de neutrones (PNS) o un agujero negro rodeado por un disco de acrecimiento, es la base de los modelos de algunos de los fenómenos observables más energéticos del universo: supernovas tipo Ib/Ic/II, erupciones de rayos gamma (GRB) y formación de chorros. Todas estas son fuentes prometedoras de ondas gravitatorias, y su investigación teórica es de gran interés para entender las implicaciones de las observaciones. El objetivo principal de esta tesis es el estudio de la radiación

gravitatoria producida en un escenario en particular, el colapso gravitatorio de núcleos estelares en rotación y la posterior evolución de las PNS que se forman.

El paradigma del colapso de núcleos estelares

Actualmente, el paradigma aceptado para explicar las supernovas de tipo Ib/Ic/II es el del colapso de núcleos estelares. Aunque todavía quedan preguntas por resolver, el progreso científico realizado en las últimas décadas ha llevado a un amplio consenso sobre como se produce una supernova. A continuación describiremos brevemente el actual conocimiento sobre el mencionado paradigma del colapso de núcleos, remitiendo al lector interesado a Arnett et al. (1989); Bethe (1990); Fryer & New (2003); Kotake et al. (2005a) para más información.

Una estrella es un objeto en el que la autogravedad y los gradientes de presión alcanzan un equilibrio. Las altas temperaturas y presiones de su interior inician una cadena de reacciones termonucleares empezando por el combustible original de la estrella, el hidrógeno. A lo largo de la evolución de una estrella masiva (entre $9M_{\odot}$ y $30M_{\odot}$), el hidrógeno se transforma en helio, el helio en carbono y así consecutivamente, de modo que en unos diez millones de años se forma una estructura en capas en la que los diferentes productos resultantes de los distintos procesos de fusión nuclear quedan estratificados. El último eslabón de la cadena de reacciones termina con la formación de elementos del grupo del hierro-níquel, que son estables, ya que la energía de ligadura por nucleón alcanza su valor mínimo. Estos elementos se acumulan en el centro a medida que la capa de silicio que los rodea va consumiéndose, formando el núcleo de hierro. Cuando el núcleo alcanza la denominada masa de Chandrasekhar, con un valor de $\sim 1{,}5M_{\odot}$, la presión de electrones relativistas que sostiene al núcleo no puede contrarrestar su autogravedad y el colapso es inevitable.

Dos procesos inducen dicho colapso. En primer lugar, las capturas electrónicas por los núcleos reducen la presión de electrones al mismo tiempo que los neutrinos emitidos se llevan energía del núcleo. En segundo lugar, para densidades superiores a 10^{10} g cm^{-3}, la fotodesintegración de núcleos de hierro en helio (que es un proceso endotérmico) enfría el núcleo. Al principio del colapso el núcleo de hierro tiene un radio de unos miles de kilómetros, una densidad central de $\rho \sim 10^{10}$ g cm^{-3}, y una temperatura de $T \sim 10^{10}$ K. Parte de la

energía del campo gravitatorio del núcleo se libera en forma de energía cinética lo que acelera la materia que cae a una fracción significativa de la velocidad de la luz. A densidades superiores a $\sim 10^{12}$ g cm^{-3}, los neutrinos quedan atrapados y la composición alcanza rápidamente el equilibrio beta al exceder los $\sim 10^{13}$ g cm^{-3}. Como los neutrinos atrapados sólo escapan en escalas de tiempo de su difusión (mayores que la escala de tiempo del colapso), no se pierde más energía por neutrinos, y el colapso procede casi adiabáticamente. Mientras la densidad aumenta, el equilibrio beta se desplaza hacia estados de materia rica en neutrones. Al llegar a densidades del orden de la densidad de la materia nuclear, $\rho_n \sim 2 \times 10^{14}$ g cm^{-3}, la fuerza nuclear entre nucleones empieza a jugar un papel predominante como fuente fundamental de presión. Si la masa del núcleo es suficientemente baja para no colapsar a un agujero negro, la caída de la parte interior se detiene a unos $\sim$ 10 km, rebotando y formando una fuerte onda de choque que se propaga hacia el exterior contra el material que todavía cae. Mientras ésta se propaga, la fotodisociación de núcleos de hierro transforman la energía cinética del choque en energía térmica, y, cuando la onda de choque sale de la neutrino-esfera, los neutrinos abandonan libremente el choque llevándose parte de la energía. Como consecuencia la onda de choque se detiene a unos 100 km del centro unas decenas de milisegundos después. Para entonces, una proto-estrella de neutrones caliente se ha formado en los $\sim$ 30 km interiores con una enorme cantidad de neutrinos atrapados en el interior. Las escalas de tiempo de difusión de los neutrinos se vuelven importantes, y una gran cantidad de pares neutrino-antineutrino son emitidos, llevándose consigo energía de la PNS y enfriándola para formar una estrella de neutrones (NS) compacta de $\sim$ 10 km. Una pequeña fracción de la inmensa energía que transportan los neutrinos emitidos se deposita detrás del choque, el cual revive, y se produce una explosión supernova retardada. Al alcanzar la explosión regiones de menor densidad, el choque se acelera y destruye la estrella entera llevandose la mayor parte de la masa. Únicamente queda una pequeña fracción de ~ 1 M$_\odot$ en el centro formando una estrella de neutrones.

Ondas gravitatorias del colapso de núcleos estelares

La radiación electromagnética y los neutrinos no son las únicas emisiones de una explosión supernova. El movimiento global de la estrella colapsante, que rebota a densidades en torno a las de la materia nuclear, y las asimetrías

del núcleo, producen un destello (*burst*) de ondas gravitatorias. Según como gire la estrella progenitora y como proceda el colapso, las ondas gravitatorias emitidas son de distinto tipo (Zwerger & Müller 1997). Aunque las amplitudes estimadas para progenitores realistas fuera de nuestra galaxia son pequeñas para ser detectadas con los actuales detectores de ondas gravitatorias (Müller et al. 2004), otros procesos pueden producir ondas gravitatorias más intensas tras el colapso. En particular, los movimientos convectivos tras la onda de choque producidos por la deposición de la energia de los neutrinos emitidos en la PNS, pueden dar lugar a amplitudes mayores incluso para núcleos girando lentamente (Müller et al. 2004).

Además, la proto-estrella de neutrones es en si misma una fuente prometedora de ondas gravitatorias detectables. Para ritmos de rotación y grados de rotación diferencial suficientemente altos se desarrollan inestabilidades no axisimétricas en escalas de tiempo dinámicas [1] como la llamada inestabilidad de tipo barra (Tohline et al. 1985; Shibata et al. 2002), que produce fuertes señales de ondas gravitatorias. Cuando la estrella de neutrones se ha enfriado hasta alcanzar unos 10^{10} K, puede estar sujeta a la denominada inestabilidad de Chandrasekhar-Friedman-Schutz (Chandrasekhar 1970; Friedman & Schutz 1978) y se convierte en una importante fuente de ondas gravitatorias (consúltese Stergioulas 2003, para más información). Como consecuencia, un modelado en detalle de la transformación de la PNS caliente a la NS fria es esencial para poder realizar predicciones en la emisión de ondas gravitatorias de estrellas de neutrones. Especial atención hay que dedicar a los ritmos de rotación, la distribución de momento angular y la estructura e intensidad del campo magnético.

Física involucrada en el colapso

Para poder estudiar apropiadamente el colapso gravitatorio de núcleos de hierro y las ondas gravitatorias emitidas por éste, se deben incluir una cierta cantidad de ingredientes físicos. Aquí resumimos los más importantes a tener en cuenta:

[1] Estos valores, sin embargo, pueden no ser realistas, ya que no se conoce un camino evolutivo que lleve a la creación de PNS con los ritmos de rotación necesarios.

- **Relatividad general:** La masa involucrada en el colapso es del orden de $\sim 1 M_{\odot}$. En la etapa final del colapso, esta masa se halla encerrada en la PNS, con un radio de unas decenas de kilómetros. Para estas configuraciones tan compactas, los efectos de la relatividad general empiezan a aparecer, y la gravedad Newtoniana no es suficiente para describir el equilibrio y la dinámica del sistema (ver por ejemplo el Cap. 29 de Misner et al. 1973).

- **Ecuación de estado de la materia nuclear:** Se necesita una descripción termodinámica de la materia nuclear para poder calcular correctamente la dinámica del proceso entero, cómo se produce el rebote y la configuración final de la PNS (vease Glendenning 1997; Prakash et al. 2001, para más información).

- **Transporte de neutrinos:** Éste es un aspecto crucial en el modelado para ser capaces de describir el mecanismo de la explosión retardada, así como el enfriamiento de la recién formada PNS que da lugar a la NS final (ver Janka et al. 2005, y referencias allí citadas).

- **Campos magnéticos:** Algunas observaciones sugieren la presencia de campos magnéticos en el escenario de colapso y en los objetos resultantes. El descubrimiento de púlsares de rayos X anómalos y *Soft Gamma-Ray Repeaters*, interpretados como estrellas de neutrones fuertemente magnetizadas (magnetares) (Duncan & Thompson 1992; Thompson & Duncan 1996; Kouveliotou et al. 1999), hace que el estudio del colapso magnetizado sea de gran interés.

- **Otros mecanismos de transporte de energía:** Probablemente existen otros mecanismos de transporte de energía dentro del núcleo que juegan un papel importante en la dinámica del colapso, y no deben ser despreciados. Algunos de estos son la convección, la turbulencia, el transporte radiativo y la difusión por viscosidad.

Conviene enfatizar que la inclusión de todos estos efectos en un código numérico no se puede acometer hoy en dia, principalmente debido a los costes computacionales prohibitivos tanto en memoria como en tiempo de cálculo. Por lo tanto se deben hacer algunas simplificaciones en las simulaciones requeridas

para describir la dinámica altamente no lineal que involucra el colapso de núcleos estelares.

Marco teórico

El marco general utilizado en la presente tesis es el de la relatividad general en el formalismo $3 + 1$ (Lichnerowicz 1944; Choquet-Bruhat 1952). Dicho formalismo, descrito en el capítulo 2, nos permite foliar el espacio-tiempo en una serie de hipersuperficies espaciales sin intersección, parametrizadas por el tiempo propio. De este modo, cada hipersuperficie contiene el espacio tridimensional completo para cierto valor del tiempo propio. Este tipo de foliación del espacio-tiempo nos permite tratar el problema de la evolución de las ecuaciones de Einstein como un problema de condiciones iniciales, en el que a partir del contenido de energía y materia en una hipersuperficie dada podemos evolucionar el sistema en el tiempo.

Esta descomposición todavía deja algunos parámetros libres que fijar. Debemos especificar como serán las coordenadas que describen las hipersuperficies espaciales, y el modo particular en que se folia el espacio-tiempo (el *slicing*). Para ello debemos imponer cuatro condiciones de *gauge*. La elección de éstas es crucial para la correcta resolución del problema, muy especialmente si esto implica la resolución numérica de las ecuaciones de Einstein. Por otro lado, la resolución del sistema completo de ecuaciones de Einstein es, en general, un problema de gran dificultad. Por ello puede ser conveniente, al menos en algunos escenarios, realizar alguna aproximación que facilite la resolución de las ecuaciones, sin eliminar ningún elemento imprescindible.

En el capítulo 3 se describen las ecuaciones que gobiernan la dinámica de fluidos y de campos electromagnéticos en el formalismo 3+1 de la relatividad general. Estas ecuaciones se expresan de manera adecuada para su resolución numérica. Asumimos que el fluido que modelamos es tanto un fluido perfecto (sin viscosidad) como un conductor perfecto (condición de la magnetohidrodinámica ideal). Bajo estas condiciones las ecuaciones se simplifican notablemente.

En el capítulo 5 presentamos una nueva aproximación de las ecuaciones de Einstein del campo gravitatorio, a la cual llamamos CFC+. Esta aproximación está basada en las correcciones a segundo orden en el desarrollo post-

Newtoniano de la métrica conformemente plana, i.e. CFC+ representa una extensión de la aproximación CFC (o de Isenberg–Wilson–Mathews) descrita en el capítulo 4. La derivación del sistema extendido de ecuaciones se realiza con gran detalle, así como las condiciones de contorno que es necesario aplicar para resolver numéricamente el sistema. Todas las ecuaciones de CFC+ son elípticas, ya que a segundo orden post-Newtoniano el carácter hiperbólico de las ecuaciones de Einstein desaparece. Además notamos que el hecho de resolver ecuaciones elípticas asegura la estabilidad numérica de la solución y evita algunos problemas numéricos que pueden aparecer en evoluciones de largo término de sistemas con gravedad intensa (agujeros negros) al usar la formulación $3+1$ de la relatividad general. Por otro lado, el precio que debe pagarse por usar la aproximación CFC+ es la ausencia de la reacción de la radiación gravitatoria en la dinámica, responsable de la extracción de energía y momento angular del sistema transportados por las ondas gravitatorias. Sin embargo en los escenarios en que utilizamos esta aproximación, este efecto puede considerarse despreciable ya que las pérdidas de energía son insignificantes en escalas de tiempo dinámicas.

La extracción de las ondas gravitatorias se describe en el capítulo 6, y se realiza mediante la fórmula cuadrupolar de Einstein-Landau-Lifshitz. Esta fórmula incorpora el término dominante en la aproximación de velocidades bajas, y se obtiene realizando un desarrollo multipolar de la métrica en el infinito futuro nulo, además de un desarrollo post-Newtoniano de las fuentes a primer orden (Newtoniano). También se obtiene una relación entre la onda gravitatoria dada por la fórmula cuadrupolar y el comportamiento asintótico de la métrica en la aproximación CFC+.

Métodos numéricos

El capítulo 7 está dedicado a la descripción de los métodos numéricos empleados en la resolución de las ecuaciones de la (magneto-)hidrodinámica en relatividad general. La resolución de estas ecuaciones debe realizarse de manera que se respeten las leyes de conservación que representan (energía, momento y número de bariones). Para ello utilizamos métodos de alta resolución de captura de choques (HRSC de su acrnimo en inglés) (ver por ejemplo Leveque 1990; Toro 1999; Martí & Müller 2002; Font 2003), que permiten resolver siste-

mas hiperbólicos de leyes de conservación, utilizando un método que describe correctamente la formación y propagación de ondas de choque.

El caso de las ecuaciones de la magneto-hidrodinámica ideal se trata aparte, ya que la ecuación adicional que se introduce (ecuación de inducción) necesita también un tratamiento especial. Para que la divergencia del campo magnético se mantenga cero durante la evolución, es decir se conserve el flujo magnético, usamos el método *flux-CT* (Evans & Hawley 1988). En particular, utilizamos el esquema de Antón et al. (2006), en el que se hace uso de una reconstrucción lineal de las variables primitivas y esquemas centrados para el cálculo de los flujos numéricos (Kurganov & Tadmor 2000).

El capítulo 8 está dedicado a los métodos numéricos utilizados para resolver las ecuaciones de la métrica, ya sea en la aproximación CFC o en su extensión CFC+. Todas las ecuaciones con las que nos encontramos son de tipo elíptico, y se pueden expresar como pseudo-ecuaciones de Poisson. Los diferentes métodos utilizados dependen de las distintas fases del cálculo de la métrica CFC+. En primer lugar se calcula el potencial Newtoniano mediante una expansión de la parte angular de las ecuaciones en simetría axial en polinómios de Legendre (Müller & Steinmetz 1995; Zwerger 1995). La segunda fase consiste en calcular la parte sin traza y transversa de la 3-métrica. Este cálculo se reduce a la resolución de sistemas lineales de ecuaciones de Poisson, que se realiza mediante la inversión directa del sistema discretizado expresado en forma matricial. La inversión del sistema se realiza por medio de la descomposición LU, que aumenta la eficiencia del esquema numérico utilizado para estas ecuaciones. Por último se resuelve el sistema CFC modificado por las correcciones 2PN de CFC+, que consiste en cinco ecuaciones elípticas no lineales acopladas. Para cada ecuación utilizamos el mismo resolvedor de Poisson que en el caso del potencial Newtoniano, realizando una iteración de punto fijo hasta obtener la convergencia.

Conclusiones

CFC+: dinámica del colapso y radiación gravitatoria mejoradas.

En el capítulo 9 de esta tesis se realizan tests y simulaciones de colapso de núcleos estelares en rotación utilizando la nueva aproximación CFC+, presentada en el capítulo 5. Se realizan tests para comprobar su aplicabilidad a la simulación del espacio-tiempo de estrellas de neutrones en rotación, ya sea en equilibrio o para las configuraciones resultantes del colapso gravitatorio de núcleos estelares.

También comparamos la nueva aproximación CFC+ con la aproximación CFC usada por Dimmelmeier et al. (2002a,b) en dos escenarios diferentes, oscilaciones de estrellas de neutrones y colapso de núcleos estelares a NS. En el caso de las NS pulsantes, no hemos encontrado ninguna diferencia en el cálculo de las frecuencias de los modos cuasi-normales de dichos objetos, incluso en las situaciones más extremas (i.e. con rotación Kepleriana, cercana al límite de pérdida de masa por rotación). También hemos podido comparar nuestros resultados directamente con simulaciones en relatividad general sin aproximaciones, obteniendo de nuevo un acuerdo excelente. Nuestras simulaciones de colapso de núcleos en rotación cubren las distintas tipologías de colapso estudiadas por Dimmelmeier et al. (2002b), incluyendo además un caso extremo de un núcleo con fuerte rotación diferencial y una estructura casi toroidal. De nuevo, no se han encontrado diferencias significativas entre las dos aproximaciones usadas. Por tanto podemos concluir que las correcciones a segundo orden post-Newtoniano de la métrica CFC no mejoran significativamente los resultados de la dinámica del colapso de núcleos estelares a estrellas de neutrones, ni la dinamica de las estrellas de neutrones en si.

En cuanto a la extracción de la radiación gravitatoria tampoco hemos observado diferencias sustanciales entre CFC y CFC+. La comparación ha sido realizada usando la formula cuadrupolar de Einstein-Landau-Lifshitz, empleada comúnmente en la literatura para extraer las formas de onda. Además hemos calculado las ondas gravitatorias directamente de las componentes de la métrica CFC+. Aunque el cálculo de formas de onda de este último modo no puede considerarse un método independiente de cálculo de las ondas, proporciona un test de consistencia de la aproximación CFC+ que sirve para

validar el esquema numérico utilizado para calcular la métrica.

La principal conclusión del capítulo 9 es la confirmación de la aproximación CFC como una alternativa sumamente útil a las ecuaciones de Einstein completas en escenarios axisimétricos que involucren estrellas de neutrones en rotación, en equilibrio y como estado final de un colapso. Estos descubrimientos estan fundamentados por dos hechos: en primer lugar, hemos demostrado que las correcciones de segundo orden post-Newtoniano no juegan un papel importante ni en la dinámica ni en la forma de las ondas gravitatorias emitidas en el colapso. Este hecho sugiere que correcciones de orden superior serán completamente insignificantes, al menos en escalas de tiempo dinámicas. En segundo lugar, la comparación directa de la aproximación CFC con simulaciones en relatividad general ha sido recientemente realizada por Shibata & Sekiguchi (2004) en el contexto de simulaciones de colapso de núcleos estelares en simetría axial. De nuevo, las diferencias encontradas tanto en la dinámica como en la forma de las ondas no son significativas, lo que resalta la aplicabilidad de CFC (y CFC+) para realizar simulaciones precisas de estos escenarios sin la necesidad de resolver el sistema completo de ecuaciones de Einstein.

Colapso magnetizado

En el capítulo 10 se presentan simulaciones del colapso de núcleos estelares magnetizados en rotación, así como los tests que validan la aproximación numérica usada para resolver las ecuaciones de la magneto-hidrodiámica ideal en relatividad general.

Se ha diseñado un método para calcular configuraciones estacionarias de estrellas débilmente magnetizadas en relatividad general, ya sea con componente toroidal o poloidal (o ambas) del campo magnético. Se utiliza la aproximación de campo pasivo (o campo prueba) para los modelos iniciales, en los cuales la presión magnética es varios órdenes de magnitud menor que la presión (térmica) del fluido.

También se han realizado tests para comprobar la precisión y las propiedades de convergencia de la extensión "magnetizada" de nuestro código numérico. Como resultado se encuentra un orden de convergencia mayor de uno en el campo magnético en todos los tests realizados. En los casos estacionarios el orden de convergencia que se obtiene es superior a dos. Estos resultados son consistentes con el segundo orden, espacial y temporal, del esquema numérico

utilizado, únicamente reducido a primer orden en los choques. Se establece la resolución necesaria para poder evolucionar correctamente el campo magnético en una simulación de colapso de núcleos estelares. Los errores en todos los casos en los que la solución teórica es conocida están por debajo del 0,1 %, excepto en los choques, que son correctamente capturados en un par de celdas numéricas gracias al uso de esquemas HRSC.

En cuanto a las simulaciones de colapso de núcleos magnetizados en la aproximación CFC, se han considerado casos con campo magnético puramente poloidal al inicio (serie D3M0) y puramente toroidal (serie T3M0), en la aproximación de campo pasivo. Los modelos D3M0 son una extensión a relatividad general de algunos de los modelos considerados por Obergaulinger et al. (2005) en gravedad Newtoniana y magneto-hidrodinámica ideal. Nuestra intención es comparar la dinámica y las ondas gravitatorias con estos resultados previos. No se encuentran diferencias cualitativas en los modelos estudiados, aunque la magnitud del campo magnético en el rebote y después de éste es en el caso CFC consistentemente menor ($50 - 80\,\%$) que en el caso Newtoniano.

En cada serie de modelos, la amplificación del campo magnético procede de un modo distinto. Mientras que en los modelos D3M0 el enrollamiento de las lineas de campo poloidales en lineas toroidales, debido a la rotación diferencial (dínamo-Ω), es el mecanismo de amplificación principal en el colapso, en los modelos T3M0 el campo magnético se amplifica únicamente debido a la compresión radial, ya que la componente poloidal del campo está ausente en la evolución. Encontramos pues que para los modelos estudiados, la dínamo-Ω es mucho más eficiente amplificando el campo magnético que la compresión radial. Por lo tanto, la componente toroidal del campo magnético al final de la evolución es más débil en los modelos T3M0 que en los modelos D3M0, en los cuales no había tal componente inicialmente.

Al final de nuestras simulaciones las variables del fluido alcanzan un estado de cuasi-equilibrio. Para los modelos D3M0, la proto-estrella de neutrones formada tiene una estructura de núcleo/envoltura. Dentro del núcleo, donde la densidad de materia nuclear ha sido alcanzada, la componente dominante del campo magnético es la poloidal, y los perfiles de rotación son practicamente planos, i.e. el núcleo de la PNS gira rígidamente. Por otro lado, la envoltura que lo rodea gira diferencialmente, y por lo tanto la componente toroidal del campo magnético domina en esta región debido al mecanismo de la dínamo-Ω. Este efecto produce un crecimiento lineal sostenido de la componente toroidal

después del rebote. Si no hubieran otros procesos, el campo magnético se saturaria en ~ 1 s en valores de $B^{\varphi} \sim 10^{15}$ G. En los modelos T3M0 la dínamo-Ω no está activa ya que no hay componente poloidal del campo magnético. Por lo tanto, al alcanzar la PNS el estado de cuasi-equilibrio, el campo magnético permanece estacionario.

Otros mecanismos de amplificación del campo pueden actuar si no se considera la aproximación de campo pasivo o se elimina la condición de axisimetría. Se ha estimado el efecto del mecanismo de amplificación que probablemente sea dominante, es decir, la inestabilidad magneto-rotacional (MRI). Encontramos que durante el colapso, la escala temporal típica del modo que crece más rápidamente en la MRI es de aproximadamente 1 s, y por tanto no afectará a la fase de colapso. Sin embargo, tras el rebote, hay dos regiones susceptibles de desarrollar la MRI: la región tras la onda de choque y la región convectiva que rodea la PNS. En ambas regiones la escala de tiempo estimada de la MRI, ~ 1 ms, es del orden de la escala de tiempo dinámica. En simulaciones sin la aproximación de campo pasivo y con resolución suficientemente grande, se espera que la MRI se desarrolle en estas regiones y domine su dinámica en unos pocos ms.

Secuencias evolutivas de proto-estrellas de neutrones en rotación

En el capítulo 11 se trata el problema de la evolución a largo término de proto-estrellas de neutrones en rotación, construyendo secuencias evolutivas de configuraciones estacionarias en axisimetría y relatividad general. La estructura termodinámica y la evolución de estas secuencias han sido extrapoladas de simulaciones con simetría esférica que incluían transporte de neutrinos. Aunque esto es una simplificación del problema, nos da una visión interesante sobre como evolucionan las diferentes cantidades relevantes cuando la PNS pierde su contenido leptónico y su exceso de energía de ligadura, contrayéndose. Además, encontramos que las estimaciones de luminosidad no son muy diferentes de lo que se esperaría.

Se ha realizado un esfuerzo especial para entender en que lugar del espacio de parámetros se encontraría un caso realista. La mayor incertidumbre concierne a la ley de rotación de la PNS al nacer. Analizando resultados de simulaciones de colapso de núcleos estelares, parece que la escala típica de

variación de la velocidad angular se situa sobre los 10 km, y que la conservación de momento angular durante el colapso de un núcleo estelar (inicialmente girando rígidamente) no parece permitir velocidades angulares que varien en escalas espaciales menores que algunos km. En recientes simulaciones se muestra la presencia de importantes corrientes meridionales y turbulencias, pero poco más se conoce sobre la distribución de momento angular. Para simplificar, nos restringimos al caso estacionario. Esto implica una distribución cuasi-cilíndrica (con desviaciones debidas a efectos relativistas) de la velocidad angular. Este estado sólo se puede alcanzar tras varios giros de la PNS, cuando ha tenido suficiente tiempo para relajarse. Por otro lado, debe tenerse en cuenta que en los primeros 0.5 s el sistema está lejos de ser estacionario, pero después la evolución se produce de modo cuasi-estacionario, excepto por movimientos convectivos de baja velocidad. De nuestro estudio de secuencias cuasi-estacionarias podemos deducir una serie de resultados cualitativos:

i) Para cada instante de la evolución, estrellas girando con altos grados de rotación diferencial pueden tener velocidades angulares en el centro de 5 a 10 veces mayores, y sobre un 50 % más de momento angular. El momento angular específico, J/M, máximo varia entre $(1-2)\ GM_{\odot}/c \approx (0{,}5-1) \times 10^{16}$ cm^2/s, dependiendo del grado de rotación diferencial.

ii) El valor máximo del cociente de la energía cinética de rotación y la energía potencial, $T/|W|$, que se obtiene en el caso de rotación diferencial es de 0.2, mientras que para rotación rígida es $\sim$ 0,11. Así pues, PNS con rotación diferencial pueden desarrollar la inestabilidad CFS, que aparece a $\sim$ 0,14, y también la inestabilidad discutida recientemente para valores pequeños de $T/|W|$ (Shibata et al. 2002, 2003; Watts et al. 2003).

iii) Más interesante es el hecho de que se encuentran varias situaciones en las que, incluso si el modelo inicial está por debajo del valor crítico de $T/|W|$, como la estrella se contrae en la escala de difusión de los neutrions (5-10 s), se acelera entrando en la ventana de inestabilidad. Un efecto observacional de este efecto podía ser un retraso de unos pocos segundos entre el pico de emisión de los neutrinos, y el máximo de ondas gravitatorias en una supernova galáctica. Esto depende de la cantidad inicial de momento angular, que es aproximadamente igual al momento angular del núcleo de hierro del progenitor. Cálculos recientes de evolución estelar sugieren que el momento angular específico del núcleo ($\sim 1{,}7 M_{\odot}$) de una estrella de $15 M_{\odot}$ puede ser tan alto como 3×10^{16} cm^2 s^{-1}, si se desprecia el frenado magnético, o 10^{12} cm^2 s^{-1} incluyendo la tensión

magnética en la evolución (Heger et al. 2004). Estos valores corresponden a $J/M = (0{,}2 - 6)\ GM_{\odot}/c$. Si el momento angular es alto ($J/M > 2$), las fuerzas centrífugas pararían el colapso antes de la formación de la PNS. Valores intermedios ($J/M = 1$) pueden llevar a la formación de una PNS en rotación rápida que entra en la región de inestabilidad varios segundos después de su nacimiento. Si el frenado magnético es muy eficiente durante la evolución de la estrella masiva, $J/M < 0{,}5$, se formará la PNS tras el colapso sin alcanzar valores extremos de velocidad angular y del cociente $T/|W|$.

La continuación natural de este trabajo es incluir mecanismos posibles de transporte de momento angular entre las diferentes capas de la estrella, lo que puede involucrar el transporte de neutrinos, el transporte debido a turbulencias, campos magnéticos, viscosidad por neutrinos, movimientos convectivos y/o pérdidas de momento angular debidas a emisión de ondas gravitatorias. A menos que la estrella nazca con casi la máxima velocidad angular posible, algunos o todos estos mecanismos disipativos pueden modificar nuestra visión actual de la evolución de una PNS.

La inestabilidad tipo barra para bajos $T/|W|$ en estrellas de neutrones

Finalmente en el capítulo 12 se presentan simulaciones AMR (*Adaptative Mesh Refinement*) de alta resolución de la inestabilidad tipo barra para bajos $T/|W|$, de estrellas de neutrones en rotación con grados extremos de rotación diferencial. Nuestra motivación principal es revisitar las simulaciones de Shibata et al. (2002), comprobando cuán sensible es el desarrollo de esta inestabilidad a efectos numéricos como la resolución de la malla. Resaltamos la importancia de un correcto tratamiento de los delicados aspectos numéricos que pueden afectar a las simulaciones en tres dimensiones usando códigos basados en mallas cartesianas, en particular la falta de resolución, el tratamiento de la atmósfera numérica que rodea a la estrella, la corrección del desplazamiento del centro de masas y las propiedades de conservación de masa y momento lineal del esquema numérico. Las simulaciones revelan la compleja morfología involucrada en la dinámica no lineal de la inestabilidad. Encontramos que en la fase no lineal de la evolución, la excitación de modos tipo Kelvin-Helmholtz del fluido en el exterior del radio de corrotación de los modelos estelares estudiados, lleva a la saturación de la inestabilidad de tipo barra. Mientras que nuestro

trabajo confirma las tendencias generales mostradas en el trabajo de Shibata et al. (2002), la resolución usada para realizar las simulaciones puede jugar un papel relevante en el comportamiento a largo plazo de la inestabilidad y en la dinámica no-lineal de la estrella en rotación, que sólo se hace patente en un modelo específico de nuestra selección (el modelo D2). Estos resultados tienen implicaciones en las amplitudes alcanzables por las ondas gravitatorias asociadas.

Contents

Part I

INTRODUCTION

Chapter 1

Introduction

1.1 Gravitational wave astronomy

At the beginning of the twentieth century, Einstein's theory of General Relativity revolutionized our way of understanding the physical world by providing a new paradigm to describe not only the gravitation but also spacetime itself. Nowadays this theory is deeply established, and is in the grounds of most feasible models in cosmology and astrophysics. However, since relativity was first formulated, not all its predictions have been confirmed by observations. A remarkable example is the direct measurement of gravitational waves (GWs). At the dawn of the new century, a whole new branch of astronomy, gravitational wave astronomy, is emerging, devoted to the study of astrophysical and cosmological objects through the detection of the GWs they emit.

Detectable GWs are produced at strong and dynamical gravitational compact sources. They constitute an excellent tool for observing the most elusive parts of astrophysical objects, their deepest regions obscured to electromagnetic observations, like collapsing cores of supernovae or the neighborhood of black holes surrounded by infalling material. The perturbations of spacetime produced by the merging of black holes, invisible otherwise, will be amenable to detection, and complementary observations of known electromagnetic-radiating sources will be possible, as scenarios involving neu-

tron stars or white dwarfs. These observations will help us to better constrain parameters of these systems (mass, angular momentum, size, equation of state of nuclear matter). To boost the growth of this new branch of astronomy, a parallel and a tight development of detectors and source modelling appears indispensable.

During the last two decades a number of GW detectors have been designed. Huge laser interferometers have been built in Europe (VIRGO, GEO), USA (LIGO), and Japan (TAMA) to detect GWs in the kHz band. Extensions of these interferometers are planned (Advanced LIGO in USA, LCGT in Japan, and EURO in Europe), as well as a space-based interferometer (the ESA/NASA collaboration LISA) to observe in the mHz band. Source modelling, on the other hand, is necessary to establish which astrophysical and cosmological objects will be detectable in terms of both, amplitude of the signal and frequency range, as well as to provide feedback in the design of current and future detectors. But theoretical models are not only useful for the detector design, they are also an essential part of the detection process. The low signal-to-noise level of the detectors place challenging obstacles for successful detection, which observers can only pave away by using, whenever possible, specific techniques based on matched filtering. In such techniques GW templates provided by source modelling are crucial to help the data analysis. In addition, theoretical models are needed to interpret the GWs detected and to extract their physical content, the final goal of GW astronomy.

One of the most interesting astrophysical scenarios to search for GWs is the gravitational collapse of the inner iron cores of massive stars ($M \geq 8M_{\odot}$). The resulting object, a hot proto-neutron star (PNS hereafter) or a black hole surrounded by accreting material, lie at the heart of the models of some of the most energetic observable events in the universe: type Ib/Ic/II supernovae, gamma ray bursts (GRBs), and jet formation. These are all promising sources of GWs, and their theoretical investigation is of paramount interest in order to understand their observational implications. The main goal of this thesis is the study of the gravitational radiation produced in this particular scenario, the gravitational collapse of rotating stellar cores, and during the dynamical evolution of the PNS formed.

1.2 The core collapse paradigm

Nowadays, the accepted paradigm to explain type Ib/Ic/II supernovae is the core collapse mechanism. Although a number of questions still await to be addressed, the scientific progress achieved in the last decades have led to a wide consensus of how a supernova is produced. In the following we briefly describe the current understanding of the core collapse paradigm, addressing the interested reader to Arnett et al. (1989); Bethe (1990); Fryer & New (2003); Kotake et al. (2005a); Woosley & Janka (2005) for comprehensive reviews on the subject.

A star is an object in which the self-gravity and the pressure gradients struggle to reach an equilibrium. The high temperature and pressure of its interior ignites a chain of thermonuclear reactions beginning with the original fuel of the star, the hydrogen. Along the evolution of a massive star (between $9M_{\odot}$ and $30M_{\odot}$), the hydrogen is burned into helium, the helium into carbon and so on, forming in about ten million years a shell structure in which the different products of the various nuclear fusion processes are stratified. The last link in the chain ends with the formation of elements of the iron-nickel group, which are stable, as the nuclear binding energy reaches the minimum. These elements can not be burned any more and accumulate at the center in the so-called iron core. The iron core is fed by the silicon-burning shell surrounding it, and it grows until the so-called Chandrasekhar mass is reached. For such mass, of about $1.5M_{\odot}$, the degenerate relativistic electron pressure sustaining the iron core cannot counteract its self-gravity any longer and the collapse is inevitable.

Two processes induce the collapse. First, electron captures by nuclei reduce the electron pressure while the neutrinos produced carry away energy from the core. Second, for densities above 10^{10} g cm^{-3}, photodisintegration of the iron nuclei into helium (which is an endothermic process), cools the core. At the beginning of the collapse the iron core has a radius of about a few 1000 km, a central density of $\rho \sim 10^{10}$ g cm^{-3}, and a temperature of $T \sim 10^{10}$ K. Part of the gravitational binding energy of the core is released into kinetic energy which accelerates the infalling material to a significant fraction of the speed of light. Beyond densities of $\sim 10^{12}$ g cm^{-3} neutrinos become trapped and the composition quickly approaches beta-equilibrium when the density exceeds $\sim 10^{13}$ g cm^{-3}. As the trapped neutrinos only escape on their diffusion timescale

(larger than the collapse timescale), no further energy losses by neutrinos are produced, and the collapse proceeds almost adiabatically. While the density increases beta-equilibrium shifts towards more neutron-rich matter. As the density reaches nuclear matter density, $\rho_{\rm n} \sim 2 \times 10^{14}$ g cm^{-3}, nuclear forces between nucleons begin to play a prevailing role as the fundamental source of pressure. If the mass of the collapsing core is low enough not to undergo black hole formation, the collapse of the inner part is stopped at about $\sim$ 10 km, bouncing back and forming a strong shock wave that propagates outwards through the infalling material. As it propagates photo-dissociation of iron nuclei transform the kinetic energy of the shock into thermal energy, and, when the shock exits the neutrino sphere, neutrinos leave freely carrying energy from the shock. As a consequence the shock stalls at about 100 km after a few 10 ms. At this time a hot proto-neutron star has formed in the inner $\sim$ 30 km, with a huge amount of neutrinos trapped inside. Neutrino diffusion timescales become important, and copious amounts of thermal neutrino-antineutrino pairs are emitted, which carry away energy of the PNS and cool it to form a compact neutron star (NS hereafter) of $\sim$ 10 km. A small fraction of the immense energy that leaves with the neutrinos is deposited behind the stalled shock which is revived, and a delayed supernova explosion is produced. As the explosion reaches lower density regions, the shock accelerates and disrupts the whole star carrying away most of the mass. Only a fraction of about 1 $M_{\odot}$ remains at the center forming the neutron star. The electromagnetic radiation emitted by the outer layers forms the observable supernova.

1.3 Gravitational waves from core collapse

Not only electromagnetic radiation and neutrinos are emitted in the supernova explosion. The bulk motion of the collapsing star, that bounces at densities around nuclear matter density, produces a gravitational wave burst if aspherical. Depending on how the progenitor star rotates and on how the collapse proceeds, different types of waveforms are emitted (Zwerger & Müller 1997). Although the estimated amplitudes for realistic progenitors are small to be detectable in present-day GW detectors beyond the Galaxy (Müller et al. 2004), other processes can lead to stronger GWs after the collapse. In particular, convective motions behind the shock driven by neutrinos can lead to high-

amplitude GWs even for slowly rotating cores (Müller et al. 2004).

In addition, the rotating PNS itself is a very promising source of detectable GWs. For high enough rotation rates or for high degrees of differential rotation (which may not be realistic, as there is no known evolutionary path to such fast rotating PNS), nonaxisymmetric instabilities develop in dynamical timescales, namely the so-called bar-mode instability (Tohline et al. 1985; Shibata et al. 2002), which produce strong GW signals. When the neutron star has cooled to about 10^{10}K after its formation, it can be subject to the Chandrasekhar-Friedman-Schutz instability (Chandrasekhar 1970; Friedman & Schutz 1978) and it becomes an important source of gravitational waves (for a review see Stergioulas 2003). Therefore, a detailed modelling of the transformation of the hot PNS into a cold NS is essential in making predictions about the emission of GWs from NS. Particular attention has to be paid to the rotation rates, the distribution of angular momentum, and the magnetic field structure and strength.

1.4 Physics involved in the collapse

In order to properly study the gravitational collapse of iron cores and the emitted gravitational waves one has include a large number of physical ingredients. Here, we summarize the most important ones that have to be taken into account:

- **General relativity**: The mass involved in the core collapse is of the order of $\sim 1 M_{\odot}$. In the final stage of the collapse such mass is inside the PNS, which has a radius of a few 10 km. For such compact configurations general relativistic effect arise, and Newtonian gravity is not enough to describe both, the equilibrium and the dynamics. (see e.g. Misner et al. 1973, Chap. 29).

- **Equation of state for nuclear matter**: A thermodynamical description of nuclear matter is needed in order to correctly calculate the dynamics of the entire process, how the bounce proceeds and the final configuration of the PNS (see Glendenning 1997; Prakash et al. 2001, for reviews).

- **Neutrino transport**: This is a crucial aspect to include in the modelling to describe the delayed explosion mechanism, and also for the cooling of the newly formed PNS into the final NS (see Janka et al. 2005, and references therein).

- **Magnetic fields**: Observations suggest that magnetic fields could play a role in core collapse scenarios. The discovery of very asymmetric explosions (Wang et al. 1996, 2001; Leonard et al. 2001) and of Anomalous X-Ray Pulsars and Soft Gamma-Ray Repeaters, interpreted as very strongly magnetized neutron stars (magnetars) (Duncan & Thompson 1992; Thompson & Duncan 1996; Kouveliotou et al. 1999), make the study of magnetized core collapse of outstanding interest.

- **Other energy transport mechanisms**: Other mechanisms to transport energy inside the core do probably play a role in the dynamics of the core collapse and should not be neglected. Some of these are convection, turbulence, radiative transport, and diffusion by viscosity.

Needless to say, the inclusion of all such effects in a computer code is not affordable nowadays, mainly due to the prohibitive computational cost (both in terms of memory and running time) of the simulations required to describe the highly nonlinear dynamics involved in core collapse. Therefore, many simplifications need to be done. In the following section we summarize the different approaches to the modelling of core collapse that can be achieved nowadays.

1.5 State-of-the-art in numerical simulations of core collapse

1.5.1 Hydrodynamical core collapse

During the last three decades many efforts have been made to numerically simulate the collapse of stellar cores. As listed in the preceding section the main difficulties arise from the fact that many physical effects are involved in a process whose dynamics is highly nonlinear. Analytical approaches are of limited use to study core collapse and numerical simulations are needed to solve

the coupled system of equations describing the fluid motion, the spacetime evolution, the dynamics of the magnetic fields, and the neutrino transport. Numerical simulations are driving progress in the field of core collapse supernovae despite the limited knowledge on issues such as realistic precollapse stellar models (including rotation and magnetic field strength and distribution) or realistic equation of state, as well as numerical limitations due to Boltzmann neutrino transport, multidimensional hydrodynamics, and relativistic gravity. It is out of the scope of this introduction to review the field of existing simulations of core collapse supernovae, a topic which is covered in a number of excellent reviews (see e.g. Müller (1998) and references therein). Here, we limit ourselves to describe those representative simulations in which *gravitational waveforms have been extracted.* The reader is addressed to the online review by Fryer & New (2003) and references therein for further information.

Let us first begin with purely hydrodynamical simulations performed within the framework of Newtonian physics. This approach is characterized by simplified treatments for the fluid motion and spacetime dynamics, which allows to put most of the effort in issues such as realistic microphysics and approximate neutrino transport. Simulations are available in the literature, both in axisymmetry and in full 3D. First attempts used Eulerian codes with artificial viscosity (Müller 1982; Finn 1989; Mönchmeyer et al. 1991) to account for the presence of shock waves in the hydrodynamics. Pseudo-spectral methods were used in the 3D simulations of Bonazzola & Marck (1993), who could only follow the infalling phase of the entire process, due to the appearance of numerical instabilities associated with the presence of shocks. The need for correctly resolving the shock wave which forms after core bounce gradually led to the use of high-resolution shock-capturing (HRSC) schemes. Zwerger & Müller (1997) first used HRSC methods to simulate a sequence of collapsing rotating polytropes in axisymmetry and provided a comprehensive waveform catalog. Extensions to 3D were carried out by Rampp et al. (1998b); Fryer et al. (2004). In these works simple equations of state were used (e.g. Janka et al. (1993)). Recently, there have been attempts to include more realistic physics in Newtonian simulations: Ott et al. (2004) used the equation of state of Lattimer & Swesty (1991), while Müller et al. (2004) also incorporated 2D neutrino transport and computed the GW emission produced by neutrino-driven con-

vection [1]. Unfortunately, Newtonian physics does not suffice to fully describe the dynamics of the system nor the GWs emitted, and relativistic gravity and hydrodynamics had to be incorporated in the modelling (Dimmelmeier et al. 2001, 2002a,b).

General relativistic simulations involve the challenging computational task of solving Einstein's field equations coupled to the fluid evolution. This part is where the burden of the simulations resides, and less attention (compared to the case of Newtonian simulations) is paid to issues such as microphysics, where only simplified equations of state (polytropes, ideal gas, hybrid EOS), have been used so far. Most of the existing simulations are performed only in 2D and use the 3+1 formulation of Einstein's equations. This formulation (as well as recent reformulations of the 3+1 equations) is based on directly solving the hyperbolic equations for the three-metric and extrinsic curvature. The main drawback of this approach is the violation of the momentum and Hamiltonian constraints during the evolution due to numerical errors. Although significant improvements have been recently accomplished, 3+1-based formulations still lack robustness and stability for long-term evolutions, especially in spacetimes involving black holes (curvature singularities). An alternative approach relies on constrained evolution of Einstein's equations, explicitly solving the constraint equations to reduce the number of evolution equations. The basic formulation of this kind is the so-called *conformally flat condition*, or CFC (Isenberg 1978; Wilson et al. 1996), which is an approximation of Einstein's equations in which the spatial part of the metric is assumed to be comformally flat. This approximation, and its 2nd post-Newtonian extension CFC+ have proved very accurate to describe core collapse to neutron stars (Dimmelmeier et al. 2001, 2002b; Cerdá-Durán et al. 2005), even upon comparing to exact formulations such as BSSN (Shibata & Sekiguchi 2004). Contrary to ADM-like approaches, CFC/CFC+ are based on elliptic equations. The main drawback of both CFC and CFC+ is the fact that the gravitational waves degrees of freedom are lost in the approximation made. As a result GWs have to be extracted in an approximate way directly from the sources. Recently, a new constrained formulation has been proposed by Bonazzola et al. (2004), which appears very promising to solve Einstein's equations in a numer-

[1] We note that Müller et al. (2004) used a modified relativistic potential, and general relativistic effects were taken into account in the neutrino transport.

ically stable way. As for 3D general relativistic simulations of core collapse, numerical codes to study this problem have been developed only very recently, both based on the BSSN formulation (Shibata & Sekiguchi 2004, 2005), and on the CFC approximation (Dimmelmeier et al. 2005b).

1.5.2 Magnetized core collapse

Magneto-rotational core collapse simulations were first performed as early as 1970 (LeBlanc & Wilson 1970; Bisnovatyi-Kogan et al. 1976; Meier et al. 1976; Müller & Hillebrandt 1979; Ohnishi 1983; Symbalisty 1984). Nowadays, the inclusion of magnetic fields in the collapse modelling has been carried out by a growing number of groups, becoming the study of magneto-rotational collapse a very active field of research. All simulations performed so far have considered Newtonian magnetohydrodynamics and gravity, either using simplified parametric equations of state (Yamada & Sawai 2004; Ardeljan et al. 2005; Sawai et al. 2005; Obergaulinger et al. 2005) or more sophisticated microphysics. In the later case Kotake et al. (2004a,b); Takiwaki et al. (2004); Kotake et al. (2005b) used an equation of state based on the relativistic mean-field theory with a Thomas-Fermi approach, and a leakage scheme to treat the electron captures and the neutrino transport, while Akiyama et al. (2003) used a LLPR equation of state with one dimensional neutrino transport in the Fokker-Planck approximation. The interested reader is addressed to to Wheeler et al. (2002); Wheeler & Akiyama (2004) for reviews on this topic. Only very recently Obergaulinger et al. (2006) have performed simulations using a modified Newtonian potential to take into account general relativistic effects. But, to date, fully general relativistic simulations of magneto-rotational core collapse are not yet available in the literature.

The main implications of the presence of strong magnetic fields in the collapse are the redistribution of the angular momentum and the appearance of jet-like explosions. However, the presence of strong magnetic fields in the simulations needs to be justified, resorting to mechanisms for the amplification of the initial field which exists in weakly-magnetized progenitor stars. Different amplification processes have been taken into account in the different simulations listed before. As the collapse proceeds, differential rotation winds up the poloidal component of the magnetic field lines, creating a toroidal field (Meier et al. 1976). This mechanism extracts energy from the rotational energy of

the star into the magnetic field. If meridional flows are present, the toroidal field can be transformed into the poloidal one via the α-Ω-dynamo. Yet the most relevant mechanism is likely to be the so-called magneto-rotational instability (Balbus & Hawley 1998), which, irrespective of the initial strength of the magnetic field, may amplify it exponentially until it reachs saturation (about 10^15 G). Akiyama et al. (2003); Yamada & Sawai (2004); Kotake et al. (2005b); Sawai et al. (2005); Obergaulinger et al. (2005); Obergaulinger et al. (2006) have recently studied the effects of this instability in the context of magneto-rotational core collapse.

1.5.3 Gravitational wave extraction

Two main approaches have been traditionally followed to extract GWs from astrophysical sources. In the first approach the behaviour of the metric is directly computed in the wave zone, far from the sources, through a multipole expansion of the metric potentials when $r \to \infty$. Since GWs can be considered, in most cases, as small perturbations of the metric (the expected GW energy from a core collapse is $< 10^{-6} M_\odot c^2$), extensive work has been based upon perturbation theory (Regge & Wheeler 1957; Zerilli 1970; Moncrief 1974). For a recent review on perturbative approaches see Sasaki & Tagoshi (2003). The full nonlinear theory, the Bondi-Sachs-Penrose approach, has been developed by Bondi et al. (1962); Sachs (1962); Penrose (1963, 1965); Geroch & Horowitz (1978). This approach is very powerful, but only gives information about the metric in the limit where $r \to \infty$, and, therefore, there is no way to connect the GWs with the source. From the numerical point of view, this implies that one needs to numerically evolve the spacetime variables from the near zone (close to the sources) to the wave zone (asymptotically flat region) in full general relativity, and then extract the waveform in a gauge invariant way (Abrahams et al. 1992) by comparing with the linearized GW of perturbation theory. The spatial scales involved in this approach, in which the size of the computational grid needs to be much larger than the size of the sources, and the (demanding) numerical precision required to correctly extract the waveforms, make this approach ineffective for some scenarios, as core collapse, even for the present-day, largest supercomputers.

The second approach is the wave-generation formalism (see Blanchet 2002, for a review). In this case a multipolar and post-Minkowskian (PM) expan-

sion of the metric is performed. As this expansion is possible for the entire spacetime, it connects the gravitational waves at future null infinity with the sources. The problems arise when computing the required multipoles, as most of the integrals diverge. To solve this problem a regularization is needed, and in order to explicitly calculate the GWs a post-Newtonian (PN) expansion of the sources is necessary. Using both ingredients it is possible to calculate the GWs taking into account information from the sources only. Since this is the only information needed, no accuracy is lost because of wave evolution, and the waveforms are computed in a straightforward way even in a post-processing process of the simulated data. Within this approach the most commonly used approximation is the so-called Newtonian standard quadrupole formula [2], based upon a linearization of the gravitational radiation field and a Newtonian approximation of the sources.

It is worth noticing that in all simulations of core collapse performed to date, the gravitational wave signals have been extracted using the Newtonian quadrupole formula or, at most, higher order Newtonian multipoles have been employed (Mönchmeyer et al. 1991). The only remarkable exception is the work by Siebel et al. (2003), who used the Bondi news to extract the GWs directly at future null infinity. Comparisons between the quadrupole formula and gauge invariant calculations in pulsating neutron stars (Shibata & Sekiguchi 2003) show good agreement. This also holds true for the comparison between the quadrupole news and the Bondi news (Siebel et al. 2002), but however, significant disagreement is found between the latter two approaches in the case of core collapse simulations (Siebel et al. 2003).

1.6 Organization of the thesis

The remaining of this thesis is organized in four parts.

In Part II the theoretical framework for the results obtained in the thesis is presented. We describe the particular formalism of the general theory that we use (Chapter 2), the resulting equations for both relativistic hydrodynamics and magnetohydrodynamics (Chapter 3), and the approximations used to

[2] This formula is also referenced in the literature as Einstein quadrupole formula or Einstein-Landau-Lifshitz quadrupole formula.

formulate Einstein's equations: the comformally flat condition (CFC) approximation (Chapter 4) and the new CFC+ approximation (Chapter 5). At the end of this part we describe the formalism used for the computation of the gravitational waves in our simulations (Chapter 6) .

Part III is devoted to the numerical methods used to perform our simulations, for both the hydrodynamics and magnetohydrodynamics (Chapter 7), and for the metric evolution (Chapter 8).

In Part IV we present the results of our simulations and the tests performed to validate those simulations. In Chapter 9 we discuss our results on core collapse simulations in the CFC+ approximation for the metric, comparing this approach with CFC. General relativistic magnetized core collapse simulations are considered in Chapter 10. Chapters 11 and 12 are self-contained and discuss topics related to the aftermath of core collapse. The first chapter is devoted to the study of the long-term evolution of neutron stars after core collapse, and the second one to nonaxisymmetric bar-mode instabilities that can occur in rapidly rotating stars.

Finally, in Part V we summarize our results and give a brief outlook of some issues we plan to investigate in future work.

1.7 Conventions

We use a spacelike signature $(-,+,+,+)$ and units in which $c = G = 1$, except in some passages, particularly in the Appendices, where c and G are retained for a better understanding of the post-Newtonian expansion. For the Einstein's equations we use the sign convention of Misner et al. (1973). Greek indices run from 0 to 3, Latin indices from 1 to 3, and we adopt the standard Einstein convention for summation over repeated indices. The indices of three-vectors and three-tensors are raised and lowered by means of the three-metric.

Part II

THEORETICAL FRAMEWORK

Chapter 2

General framework

In this chapter we describe the basic physical principles that lie behind gravitational collapse. Owing to the compactness of the astrophysical objects involved in gravitational core collapse, i.e. the low value of the mass-to-radius ratio, Newtonian theory is insufficient to correctly describe the system, and it is necessary to employ Einstein's theory of general relativity. Although simple in concept, the mathematical structure of general relativity is far more involved than Newton's classical theory. Therefore, a careful choice of the formulation of Einstein's equations should be done, in order to perform numerical simulations successfully.

2.1 Einstein's equations

Spacetime is described as a four-dimensional pseudo-Riemannian manifold $\mathcal{M}$ with a non positive-definite metric $\mathbf{g}$. For a given set of coordinates $\{x^\mu\}$ the metric tensor $g_{\mu\nu}$ describes the line element as

$$ds^2 = g_{\mu\nu} dx^\mu dx^\nu, \tag{2.1}$$

and an inverse metric $g^{\mu\nu}$ can be defined by the fact that $g_{\alpha\mu} g^{\mu\beta} = \delta^\beta_\alpha$, with δ^β_α being the Kronecker delta. Given a metric $g_{\mu\nu}$, the curvature of spacetime

can be fully determined. The Riemann curvature tensor is defined as

$$R^{\rho}_{\sigma\mu\nu} \equiv \partial_{\mu}\Gamma^{\rho}_{\nu\sigma} - \partial_{\nu}\Gamma^{\rho}_{\mu_{\sigma}} + \Gamma^{\rho}_{\mu\lambda}\Gamma^{\lambda}_{\nu\sigma} - \Gamma^{\rho}_{\nu\lambda}\Gamma^{\lambda}_{\mu\sigma}, \tag{2.2}$$

where $\Gamma^{\lambda}_{\mu\nu}$ are the Christoffel symbols given by

$$\Gamma^{\lambda}_{\mu\nu} = \frac{1}{2}g^{\lambda\rho}\left(\frac{\partial g_{\rho\mu}}{\partial x^{\nu}} + \frac{\partial g_{\rho\nu}}{\partial x^{\mu}} - \frac{\partial g_{\mu\nu}}{\partial x^{\rho}}\right). \tag{2.3}$$

From the Riemann tensor related tensorial quantities can be derived as the Ricci tensor

$$R_{\mu\nu} \equiv R^{\sigma}_{\mu\sigma\nu}, \tag{2.4}$$

and the scalar curvature

$$R \equiv R^{\mu}_{\mu}. \tag{2.5}$$

Within this spacetime, Einstein's equations can be easily expressed in a covariant manner as

$$G_{\mu\nu} = 8\pi T_{\mu\nu}. \tag{2.6}$$

This rather compact form of the equations yields a relation between the mass and the energy content, given by the energy-momentum tensor $T_{\mu\nu}$, and the structure of the spacetime, given by the Einstein tensor

$$G_{\mu\nu} = R_{\mu\nu} - \frac{1}{2}g_{\mu\nu}R. \tag{2.7}$$

As a consequence of the symmetry properties of the Riemann tensor, the contracted Bianchi identities (see e.g. Misner et al. 1973, Chap. 15) lead to

$$G^{\mu\nu}{}_{;\nu} = 0, \tag{2.8}$$

where "$;\nu$" is the covariant derivative with respect to the metric $g_{\mu\nu}$. Through the Einstein's equations it immediately follows that

$$T^{\mu\nu}{}_{;\nu} = 0, \tag{2.9}$$

which expresses the local conservation law of energy and momentum.

Due to the mathematical structure of the Einstein's equations embedded into a pseudo-Riemannian spacetime, physical implications can not be easily interpreted, and some previous effort has to be done. The main difficulties can be summarized as follows:

- Contrary to Newtonian theory, built up in a three-dimensional space evolving in time, general relativity resides in a four-dimensional manifold in which the spacelike or timelike character of the coordinates is not a priori well defined.

- Einstein's equations tightly couple the spacetime geometry and the energy-matter content of the system and their evolution. The curvature of the spacetime is modified by the presence of an energy-matter distribution, but at the same time, the laws governing the evolution of the system depend on the curvature of the spacetime. Therefore, the resulting system of equations becomes highly nonlinear and coupled, what makes difficult to find solutions of Einstein's equations for a general dynamical scenario without time or space symmetries (and even if they are present).

- Spacetime geometry, represented by the symmetric metric tensor $g_{\mu\nu}$, can be described by six independent functions, the six physical degrees of freedom of the system. But it has ten components. Therefore, one has the freedom to select four gauge conditions to constrain the number of independent components of the metric.

As we want to perform numerical simulations of fluid evolution in dynamical spacetimes, the easiest approach is to adopt a formulation that allows us to separate time and space coordinates, and that allows one to numerically calculate the fluid evolution and the spacetime evolution in two consective steps. The rest of this chapter describes the general formalism we adopt for spacetime evolution, while the fluid evolution formalism is described in Chapter 3.

2.2 3+1 formalism

We adopt the $3+1$ formalism (Lichnerowicz 1944; Choquet-Bruhat 1952) to foliate the spacetime manifold $\mathcal{M}$ into a set of non-intersecting space-like hypersurfaces $\Sigma_{\hat{t}}$, parametrized by the scalar time parameter $\hat{t}$ (proper time) [1]. In this way, each hypersurface $\Sigma_{\hat{t}}$ contains the entire three-dimensional space for a given value of the timelike parameter $\hat{t}$. We can hence introduce a set

[1] Alternative formulations are available in the literature, see e.g. Winicour (2005) for a review on the characteristic formulation.

of coordinates $\{x^\mu\} = \{t; x^i\}$ covering the entire manifold $\mathcal{M}$ with a definite time or space character, as the coordinate t is timelike and x^i spacelike. This foliation allows us to treat the problem as an initial value problem. For initial conditions given at a certain initial proper time $\hat{t}_0$, i.e. for a matter-energy distribution at a certain time slice $\Sigma_{\hat{t}_0}$, we can evolve the system forward in time by means of Einstein's equations, until $\hat{t} > \hat{t}_0$. We define n^μ as a unit four-vector normal to the hypersurface and thus with timelike character:

$$n^\mu n_\mu = -1. \tag{2.10}$$

Consequently we can define the projection operator

$$\perp^\mu_\nu \equiv g^\mu_\nu + n^\mu n_\nu, \tag{2.11}$$

that projects tensor quantities from the four-dimensional manifold $\mathcal{M}$ onto the three-dimensional hypersurface $\Sigma_{\hat{t}}$. The result of projecting the metric $g_{\mu\nu}$ is the induced three-metric

$$\gamma_{ij} \equiv \perp^\mu_i \perp^\nu_j g_{\mu\nu}. \tag{2.12}$$

If we consider two time slices (see Fig. 2.1) $\Sigma_{\hat{t}}$ and $\Sigma_{\hat{t}+d\hat{t}}$ infinitesimally separated by $d\hat{t}$, the variation dt of the coordinate time t will depend on the location x^i on the hypersurface $\Sigma_{\hat{t}}$ as

$$d\hat{t} = \alpha dt. \tag{2.13}$$

The function α is the so-called lapse function which describes the rate of advance of time along n^μ. In general the world line of the observer associated with the chart $\{t; x^i\}$ is not tangent to n^μ. Thus, if we consider a point in $\Sigma_{\hat{t}}$ with coordinates $(t; x^i)$ and we project it along n^μ into $\Sigma_{\hat{t}+d\hat{t}}$, the spatial coordinates will be shifted into $(t + dt; x^i - \beta^i dt)$, where β^i is a space-like three-vector called shift vector. Taking this into account, the line element can be written as

$$ds^2 = -\alpha^2 dt^2 + \gamma_{ij}(dx^i + \beta^i dt)(dx^j + \beta^j dt), \tag{2.14}$$

where the ten independent components of the metric have been rewritten into the lapse function α, the shift vector β^i and the three-metric γ_{ij}. The vector n^μ can be expressed in terms of the metric as

$$n^\mu = \left(\frac{1}{\alpha}; \frac{\beta^i}{\alpha}\right) \tag{2.15}$$

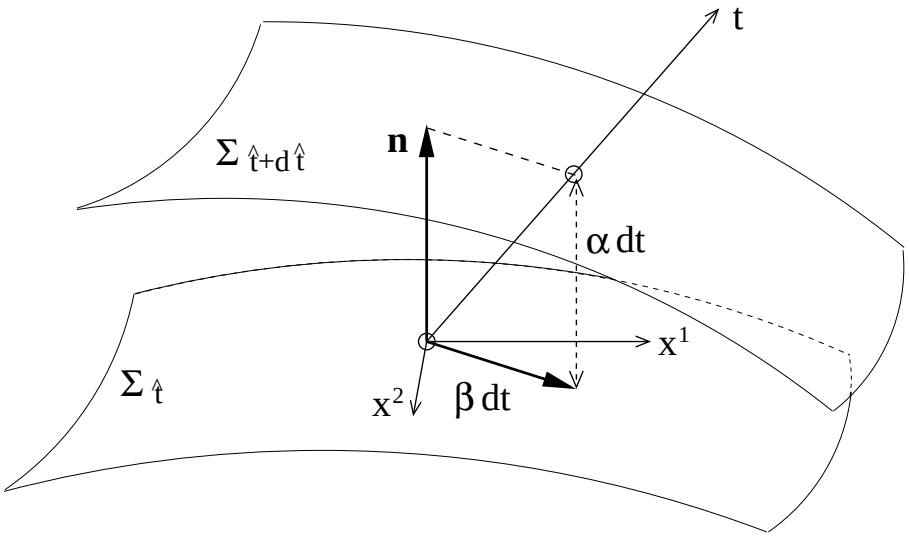

Figure 2.1: Schematic representation of the 3+1 foliation of the spacetime. See text for explanations.

Once the spacetime foliation is set up, we can project any tensor quantities from the four-dimensional manifold $\mathcal{M}$ onto a three-dimensional hypersurface $\Sigma_{\hat{t}}$ using the projection operator $\perp^{\mu}_{\nu}$, or along the time direction using n^{μ}. By applying such projections to the energy-momentum tensor $T^{\mu\nu}$ one obtains the following quantities:

$$E \equiv n^{\mu} n^{\nu} T_{\mu\nu} = \alpha^2 T^{00}, \tag{2.16}$$

$$S_i \equiv - \perp^{\mu}_{i} n^{\nu} T_{\mu\nu} = -\frac{1}{\alpha}(T_{0i} - T_{ij}\beta^j), \tag{2.17}$$

$$S_{ij} \equiv \perp^{\mu}_{i} \perp^{\nu}_{j} T_{\mu\nu} = T_{ij}, \tag{2.18}$$

which live in the hypersurface $\Sigma_{\hat{t}}$. Therefore, the spatial metric γ_{ij} is used to raise and lower indices

$$S^i \equiv \gamma^{ij} S_j, \tag{2.19}$$

$$S^{ij} \equiv \gamma^{ki}\gamma^{lj} S_{kl}, \tag{2.20}$$

$$S \equiv \gamma^{ij} S_{ij} \equiv S^i_i. \tag{2.21}$$

Another very helpful quantity in the hypersurface $\Sigma_{\hat{t}}$ is the extrinsic curvature defined as

$$K_{ij} = -\frac{1}{2}\mathcal{L}_{n^\mu}\gamma_{ij}, \tag{2.22}$$

where $\mathcal{L}_{n^\mu}$ is the Lie derivative with respect to n^μ [2].

In the $3+1$ formalism, the Einstein's equations split into (i) evolution equations for the three-metric γ_{ij} and the extrinsic curvature K_{ij},

$$\partial_t \gamma_{ij} = -2\alpha K_{ij} + 2\nabla_{(i}\beta_{j)}, \tag{2.23}$$

$$\begin{aligned}\partial_t K_{ij} = &-\nabla_i\nabla_j\alpha + \alpha(R_{ij} + KK_{ij} - 2K_{ik}K^k_j) \\ &+ \beta^k\nabla_k K_{ij} + 2K_{k(i}\nabla_{j)}\beta^k \\ &- 8\pi\alpha\Big(S_{ij} - \frac{\gamma_{ij}}{2}(S-E)\Big),\end{aligned} \tag{2.24}$$

and (ii) Hamiltonian and momentum constraint equations,

$$R + K^2 - K_{ij}K^{ij} - 16\pi E = 0, \tag{2.25}$$

$$\nabla_i(K^{ij} - \gamma^{ij}K) - 8\pi S^j = 0, \tag{2.26}$$

which must be fulfilled at every space-like hypersurface. In these equations ∇_i is the covariant derivative with respect to the three-metric γ_{ij}, and $K \equiv \gamma^{ij}K_{ij}$. Curly brackets around indices indicate symmetrization:

$$a_{(i}b_{j)} = \frac{1}{2}(a_i b_j + a_j b_i). \tag{2.27}$$

Additionally, it is interesting to take the trace of Eqs. (2.23) and (2.24), that lead to evolution equations for the determinant of the three-metric γ and for K,

[2] For a detailed discussion of the Lie derivative, see e.g.Wald (1984).

$$\partial_t \ln\gamma = -2\alpha K + 2\nabla_i\beta^i, \tag{2.28}$$

$$\partial_t K = \alpha(R + K^2) - \nabla^i\nabla_i\alpha + \beta^j\nabla_j K - 4\pi\alpha\,(3E - S)\,. \tag{2.29}$$

Given the mass-energy content of the system (i.e. the energy-momentum tensor $T_{\mu\nu}$) and its evolution, we can use the above equations to evolve the spacetime. The first set of equations, (2.23) and (2.24), are evolution equations for the six independent components of the three-metric γ_{ij}. The extrinsic curvature K_{ij} is an auxiliary variable used to cast the evolution system as a first order (in time) system. The second set of equations is formed by the so-called Hamiltonian constraint, Eq. (2.25), and the momentum constraint, Eq. (2.26). In total there are ten equations (not including the 6 auxiliary equations for K_{ij}) and ten unknowns: α, β_i and the six independent components of γ_{ij}. Therefore, we still have to select four gauge conditions in order to reduce the number of variables to the 6 physical degrees of freedom. This implies the choice of the observer associated with the coordinates, and thus values for α and β^i. It is also possible to impose conditions for the three-metric in such a way that they constrain the values of α and β^i. By the term *slicing* we usually refer to the gauge conditions imposed to the lapse or to those that constrain its value, and by *spatial gauge* we refer to those conditions that restrict the choice of the shift vector. The gauge choice is crucial in order to successfully solve Einstein's equations for a given problem, either analytically or numerically. Depending on the choice, four of the ten equations will be removed. Therefore, one has to think beforehand about the equations to solve before imposing the gauge conditions. Typically two approaches are followed in the literature:

Hyperbolic formulations: In this family of formulations the gauge conditions are such that only hyperbolic equations are solved, and the constraints are automatically preserved if they were fulfilled at the initial time. This is done usually by imposing gauge conditions directly to the lapse and shift. With this choice, one can remove the constraint equations from the evolution scheme, and the six physical degrees of freedom are contained into the three-metric. The remaining equations are hyperbolic and therefore form an initial value problem. Different formulations exist, which mainly differ by the choice

of variables to evolve. A variation of the 3+1 decomposition is the ADM formulation (Arnowitt et al. 1962) that evolves γ_{ij} and its conjugate momentum π^{ij} (instead of K_{ij}), yielding a Hamiltonian approach to the equations. The most promising formulation, from the numerical point of view, is the so-called BSSN (Baumgarte & Shapiro 1999; Shibata & Nakamura 1995) formulation and its multiples variations, that are extensively used in numerical relativity (see e.g. Reula 1998; Alcubierre 2005; Shapiro 2005). The main drawback of these formulations appears in numerical simulations. Since the constraint equations are not explicitly solved, numerical errors rise which produce violations of the constraints growing with time. This fact limits their applicability to perform long time evolution of dynamical spacetimes, particularly in the presence of curvature singularities.

Constrained evolution formulations: The second approach is based on imposing conditions on the three-metric, in such a way to restrict the values for the lapse. The resulting slicing condition leads to an elliptic equation for the lapse function, α. Together with the constraint equations 2.25 and 2.26 it yields a system of five elliptic equations (four physical degrees of freedom + one slicing condition). The system is completed with two hyperbolic or parabolic equations, for the remaining two degrees of freedom which take into account the gravitational waves at large distances from the sources. In this case we have mixed initial boundary value problem. Examples of formulations of this kind can be found in Bonazzola et al. (2004) and references therein. Furthermore this type of formulations has been extensively used for stationary problems, such as to build equilibrium models of e.g. isolated netron stars in equilibrium, sequences of binary black holes and binary neutron stars. In these cases, time derivatives disappear and only four elliptic equations remain. There are also approximate formulations, that can be used for dynamical spacetimes if the assumptions done in the approximation are fulfilled in a particular scenario. Some of these approximate formulations are:

- The post-Newtonian (PN) approximation (see e.g. Misner et al. 1973; Blanchet 2002, and references therein), in which all quantities are expanded in powers of v/c, truncating the equations at some order. The gauge used in these calculations is such that low order expansions (up to 2 PN) are purely elliptic, and only at further extensions (from 2.5 PN)

GWs degrees of freedom appear and, therefore, also hyperbolic equations. The well-known Newtonian approximation, as a 0 PN expansion, is a formulation of this kind in which only one elliptic equation, the Poisson equation, has to be solved.

- The conformally flat condition (CFC) (see below and Isenberg 1978; Wilson et al. 1996), that consists in removing degrees of freedom contained in γ_{ij} and only solving the constraints.
- CFC+ (presented as part of this thesis and in Cerdá-Durán et al. 2005) is a post-Newtonian correction to the CFC metric.
- The Minimal no-radiation approximation (Schäfer & Gopakumar 2004), that tries to maximize the ellipticity of the system of equations, by removing only "hyperbolic" (radiative) degrees of freedom.

These formulations do not have the problem of constraint violation during a numerical evolution, as constraint equations are solved at each time step, allowing for more stable and longer evolutions than hyperbolic formalisms.

As a drawback, elliptic equations have to be numerically solved, which implies more computational effort in the full three-dimensional case. Furthermore, approximate formulations used to perform constrained numerical simulations of dynamical spacetimes loose some physical content in the approximation process. For example, CFC, CFC+ and PN approximations up to order 2, do not contain gravitational wave information. This implies that the system cannot loose energy or momentum carried away by GWs and that waveforms cannot be extracted directly from the metric (but can be extracted in other ways). However, since GW effects are usually small to affect the dynamics of the systems we study in a significant way, such drawbacks are innocuous.

2.3 The gauge conditions

2.3.1 General metric decomposition

A general three-metric in the $3+1$ decomposition can be written as

$$\gamma_{ij} = \phi^4 \hat{\gamma}_{ij} + \gamma_{<ij>}, \tag{2.30}$$

where $\hat{\gamma}_{ij}$ is the flat three metric (in a Cartesian basis $\hat{\gamma}_{ij} = \delta_{ij}$). The function ϕ, the conformal factor, is related to the trace of the three-metric $\hat{\gamma}^{kl}\gamma_{kl}$, and $\gamma_{<ij>}$ is the traceless part of γ_{ij}. These quantities are defined as

$$\gamma_{<ij>} \equiv \gamma_{ij} - \frac{1}{3}\hat{\gamma}^{kl}\gamma_{kl}\hat{\gamma}_{ij}, \tag{2.31}$$

$$\phi^4 \equiv \frac{1}{3}\hat{\gamma}^{ij}\gamma_{ij}. \tag{2.32}$$

For an asymptotically flat space $\phi \to 1$ and $\gamma_{<ij>} \to 0$ at infinity, to recover the flat metric $\hat{\gamma}_{ij}$. In the particular case of spherically symmetric spacetimes, the three-metric becomes conformal to the flat three-metric, although a general metric does not show explicitly this behavior but for a specific set of coordinates, i.e. for some spatial gauge conditions. This special set of coordinates is called isotropic coordinates. In the form of the three-metric given by Eq. (2.30), a spherically symmetric spacetime in isotropic coordinates is such that $\gamma_{<ij>} = 0$. This coordinate choice in spherical symmetry is unique. It can guide the choice of coordinate systems for non spherical spacetimes with the condition that they reduce to the isotropic coordinates in the particular case of spherical symmetry. Examples of this kind of spatial gauges are the quasi-isotropic (QI) coordinates, the Dirac gauge, and the ADM gauge. We will discuss briefly these three spatial gauges, as they are of special interest for the work presented in this thesis. In addition to the spatial gauge a slicing condition must be chosen in order to complete the four gauge conditions. As we are interested in constrained formulations of Einstein's equations, we will describe the maximal slicing condition.

2.3.2 Quasi-isotropic coordinates

In the particular case of axisymmetric spacetimes, a symmetry given by a spacelike Killing vector exists, and therefore the number of physical degrees of freedom is reduced to five. In this case it is natural to select the x^3 coordinate as the azimuthal component φ in the direction of the Killing vector associated with the symmetry. Thus, the coordinate system becomes $\{t; x^1, x^2, \varphi\}$. The

metric can be written in this case as

$$\begin{aligned} ds^2 = &- \alpha^2 dt^2 + \gamma_{\varphi\varphi}(d\varphi - \beta^\varphi dt)^2 + \gamma_{11}(dx^1 - \beta^1 dt)^2 \\ &+ \gamma_{22}(dx^2 - \beta^2)^2 + 2\gamma_{12}(dx^1 - \beta^1 dt)(dx^2 - \beta^2 dt), \end{aligned} \tag{2.33}$$

with eight independent components α, β^i, $\gamma_{\varphi\varphi}$, γ_{11}, γ_{22} and γ_{12}. In this case it is very useful to use the QI coordinates defined as those in which the components of the three-metric expressed in an orthonormal basis are $\gamma_{12} = 0$ and $\gamma_{11} = \gamma_{22}$. These two conditions together with a slicing condition, reduce the number of independent variables to the five degrees of freedom of axisymmetric spacetimes.

2.3.3 Dirac gauge

This gauge was originally introduced by Dirac (1959) in Cartesian coordinates, and has been extended to a general type of coordinates (e.g. spherical) by Bonazzola et al. (2004). We define the conformal metric as

$$\gamma_{ij}^{(\mathrm{conf.})} \equiv \bar{\gamma}^{-1/3}\gamma_{ij}, \tag{2.34}$$

where $\gamma_{ij}^{(\mathrm{conf.})}$ is invariant under conformal trasformations of the three-metric γ_{ij}, and where

$$\bar{\gamma} \equiv \gamma/\hat{\gamma}, \tag{2.35}$$

$\hat{\gamma}$ being the determinant of the flat three-metric (in Cartesian coordinates $\hat{\gamma} = 1$). One can then define h^{ij} such that

$$\gamma^{(\mathrm{conf.})ij} = \hat{\gamma}^{ij} + h^{ij}. \tag{2.36}$$

Following the terminology of Bonazzola et al. (2004), the generalized Dirac gauge consists in making the conformal metric transverse, i.e.

$$\hat{\nabla}_i \gamma^{(\mathrm{conf.})ij} = \hat{\nabla}_i h^{ij} = 0, \tag{2.37}$$

where $\hat{\nabla}_i$ is the covariant derivative with respect to the flat metric $\hat{\gamma}_{ij}$. With this choice, the traceless part of the three-metric $\gamma_{<ij>}$ is asymptotically transverse far from the sources, as the spacetime becomes flat ($\bar{\gamma} \to 1$).

2.3.4 ADM gauge

This gauge is defined as the gauge for which the three-metric can be decomposed into a conformally flat term plus a transverse traceless term,

$$\gamma_{ij} = \phi^4 \hat{\gamma}_{ij} + h_{ij}^{\rm TT}, \tag{2.38}$$

with

$$h_{ij}^{\rm TT} \hat{\gamma}^{ij} = 0, \qquad \hat{\gamma}^{ik} \hat{\nabla}_k h_{ij}^{\rm TT} = 0, \tag{2.39}$$

where ϕ is the conformal factor, and $h_{ij}^{\rm TT}$ is transverse and traceless. The conjugate momentum π^{ij} of γ_{ij} is traceless as well:

$$\pi^{ij} \hat{\gamma}_{ij} = 0. \tag{2.40}$$

Although the ADM gauge is similar to the Dirac gauge, there are important differences to point out. While in the Dirac gauge $\gamma_{<ij>}$ is asymptotically transverse, in the ADM gauge $\gamma_{<ij>} = h_{ij}^{\rm TT}$ is transverse everywhere. This condition eliminates the three degrees of freedom coming from the traceless but not transverse part of the three-metric. The ADM gauge has been extensively used in Post-Newtonian expansions (see Blanchet et al. 1990, and references therein), hence it is of paramount importance in the development of the CFC+ formalism.

2.3.5 The maximal slicing condition

The three possible gauge choices explained above (QI, Dirac, and ADM), remove three non-physical degrees of freedom (QI only removes two, but as it is used in axisymmetric spacetimes an aditional symmetry condition is imposed). Therefore, we still need to impose a fourth gauge condition for the lapse function in order to solve Einstein's equations. Usually the maximal slicing (MS) condition is used, i.e. we require the trace of the extrinsic curvature to vanish, $K = 0$. This condition transforms the hyperbolic equation (2.24) for the evolution of K into an elliptic equation for the lapse

$$\Delta \alpha = \alpha R - 4\pi \alpha \left(3E - S\right), \tag{2.41}$$

where the scalar curvature can be calculated from the Hamiltonian constraint equation (2.25) as

$$R = K_{ij} K^{ij} + 16\pi E. \tag{2.42}$$

Eq. (2.41), together with the three momentum constraints (2.26) under the assumption of maximal slicing

$$\nabla_i K^{ij} - 8\pi S^j = 0, \tag{2.43}$$

completes the set of four elliptic equations characteristic of constrained evolution formulations of Einstein's equations. The character of the remaining equations will depend on the spatial gauge chosen, on the particular choice of the variables, and on the approximations done.

Chapter 3

General relativistic hydrodynamics and magnetohydrodynamics

In this chapter we describe the equations governing the dynamics of fluids and electromagnetic fields in general relativity. We cast these equations in forms which are suitable for their numerical solution. We assume that the fluid has no viscosity (perfect fluid) and is a perfect conductor of infinite conductivity (ideal MHD condition). Under these assumptions the equations are greatly simplified. For a more extended discussion see Font (2003); Antón et al. (2006) and references therein.

3.1 General relativistic hydrodynamics

3.1.1 Conservation laws

We consider a perfect fluid of rest-mass current J^μ and energy-momentum tensor $T_{\mu\nu}$,

$$J^\mu = \rho u^\mu, \tag{3.1}$$
$$T_{\mu\nu} = \rho h u_\mu u_\nu + P g_{\mu\nu}, \tag{3.2}$$

where u_μ is the four-velocity of the fluid, ρ the rest-mass density, P the pressure, and h the relativistic enthalpy defined by

$$h = 1 + \epsilon + P/\rho, \tag{3.3}$$

ϵ being the specific internal energy. The evolution of the fluid is determined by the energy-momentum conservation laws and by the continuity equation (conservation law for the rest-mass current),

$$T^{\mu\nu}{}_{;\mu} = 0, \tag{3.4}$$
$$J^\mu{}_{;\mu} = 0. \tag{3.5}$$

Additionally to the conservation equations, one has to consider an equation of state $P = P(\rho, \epsilon)$ in order to close the system.

Following the derivation laid out in Banyuls et al. (1997), if we consider an Eulerian observer at rest in a spacelike hypersurface Σ_t, the three-velocity as measured by this observer reads

$$v^i = \frac{u^i}{\alpha u^0} + \frac{\beta^i}{\alpha}, \tag{3.6}$$

and the Lorentz factor, defined as $W \equiv \alpha u^0$, satisfies the relation

$$W = \frac{1}{\sqrt{1 + \gamma_{ij} v^j v^i}}. \tag{3.7}$$

Upon the introduction of a suitable set of conserved quantities (the relativistic

densities of mass, momentum, and energy)

$$D \equiv -J^{\mu} n_{\mu} = \rho W, \tag{3.8}$$

$$S^{i} = \rho h W^{2} v^{i}, \tag{3.9}$$

$$\tau \equiv E - D = \rho h W^{2} - P - D, \tag{3.10}$$

defined from the projections E, S^i of the $T^{\mu\nu}$ (Eqs. 2.16 and 2.17), it was shown by Banyuls et al. (1997), that the conservation laws of stress-energy and rest-mass current can be cast as a first-order, flux-conservative hyperbolic system of equations [1]:

$$\frac{1}{\sqrt{-g}} \left[\frac{\partial \sqrt{\gamma} \boldsymbol{U}}{\partial t} + \frac{\partial \sqrt{-g} \boldsymbol{F}^{i}}{\partial x^{i}} \right] = \boldsymbol{Q}, \tag{3.11}$$

with the state vector, flux vector, and source vector given by

$$\boldsymbol{U} = [D, S_j, \tau], \tag{3.12}$$

$$\boldsymbol{F}^{i} = \left[D\hat{v}^{i}, S_j \hat{v}^{i} + \delta^{i}_{j} P, \tau \hat{v}^{i} + P v^{i} \right], \tag{3.13}$$

$$\boldsymbol{Q} = \left[0, \frac{1}{2} T^{\mu\nu} \frac{\partial g_{\mu\nu}}{\partial x^{j}}, \alpha \left(T^{\mu 0} \frac{\partial \ln \alpha}{\partial x^{\mu}} - T^{\mu\nu} \Gamma^{0}_{\mu\nu} \right) \right], \tag{3.14}$$

where $\hat{v}^i = v^i - \beta^i/\alpha$.

If we integrate the system (3.11) inside a volume $V \equiv \int d\boldsymbol{x}^3 \sqrt{\bar{\gamma}}$, then

$$\frac{\partial}{\partial t} \int_V d\boldsymbol{x}^3 \sqrt{\bar{\gamma}} \boldsymbol{U} + \int_V d\boldsymbol{x}^3 \frac{\partial (\alpha \sqrt{\bar{\gamma}} \boldsymbol{F}^{i})}{\partial x^{i}} = \int_V d\boldsymbol{x}^3 \alpha \sqrt{\bar{\gamma}} \boldsymbol{Q}. \tag{3.15}$$

Applying Gauss theorem on the surface $A = \partial V$ enclosing volume V the above equation reads

$$\frac{\partial}{\partial t} \int_V dV \ \boldsymbol{U} + \oint_{\partial V = A} dA_i \ (\alpha \boldsymbol{F}^{i}) = \int_V dV \ (\alpha \boldsymbol{Q}), \tag{3.16}$$

[1] To write the conservation laws we have chosen a coordinate basis $\{e_i\} = \{\frac{\partial}{\partial x^i}\}$ (see section 8.4 in Misner et al. 1973). Note that this basis in not normalized, and therefore some operators, in particular divergence, curl and surface and line elements, are different to the usual ones in an orthonormal basis. Eqs. (3.19) are a version of these equations in a general basis.

where $dV = \sqrt{\bar{\gamma}} d\boldsymbol{x}^3$ and $dA_i = \sqrt{\bar{\gamma}} d\hat{A}_i$ are the volume and surface elements respectively, $d\hat{A}_i$ being the coordinate surface element (e.g. in Cartesian coordinates x^1, x^2, x^3 they read $dV = dx^1 dx^2 dx^3$ and $d\hat{A}_i = dx^j dx^k$ with $i \neq j \neq k$). We can interpret Eq. (3.16) as a conservation law for $\boldsymbol{U}$ integrated in V, with a flux $\alpha \boldsymbol{F}^i$ over the surface A and sources $\alpha \boldsymbol{Q}$. Since the metric terms appearing in dV evolve in time, it is better to study the conservation laws inside a coordinate volume $\hat{V} \equiv \int d\boldsymbol{x}^3$. Thus, we define the new conserved quantities D^*, S_j^*, and τ^* related to the original ones as

$$D^* \equiv \sqrt{\bar{\gamma}} D; \qquad S_i^* \equiv \sqrt{\bar{\gamma}} S_i; \qquad \tau^* \equiv \sqrt{\bar{\gamma}} \tau, \tag{3.17}$$

so that Eq. (3.16) reads

$$\frac{\partial}{\partial t} \int_{\hat{V}} d\boldsymbol{x}^3 \boldsymbol{U}^* + \oint_{\partial \hat{V} = \hat{A}} d\hat{A}_i \ \boldsymbol{F}^{*i} = \int_{\hat{V}} d\boldsymbol{x}^3 \boldsymbol{Q}^*, \tag{3.18}$$

where $\boldsymbol{U}^* \equiv \sqrt{\bar{\gamma}} \boldsymbol{U}$, $\boldsymbol{F}^{*i} \equiv \alpha \sqrt{\bar{\gamma}} \boldsymbol{F}^i$ and $\boldsymbol{Q}^* \equiv \alpha \sqrt{\bar{\gamma}} \boldsymbol{Q}$ represent the state vector inside $\hat{V}$, the fluxes over the surface $\hat{A}$, and the sources, respectively. This interpretation is very useful when performing numerical simulations with finite volume schemes, in which the volumes are going to be cells of constant coordinate volume $\hat{V}$.

3.1.2 The Riemann problem

An important property of the system of Eqs. (3.11) is that it is hyperbolic for causal EOS (Anile 1989). To simplify the notation we can rewrite this system of equations in terms of the conserved quantities inside a coordinate volume,

$$\frac{\partial \boldsymbol{U}^*}{\partial t} + \frac{1}{\sqrt{\hat{\gamma}}} \frac{\partial \sqrt{\hat{\gamma}} \boldsymbol{F}^{*i}}{\partial x^i} = \boldsymbol{Q}^*, \tag{3.19}$$

where the operator acting on $\boldsymbol{F}^{*i}$ is the flat nabla operator

$$\hat{\nabla}_i \equiv \frac{1}{\sqrt{\hat{\gamma}}} \frac{\partial}{\partial x^i} \left(\sqrt{\hat{\gamma}} \right). \tag{3.20}$$

For hyperbolic systems of conservation laws, the associated flux-vector Jacobians in every direction are

$$\boldsymbol{B}^i \equiv \frac{\partial \boldsymbol{F}^{*i}}{\partial \boldsymbol{U}^*} = \alpha \frac{\partial \boldsymbol{F}^i}{\partial \boldsymbol{U}}, \tag{3.21}$$

since the flux in each direction $\boldsymbol{F}^{*i}$ is a function of $\boldsymbol{U}^*$. These Jacobian matrices have real eigenvalues and a complete set of eigenvectors.

Information about the solution of the system propagates at finite velocities given by the eigenvalues of the Jacobians. Hence, if the solution is known (in some spatial domain) at some given time, this fact can be used to advance the solution to some later time (initial value problem, IVP). However, in general, it is not possible to derive the exact solution for the time evolution of the IVP. Instead one has to rely on numerical methods which provide an approximation to the solution. Moreover, these numerical methods must be able to handle discontinuous (weak) solutions, which are inherent to nonlinear hyperbolic systems.

The simplest one-dimensional IVP with discontinuous data is called a Riemann problem, in which the initial state consists of two constant states separated by a discontinuity. The majority of modern finite-volume numerical methods, the so-called Godunov-type methods, are based on exact or approximate solutions of Riemann problems (see Leveque 1990; Toro 1999, and references therein).

As the state vector and the fluxes have five components, the three flux-vector Jacobians, $\boldsymbol{B}^i$ are 5×5 matrices. The solution of the associated eigenvalue problem is such that

$$\boldsymbol{B}^i = \boldsymbol{R}^i \boldsymbol{\Lambda}^i (\boldsymbol{R}^i)^{-1} = \boldsymbol{R}^i \boldsymbol{\Lambda}^i \boldsymbol{L}^i, \tag{3.22}$$

$\boldsymbol{\Lambda}^i$ being the diagonal matrices of eigenvalues for each spatial direction

$$\lambda_0^i = \alpha v^i - \beta^i, \tag{3.23}$$

$$\lambda_\pm^i = \frac{\alpha}{1 - v^i v_i c_s^2} \Bigg\{ v^i (1 - c_s^2) \tag{3.24}$$

$$\pm c_s \sqrt{(1 - v^j v_j)[\gamma^{ii}(1 - v^j v_j c_s^2) - (v^i)^2 (1 - c_s^2)]} \Bigg\} - \beta^i, \tag{3.25}$$

where c_s is the sound speed and λ_0^i has a threefold degeneracy. The right eigenvectors $r_{0,j}^i, r_\pm^i$ (columns of $\boldsymbol{R}^i$) and the left eigenvectors $l_{0,j}^i, l_\pm^i$ (rows of $\boldsymbol{L}^i$) can be found in Ibáñez et al. (1999); Font (2003).

If one considers now a one dimensional problem in the x direction without

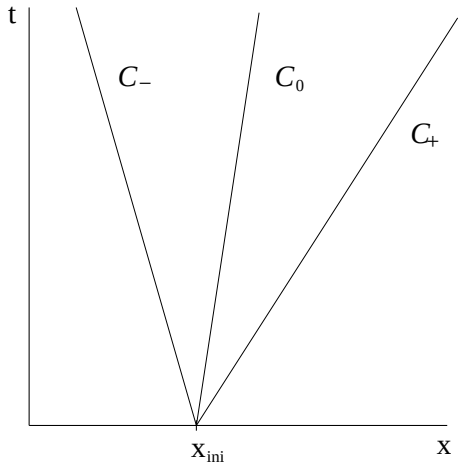

Figure 3.1: Characteristics $C_{0,\pm}$ of the system, along which the initial value of $[\boldsymbol{V}(t=0;x_{\rm ini})]_{0,\pm}$ propagates.

sources ($\boldsymbol{Q}^*=0$) the conservation laws (3.19) can be written as

$$\frac{\partial \boldsymbol{U}^*}{\partial t}+\boldsymbol{B}^x\frac{\partial \boldsymbol{U}^*}{\partial x}=0 \tag{3.26}$$

The equations can be completely decoupled in the linear case in which the eigenvalues, $\lambda^x_a(a=0,\pm)$, do not depend on the state vector $\boldsymbol{U}^*$. The resulting decoupled (advection) equations are

$$\frac{\partial \boldsymbol{V}}{\partial t}+\boldsymbol{\Lambda}^x\frac{\partial \boldsymbol{V}}{\partial x}=0, \tag{3.27}$$

for the new variables $\boldsymbol{V}\equiv\boldsymbol{R}^x\boldsymbol{U}^*\boldsymbol{L}^x$. The solution of this linear Riemann problem is trivial and reads

$$[\boldsymbol{V}(t;x)]_a=[\boldsymbol{V}(t=0;x-\lambda^x_a t)]_a \quad ; \quad a=0,\pm \tag{3.28}$$

in which the information at $t=0$ propagates along the characteristics $x=x_0+\lambda^x_a t$ as depicted in Fig. 3.1.

In the most general nonlinear case in which the system of equations has sources, the eigenvalues depend on the evolved variables, and the fluxes in the three directions are considered, the previous solution is only valid locally, but

is still useful to understand the behavior of hyperbolic systems of conservation laws. The use of exact Riemann solutions of linearized systems of conservation laws, and the associated wave information, is at the basis of approximate Riemann solvers (upwing Godunov methods)(see e.g. Roe 1981; Leveque 1990). As a conclusion, the characteristic information of the system (eigenvalues and eigenvectors) gives important information about the behavior of the system, and, therefore, it is helpful in order to design a numerical method for solving the conservation laws. How this can be done is discussed in Chapter 7.

3.2 General relativistic magnetohydrodynamics

3.2.1 Maxwell's equations

A general description for the electromagnetic field in general relativity is given by the Faraday tensor $F^{\mu\nu}$, which is related to the electric field E^μ and the magnetic field B^μ as measured by an observer with four-velocity U^μ

$$F^{\mu\nu} = U^\mu E^\nu - U^\nu E^\mu - \varepsilon^{\mu\nu\lambda\delta} U_\lambda B_\delta, \tag{3.29}$$

where $\varepsilon^{\mu\nu\lambda\delta}$ is the permutation tensor for the metric $g_{\mu\nu}$. It can be written in terms of the flat permutation tensor as $\varepsilon^{\mu\nu\lambda\delta} = \frac{1}{\alpha\sqrt{\hat{\gamma}}}\hat{\varepsilon}^{\mu\nu\lambda\delta}$, where

$$\hat{\varepsilon}^{\mu\nu\lambda\delta} \equiv \begin{cases} \frac{1}{\sqrt{\hat{\gamma}}} & \text{if } \mu\nu\lambda\delta \text{ is an even permutation of } 0123 \\ -\frac{1}{\sqrt{\hat{\gamma}}} & \text{if } \mu\nu\lambda\delta \text{ is an odd permutation of } 0123 \\ 0 & \text{otherwise} \end{cases} \tag{3.30}$$

The dual of the Faraday tensor reads

$${}^*F^{\mu\nu} = \frac{1}{2}\varepsilon^{\mu\nu\lambda\delta} F_{\lambda\delta} = U^\mu B^\nu - U^\nu B^\mu + \varepsilon^{\mu\nu\lambda\delta} U_\lambda E_\delta. \tag{3.31}$$

In this way the electric and magnetic field measured by U^μ can be calculated as

$$E^\mu = F^{\mu\nu} U_\nu, \qquad B^\mu = {}^*F^{\mu\nu} U_\nu. \tag{3.32}$$

The corresponding expressions for the comoving observer with four-velocity u^μ read

$$e^\mu = F^{\mu\nu}u_\mu, \qquad b^\mu = {}^*F^{\mu\nu}u_\nu. \tag{3.33}$$

In terms of the Faraday tensor Maxwell's equations read

$${}^*F^{\mu\nu}{}_{;\nu} = 0, \qquad F^{\mu\nu}{}_{;\nu} = 4\pi\mathcal{J}^\mu, \tag{3.34}$$

where $\mathcal{J}^\mu$ is the electric four-current, which, under the assumption that Ohm's law is fulfilled, reads

$$\mathcal{J}^\mu = \rho_q u^\mu + \sigma F^{\mu\nu}u_\nu = \rho_q u^\mu + \sigma e^\mu, \tag{3.35}$$

ρ_q being the proper charge density and σ the electric conductivity.

Maxwell's equations can be simplified if the fluid is a perfect conductor. In this case the conductivity of the fluid is infinite $\sigma \to \infty$ and, to keep the current finite, the term $F^{\mu\nu}u_\nu$ in Eq. (3.35) must vanish, which results in a vanishing electric field for the comoving observer $e^\mu = 0$. This case corresponds to the so-called ideal magnetohydrodynamics (MHD) condition, or ideal GRMHD in the general relativistic case. Under this condition the four-vector electric field E^μ can be expressed in terms of the four-vector magnetic field B^μ as

$$E^\mu = \frac{1}{W}\varepsilon^{\mu\nu\lambda\delta}u_\nu U_\lambda B_\delta. \tag{3.36}$$

It is very convenient to choose as observer the Eulerian observer, $U^\mu = n^\mu$, for which the temporal component of the electric field vanishes

$$E^0 = 0, \qquad E^i = -\varepsilon_{ijk}v^j B^k. \tag{3.37}$$

We can rewrite this equation in terms of vectors as

$$\vec{E} = -\sqrt{\gamma}\,\vec{v}\times\vec{B}, \tag{3.38}$$

where $\vec{E}$, $\vec{v}$ and $\vec{B}$ are vectors of components E^i, v^i and B^i respectively. The cross product $\times$ in Eq. (3.38) is defined with respect to the flat three-metric $\hat{\gamma}_{ij}$. Hence, the electric field can always be expressed in terms of the magnetic field and therefore we only need equations for B^i. In this case the first set of

Maxwell's equations ${}^*F^{\mu\nu}{}_{;\nu} = 0$ reduce to the divergence-free condition plus the induction equation for the magnetic field

$$\frac{1}{\sqrt{\gamma}}\frac{\partial(\sqrt{\gamma}B^i)}{\partial x^j} = 0, \tag{3.39}$$

$$\frac{1}{\sqrt{\gamma}}\frac{\partial(\sqrt{\gamma}B^i)}{\partial t} = \frac{1}{\sqrt{\gamma}}\frac{\partial}{\partial x^j}\left[\alpha\sqrt{\gamma}(\hat{v}^i B^j - \hat{v}^j B^i)\right]. \tag{3.40}$$

By introducing the following quantities

$$B^{*i} \equiv \sqrt{\gamma}B^i, \tag{3.41}$$

$$v^{*i} \equiv \alpha\hat{v}^i = \alpha v^i - \beta^i, \tag{3.42}$$

we can rewrite the above equations as

$$\hat{\nabla}_i B^{*i} = 0, \tag{3.43}$$

$$\frac{\partial B^{*i}}{\partial t} = \hat{\nabla}_j(v^{*i}B^{*j} - v^{*j}B^{*i}). \tag{3.44}$$

Taking into account the property of the triple cross product, $\vec{A}\times\left(\vec{B}\times\vec{C}\right) = (\vec{A}\cdot\vec{C})\cdot\vec{B} - (\vec{A}\cdot\vec{B})\cdot\vec{C}$, these equations can be expressed in a vectorial form

$$\vec{\hat{\nabla}}\cdot\vec{B}^* = 0, \tag{3.45}$$

$$\frac{\partial\vec{B}^*}{\partial t} = \vec{\hat{\nabla}}\times\left(\vec{v}^*\times\vec{B}^*\right), \tag{3.46}$$

where the scalar product $(\cdot)$ is defined with respect to the flat metric $\hat{\gamma}_{ij}$. In the Newtonian limit $v^{i*}\to v^i$ and $B^{i*}\to B^i$, and the Newtonian induction equation and divergence constraint are recovered. If we define $E^{*i} = \alpha E^i$ then the second equation reads

$$\frac{\partial\vec{B}^*}{\partial t} + \vec{\hat{\nabla}}\times\vec{E}^* = 0, \tag{3.47}$$

which is the general relativistic version of Faraday's law.

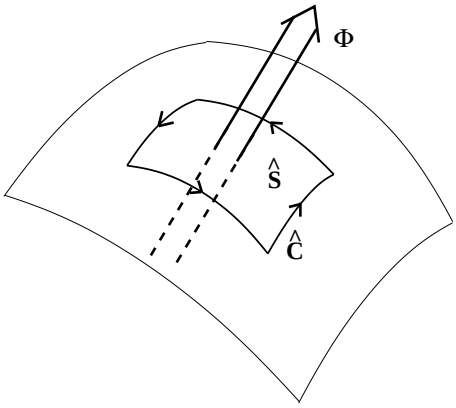

Figure 3.2: The magnetic flux Φ through a surface $\hat{A}$ can be calculated as the "electric field" $\vec{E}^*$ integrated along the closed curve $\hat{C}$.

3.2.2 Magnetic flux conservation

The total magnetic flux through a closed surface $\hat{A}$ enclosing a volume $\hat{V}$ can be calculated as a surface integral of the "starred" magnetic field as

$$\Phi_{\rm T} = \oint_{\hat{A}=\partial\hat{V}} \vec{B}^* \cdot d\vec{\hat{A}} = \int_{\hat{V}} \vec{\hat{\nabla}} \cdot \vec{B}^* d\hat{V} = 0 \tag{3.48}$$

where we have applied Gauss theorem and the divergence constraint given in Eq. (3.45). This equation implies that no magnetic flux source exists inside the volume $\hat{V}$ and therefore, the magnetic flux is a conserved quantity as $\frac{\partial \Phi_{\rm T}}{\partial t} = 0$.

If we consider any surface $\hat{A}$ (without the restriction of enclosing a volume, see Fig. 3.2), the time variation of the magnetic flux through the surface is

$$\begin{aligned} \frac{\partial \Phi}{\partial t} &= \frac{\partial}{\partial t} \int_{\hat{A}} \vec{B}^* \cdot d\vec{\hat{A}} = \int_{\hat{A}} \left[\vec{\hat{\nabla}} \times \left(\vec{v}^* \times \vec{B}^* \right) \right] \cdot d\vec{\hat{A}} \\ &= - \int_{\hat{A}} \left(\vec{\hat{\nabla}} \times \vec{E}^* \right) \cdot d\vec{\hat{A}} = - \oint_{\hat{C}=\partial\hat{A}} \vec{E}^* \cdot d\vec{\hat{l}}, \end{aligned} \tag{3.49}$$

where we have applied the induction equation (3.46) and Stokes theorem to transform the surface integral into a line integral along the curve $\hat{C}$ enclosing $\hat{A}$.

These two properties will allow us to design a numerical algorithm to solve the induction equation and the divergence constraint in a way ensuring the conservation of the magnetic flux.

3.2.3 Conservation laws

For a fluid endowed with a magnetic field the energy-momentum tensor is the sum of that of the fluid and that of the electromagnetic field

$$T^{\mu\nu} = T^{\mu\nu}_{\rm Fluid} + T^{\mu\nu}_{\rm EM}, \tag{3.50}$$

where $T^{\mu\nu}_{\rm Fluid}$ is given by Eq. (3.2) for a perfect fluid, and $T^{\mu\nu}_{\rm EM}$ can be obtained from the Faraday tensor as follows:

$$T^{\mu\nu}_{\rm EM} = F^{\mu\lambda}F^{\nu}_{\lambda} - \frac{1}{4}g^{\mu\nu}F^{\lambda\delta}F_{\lambda\delta}, \tag{3.51}$$

which, in ideal GRMHD, can be written in terms of the magnetic field b^μ measured by a comoving observer as

$$T^{\mu\nu}_{\rm EM} = \left(u^\mu u^\nu + \frac{1}{2}g^{\mu\nu}\right) b^2 - b^\mu b^\nu, \tag{3.52}$$

where $b^2 = b^\mu b_\mu$. The total energy-momentum tensor is thus given by

$$T^{\mu\nu} = \rho h_{\rm T}\, u^\mu u^\nu + P_{\rm T} g^{\mu\nu} - b^\mu b^\nu, \tag{3.53}$$

with the definitions

$$P_{\rm T} = P + \frac{b^2}{2} = P + P_{\rm mag}, \tag{3.54}$$

$$h_{\rm T} = h + \frac{b^2}{\rho} = 1 + \epsilon_{\rm T} + \frac{P_{\rm T}}{\rho}, \tag{3.55}$$

$$\epsilon_{\rm T} = \epsilon + \frac{b^2}{2\rho} = \epsilon + \epsilon_{\rm mag}, \tag{3.56}$$

where $P_{\rm mag} \equiv \frac{b^2}{2}$ is the magnetic pressure and $\epsilon_{\rm mag} = \frac{b^2}{2\rho}$ is the specific magnetic energy.

The evolution of the fluid is determined by the energy-momentum conservation laws and the continuity equation given in Eqs. (3.4) and (3.5). Following Antón et al. (2006), in order to account for the magnetic field the conserved quantities are chosen in a similar way to the pure hydrodynamical case

$$D = \rho W, \tag{3.57}$$

$$S_i = \rho h_{\rm T} W^2 v_i - \alpha b_i b^0, \tag{3.58}$$

$$\tau = E - D = \rho h_{\rm T} W^2 - P_{\rm T} - \alpha^2 (b^0)^2 - D. \tag{3.59}$$

With this choice the system of conservation equations for the fluid and the induction equation for the magnetic field can be written as a first-order, flux-conservative, hyperbolic system, as Eq. (3.11), with the state vector, flux vector, and source vector given by

$$\boldsymbol{U} = [D, S_j, \tau, B^k], \tag{3.60}$$

$$\boldsymbol{F}^i = \left[D\hat{v}^i, S_j \hat{v}^i + \delta^i_j P_{\rm T} - \frac{b_j B^i}{W}, \tau \hat{v}^i + P_{\rm T} v^i - \alpha \frac{b^0 B^i}{W}, \hat{v}^i B^k - \hat{v}^k B^i \right], \tag{3.61}$$

$$\boldsymbol{Q} = \left[0, \frac{1}{2} T^{\mu\nu} \frac{\partial g_{\mu\nu}}{\partial x^j}, \alpha \left(T^{\mu 0} \frac{\partial \ln \alpha}{\partial x^\mu} - T^{\mu\nu} \Gamma^0_{\mu\nu} \right), 0^k \right]. \tag{3.62}$$

We note that in these expressions appear components of the magnetic field as measured by both a comoving observer and an Eulerian observer. These are related by

$$b^0 = \frac{B^i u_i}{\alpha} = \frac{W B^i v_i}{\alpha}, \tag{3.63}$$

$$b^i = \frac{B^i + \alpha b^0 u^i}{W} = \frac{B^i + W^2 v^j B^j \hat{v}^i}{W}. \tag{3.64}$$

Finally, the modulus of the magnetic field can be written as

$$b^2 = b^\mu b_\mu = \frac{B^2 + \alpha^2 (b^0)^2}{W^2} = \frac{B^2 + W^2 (v^i B_i)^2}{W^2}, \tag{3.65}$$

where $B^2 \equiv B^i B_i$. Note that b^i is not a three-vector but the spacial components of the four-vector b^μ, and hence the index can not be lowered with the three-metric.

3.2.4 Riemann problem

By defining the conserved quantities $\boldsymbol{U}^*$, fluxes $\boldsymbol{F}^{*i}$ and sources $\boldsymbol{Q}^*$ in the same way as in the previous section (but now considering that each vector has seven components), we can rewrite the above equations in a similar way as in Eq. (3.19).

$$\partial_t \boldsymbol{U}^* + \hat{\nabla}_i \boldsymbol{F}^{*i} = \boldsymbol{Q}^*. \tag{3.66}$$

The associated Jacobians in every direction, Eq. (3.21), are 7×7 matrices, and the solution of the eigenvalue problem (Antón 2006) leads to seven types of waves that can appear when solving the Riemann problem for each direction i:

- Entropic wave:

$$\lambda^i_e = \alpha v^i - \beta^i. \tag{3.67}$$

- Alfven waves:

$$\lambda^i_{a\pm} = \frac{b^i \pm \sqrt{\mathcal{C}} u^i}{b^0 \pm \sqrt{\mathcal{C}} u^0}, \tag{3.68}$$

  where $\mathcal{C} \equiv \rho h + B^2$

- Magnetosonic waves: There is no analytic expression for the magnetosonic waves. Instead, they must be computed as the solution of the quartic equation

$$A^i_4 (\eta^i)^4 + A^i_3 (\eta^i)^3 + A^i_2 (\eta^i)^2 + A^i_1 \eta^i + A^i_0 = 0, \tag{3.69}$$

  with

$$\eta^i \equiv \frac{\lambda^i + \beta^i}{\alpha}. \tag{3.70}$$

The coefficients of Eq. (3.69) read (Antón 2006):

$$A_4^i = 1 - \Omega^2 v^2 - \frac{(\bar{b}^0)^2 c_{\rm s}^2}{\mathcal{C} W^4}, \tag{3.71}$$

$$A_3^i = -4v^i(1-\Omega^2) - 2v^i\frac{\Omega^2}{W^2} + \frac{2\bar{b}^0\bar{b}^i c_{\rm s}^2}{\mathcal{C} W^4}, \tag{3.72}$$

$$A_2^i = 6(v^i)^2(1-\Omega^2) - (\gamma^{ii} - (v^i)^2)\frac{\Omega^2}{W^2} + \frac{((\bar{b}^0)^2\gamma^{ii} - (\bar{b}^i)^2)c_{\rm s}^2}{\mathcal{C} W^4}, \tag{3.73}$$

$$A_1^i = -4(v^i)^3(1-\Omega^2) + 2v^i\frac{\Omega^2}{W^2} - \frac{2\bar{b}^0\bar{b}^i\gamma^{ii}c_{\rm s}^2}{\mathcal{C} W^4}, \tag{3.74}$$

$$A_0^i = (v^i)^4(1-\Omega^2) - \gamma^{ii}(v^i)^2\frac{\Omega^2}{W^2} + \frac{(\bar{b}^i)^2\gamma^{ii}c_{\rm s}^2}{\mathcal{C} W^4}, \tag{3.75}$$

where

$$\Omega^2 \equiv c_{\rm s}^2 + c_{\rm a}^2 - c_{\rm a}^2 c_{\rm s}^2\,, \qquad c_{\rm a}^2 \equiv \frac{b^2}{\mathcal{C}}. \tag{3.76}$$

and

$$\bar{b}^0 = W(v^i B_i), \qquad \bar{b}^i = \frac{B^i}{W} + W(v^j B_j)v^i. \tag{3.77}$$

Among the magnetosonic waves, the two solutions with maximum and minimum speeds are called *fast* magnetosonic waves $\lambda^i_{f\pm}$, and the two solutions in between are the so-called *slow* magnetosonic waves $\lambda^i_{s\pm}$.

The seven waves can be ordered as follows

$$\lambda^i_{f-} \leq \lambda^i_{a-} \leq \lambda^i_{s-} \leq \lambda^i_{e} \leq \lambda^i_{s+} \leq \lambda^i_{a+} \leq \lambda^i_{f+} \tag{3.78}$$

which is also depicted in Fig. 3.3.

3.2.5 The passive field approximation

For many astrophysical scenarios, e.g. in the collapse of weakly magnetized stellar cores, it is a good approximation to consider that the magnetic field entering in the energy-momentum tensor of Eq. (3.53) is negligible when compared with the fluid part, i.e. $P_{\rm mag} \ll P$, $\epsilon_{\rm mag} \ll \epsilon$, and the components of the anisotropic term of $T^{\mu\nu}$ satisfying $b^\mu b^\nu \ll \rho h u^\mu u^\nu + P g^{\mu\nu}$. With such simplifications, the magnetic field evolution, given by the induction equation (3.46),

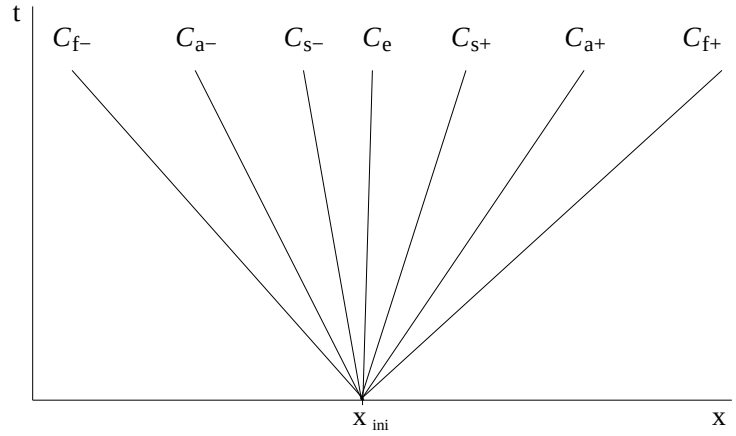

Figure 3.3: Characteristics C_e, $C_{a\pm}$, $C_{s\pm}$ and $C_{f\pm}$ of the GRMHD system, corresponding to the entropic wave , the Alfven waves and the slow and fast magnetosonic waves, respectively.

does not affect the dynamics of the fluid, which is governed solely by the hydrodynamics equations (3.11). However, the magnetic field evolution depends on the fluid evolution, due to the effect of the velocities in the induction equation.

In this particular case of a "test magnetic field" (or passive field hereafter) approximation, the seven eigenvalues of the GRMHD Riemann problem reduce to three

$$\lambda^i_{0\,\mathrm{hydro}} = \lambda^i_e = \lambda^i_{a\pm} = \lambda^i_{s\pm}, \tag{3.79}$$

$$\lambda^i_{\pm\,\mathrm{hydro}} = \lambda^i_{f\pm}, \tag{3.80}$$

where $\lambda^i_{0\,\mathrm{hydro}}$ and $\lambda^i_{\pm\,\mathrm{hydro}}$ are the eigenvalues of the Jacobian matrices of the hydrodynamics equations given in Eqs. (3.23) and (3.25), respectively.

Chapter 4

CFC

The conformally flat condition (CFC) approximation for the 3+1 Einstein's equations was originally proposed by Isenberg (Isenberg 1978). It was later revisited by Wilson and Mathews (Wilson et al. 1996) in the context of numerical simulations of the merging of two neutron stars. CFC assumes that the three-metric is conformal to the flat metric. In this chapter we will justify this approximation and will write Einstein's field equations under this approximation. Note that although in the previous chapter the discussion was restricted to a perfect fluid embedded in an electro-magnetic field, all the considerations made in this chapter apply to any form of the energy-momentum tensor, and thus are completely general.

4.1 The conformal flat condition

In Chapter 2 we have established the formalism of Einstein's equations that we will use in this thesis. We have selected the 3+1 split to foliate the spacetime, we have chosen maximal slicing, and we have described the general features that we require of the spatial gauge. The three-metric can be decomposed into a conformally-flat part and a traceless part as

$$\gamma_{ij} = \phi^4 \hat{\gamma}_{ij} + \gamma_{<ij>}. \tag{4.1}$$

The spatial gauge is chosen is such that (i) far from the sources, (ii) for weak gravitational fields, (iii) or in spherical symmetry, the traceless part of the three-metric vanishes, $\gamma_{<ij>} \to 0$. Therefore, a natural approximation of the three-metric when dealing with sources with moderate gravitational fields or sources whose morphology is close to spherical symmetry, is to impose $\gamma_{<ij>} = 0$. Then, the three-metric is conformal to the flat metric

$$\gamma_{ij}^{\rm CFC} = \phi^4 \hat{\gamma}_{ij}. \tag{4.2}$$

Under this approximation the three spatial gauges described in Section 2.3, i.e. the QI coordinates, the Dirac gauge, and the ADM gauge, become equivalent to the isotropic coordinates. The only free parameters of the CFC metric are α, β^i and ϕ. If one considers the limits of weak gravitational fields or very far from the sources, then $\alpha \to 1$, $\beta^i \to 0$ and $\phi \to 1$, and one recovers the flat metric. But in the limit of spherically symmetric spacetimes, only components of β^i orthogonal to the radial direction vanish, i.e. $\beta^\theta \to 0$ and $\beta^\varphi \to 0$ (in spherical polar coordinates), while all other functions (α, ϕ and β^r) have to be calculated. In this case (spherical symmetry) the CFC metric is exact and the CFC equations describe the system without approximations in the full general relativistic regime. Furthermore, in a general case without symmetries, the traceless part of the three-metric is a quantity that first appears at second-order terms in a post-Newtonian expansion of the metric. Therefore, the CFC metric behaves as a first post-Newtonian approximation for highly non-spherical sources (Kley & Schäfer 1999).

These properties make the CFC approximation very attractive when dealing with quasi-spherical systems with moderately large gravitational fields, such as neutron stars. The main physical restriction of this approximation is that, as the traceless part of the three-metric is set to zero, all gravitational wave content of the system is lost. Thus, one cannot use the CFC metric to extract gravitational waves or to study the loss of energy and momentum by GWs. The last feature imposes an additional restriction to the use of the CFC metric: this approximation is only valid for dynamical timescales, where the smallness of the $h_{<ij>}$ ensures that gravitational radiation reaction is negligible. But for secular time scales, the accumulated energy and momentum lost of the system could lead to noticeable effects.

4.2 Conformal scaling

Under the assumption of CFC the three-metric becomes diagonal. This simplifies Einstein's equations. The square root of the determinants of the three-metric and the four-metric are easily calculated as:

$$\sqrt{\gamma} = \phi^6 \sqrt{\hat{\gamma}}\,; \qquad \sqrt{-g} = \alpha\sqrt{\gamma} \tag{4.3}$$

$$\sqrt{\bar{\gamma}} = \frac{\sqrt{\gamma}}{\sqrt{\hat{\gamma}}} = \phi^6. \tag{4.4}$$

In the same way that the three-metric is conformally scaled to the flat three-metric with a factor ϕ^4, all tensor quantities defined at the hypersurfaces scale in a similar way. One can thus define quantities calculated with respect to the flat metric, which are easily related to the corresponding quantities with respect to the three-metric by the conformal factor. For example:

$$R = \frac{1}{\phi^4}\left(\hat{R} - \frac{8}{\phi}\hat{\Delta}\phi\right) = -\frac{8}{\phi^5}\hat{\Delta}\phi, \qquad \text{as} \quad \hat{R} = 0, \tag{4.5}$$

$$\Delta(\alpha\phi) = \frac{1}{\phi^5}\left(\phi\hat{\Delta}(\alpha\phi) + 2\hat{\gamma}^{ij}\hat{\nabla}_i(\alpha\phi)\hat{\nabla}_j\phi\right), \tag{4.6}$$

$$\nabla_i s = \hat{\nabla}_i s, \tag{4.7}$$

$$K_{ij} = \frac{1}{\phi^2}\hat{K}_{ij}, \qquad K^{ij} = \frac{1}{\phi^{10}}\hat{K}^{ij}, \tag{4.8}$$

s being a scalar function, and tilde denoting quantities related to the flat three-metric. Using these properties one can simplify Einstein's equations transforming γ_{ij} and the operators ∇_i and $\Delta \equiv \nabla_i\nabla^i$, into the flat metric $\hat{\gamma}_{ij}$ and the flat operators $\hat{\nabla}_i$ and $\hat{\Delta} \equiv \hat{\nabla}_i\hat{\nabla}^i$, respectively.

4.3 The CFC equations

The four constraint equations together with the equation for $\partial_t K = 0$, lead to a system of five elliptic equations for the free parameters of the CFC metric.

They form a system of five nonlinear Poisson-like equations for α, ϕ and β^i

$$\hat{\Delta}\phi = -2\pi\phi^5 \left(E + \frac{K_{ij}K^{ij}}{16\pi} \right), \tag{4.9}$$

$$\hat{\Delta}(\alpha\phi) = 2\pi\alpha\phi^5 \left(E + 2S + \frac{7K_{ij}K^{ij}}{16\pi} \right), \tag{4.10}$$

$$\hat{\Delta}\beta^i = 16\pi\alpha\phi^4 S^i + 2\hat{K}^{ij}\hat{\nabla}_j \left(\frac{\alpha}{\phi^6} \right) - \frac{1}{3}\hat{\nabla}^i\hat{\nabla}_k\beta^k. \tag{4.11}$$

Note that as $\hat{\nabla}$ and $\hat{\Delta}$ are flat operators, i.e. defined with respect to the flat three-metric $\hat{\gamma}_{ij}$, the metric does not appear in its definition. Appendix A presents explicit expressions for these operators acting on different quantities, written in spherical coordinates. These equations have to be complemented with an expression for the flat extrinsic curvature

$$\hat{K}_{ij} = \frac{1}{2\alpha} \left(\hat{\nabla}_i\beta_j + \hat{\nabla}_j\beta_i - \frac{2}{3}\gamma_{ij}\hat{\nabla}_k\beta^k \right). \tag{4.12}$$

Alternatively the conformal factor can be calculated from an evolution equation

$$\partial_t\phi = \frac{\phi}{6}\nabla_k\beta^k. \tag{4.13}$$

This equation will be helpful in the implementation of the numerical scheme to solve the fluid equations (see Section 7.1), while Eqs. (4.9), (4.10) and (4.11) will be used to calculate the metric. As these equations have to be solved numerically it is interesting to formulate them in a way that lead to numerically stable evolutions. With this purpose we define the variables

$$E^* \equiv \sqrt{\bar{\gamma}}E = \phi^6 E, \tag{4.14}$$

$$S^{*i} \equiv \sqrt{\bar{\gamma}}S^i = \phi^6 S^i, \tag{4.15}$$

$$S^* = \sqrt{\bar{\gamma}}S = \phi^6 S, \tag{4.16}$$

which are directly related with the conserved quantities of the fluid evolution (see Chapter 3). With these definitions and making explicit the dependence

on ϕ, the CFC equations are transformed into

$$\hat{\Delta}\phi = -2\pi \left(\phi^{-1} E^* + \phi^{-7} \frac{\hat{K}_{ij}\hat{K}^{ij}}{16\pi} \right) = \mathcal{O}(\phi^{-1}), \quad (4.17)$$

$$\hat{\Delta}(\alpha\phi) = 2\pi\alpha \left[\phi^{-1}(E^* + 2S^*) + \phi^{-7} \frac{7\hat{K}_{ij}\hat{K}^{ij}}{16\pi} \right] = \mathcal{O}(\phi^{-1}), \quad (4.18)$$

$$\hat{\Delta}\beta^i = 16\pi\alpha\phi^{-2}S^{*i} + 2\hat{K}^{ij}\hat{\nabla}_j \left(\frac{\alpha}{\phi^6} \right) - \frac{1}{3}\hat{\nabla}^i\hat{\nabla}_k\beta^k = \mathcal{O}(\phi^{-2}), \quad (4.19)$$

where the sources of the equations behave at least as ϕ^{-1}. This property ensures the convergence of the numerical method for solving these equations for large values of ϕ, for example close to the formation of a black hole.

Chapter 5

CFC+

This chapter presents the CFC+ approximation as an extension of CFC. Einstein's field equations are formulated, as well as related expressions necessary for their numerical solution. The work presented in this chapter has been published in Cerdá-Durán et al. (2005).

5.1 Preliminary considerations

So far, we have tried to preserve the metric formulation as general as possible. But before presenting the CFC+ approximation some considerations should be done. The CFC+ approach involves a post-Newtonian expansion of the traceless part of the three-metric, adding new degrees of freedom to the CFC metric. As the metric will be now more general, it is necessary to be more explicit in the choice of spatial gauge. We will impose the ADM gauge (see section 2.3.4) as it is of common usage in post-Newtonian calculations. The traceless part of the three-metric becomes then transverse. It is denoted $h_{ij}^{\rm TT}$, where the TT superscript will be used hereafter to denote transverse and traceless quantities. Hence, the three-metric takes the form (see Eq. 2.38)

$$\gamma_{ij} = \phi^4 \hat{\gamma}_{ij} + h_{ij}^{\rm TT}. \tag{5.1}$$

The second consideration involves the energy-momentum tensor $T_{\mu\nu}$. In order to facilitate the post-Newtonian calculations we will consider a perfect fluid, for which the energy-momentum tensor is given by Eq. (3.2). As variables for the post-Newtonian expansion we choose the "starred" conserved variables D^* and S_i^*, as these quantities are known directly from the fluid evolution.

5.2 The natural extension of CFC

One of the most important features of the CFC approximation is that it is more accurate the closer the system is to spherical symmetry, in which case the CFC equations are exact. But for a general non spherically symmetric scenario CFC behaves as a first post-Newtonian approximation, i.e. the CFC three-metric differs in $\mathcal{O}(1/c^4)$ with respect to the exact one

$$\gamma_{ij} = \phi^4 \hat{\gamma}_{ij} + \mathcal{O}\left(\frac{1}{c^4}\right) = \gamma_{ij}^{\rm CFC} + \mathcal{O}\left(\frac{1}{c^4}\right). \tag{5.2}$$

Therefore, Eq. (2.23) for the three-metric differs in $\mathcal{O}(1/c^5)$. Hence, for strong enough gravitational fields, even small deviations from sphericity should produce differences with respect to the exact solution. The natural way of improving the CFC approximation is through a post-Newtonian expansion of the traceless part of the three-metric

$$\gamma_{ij} = \phi^4 \hat{\gamma}_{ij} + h_{ij}^{\rm TT} = \gamma_{ij}^{\rm CFC} + \left[h_{ij}^{\rm 2PN} + \mathcal{O}\left(\frac{1}{c^5}\right)\right], \tag{5.3}$$

$h_{ij}^{\rm 2PN}$ being the leading order in the expansion of $h_{ij}^{\rm TT}$. Note that this is not an expansion of the three-metric, but of its traceless part. By expanding the whole three-metric instead of its traceless part we obtain:

$$\begin{aligned}\gamma_{ij} &= \underbrace{\left[1 + (\phi^4)^{\rm 1PN} + (\phi^4)^{\rm 2PN} + \mathcal{O}\left(\frac{1}{c^6}\right)\right]\hat{\gamma}_{ij}}_{\rm CFC} + \underbrace{\left[h_{ij}^{\rm 2PN} + \mathcal{O}\left(\frac{1}{c^5}\right)\right]}_{\rm TT} \\ &= \underbrace{\hat{\gamma}_{ij}}_{\rm 0PN} + \underbrace{(\phi^4)^{\rm 1PN}\hat{\gamma}_{ij}}_{\rm 1PN} + \underbrace{\left[(\phi^4)^{\rm 2PN}\hat{\gamma}_{ij} + h_{ij}^{\rm 2PN}\right]}_{\rm 2PN} + \mathcal{O}\left(\frac{1}{c^5}\right).\end{aligned} \tag{5.4}$$

If this expression is truncated at first post-Newtonian level we do not recover the CFC metric, but only the first post-Newtonian approximation of the three-metric. In this case the exact solution for spherical symmetry is not recovered. If Eq. (5.3) is truncated at second post-Newtonian terms in the traceless and transverse part, we obtain the CFC+ metric

$$\gamma_{ij}^{\mathrm{CFC}+} \equiv \gamma_{ij}^{\mathrm{CFC}} + h_{ij}^{2\mathrm{PN}}. \tag{5.5}$$

The main features of this approximation are that :

- CFC+ becomes exact for spherically symmetric spacetimes, as CFC, since in this case the TT part vanishes.

- In a general non spherical spacetime, CFC+ behaves as a second post-Newtonian approximation of the metric.

5.3 Equations of motion in the ADM formalism

After the basis of the CFC+ approximation has been introduced, we have to calculate the metric under this approximation. The approach leading to the CFC+ equations is to build up the new approximation by modifying the CFC equations. In this way, any method previously used to numerically solve the CFC equations will be straightforwardly applicable to the modified equations of CFC+. By adding second post-Newtonian terms the CFC equations are changed in two ways:

1. As new degrees of freedom are added to the system, given by the h_{ij}^{TT}, additional equations are needed for these new quantities.

2. The equations for the lapse function α, shift vector β^i and, conformal factor ϕ change with respect to the CFC equations due to the addition of the h_{ij}^{TT}.

We will proceed next to obtain the CFC+ equations, and to design a procedure for solving these equations.

5.3.1 Equations for $h_{ij}^{\rm TT}$

The derivation of the $h_{ij}^{\rm TT}$ equations up to second post-Newtonian order can be achieved in the Hamiltonian framework of ADM (Arnowitt et al. 1962) in two steps:

1. Calculate the ADM Hamiltonian in terms of the canonical variables of the system and its conjugate momentum. To do that one has to consider terms up to second post-Newtonian order.

2. Use the variational principle to calculate the equations of motion for $h_{ij}^{\rm TT}$ from the Hamiltonian, and check that they only include terms up to second post-Newtonian order.

The original canonical variables are chosen to be the three-metric γ_{ij} and its conjugate momentum

$$\pi^{ij}_{\rm true} = c^3\pi^{ij}/(16\pi G); \qquad \pi^{ij} = -\sqrt{\bar{\gamma}}(K^{ij} - K\gamma^{ij}). \tag{5.6}$$

Here π^{ij} is used instead of the "true" conjugate momentum because of historical reasons. Once the coordinate system has been fixed, only 6 physical degrees of freedom are left. Four of this six remaining field degrees of freedom are eliminated by imposing the Hamiltonian constraint (2.25) and the three momentum constraints (2.26). These four field degrees of freedom correspond to the conformal factor ϕ and to the symmetric trace-free part $\pi_{\rm L}^{ij}$ (longitudinal)of the tensor $2\hat{\Delta}^{-1}(\hat{\gamma}^{ik}\hat{\nabla}_k\hat{\nabla}_l\pi^{jl}) - \hat{\Delta}^{-2}(\hat{\gamma}^{im}\hat{\gamma}^{jn}\hat{\nabla}_k\hat{\nabla}_l\hat{\nabla}_m\hat{\nabla}_n\pi^{kl})/2$, respectively. Only two transverse trace-free (TT) field variables are left, namely $h_{ij}^{\rm TT} = \gamma_{ij} - \phi^4\hat{\gamma}_{ij}$ on the one hand, and $\pi_{\rm TT}^{ij} = \pi^{ij} - \pi_{\rm L}^{ij}$ on the other. By construction, we have:

$$\hat{\gamma}^{kl}\hat{\nabla}_k h_{il}^{\rm TT} = 0, \qquad \hat{\gamma}^{ij}h_{ij}^{\rm TT} = 0, \tag{5.7}$$

$$\hat{\nabla}_j\pi_{\rm TT}^{ij} = 0, \qquad \hat{\gamma}_{ij}\pi_{\rm TT}^{ij} = 0. \tag{5.8}$$

The reduced Hamiltonian H is obtained by substituting all metric variables by its dependence on $h_{pq}^{\rm TT}$ and $\pi_{\rm TT}^{pq}$ in the Hamiltonian of general relativity for asymptotically flat spacetimes. The contributions of the super-Hamiltonian[1]

[1]See Chapter 21 in Misner et al. (1973), for differences between Hamiltonian and Super-Hamiltonian.

and super-momentum densities vanish, so that $H[\text{matter variables}, h^{\rm TT}_{pq}, \pi^{pq}_{\rm TT}]$ is given by the surface integral defining the ADM mass "on a shell",

$$\begin{aligned} H &= \frac{c^4}{16\pi G} \int \mathrm{d}^2\hat{S}^i \, \sqrt{\hat{\gamma}} \gamma^{jk} \left(\hat{\nabla}_j \gamma_{ik} - \hat{\nabla}_i \gamma_{jk} \right) \\ &= -\frac{c^4}{2\pi G} \int \mathrm{d}^3\boldsymbol{x} \, \sqrt{\hat{\gamma}} \hat{\Delta} \phi, \end{aligned} \tag{5.9}$$

where the surface element $d\hat{S}^i \sqrt{\hat{\gamma}}$ refers to the flat metric. The reduced Hamiltonian (5.9) contains the full dynamical information about the system. In particular, as shown by Regge & Teitelboim (1974), the field evolution is governed by the equations of motion

$$\partial_t h^{\rm TT}_{ij} = \frac{16\pi G}{c^3} \hat{\gamma}^{\rm TT}_{ij\,kl} \frac{\delta H}{\delta \pi^{kl}_{\rm TT}}, \tag{5.10}$$

$$\partial_t \pi^{ij}_{\rm TT} = -\frac{16\pi G}{c^3} \hat{\gamma}^{ij}_{\rm TT\,kl} \frac{\delta H}{\delta h^{\rm TT}_{kl}}, \tag{5.11}$$

with

$$\begin{aligned} \hat{\gamma}^{\rm TT}_{ij\,kl} &= \frac{1}{2} \left(\delta^k_i - \hat{\gamma}^{kp} \hat{\Delta}^{-1} \hat{\nabla}_i \hat{\nabla}_p \right) \left(\delta^l_j - \hat{\gamma}^{lq} \hat{\Delta}^{-1} \hat{\nabla}_j \hat{\nabla}_q \right) \\ &+ \frac{1}{2} \left(\delta^k_j - \hat{\gamma}^{kp} \hat{\Delta}^{-1} \hat{\nabla}_j \hat{\nabla}_p \right) \left(\delta^l_i - \hat{\gamma}^{lq} \hat{\Delta}^{-1} \hat{\nabla}_i \hat{\nabla}_q \right) \\ &- \frac{1}{2} \left(\hat{\gamma}_{ij} - \hat{\Delta}^{-1} \hat{\nabla}_i \hat{\nabla}_j \right) \left(\hat{\gamma}^{kl} - \hat{\gamma}^{kp} \hat{\gamma}^{lq} \hat{\Delta}^{-1} \hat{\nabla}_p \hat{\nabla}_q \right), \end{aligned} \tag{5.12}$$

and a similar formula for $\hat{\gamma}^{ij}_{\rm TT\,kl}$. The role of these operators is to ensure the transverse trace-free projection of the Fréchet derivative $\delta H/\delta \pi^{kl}_{\rm TT}$ and $\delta H/\delta h^{\rm TT}_{kl}$, respectively. The calculation of H in terms of D^*, S^*_i, P, as well as the field variables $h^{\rm TT}_{ij}$ and $\pi^{ij}_{\rm TT}$, can be done essentially by eliminating ϕ in Eq. (5.9) with the help of the Hamiltonian constraint (2.25). This is achievable in perturbative treatments such as the post-Minkowskian or the post-Newtonian ones, consisting of the formal expansion of all quantities at play in powers of the gravitational constant G or of the inverse of the square of the speed of light $1/c^2$.

2PN Hamiltonian constraint

In the course of eliminating ϕ we use the Hamiltonian constraint

$$R + K^2 - K_{ij}K^{ij} - 16\pi E = 0 \tag{5.13}$$

in a more explicit form, by expressing it as a function of ϕ and $h_{ij}^{\rm TT}$. We check one by one the three terms in the equation.

We first expand the 3-curvature R. By making extensive use of the relations

$$\gamma_{ij}\hat{\nabla}_l\gamma^{jk} = -\gamma^{jk}\hat{\nabla}_l\gamma_{ij} \tag{5.14}$$

and

$$\hat{\nabla}_k\bar{\gamma} = (\bar{\gamma}\gamma^{ij})\hat{\nabla}_k\gamma_{ij}, \tag{5.15}$$

the combination $\bar{\gamma}^3 R$ can be written as (cf. Schwinger 1963)

$$\begin{aligned}\bar{\gamma}^3 R = &-\bar{\gamma}^2\hat{\nabla}_i\hat{\nabla}_j\left(\bar{\gamma}\gamma^{ij}\right) + \frac{1}{2}\hat{\nabla}_i\bar{\gamma}^2\hat{\nabla}_j\left(\bar{\gamma}\gamma^{ij}\right) - \frac{1}{4}\left(\bar{\gamma}\gamma^{ij}\right)\hat{\nabla}_i\bar{\gamma}\hat{\nabla}_j\bar{\gamma} \\ &- \frac{1}{2}\bar{\gamma}\left(\bar{\gamma}\gamma^{jl}\right)\hat{\nabla}_j\left(\bar{\gamma}\gamma^{ik}\right)\hat{\nabla}_i\gamma_{kl} + \frac{1}{2}\left(\bar{\gamma}\gamma^{ik}\right)\left(\bar{\gamma}\gamma^{jl}\right)\hat{\nabla}_j\bar{\gamma}\hat{\nabla}_i\gamma_{kl} \\ &+ \frac{1}{4}\bar{\gamma}\left(\bar{\gamma}\gamma^{ik}\right)\hat{\nabla}_k\left(\bar{\gamma}\gamma^{jl}\right)\hat{\nabla}_i\gamma_{jl} - \frac{1}{4}\left(\bar{\gamma}\gamma^{jl}\right)\left(\bar{\gamma}\gamma^{ik}\right)\hat{\nabla}_k\bar{\gamma}\hat{\nabla}_i\gamma_{jl}.\end{aligned} \tag{5.16}$$

By definition, the determinant $\bar{\gamma}$ is equal to the antisymmetric sum of products $3!\,\hat{\gamma}^{p[1}\hat{\gamma}^{2\underline{q}}\hat{\gamma}^{3]r}\gamma_{p1}\gamma_{q2}\gamma_{r3} = \hat{\gamma}^{p[i}\hat{\gamma}^{j\underline{q}}\hat{\gamma}^{k]r}\gamma_{pi}\gamma_{qj}\gamma_{rk}$ on a Cartesian grid, the square brackets denoting antisymmetrization of non-underlined indices. Its explicit expression is given, e.g., by Schäfer (1985). Similarly

$$\bar{\gamma}\gamma^{ij} = \varepsilon^{ikl}(\varepsilon_{rmn}\hat{\gamma}^{jr}\hat{\gamma}^{mp}\hat{\gamma}^{nq}\gamma_{pk}\gamma_{ql})/2, \tag{5.17}$$

where ε^{ikl} is the permutation operator. From the identity $\varepsilon^{rkl}\varepsilon_{jmn} = 3!\,\delta_j^{[r}\delta_m^k\delta_n^{l]}$ it is straightforward to obtain $\hat{\gamma}_{ik}\hat{\gamma}_{jl}\bar{\gamma}\hat{\gamma}^{kl}$ as a function of ϕ and $h_{ij}^{\rm TT}$,

$$\begin{aligned}\hat{\gamma}_{ik}\hat{\gamma}_{jl}\bar{\gamma}\gamma^{kl} = &\left[\phi^8 - \frac{1}{2}\hat{\gamma}^{km}\hat{\gamma}^{ln}h_{kl}^{\rm TT}h_{mn}^{\rm TT}\right]\hat{\gamma}_{ij} - \phi^4 h_{ij}^{\rm TT} \\ &+ \hat{\gamma}^{kl}h_{ik}^{\rm TT}h_{jl}^{\rm TT}.\end{aligned} \tag{5.18}$$

After inserting the relations for $\bar{\gamma}$ and $\bar{\gamma}\gamma^{ij}$ in the right-hand side of Eq. (5.16), it is expanded in powers of $h_{ij}^{\rm TT}$ and truncated consistently at the post-Newtonian level of $h_{ij}^{\rm TT}h_{kl}^{\rm TT}$, denoted as $\mathcal{O}(h^2)$. At this point we have an expression for $\bar{\gamma}R$ as a function of $\hat{\Delta}\phi$,

$$\begin{aligned}\bar{\gamma}^3 R = &-8\phi^{31}\hat{\Delta}\phi \\ &+ 4\phi^{26}\left(\phi\hat{\nabla}_i\hat{\nabla}_j\phi - 3\hat{\nabla}_i\phi\hat{\nabla}_j\phi\right)\hat{\gamma}^{ik}\hat{\gamma}^{jl}h_{kl}^{\rm TT} \\ &- \frac{1}{4}\hat{\gamma}^{kl}\hat{\gamma}^{im}\hat{\gamma}^{jn}\hat{\nabla}_k h_{ij}^{\rm TT}\hat{\nabla}_l h_{mn}^{\rm TT} + \frac{1}{2}\hat{\Delta}\left(\hat{\gamma}^{kl}\hat{\gamma}^{ij}h_{ik}^{\rm TT}h_{jl}^{\rm TT}\right) \\ &- \frac{1}{2}\hat{\nabla}_i\hat{\nabla}_j\left(\hat{\gamma}^{kl}\hat{\gamma}^{mi}\hat{\gamma}^{nj}h_{km}^{\rm TT}h_{ln}^{\rm TT}\right) + \mathcal{O}\left(\frac{h^2}{c^2}\right). \end{aligned} \tag{5.19}$$

In addition to R, there is a second contribution to the left-hand side of the Hamiltonian constraint surviving in the absence of matter, namely $K_{ij}K^{ij} - K^2 = [\pi^i_j\pi^j_i - \frac{1}{2}(\pi^i_i)^2]/\bar{\gamma}$. In the ADM formulation, the momentum π^{ij} decomposes into $\pi^{ij}_{\rm L} + \pi^{ij}_{\rm TT}$. The first term $\pi^{ij}_{\rm L}$ is of order $1/c^3$, being a sum of derivatives of Poisson inverse operators acting on $\hat{\nabla}_j\pi^{ij} = \mathcal{O}(\nabla_j K^{ij})$, which is itself $\mathcal{O}(1/c^3)$ according to the momentum constraint equation. The second term, linear in $h_{ij}^{\rm TT}$, is transverse and trace-free, hence $\hat{\gamma}_{ij}\pi^{ij}_{\rm TT} = 0$ [2]. Moreover, the ADM gauge condition implies $\hat{\gamma}_{ij}\pi^{ij} = \hat{\gamma}_{ij}\pi^{ij}_{\rm L} = 0$. This yields

$$\begin{aligned}&\sqrt{\bar{\gamma}}\left(K_{ij}K^{ij} - K^2\right) \\ &= \left(\hat{\gamma}_{ik}\hat{\gamma}_{jl} - \frac{1}{2}\hat{\gamma}_{ij}\hat{\gamma}_{kl}\right)\pi^{ij}\pi^{kl} + \mathcal{O}\left(\frac{h}{c^6}\right) + \mathcal{O}\left(\frac{h^2}{c^2}\right) \\ &= \hat{\gamma}_{ik}\hat{\gamma}_{jl}\left(\pi^{ij}_{\rm L}\pi^{kl}_{\rm L} + 2\pi^{ij}_{\rm L}\pi^{kl}_{\rm TT} + \pi^{ij}_{\rm TT}\pi^{kl}_{\rm TT}\right) \\ &+ \mathcal{O}\left(\frac{h}{c^6}\right) + \mathcal{O}\left(\frac{h^2}{c^2}\right). \end{aligned} \tag{5.20}$$

Finally, we consider the matter source term E in the Hamiltonian con-

[2] This condition is also satisfied by the ADM gauge condition

straint. The corresponding density $E^* = \sqrt{\bar{\gamma}}E$ may be written as

$$\frac{16\pi G}{c^4}E^* = \frac{16\pi G}{c^2}\left\{\left[(D^*h)^2 + \phi^{-4}\hat{\gamma}^{mn}\frac{S^*_m S^*_n}{c^2}\right]^{1/2} \times \left(1 - \frac{1}{2}\hat{\gamma}^{ik}\hat{\gamma}^{jl}h^{\rm TT}_{kl}\frac{S^*_i S^*_j}{c^2 D^{*\,2}}\right) - \frac{\phi^6 P}{c^2}\right\} + \mathcal{O}\left(\frac{h}{c^6}\right) + \mathcal{O}\left(\frac{h^2}{c^2}\right). \tag{5.21}$$

This yields the Hamiltonian constraint as an elliptic equation for $V \equiv 2(\phi - 1) = \mathcal{O}(1/c^2)$ up to $\mathcal{O}(h/c^6)$ and $\mathcal{O}(h^2/c^2)$ corrections:

$$\begin{aligned}
-4\hat{\Delta}V = {} & -4\hat{\nabla}_i\phi\hat{\nabla}_j\phi\,\hat{\gamma}^{ik}\hat{\gamma}^{jl}h^{\rm TT}_{kl} \\
& + \frac{1}{4}\hat{\gamma}^{kl}\hat{\gamma}^{im}\hat{\gamma}^{jn}\hat{\nabla}_k h^{\rm TT}_{ij}\hat{\nabla}_l h^{\rm TT}_{mn} \\
& - 4\hat{\nabla}_i\left(\phi^{-4}\hat{\nabla}_j\phi\,\hat{\gamma}^{ik}\hat{\gamma}^{jl}h^{\rm TT}_{kl}\right) - \frac{1}{2}\hat{\Delta}\left(\hat{\gamma}^{ij}\hat{\gamma}^{kl}h^{\rm TT}_{ik}h^{\rm TT}_{jl}\right) \\
& + \frac{1}{2}\hat{\nabla}_i\hat{\nabla}_j\left(\hat{\gamma}^{kl}\hat{\gamma}^{mi}\hat{\gamma}^{nj}h^{\rm TT}_{km}h^{\rm TT}_{ln}\right) \\
& + \hat{\gamma}_{ik}\hat{\gamma}_{jl}\left(\pi^{ij}_{\rm L}\pi^{kl}_{\rm L} + 2\pi^{ij}_{\rm L}\pi^{kl}_{\rm TT} + \pi^{ij}_{\rm TT}\pi^{kl}_{\rm TT}\right) \\
& + \frac{16\pi G}{c^2}\phi^{-1}\left\{\left[(D^*h)^2 + \phi^{-4}\hat{\gamma}^{mn}\frac{S^*_m S^*_n}{c^2}\right]^{1/2} \times \left(1 - \frac{1}{2}\hat{\gamma}^{ik}\hat{\gamma}^{jl}h^{\rm TT}_{kl}\frac{S^*_i S^*_j}{c^2 D^{*\,2}}\right) - \frac{\phi^6 P}{c^2}\right\} \\
& + \mathcal{O}\left(\frac{h}{c^6}\right) + \mathcal{O}\left(\frac{h^2}{c^2}\right).
\end{aligned} \tag{5.22}$$

The 2PN Hamiltonian

Equation (5.22) gives an expression for the integrand of the equation (5.9) for the Hamiltonian. But it has to be expressed only in terms of $h^{\rm TT}_{pq}$ and $\pi^{pq}_{\rm TT}$. Therefore, we still need an expression for $\phi = \phi[h^{\rm TT}_{pq}, \pi^{pq}_{\rm TT}]$.

As the terms containing a factor $h_{ij}^{\rm TT}$ or $\pi_{\rm TT}^{ij}$ in Eq. (5.22) are proportional to the coupling constant G/c^2 of general relativity, it reduces to

$$\hat{\Delta}V = -4\pi G D^*/c^2 + \mathcal{O}(1/c^4) \tag{5.23}$$

at the lowest post-Newtonian approximation. Thus, if we introduce the "Newtonian" potential U defined as the smooth solution of the Poisson equation

$$\hat{\Delta}U = -4\pi G D^*, \tag{5.24}$$

vanishing at spatial infinity, we have $V = U/c^2 + \mathcal{O}(1/c^4)$, plus a possible harmonic function. Assuming an asymptotically flat spacetime, this function must tend asymptotically towards zero while being regular, and so it has to be identically zero. Another important piece of information provided by Eq. (5.22) is the value of the lowest order contribution to the potential V that depends on the field variables. It is given by the equation

$$\begin{aligned} -4V = \hat{\Delta}^{-1}\left(-4\hat{\nabla}_i\hat{\nabla}_j\phi\hat{\gamma}^{ik}\hat{\gamma}^{jl}h_{kl}^{\rm TT}\right) + \mathcal{O}\left(\frac{h}{c^4}\right) \\ + \text{pure matter part}, \end{aligned} \tag{5.25}$$

which shows incidentally that $\phi = 1 + V/2$ is not affected by a non-zero $h_{ij}^{\rm TT}$ at the leading post-Newtonian approximation in the field.

Inserting the resulting expression for the conformal factor into the Hamiltonian constraint (5.22), we arrive at

$$\begin{aligned} -4\hat{\Delta}V = &-\frac{1}{c^4}\left(2\hat{\nabla}_i U\hat{\nabla}_j U + 8\pi G\frac{S_i^* S_j^*}{D^*}\right)\hat{\gamma}^{ik}\hat{\gamma}^{jl}h_{kl}^{\rm TT} \\ &+ \frac{1}{4}\hat{\gamma}^{kl}\hat{\gamma}^{im}\hat{\gamma}^{jn}\hat{\nabla}_k h_{ij}^{\rm TT}\hat{\nabla}_l h_{mn}^{\rm TT} \\ &+ \hat{\gamma}_{ik}\hat{\gamma}_{jl}\left(2\pi_{\rm L}^{ij}\pi_{\rm TT}^{kl} + \pi_{\rm TT}^{ij}\pi_{\rm TT}^{kl}\right) \\ &+ \mathcal{O}\left(\frac{h}{c^6}\right) + \mathcal{O}\left(\frac{h^2}{c^2}\right) \\ &+ \text{total derivative} + \text{pure matter part}. \end{aligned} \tag{5.26}$$

The pure matter part has been kept aside because it does not enter the computation of $h_{ij}^{\rm TT}$. The total derivative terms are irrelevant for the investigation

of the field evolution. Indeed, by virtue of relation (5.9), the Hamiltonian is given by the spatial integral of $-c^4\hat{\Delta}V/(4\pi G)$. Thus the dynamics of the gravitational interaction is described by

$$\begin{aligned} H_{\substack{\text{field}\\+\text{int.}}} &= \frac{c^4}{16\pi G}\int \mathrm{d}^3\boldsymbol{x}\,\sqrt{\hat{\gamma}} \\ &\quad\times\left[-\frac{1}{c^4}\left(2\hat{\nabla}_i U\hat{\nabla}_j U + 8\pi G\frac{S_i^* S_j^*}{D^*}\right)\hat{\gamma}^{ik}\hat{\gamma}^{jl}h_{kl}^{\mathrm{TT}}\right. \\ &\qquad -\frac{1}{4}\hat{\Delta}\left(\hat{\gamma}^{im}\hat{\gamma}^{jn}h_{mn}^{\mathrm{TT}}\right)h_{ij}^{\mathrm{TT}} \\ &\qquad \left.+\hat{\gamma}_{ik}\hat{\gamma}_{jl}\left(2\pi_{\mathrm{L}}^{ij}\pi_{\mathrm{TT}}^{kl}+\pi_{\mathrm{TT}}^{ij}\pi_{\mathrm{TT}}^{kl}\right)\right] \\ &\quad +\mathcal{O}\left(\frac{h}{c^6}\right)+\mathcal{O}\left(\frac{h^2}{c^2}\right), \end{aligned} \tag{5.27}$$

in agreement with Schäfer (1990).

Equations of motion

The Hamilton equations provide the evolution of the field. They take the explicit form

$$\begin{aligned} \partial_t h_{ij}^{\mathrm{TT}} &= 2c\hat{\gamma}_{ij}^{\mathrm{TT}kl}[\hat{\gamma}_{km}\hat{\gamma}_{ln}\left(\pi_{\mathrm{L}}^{mn}+\pi_{\mathrm{TT}}^{mn}\right)] \\ &\quad +\mathcal{O}\left(\frac{1}{c^5}\right)+\mathcal{O}\left(\frac{h}{c}\right) \\ &= 2c\hat{\gamma}_{ik}\hat{\gamma}_{jl}\pi_{\mathrm{TT}}^{kl}+\mathcal{O}\left(\frac{1}{c^5}\right)+\mathcal{O}\left(\frac{h}{c}\right), \end{aligned} \tag{5.28}$$

$$\begin{aligned} \partial_t \pi_{\mathrm{TT}}^{ij} &= -c\hat{\gamma}_{\mathrm{TT}kl}^{ij}\left[-\frac{2}{c^4}\left(\hat{\nabla}_m U\hat{\nabla}_n U+4\pi G\frac{S_m^* S_n^*}{D^*}\right)\hat{\gamma}^{km}\hat{\gamma}^{ln}\right. \\ &\qquad \left.-\frac{1}{2}\hat{\Delta}\left(\hat{\gamma}^{km}\hat{\gamma}^{ln}h_{mn}^{\mathrm{TT}}\right)\right] \\ &\quad +\mathcal{O}\left(\frac{1}{c^5}\right)+\mathcal{O}\left(\frac{h}{c}\right). \end{aligned} \tag{5.29}$$

The non-conformally flat part of the 3-metric appears first at the second post-Newtonian approximation. Its leading order is obtained by inserting the above expression for $\partial_t \pi^{ij}_{\rm TT}$ into the time derivative of Eq. (5.28). The resulting equation is of wave type. In the near zone, all terms of order $1/c^6$ may be neglected, in particular the time derivative contribution to the d'Alembertian operator. Hence the non-conformally flat part of the 3-metric satisfies

$$\hat{\Delta} h^{\rm TT}_{ij} = -\frac{\hat{\gamma}^{\rm TT\,kl}_{ij}}{c^4}\left(4\hat{\nabla}_k U \hat{\nabla}_l U + 16\pi G \frac{S^*_k S^*_l}{D^*}\right) + \mathcal{O}\left(\frac{1}{c^6}\right), \tag{5.30}$$

which is identical up to second post-Newtonian order to the equation

$$\hat{\Delta} h^{\rm 2PN}_{ij} = \hat{\gamma}^{\rm TT\,kl}_{ij} F_{kl}, \tag{5.31}$$

where the source F_{kl} is given by

$$F_{kl} = -4\hat{\nabla}_k U \hat{\nabla}_l U - 16\pi \frac{S^*_k S^*_l}{D^*}. \tag{5.32}$$

This equation has to be solved in order to calculate the second post-Newtonian correction to the CFC metric.

5.3.2 Modified CFC equations

Equation for the lapse

The equation for the lapse function α is derived from the gauge conditions (2.39, 2.40) combined with the evolution equation (2.24) for the extrinsic curvature K_{ij}. From the identity $\pi^{ij}\hat{\gamma}_{ij} = 0$, we deduce that the trace is negligible at this level of approximation:

$$\begin{aligned}\hat{\gamma}^{ij} K_{ij} &= \frac{1}{2\sqrt{\bar{\gamma}}}(2\sqrt{\bar{\gamma}}\hat{\gamma}_{ij} K^{ij}) + \mathcal{O}\left(\frac{h}{c^3}\right) \\ &= \frac{1}{2\sqrt{\bar{\gamma}}}\pi^{ij}\hat{\gamma}_{ij} + \mathcal{O}\left(\frac{h}{c^3}\right) \\ &= \mathcal{O}\left(\frac{1}{c^7}\right).\end{aligned} \tag{5.33}$$

This implies that the ADM gauge in combination with the CFC+ approximation restrict the gauge selection, as the only slicing possible is the maximal slicing. By contracting Eq. (2.24) with the inverse 3-metric γ^{ij}, we arrive at

$$\frac{\gamma^{ij}}{c}\partial_t K_{ij} = \frac{\phi^{-4}}{c}\partial_t\left(\hat{\gamma}^{ij}K_{ij}\right) + \mathcal{O}\left(\frac{1}{c^8}\right) = \mathcal{O}\left(\frac{1}{c^8}\right), \tag{5.34}$$

from which follows that

$$\begin{aligned} &- \nabla_i\nabla^i\alpha + \alpha R + K^{ik}\left(-2\alpha K_{ik} + 2\nabla_i\beta_k\right) \\ &- \frac{4\pi G}{c^4}(-S+3E) = \mathcal{O}\left(\frac{1}{c^8}\right). \end{aligned} \tag{5.35}$$

Due to the fact that K^{ik} is symmetric and trace-free, neglecting corrections of order $\mathcal{O}(h/c^3)$, the product $K^{ik}(-2\alpha K_{ik} + 2\nabla_i\beta_k)$ can be written as $K^{ik}(-2\alpha K_{<ik>} + 2\nabla_{<i}\beta_{k>}) + \mathcal{O}(h/c^6)$. The terms inside the parentheses vanish according to the symmetric trace-free version of Eq. (2.23),

$$-2\alpha K_{<ij>} + 2\nabla_{<i}\beta_{j>} = \frac{1}{c}\partial_t\gamma_{<ij>} = \mathcal{O}\left(\frac{1}{c^5}\right), \tag{5.36}$$

so that $K^{ik}(-2\alpha K_{ik} + 2\nabla_i\beta_k) = \mathcal{O}(1/c^8)$. Next, we see from the Hamiltonian constraint equation that the interaction and field parts of the scalar curvature R appearing in Eq. (5.35) are actually of order $\mathcal{O}(h/c^4) = \mathcal{O}(1/c^8)$. On the other hand, we know that $E^* = \mathcal{O}(h/c^4)+$pure matter terms. We have similar equalities for E and $S = S^i_i$. Therefore, we find

$$\begin{aligned} \frac{1}{\sqrt{\bar{\gamma}}}\hat{\nabla}_i\left(\sqrt{\bar{\gamma}}\gamma^{ij}\hat{\nabla}_j\alpha\right) &= \mathcal{O}\left(\frac{1}{c^8}\right) + \text{pure matter part} \\ &= \hat{\Delta}\alpha - \hat{\nabla}_i\hat{\nabla}_j\alpha\,\hat{\gamma}^{ik}\hat{\gamma}^{jl}h^{\mathrm{TT}}_{kl}. \end{aligned} \tag{5.37}$$

At the lowest approximation, we may replace α by $(-g_{00} + \beta_i\beta^i)^{1/2} = 1 - U/c^2 + \mathcal{O}(1/c^4)$. In the end, the elliptic equation for the lapse in the presence of h^{TT}_{ij} is modified to

$$\hat{\Delta}\alpha = \left(\hat{\Delta}\alpha\right)_{h^{\mathrm{TT}}_{ij}=0} - \frac{1}{c^2}\hat{\gamma}^{ik}\hat{\gamma}^{jl}\,h^{\mathrm{TT}}_{ij}\hat{\nabla}_k\hat{\nabla}_l U + \mathcal{O}\left(\frac{1}{c^8}\right). \tag{5.38}$$

This is the desired CFC+ metric equation for the lapse function α. Since U/c^2 is Newtonian, $\hat{\gamma}^{ik}\hat{\gamma}^{jl}h_{ij}^{\rm TT}\hat{\nabla}_k\hat{\nabla}_l U/c^2$ corresponds to the second post-Newtonian order for the dynamics.

Equations for the shift and the conformal factor

The equation for the shift can be obtained in principle by contracting the 3-metric evolution with the help of the Euclidean metric $\hat{\gamma}^{ij}$. However, with respect to the conformally flat case, the new terms are proportional to a product of the type K (or β) times $h_{ij}^{\rm TT}$. They are therefore negligible at the second post-Newtonian level and will not be computed here. As already pointed out, the equation for the conformal factor remains unaffected at that level as well. Thus in general, all CFC equations, except the one for the lapse function, remain unaltered.

5.4 Calculation of $h_{ij}^{\rm TT}$

Once we know the equation for $h_{ij}^{\rm TT}$ up to second post Newtonian order, we have to invert Eq. (5.31). We proceed in three steps:

1. We make the action of $\hat{\gamma}_{ij}^{{\rm TT}kl}$ explicit in Eq. (5.31). The result is integrated formally by means of the Poisson integral operator $\hat{\Delta}^{-1}$. By virtue of its linearity property, we obtain a weighted sum of Poisson potentials of generic type $\hat{\Delta}^{-1}F_{mn}$ (up to possible index contractions) or super-potentials of the form $\hat{\Delta}^{-2}\hat{\nabla}_i\hat{\nabla}_j F_{mn} = \hat{\Delta}^{-1}(\hat{\Delta}^{-1}\hat{\nabla}_i\hat{\nabla}_j F_{mn})$ and $\hat{\Delta}^{-3}\hat{\nabla}_i\hat{\nabla}_j\hat{\nabla}_k F_{mn}$.

2. We transform the super-potentials into simple Poisson potentials in order to get rid of all derivatives acting directly on the sources.

3. We insert the resulting quantities into the transverse traceless tensor $\hat{\Delta}^{-1}\hat{\gamma}_{ij}^{{\rm TT}kl}F_{kl}$ and perform some additional manipulations that lead to the final expression.

These steps are performed in detail in the following.

5.4.1 Inversion of the equation for $h_{ij}^{\rm TT}$

It is straightforward to expand the operator $\hat{\gamma}_{ij}^{{\rm TT}kl}$ defined in Eq. (5.12) and to apply it to the source F_{kl} given in Eq. (5.32). Taking the symmetry in the two indices k and l into account, inverting the tensor Poisson equation (5.31) then yields

$$\begin{aligned} h_{ij}^{\rm TT} &= \hat{\Delta}^{-1}\left(\hat{\gamma}_{ij}^{{\rm TT}kl}F_{kl}\right) \\ &= \hat{\Delta}^{-1}F_{ij} - \frac{1}{2}\hat{\gamma}_{ij}\hat{\Delta}^{-1}\left(\hat{\gamma}^{kl}F_{kl}\right) \\ &- 2\hat{\Delta}^{-2}\left(\hat{\gamma}^{kl}\hat{\nabla}_k\hat{\nabla}_{(i}F_{j)l}\right) + \frac{1}{2}\hat{\Delta}^{-2}\hat{\nabla}_i\hat{\nabla}_j\left(\hat{\gamma}^{kl}F_{kl}\right) \\ &+ \frac{1}{2}\hat{\gamma}_{ij}\hat{\Delta}^{-2}\hat{\nabla}_k\hat{\nabla}_l\left(\hat{\gamma}^{mk}\hat{\gamma}^{nl}F_{mn}\right) \\ &+ \frac{1}{2}\hat{\Delta}^{-3}\hat{\nabla}_i\hat{\nabla}_j\hat{\nabla}_k\hat{\nabla}_l\left(\hat{\gamma}^{mk}\hat{\gamma}^{nl}F_{mn}\right). \end{aligned} \tag{5.39}$$

As the Poisson integral $\hat{\Delta}^{-1}F_{kl}$ converges, all other (super-)potentials entering Eq. (5.39) are also well defined. However, they cannot be handled easily. For instance, quantities such as $\hat{\Delta}^{-2}F_{mn}$ or $\hat{\Delta}^{-3}F_{mn}$ are a priori meaningless, which shows that the derivatives cannot commute with the integrals. In order to operate on the sources without meeting any serious restrictions, it is convenient to resort to the tool of Hadamard finite part regularization (see Appendix B) This allows us to write the potentials and super-potentials in a form suitable for numerical integration. For this purpose, we can recourse to fairly standard techniques, some of which were used in particular by Blanchet et al. (1990) to deal with the derivative of the Newtonian super-potential. With the help of Eq. (B.6) and the commutation relation $\hat{\Delta}_{\boldsymbol{x}}^{-1}\hat{\nabla}_i = \hat{\nabla}_i\hat{\Delta}_{\boldsymbol{x}}^{-1}$, we transform the expression of the (super-)potentials $\hat{\Delta}^{-2}\hat{\nabla}_i\hat{\nabla}_jF_{kl}$ or $\hat{\Delta}^{-3}\hat{\nabla}_i\hat{\nabla}_j\hat{\nabla}_k\hat{\nabla}_lF_{mn}$ entering the non-conformal part of the 3-metric (with possible index contractions). By doing this, we try to minimize the number of free indices that remain inside the integral and, for numerical reasons, to get rid of all spatial derivatives of the densities D^* or S_i^* in the final expressions. The transformation of $\hat{\Delta}^{-2}\hat{\nabla}_i\hat{\nabla}_jF_{kl}$, for instance, is achieved in four steps: (i) We let both derivatives commute with the integration symbol, $\hat{\Delta}^{-2}\hat{\nabla}_i\hat{\nabla}_jF_{kl} = \hat{\nabla}_i\hat{\nabla}_j\hat{\Delta}_{\boldsymbol{x}}^{-2}F_{kl}$, (ii) we rewrite $\hat{\Delta}_{\boldsymbol{x}}^{-2}F_{kl}$ according to Eq. (B.5) with $p = 2$, (iii) we make one of the

derivatives act on the kernel $|\boldsymbol{x}-\boldsymbol{x}'|^{1+B}$ so that there remains only one unevaluated spatial derivative operating on a linear combination of simple Poisson integrals, and (iv) we let the derivative act. This yields

$$\hat{\Delta}^{-2}\hat{\nabla}_i\hat{\nabla}_j F_{kl} = \frac{1}{2}\Big[\hat{\gamma}_{ij}\hat{\Delta}_{\boldsymbol{x}}^{-1}F_{kl} + \hat{\gamma}_{jm}x^m\hat{\nabla}_i\hat{\Delta}_{\boldsymbol{x}}^{-1}F_{kl} - \hat{\nabla}_i\hat{\Delta}_{\boldsymbol{x}}^{-1}(\hat{\gamma}_{jm}x^m F_{kl})\Big]. \tag{5.40}$$

The respective transformation of $\hat{\Delta}^{-3}\hat{\nabla}_i\hat{\nabla}_j\hat{\nabla}_k F_{mn}$ is very similar:

$$\begin{aligned}
&\hat{\Delta}^{-3}\hat{\nabla}_i\hat{\nabla}_j\hat{\nabla}_k F_{mn} \\
&\quad= \frac{1}{24}\hat{\nabla}_i\hat{\nabla}_j\hat{\nabla}_k\,\mathrm{FP}_{B=0}\int\frac{\mathrm{d}^3\boldsymbol{x}'\sqrt{\hat{\gamma}}}{-4\pi r_0^B}|\boldsymbol{x}-\boldsymbol{x}'|^{3+B}F_{mn} \\
&\quad= \frac{1}{8}\hat{\nabla}_k\int\frac{\mathrm{d}^3\boldsymbol{x}'\sqrt{\hat{\gamma}}}{-4\pi}\Big[\hat{\gamma}_{ip}\hat{\gamma}_{jq}\frac{(x^p-x'^p)(x^q-x'^q)}{|\boldsymbol{x}-\boldsymbol{x}'|} \\
&\qquad\qquad + \hat{\gamma}_{ij}|\boldsymbol{x}-\boldsymbol{x}'|\Big]F_{mn} \\
&\quad= \frac{1}{8}\Big[3\hat{\gamma}_{(ij}\hat{\gamma}_{k)p}x^p\hat{\Delta}_{\boldsymbol{x}}^{-1}F_{mn} - 3\hat{\gamma}_{(ij}\hat{\gamma}_{k)p}\hat{\Delta}_{\boldsymbol{x}}^{-1}(x^pF_{mn}) \\
&\qquad - 2\hat{\gamma}_{p(i}\hat{\gamma}_{j)q}x^p\hat{\nabla}_k\hat{\Delta}_{\boldsymbol{x}}^{-1}(x^qF_{mn}) \\
&\qquad + \hat{\gamma}_{ip}\hat{\gamma}_{jq}x^px^q\hat{\nabla}_k\hat{\Delta}_{\boldsymbol{x}}^{-1}F_{mn} \\
&\qquad + \hat{\gamma}_{ip}\hat{\gamma}_{jq}\hat{\nabla}_k\hat{\Delta}_{\boldsymbol{x}}^{-1}(x^px^qF_{mn})\Big].
\end{aligned} \tag{5.41}$$

5.4.2 The intermediate potentials

The computation of $h_{ij}^{\rm 2PN}$, i.e. the inversion of the tensor Poisson equation (5.31) by means of the Poisson integral operator $\hat{\Delta}^{-1}$, is simplified by the introduction of intermediate potentials $\mathcal{S}$, $\mathcal{S}_i$, $\mathcal{T}_i$, $\mathcal{R}_i$, and $\mathcal{S}_{ij}$, which are solutions of

the following scalar/vector/tensor-Poisson equations:

$$\hat{\Delta}\mathcal{S} = -4\pi\frac{S_i^* S_j^*}{D^*}x^i x^j, \tag{5.42}$$

$$\hat{\Delta}\mathcal{S}_i = \left[-4\pi\frac{S_i^* S_j^*}{D^*} - \hat{\nabla}_i U\hat{\nabla}_j U\right]x^j, \tag{5.43}$$

$$\hat{\Delta}\mathcal{T}_i = \left[-4\pi\frac{S_j^* S_k^*}{D^*} - \hat{\nabla}_j U\hat{\nabla}_k U\right]\hat{\gamma}^{jk}\hat{\gamma}_{il}x^l, \tag{5.44}$$

$$\hat{\Delta}\mathcal{R}_i = \hat{\nabla}_i(\hat{\nabla}_j U\hat{\nabla}_k U x^j x^k), \tag{5.45}$$

$$\hat{\Delta}\mathcal{S}_{ij} = -4\pi\frac{S_i^* S_j^*}{D^*} - \hat{\nabla}_i U\hat{\nabla}_j U. \tag{5.46}$$

These equations are designed in such a way that their source terms approach zero like r^{-3} when $r = |\boldsymbol{x}|$ tends towards infinity, which ensures the existence of the corresponding Poisson integrals. With the help of these potentials we are now able to deduce the expression for h_{ij}^{TT} up to second post-Newtonian order,

$$\begin{aligned} h_{ij}^{\mathrm{TT}} = {} & \frac{1}{2}\mathcal{S}_{ij} - 3x^k\hat{\nabla}_{(i}\mathcal{S}_{j)k} + \frac{5}{4}\hat{\gamma}_{jm}x^m\hat{\nabla}_i\left(\hat{\gamma}^{kl}\mathcal{S}_{kl}\right) \\ & + \frac{1}{4}x^k x^l\hat{\nabla}_i\hat{\nabla}_j\mathcal{S}_{kl} + 3\hat{\nabla}_{(i}\mathcal{S}_{j)} - \frac{1}{2}x^k\hat{\nabla}_i\hat{\nabla}_j\mathcal{S}_k \\ & + \frac{1}{4}\hat{\nabla}_i\hat{\nabla}_j\mathcal{S} - \frac{5}{4}\hat{\nabla}_i\mathcal{T}_j - \frac{1}{4}\hat{\nabla}_i\mathcal{R}_j \\ & + \hat{\gamma}_{ij}\left[\frac{1}{4}\hat{\gamma}^{kl}\mathcal{S}_{kl} + x^k\hat{\gamma}^{lm}\hat{\nabla}_m\mathcal{S}_{kl} - \hat{\gamma}^{kl}\hat{\nabla}_k\mathcal{S}_l\right] \\ & + \mathcal{O}\left(\frac{1}{c^6}\right). \end{aligned} \tag{5.47}$$

The explicit expressions needed to write the above equations in spherical coordinates can be found in Appendix A.

5.4.3 Multipole expansion of the intermediate potentials

Due to the specific type of elliptic solvers employed in our computer code (see Chapter 8), it is not possible to use the inverse image method to evaluate the

intermediate potentials up to spatial infinity. We instead solve Eqs. (5.42–5.46) assuming specific boundary conditions. These are determined from the multipole expansion $\mathcal{M}$ of the intermediate potentials $\mathcal{S}$, $\mathcal{S}_i$, $\mathcal{T}_i$, $\mathcal{R}_i$, and $\mathcal{S}_{ij}$. The derivation of the multipole expansion is done by means of the formula (C.9) of Blanchet & Poujade (2002) specializing the matching relation first established in Blanchet (1998) for retarded quantities.

For any generic source f which admits outside the system a multipole expansion of the form $\mathcal{M}(f) = \sum_{p=-\infty}^{p_0} f_p(\boldsymbol{n}) r^p$ with $\boldsymbol{n} = \boldsymbol{x}/r$ and $p_0 < -2$, the multipole expansion of the Poisson integral $\hat{\Delta}^{-1} f$ is given by

$$\begin{aligned}\mathcal{M}\left(\hat{\Delta}^{-1} f\right) = &\sum_{l=0}^{+\infty} \frac{(-1)^l}{l!} \hat{\nabla}_{i_1} \dots \hat{\nabla}_{i_l} \left(\frac{1}{r}\right) \\ &\times \mathrm{FP}_{B=0} \int \frac{\mathrm{d}^3 \boldsymbol{x}' \sqrt{\hat{\gamma}}}{-4\pi} \left(\frac{r'}{r_0}\right)^B x'^{i_1} \dots x'^{i_l} f \\ &+ \hat{\Delta}_{\mathbf{0}}^{-1} \mathcal{M}(f). \end{aligned} \tag{5.48}$$

In the special case where the source f has compact support, $\mathcal{M}(f)$ is identically zero and thus the last term above vanishes. We recover the standard multipole formula used in electrostatics for spatially limited systems.

At this stage, the multipole expansions of all our elementary potentials may be derived by application of Eq. (5.48). We start with $\mathcal{S}_{ij}$ which goes to zero at the highest order. It involves the monopole integral with non-compact-supported source $\int \mathrm{d}^3 \boldsymbol{x} \sqrt{\hat{\gamma}} \hat{\nabla}_i U \hat{\nabla}_j U/(-4\pi)$. Remarkably, this integral admits an alternative expression whose source has compact support, which is a very useful feature for the numerical calculations. To perform the transformation, we first replace the second potential U in the integrand $\hat{\nabla}_i U \hat{\nabla}_j U/(-4\pi)$ by $\hat{\Delta}\chi/2$, where χ denotes the Newtonian super-potential $\chi = \int \mathrm{d}^3 \boldsymbol{x}' |\boldsymbol{x} - \boldsymbol{x}'| D^*$. Next, we integrate this Laplacian by parts, being careful to keep all contribu-

tions from the derivatives of r^B. The result is

$$\begin{aligned}
&\mathrm{FP}_{B=0} \int \frac{\mathrm{d}^3\boldsymbol{x}\,\sqrt{\hat{\gamma}}}{-4\pi r_0^B} r^B\,\hat{\nabla}_i\left(\frac{\chi}{2}\right)\hat{\nabla}_j\hat{\Delta}U \\
&\quad = \mathrm{FP}_{B=0} \int \frac{\mathrm{d}^3\boldsymbol{x}\,\sqrt{\hat{\gamma}}}{-4\pi r_0^B}\Big[B(B+1)r^{B-2}\,\hat{\nabla}_j U \\
&\qquad\qquad + 2Br^{B-1}n^k\,\hat{\nabla}_j\hat{\nabla}_k U\Big]\hat{\nabla}_i\left(\frac{\chi}{2}\right). \qquad (5.49)
\end{aligned}$$

We remark here that the second finite part on the right-hand side vanishes. Indeed, the integration does not generate any pole in B which is able to compensate for the cancellation of the pre-factor B itself. Consequently, after a last integration by parts, we arrive at the equality

$$\int \frac{\mathrm{d}^3\boldsymbol{x}\,\sqrt{\hat{\gamma}}}{-4\pi}\hat{\nabla}_i U\hat{\nabla}_j U = -\frac{1}{2}\int \mathrm{d}^3\boldsymbol{x}\,\sqrt{\hat{\gamma}}D^*\hat{\nabla}_i\hat{\nabla}_j\chi. \qquad (5.50)$$

It is not difficult to check that $\hat{\nabla}_j\chi = \hat{\gamma}_{jk}x^k\hat{\Delta}^{-1}(-4\pi D^*) - \hat{\Delta}^{-1}(-4\pi\hat{\gamma}_{jk}x^k D^*)$ by virtue of relation (B.6). Using an integration by parts of the type

$$\int \mathrm{d}^3\boldsymbol{x}\,\sqrt{\hat{\gamma}}f\,\hat{\Delta}^{-1}g = \int \mathrm{d}^3\boldsymbol{x}\,\sqrt{\hat{\gamma}}g\,\hat{\Delta}^{-1}f, \qquad (5.51)$$

we are finally able to show that

$$\begin{aligned}
&\int \frac{\mathrm{d}^3\boldsymbol{x}\,\sqrt{\hat{\gamma}}}{-4\pi}\hat{\nabla}_i U\hat{\nabla}_j U \\
&\quad = -\int \mathrm{d}^3\boldsymbol{x}\,\sqrt{\hat{\gamma}}D^*\left(\hat{\gamma}_{jk}x^k\hat{\nabla}_i U + \frac{1}{2}\hat{\gamma}_{ij}U\right). \qquad (5.52)
\end{aligned}$$

Inserting the latter relation into the general formula (5.48) specialized for $f = -4\pi S_i^* S_j^*/D^* - \hat{\nabla}_i U\hat{\nabla}_j U$, we get

$$\begin{aligned}
\mathcal{M}(\mathcal{S}_{ij}) &= \frac{1}{r}\int \mathrm{d}^3\boldsymbol{x}\,\sqrt{\hat{\gamma}}D^*\left(\frac{S_i^* S_j^*}{D^{*\,2}} + \hat{\gamma}_{jk}x^k\hat{\nabla}_i U + \frac{1}{2}\hat{\gamma}_{ij}U\right) \\
&\quad + \mathcal{M}\left(-4\pi\frac{S_i^* S_j^*}{D^*} - \hat{\nabla}_i U\hat{\nabla}_j U\right). \qquad (5.53)
\end{aligned}$$

When examining the second term in the above equation, one immediately observes that $\mathcal{M}(S_i^* S_j^*/D^*) = 0$ as the source $(S_i^* S_j^*/D^{*\,2})D^*$ has compact support. Furthermore we notice that $\mathcal{M}(\hat{\nabla}_i U \hat{\nabla}_j U) = \mathcal{O}(1/r^4)$, hence $\hat{\Delta}_{\mathbf{0}}^{-1}\mathcal{M}(\hat{\nabla}_i U \hat{\nabla}_j U) = \mathcal{O}(1/r^2)$ according to dimensional analysis. It may also be checked directly with the help of the Matthew formula $\hat{\Delta}_{\mathbf{0}}^{-1}(n^{<i_1}\ldots n^{i_l>} r^a) = n^{<i_1}\ldots n^{i_l>} r^{a+2}/[(a+2-l)(a+3+l)]$.

We go on by calculating $\mathcal{M}(\mathcal{S}_i)$. The part of its source with non-compact support essentially amounts to $x^k \hat{\nabla}_i U \hat{\nabla}_k U$. The integral of the latter quantity may be transformed with the same technique as the one used to establish Eq. (5.53). We find that

$$\begin{aligned}
&\mathrm{FP}_{B=0} \int \frac{\mathrm{d}^3\boldsymbol{x}\,\sqrt{\hat{\gamma}}}{-4\pi r_0^B} r^B x^k\, \hat{\nabla}_i U \hat{\nabla}_k U \\
&\quad = \frac{1}{2}\,\mathrm{FP}_{B=0} \int \frac{\mathrm{d}^3\boldsymbol{x}\,\sqrt{\hat{\gamma}}}{-4\pi r_0^B} r^B \Big(x^k \hat{\nabla}_k \chi \hat{\nabla}_i (-4\pi D^*) \\
&\qquad\qquad + 2\hat{\gamma}^{kl} \hat{\nabla}_k \chi \hat{\nabla}_l \hat{\nabla}_i U \Big). \qquad (5.54)
\end{aligned}$$

We may then perform an integration by parts affecting the derivative $\hat{\nabla}_i D^*$ of the first term and the derivative $\hat{\nabla}_k \chi$ of the second term. The contribution of $\hat{\nabla}_k r^B$ is proportional to B. It can give rise to a definite non-zero result only when it is multiplied by the factor $1/B$ coming from the radial integration of $1/r^3$. As the corresponding angular integral vanishes, so does it. Noticing that $\hat{\Delta}\chi \hat{\nabla}_i U = 2U \hat{\nabla}_i U = \hat{\nabla}_i U^2$, we see that the resulting integral reads

$$\begin{aligned}
&\frac{1}{2}\int \mathrm{d}^3\boldsymbol{x}\,\sqrt{\hat{\gamma}} D^* \left(x^k \hat{\nabla}_i \hat{\nabla}_k \chi + \hat{\nabla}_i \chi \right) \\
&\quad - \mathrm{FP}_{B=0} \int \mathrm{d}^3\boldsymbol{x}\,\sqrt{\hat{\gamma}} \left(\frac{r}{r_0} \right)^B \hat{\nabla}_i U^2. \qquad (5.55)
\end{aligned}$$

After integrating the second term by parts, we get an integral whose source is proportional to B. Following the same argument as before, it can be shown to be zero. Expressing again the super-potential as a combination of Poisson integrals, and performing other integrations by parts including those of the

form (5.51), we arrive at

$$\begin{aligned}\mathrm{FP}_{B=0} \int \frac{\mathrm{d}^3\boldsymbol{x}\,\sqrt{\hat{\gamma}}}{-4\pi r_0^B}\, r^B x^k\, \hat{\nabla}_i U \hat{\nabla}_k U \\ = -\int \mathrm{d}^3\boldsymbol{x}\,\sqrt{\hat{\gamma}} D^* \hat{\gamma}_{ij} \left(x^j U + x^j x^k \hat{\nabla}_k U \right). \end{aligned} \tag{5.56}$$

On the other hand, the source $x^k \hat{\nabla}_i U \hat{\nabla}_k U$ behaves as $M^2 \hat{\gamma}_{ik} n^k / r^3 = -M^2 \hat{\nabla}_i (r^{-2}/2)$, where M is the baryonic rest mass density defined as

$$M = \int \mathrm{d}^3\boldsymbol{x} \sqrt{\hat{\gamma}} D^*. \tag{5.57}$$

A direct integration leads to the relation $\hat{\Delta}_{\mathbf{0}}^{-1}(1/r^2) = \ln r + \text{const.}$, which can also be seen from a dimensional argument, so that $\hat{\Delta}_{\mathbf{0}}^{-1} \mathcal{M}(x^k \hat{\nabla}_i U \hat{\nabla}_k U)$ decreases asymptotically as $-M^2 \hat{\nabla}_i (\ln r)/2$. Therefore, we have proved the approximate equality

$$\begin{aligned}\mathcal{M}(\mathcal{S}_i) = \frac{1}{r} \int \mathrm{d}^3\boldsymbol{x}\, \sqrt{\hat{\gamma}} D^* \left[x^k S_i S_k + \hat{\gamma}_{ij} x^j (U + x^k \hat{\nabla}_k U) \right] \\ + \frac{M^2}{2r} \hat{\gamma}_{ik} n^k + \mathcal{O}\left(\frac{1}{r^2} \right). \end{aligned} \tag{5.58}$$

In the multipole expansion of $\mathcal{T}_i$, the only term entering its composition that is generated by a quantity with non-compact support is the Poisson potential $\hat{\Delta}^{-1}(\hat{\gamma}_{ij} \hat{\gamma}^{kl} x^j \hat{\nabla}_k U \hat{\nabla}_l U)$. Its monopole part is composed of an integral over the source, which simplifies by virtue of the relation $2\hat{\gamma}^{kl} \hat{\nabla}_k U \hat{\nabla}_l U = \hat{\Delta} U^2 - 2U \hat{\Delta} U$ to

$$\begin{aligned}\mathrm{FP}_{B=0} \int \frac{\mathrm{d}^3\boldsymbol{x}}{-4\pi} \sqrt{\hat{\gamma}} \left(\frac{r}{r_0} \right)^B \left(\hat{\gamma}_{ij} \hat{\gamma}^{kl} x^j \hat{\nabla}_k U \hat{\nabla}_l U \right) \\ = -\int \mathrm{d}^3\boldsymbol{x}\, \sqrt{\hat{\gamma}} D^* \hat{\gamma}_{ik} x^k U, \end{aligned} \tag{5.59}$$

and of a contribution originating from the Poisson inverse operator applied to $\mathcal{M}(\hat{\gamma}_{ij} \hat{\gamma}^{kl} x^j \hat{\nabla}_k U \hat{\nabla}_l U) = -M^2 \hat{\nabla}_i (r^{-2}/2) + \mathcal{O}(1/r^4)$. We thus have

$$\hat{\Delta}_{\mathbf{0}}^{-1} \mathcal{M}(\hat{\gamma}_{ij} \hat{\gamma}^{kl} x^j \hat{\nabla}_k U \hat{\nabla}_l U) = -\frac{M^2}{2r} \hat{\gamma}_{ij} n^j + \mathcal{O}\left(\frac{1}{r^2} \right). \tag{5.60}$$

The treatment of the leading term in the multipole expansion of $\mathcal{R}_i$ is similar. The integral of $\hat{\nabla}_i(x^k x^l \hat{\nabla}_k U \hat{\nabla}_l U)$ is simply zero by virtue of the Gauss theorem, and the monopole part of $-\hat{\Delta}^{-1}\hat{\nabla}_i(x^k x^l \hat{\nabla}_k U \hat{\nabla}_l U)$ is the same as that of $2\hat{\gamma}_{ij}\hat{\gamma}^{kl}x^j \hat{\nabla}_k U \hat{\nabla}_l U$.

We conclude with the multipole expansion for the potential $\mathcal{S}$. Since its source is already of compact support, it can simply be expanded with the help of the standard multipole formula mentioned after Eq. (5.48).

In the end this yields the desired multipole expansions of the elementary potentials in the second second post-Newtonian expansion,

$$\mathcal{M}(\mathcal{S}) = \frac{1}{r}\int \mathrm{d}^3\boldsymbol{x}\,\sqrt{\hat{\gamma}}\left(\frac{S_k^* S_l^*}{D^*}x^k x^l\right), \tag{5.61}$$

$$\mathcal{M}(\mathcal{S}_i) = \frac{1}{r}\int \mathrm{d}^3\boldsymbol{x}\,\sqrt{\hat{\gamma}}D^*\left(\frac{S_i^* S_k^*}{D^{*\,2}}x^k + \hat{\gamma}_{ij}x^j(U + x^k\hat{\nabla}_k U)\right) + \frac{M^2}{2r}\hat{\gamma}_{ij}n^j, \tag{5.62}$$

$$\mathcal{M}(\mathcal{T}_i) = \frac{1}{r}\int \mathrm{d}^3\boldsymbol{x}\,\sqrt{\hat{\gamma}}D^*\left(\frac{\hat{\gamma}^{kl}S_k^* S_l^*}{D^{*\,2}} + U\right)\hat{\gamma}_{ij}x^j + \frac{M^2}{2r}\hat{\gamma}_{ij}n^j, \tag{5.63}$$

$$\mathcal{M}(\mathcal{R}_i) = \frac{M^2\hat{\gamma}_{ij}n^j}{r}, \tag{5.64}$$

$$\mathcal{M}(\mathcal{S}_{ij}) = \frac{1}{r}\int \mathrm{d}^3\boldsymbol{x}\,\sqrt{\hat{\gamma}}D^*\left(\frac{S_i^* S_j^*}{D^{*\,2}} + \frac{1}{2}\hat{\gamma}_{ij}U + \hat{\gamma}_{ik}x^k\partial_j U\right), \tag{5.65}$$

modulo $\mathcal{O}(1/r^2)$ corrections. By evaluating the above expansions at a finite radius outside the star we obtain the necessary boundary conditions for $\mathcal{S}$, $\mathcal{S}_i$, $\mathcal{T}_i$, $\mathcal{R}_i$, and $\mathcal{S}_{ij}$, which are used in the numerical procedure to solve the intermediate potentials.

5.5 CFC+ in a nutshell

The procedure to calculate the CFC+ metric can be summarized in the following steps:

1. Calculate "Newtonian" potential (1 Poisson eq.):

$$\hat{\Delta}U = -4\pi G D^*$$

2. Calculate intermediate potentials (16 Poisson eqs.):

$$\begin{aligned}
\hat{\Delta}\mathcal{S} &= -4\pi \frac{S_i^* S_j^*}{D^*} x^i x^j, \\
\hat{\Delta}\mathcal{S}_i &= \left[-4\pi \frac{S_i^* S_j^*}{D^*} - \hat{\nabla}_i U \hat{\nabla}_j U \right] x^j, \\
\hat{\Delta}\mathcal{T}_i &= \left[-4\pi \frac{S_j^* S_k^*}{D^*} - \hat{\nabla}_j U \hat{\nabla}_k U \right] \hat{\gamma}^{jk} \hat{\gamma}_{il} x^l, \\
\hat{\Delta}\mathcal{R}_i &= \hat{\nabla}_i (\hat{\nabla}_j U \hat{\nabla}_k U x^j x^k), \\
\hat{\Delta}\mathcal{S}_{ij} &= -4\pi \frac{S_i^* S_j^*}{D^*} - \hat{\nabla}_i U \hat{\nabla}_j U.
\end{aligned}$$

3. Calculate h_{ij}^{TT}:

$$\begin{aligned}
h_{ij}^{\mathrm{TT}} = {} & \frac{1}{2}\mathcal{S}_{ij} - 3x^k \hat{\nabla}_{(i}\mathcal{S}_{j)k} + \frac{5}{4}\hat{\gamma}_{jm} x^m \hat{\nabla}_i \left(\hat{\gamma}^{kl} \mathcal{S}_{kl} \right) \\
& + \frac{1}{4} x^k x^l \hat{\nabla}_i \hat{\nabla}_j \mathcal{S}_{kl} + 3\hat{\nabla}_{(i}\mathcal{S}_{j)} - \frac{1}{2} x^k \hat{\nabla}_i \hat{\nabla}_j \mathcal{S}_k \\
& + \frac{1}{4}\hat{\nabla}_i \hat{\nabla}_j \mathcal{S} - \frac{5}{4}\hat{\nabla}_i \mathcal{T}_j - \frac{1}{4}\hat{\nabla}_i \mathcal{R}_j \\
& + \hat{\gamma}_{ij} \left[\frac{1}{4}\hat{\gamma}^{kl}\mathcal{S}_{kl} + x^k \hat{\gamma}^{lm} \hat{\nabla}_m \mathcal{S}_{kl} - \hat{\gamma}^{kl} \hat{\nabla}_k \mathcal{S}_l \right]
\end{aligned}$$

4. Calculate modified CFC equations (5 nonlinear Poisson-like eqs.):

$$\begin{aligned}
\hat{\Delta}(\alpha\phi) &= 2\pi\alpha\phi^5\left(E + 2S + \frac{7K_{ij}K^{ij}}{16\pi}\right) \\
&\quad - \frac{1}{c^2}\hat{\gamma}^{ik}\hat{\gamma}^{jl}\, h_{ij}^{\mathrm{TT}}\hat{\nabla}_k\hat{\nabla}_l U, \\
\hat{\Delta}\phi &= -2\pi\phi^5\left(E + \frac{K_{ij}K^{ij}}{16\pi}\right), \\
\hat{\Delta}\beta^i &= 16\pi\alpha\phi^4 S^i + 2\hat{K}^{ij}\hat{\nabla}_j\left(\frac{\alpha}{\phi^6}\right) - \frac{1}{3}\hat{\nabla}^i\hat{\nabla}_k\beta^k,
\end{aligned}$$

with

$$\begin{aligned}
\hat{K}_{ij} &= \frac{1}{2\alpha}\left(\hat{\nabla}_i\beta_j + \hat{\nabla}_j\beta_i - \frac{2}{3}\gamma_{ij}\hat{\nabla}_k\beta^k\right) \\
K_{ij}K^{ij} &= \frac{1}{\phi^{12}}\hat{K}_{ij}\hat{K}^{ij}
\end{aligned}$$

5. Calculate the metric:

$$\begin{aligned}
g_{ij} &= \gamma_{ij} = \phi^4\hat{\gamma^{ij}} + h_{ij}^{\mathrm{TT}}, \\
g_{00} &= \gamma_{ij}\beta^j\beta^i - \alpha^2, \\
g_{0i} &= \beta_i.
\end{aligned}$$

Chapter 6

Gravitational waves

6.1 Introduction

Gravitational waves can be "loosely" defined as fluctuations of the curvature of spacetime which propagate as waves. We can classify the different regions of spacetime around an isolated source depending on the distance to the source r, and the reduced wavelength of the gravitational waves $\lambda\!\!\!^{-}$. Close to the source, where $r < \lambda\!\!\!^{-}$, the curvature of spacetime is directly affected by the energy momentum distribution of the source. Gravitational waves in this region couple nonlinearly with the background metric and themselves as they move away from the sources. One has to wait until GWs reach the wave zone, defined as the region where $r \gg \lambda\!\!\!^{-}$, to have real waves travelling in a background Minkowski spacetime. The objective of this chapter is to present the theoretical framework to calculate the GWs in the wave zone from the information of the source evolution, and the spacetime surrounding it (see Blanchet 2002, for a review in this kind of formulations of the gravitational waves.).

As we aim to describe GWs as perturbations of the Minkowski metric $\eta_{\mu\nu}$ we will express the metric as

$$g_{\mu\nu} = \eta_{\mu\nu} + \bar{h}_{\mu\nu}, \tag{6.1}$$

where $\bar{h}_{\mu\nu}$ is the perturbation. Note that this does not imply any assumption on the smallness of the perturbation, since, close to the sources, $\bar{h}_{\mu\nu}$ can be

arbitrary large compared to the Minkowski metric. In some suitable radiative coordinate system (see Misner et al. (1973), sect. 36.9), Einstein's equations read

$$\Box \bar{h}^{\mu\nu} = -16\pi \left(T^{\mu\nu} + t^{\mu\nu}\right), \tag{6.2}$$

where $\Box$ is the D'Alambertian operator, and $t^{\mu\nu}$ is the effective energy-momentum tensor of the gravitational field, i.e. a pseudo-tensor that is non-zero outside the source. The direct integration of this equation leads to divergent integrals due to the non-compact support of the source $t^{\mu\nu}$ (See however Pati & Will 2000). Fortunately, if one considers that $\bar{h}^{\mu\nu}$ are small perturbations of the Minkowski metric, a multipole decomposition of the linear contribution can be performed (Thorne 1980)

$$\begin{aligned} h_{ij}^{\rm rad}(t,\boldsymbol{x}) =& \frac{2G}{c^4 r} P_{ij}^{{\rm TT}\,kl} \left\{ \mathcal{M}_{2\,kl} + \frac{1}{c}\left[\mathcal{J}_{2\,kl} + \mathcal{M}_{3\,kl}\right] \right. \\ & \left. + \frac{1}{c^2}\left[\mathcal{J}_{3\,kl} + \mathcal{M}_{4\,kl}\right] + \mathcal{O}\left(\frac{1}{c^3}\right) \right\} + \mathcal{O}\left(\frac{1}{r^2}\right), \end{aligned} \tag{6.3}$$

where $P_{ij}^{{\rm TT}kl}$ stands for the algebraic transverse traceless projector

$$\begin{aligned} P_{ij}^{{\rm TT}kl} \equiv& \hat{\gamma}_{i(p}\hat{\gamma}_{q)j}\left[\left(n^p n^k - \hat{\gamma}^{pk}\right)\left(n^q n^l - \hat{\gamma}^{ql}\right)\right. \\ & \left. - \left(n^p n^q - \hat{\gamma}^{pq}\right)\left(n^k n^l - \hat{\gamma}^{kl}\right)/2\right], \end{aligned} \tag{6.4}$$

and $\mathcal{M}_{n\,kl}$ and $\mathcal{J}_{n\,kl}$ are terms including n-th time derivatives of mass and current multipoles ($n = 2$ is the quadrupole, $n = 3$ the octupole, $n = 4$ the hexadecapole ...). Note that this expression is exact, since it keeps the nonlinear contributions to the waveform (denoted as $\mathcal{O}\left(1/r^2\right)$ terms), and the higher order multipoles (denoted as $\mathcal{O}\left(1/c^3\right)$). But the integrals appearing in the multipoles present in $\mathcal{M}_{n\,kl}$ and $\mathcal{J}_{n\,kl}$ still have to be calculated. If a post-Newtonian expansion of the GW sources is possible, then these integrals can also be expanded in the various contributions of the different post-Newtonian orders as

$$\mathcal{M}_{n\,kl} = \mathcal{M}_{n\,kl}^{\rm N} + \frac{1}{c^2}\mathcal{M}_{n\,kl}^{\rm 1PN} + \mathcal{O}\left(\frac{1}{c^4}\right), \tag{6.5}$$

$$\mathcal{J}_{n\,kl} = \mathcal{J}_{n\,kl}^{\rm N} + \frac{1}{c^2}\mathcal{J}_{n\,kl}^{\rm 1PN} + \mathcal{O}\left(\frac{1}{c^4}\right), \tag{6.6}$$

where the superscripts N and 1PN denote the Newtonian and first post-Newtonian contributions respectively. Including these post-Newtonian expansions and reordering the terms consistently with the expansion, one arrives to

$$h_{ij}^{\rm rad}(t,\boldsymbol{x}) = \frac{2G}{c^4 r} P_{ij}^{{\rm TT}\,kl}(\boldsymbol{N}) \left\{ \mathcal{M}^N_{2\,kl} + \frac{1}{c}\left[\mathcal{J}^N_{2\,kl} + \mathcal{M}^N_{3\,kl}\right] + \frac{1}{c^2}\left[\mathcal{J}^N_{3\,kl} + \mathcal{M}^N_{4\,kl} + \mathcal{M}^{1PN}_{2\,kl}\right] + \mathcal{O}\left(\frac{1}{c^3}\right)\right\} + \mathcal{O}\left(\frac{1}{r^2}\right), \quad (6.7)$$

which still is an exact expression for the metric perturbation. This expansion in terms of $1/c$ is called the slow-motion expansion (see Misner et al. (1973), sect. 36.7), and is valid for $R \ll \lambda\!\!\!^{-}$, R being the size of the source.

If one assumes (i) that the GWs amplitude is small enough for the linear approximation to be valid, and (ii) that the slow motion approximation is valid for the sources, then $h_{ij}^{\rm rad}$ can be approximated by the leading term in the multipole expansion, i.e. the Newtonian quadrupole moment

$$h_{ij}^{\rm rad}(t,\boldsymbol{x}) \approx \frac{2G}{c^4 r} P_{ij}^{{\rm TT}\,kl}(\boldsymbol{N}) \mathcal{M}^N_{2\,kl}. \quad (6.8)$$

This formula is called the *Newtonian quadrupole formula*. Note that, although only Newtonian contributions to the source affect the waveform at this level of approximation, this is a 2.5 PN formula, because it is a $1/c^4$ contribution to the three-metric, and therefore a $1/c^5$ contribution to the power loss equations. The explicit form of this formula depends on the way the post-Newtonian expansion of the sources is done, in particular on which variables are chosen for the expansion, although the calculated waveform has to be independent of this fact, as long as the approximation is fulfilled.

6.2 Newtonian quadrupole formula in the ADM gauge

The equation for null outgoing geodesics in the ADM gauge reads $t - r/c - 2M_{\rm ADM} G \ln[r/(c\eta)]/c^3 + \mathcal{O}(G^2) = \text{const.}$, where $M_{\rm ADM} = M + \mathcal{O}(1/c^2)$ is the ADM mass and η an arbitrary positive constant with the dimension of time.

For r large enough compared to the typical wavelength, this equation also gives the link between the time t and the distance r of a field point $\boldsymbol{x}$ located near future null infinity $\mathcal{I}^+$. In the post-Newtonian framework, r/c is regarded as a small quantity (with respect to t), which precisely reflects the fact that the post-Newtonian metric is not accurate in the wave zone. Therefore, the expression (5.47) for $h_{ij}^{\rm TT}$ cannot be used there. Instead, we should consider the post-Minkowskian version of Eq. (5.30), where all quantities are expanded in powers of the gravitational constant G. Higher order terms in $1/c^2$ must not be neglected a priori, as long as they appear at a level of approximation below the one we want to reach.

In general, this approach is not guaranteed to lead to a well-defined perturbative scheme in the ADM gauge in the sense that the contribution of order G^{n+1} may become greater than the contribution of order G^n in the neighborhood of $\mathcal{I}^+$. It is worthwhile briefly pointing out the origin of the possible problem. Once the field ${h_n}_{ij}^{\rm TT}$ is known at the nth post-Minkowskian (nPM) level, the next approximation ${h_{n+1}}_{ij}^{\rm TT}$ is determined by the wave-like equation of the type $\hat{\Box}{h_{n+1}}_{ij}^{\rm TT} = \hat{\gamma}_{ij}^{{\rm TT}kl}\Lambda_{n+1\,kl}(h^{\rm TT}) + \mathcal{O}(G^{n+2})$ obtained by combing Eqs. (5.10) and (5.11) as explained in Chapter 5. The source $\Lambda_{n+1\,ij}$ depends nonlinearly on $h_{ij}^{\rm TT}$, which can thus be replaced by its nPM value ${h_n}_{kl}^{\rm TT}$. In the end, the solution of the previous wave equation is the retarded integral of $\hat{\gamma}_{ij}^{{\rm TT}kl}\Lambda_{n+1\,kl}(h^{\rm TT})$, which we denote in short as $\hat{\Box}^{-1}\hat{\gamma}_{ij}^{{\rm TT}kl}\Lambda_{n+1\,kl}$. The transverse traceless projector can itself be written as a converging integral with the help of a modified version of Eq. (B.6), in which the derivatives are applied to the kernel $|\mathbf{x}-\mathbf{x}'|^{\alpha+B+2p}$ with $\alpha=-1$. Even if the retarded integral converges, it may be conveniently replaced by its Hadamard finite part. The numerical result is not affected, but the integral appearing under the operator ${\rm FP}_{B=0}$ can now be shown to commute with the integral defining ${h_{n+1}}_{ij}^{\rm TT}$ after an appropriate analytic continuation. As a consequence, the finite part of $\hat{\gamma}_{ij}^{{\rm TT}kl}$ (regarded as an integral operator, which may be referred to as $\hat{\gamma}_{ij}^{{\rm TT}kl}$ without any ambiguity) can be pulled out from the d'Alembertian inverse symbol: $\hat{\Box}^{-1}\hat{\gamma}_{ij}^{{\rm TT}kl}\Lambda_{n+1\,kl} = \hat{\gamma}_{ij}^{{\rm TT}kl}\hat{\Box}^{-1}\Lambda_{n+1\,kl}$. The behavior of $\Lambda_{n+1\,ij}({h_n}^{\rm TT})$ when $r\to+\infty$ follows from a formula extending Eq. (5.48) to the case where the quantity to be calculated is a retarded integral. In particular, the multipole expansion of $h_{ij}^{\rm TT}$ involves the retarded integral of the multipole expansion of the source, regularized by means of the Hadamard finite part $\hat{\Box}_{\mathbf{0}}^{-1}\mathcal{M}(\Lambda_{n+1\,ij})$.

This contribution turns out to generate terms tending towards zero as $(\ln r)^2/r$ at the 2PM order, which are thus out of control. The structure of the field has not been investigated yet at higher PM order in ADM gauge, but a similar phenomenon is likely to happen in that case too.

Fortunately, the previous problem can be cured at the post-linear level either by moving to some radiative gauge where $u = t - r/c$ is a conformal coordinate, or by absorbing the logarithms into the arguments of some multipole moments. In harmonic gauge, the logarithms occurring in the post-Minkowskian iteration were shown (Blanchet 1987) to be removable to all orders. In ADM gauge, the possibility of such an elimination has been checked explicitly at the post-linear level by Schäfer (1990) from a formula adapting the derivation of Chapter 5 in order to include in the Hamiltonian the relative Newtonian part of the 2PM corrections to all terms quadratic in $h_{ij}^{\rm TT}$ (or $\pi_{\rm TT}^{ij}$). The new wave equation for the field variable reads

$$\begin{aligned}\hat{\Box} h_{ij}^{\rm TT} = \gamma_{ij}^{{\rm TT}kl}\Big[F_{kl} + \frac{4}{c^2}\Big(&-2\pi G D^* h_{kl}^{\rm TT} \\ &+ \hat{\gamma}^{mn}\hat{\nabla}_m U \hat{\nabla}_n h_{kl}^{\rm TT} + U\hat{\Delta} h_{kl}^{\rm TT}\Big)\Big] \\ + \mathcal{O}\left(\frac{\left(h^{\rm TT}\right)^0}{c^6}\right) + \mathcal{O}\left(\frac{\left(h^{\rm TT}\right)^1}{c^4}\right) + \mathcal{O}\left(\left(h^{\rm TT}\right)^2\right).\end{aligned} \tag{6.9}$$

The Green function method provides the required solution, but the computation is rather delicate. The result is a retarded integral, to which it remains to apply the transverse trace-free projector $\hat{\gamma}_{ij}^{{\rm TT}kl}$. The action of the second spatial derivatives $\hat{\nabla}_k\hat{\nabla}_l$ on a quantity of the form $f(t-r/c)/r$ leads to the "monopole" term $\hat{\gamma}_{kp}\hat{\gamma}_{lq}n^p n^q \ddot{f}(t-r/c)/(rc^2)$, each dot denoting a time derivative, plus $1/r^2$ corrections. It follows that $\hat{\Delta}^{-1}\hat{\nabla}_k\hat{\nabla}_l[f(t-r/c)/r] = \hat{\gamma}_{kp}\hat{\gamma}_{lq}n^p n^q f(t-r/c)/r + \mathcal{O}(1/r^2)$. Similarly, it is not difficult to check that $\hat{\Delta}^{-2}\hat{\nabla}_i\hat{\nabla}_j\hat{\nabla}_k\hat{\nabla}_l[f(t-r/c)/r] = \hat{\gamma}_{ip}\hat{\gamma}_{jq}\hat{\gamma}_{kr}\hat{\gamma}_{ls}n^p n^q n^r n^s f(t-r/c)/r + \mathcal{O}(1/r^2)$. This implies that the operator (5.12), applied to a term $f(t-r/c)/r$, reduces to the projector $P_{ij}^{{\rm TT}kl}$. Using the latter property, we recover the well-known

relation

$$h_{ij}^{\rm TT} = \frac{1}{r} P_{ij}^{{\rm TT}kl} \times \left\{ M_{kl} \left[t - \frac{r}{c} - \frac{2G}{c^3} \left(M + \mathcal{O}\left(\frac{1}{c^2}\right)\right) \ln\left(\frac{r}{c\eta}\right) + \mathcal{O}(G^2) \right] + \mathcal{O}\left(\frac{1}{c^2}\right) \right\} + \mathcal{O}\left(\frac{1}{r^2}\right), \tag{6.10}$$

with $M_{ij}(t) = \int {\rm d}^3\boldsymbol{x}\, \sqrt{\hat{\gamma}} F_{ij}/(-4\pi)$ being the Newtonian monopole moment associated to the source F_{ij}.

Because of the algebraic transverse traceless projection, we may substitute $M_{<ij>}$ by M_{ij} without affecting the outcome in the above relation. Since we still work at the 2PN level, we do not need to include any higher order corrections in the expression of M_{ij}. The retarded argument $t - r/c - 2GM_{\rm ADM}/c^3 \ln[r/(c\eta)] + \mathcal{O}(G^2)$ coincides with the null radiative coordinate. It can be viewed as the actual retarded time $t_{\rm ret}$ of the field variable at $\mathcal{I}^+$ up to the 1PM order. Taking the preceding into account, we arrive at

$$h_{ij}^{\rm TT} \approx P_{ij}^{{\rm TT}kl} \frac{M_{<kl>}(t_{\rm ret})}{r} + \mathcal{O}\left(\frac{1}{r^2}\right). \tag{6.11}$$

We now improve the formula for M_{ij} by making use of Eq. (5.52), which leads to

$$M_{<ij>} = \frac{4G}{c^4} \int {\rm d}^3\boldsymbol{x}\, \sqrt{\hat{\gamma}} D^* \left(\frac{S^*_{<i} S^*_{j>}}{{D^*}^2} + x^k \hat{\gamma}_{k<i} \hat{\nabla}_{j>} U \right). \tag{6.12}$$

Excluding 1PN errors, this integral equals $4G \int {\rm d}^3\boldsymbol{x}\, \sqrt{\hat{\gamma}} D (\hat{\gamma}_{ki}\hat{\gamma}_{lj} v^{<k} v^{l>} + x^k \hat{\gamma}_{k<i} \hat{\nabla}_{j>} U)/c^4$. This is proportional to (twice) the second time derivative of the Newtonian quadrupole $2\ddot{Q}_{ij}$ at this level, as can be checked with the help of the relation

$$\frac{\rm d}{{\rm d}t} \int {\rm d}^3\boldsymbol{x}\, \sqrt{\hat{\gamma}} D^* f(\boldsymbol{x}, t) = \int {\rm d}^3\boldsymbol{x}\, \sqrt{\hat{\gamma}} D^* \left(v^i \hat{\nabla}_i + \partial_t \right) f(\boldsymbol{x}, t), \tag{6.13}$$

which is valid for any C^1 function f. We have thus derived the Newtonian quadrupole formula

$$h_{ij}^{\rm TT} \approx h_{ij}^{\rm quad} \equiv P_{ij}^{\rm TT kl} \frac{2G\ddot{Q}_{kl}}{rc^4} \tag{6.14}$$

in the neighborhood of future null infinity.

6.3 The stress formula

The Newtonian standard quadrupole formula has been extensively used in numerical simulations to calculate the emitted waveforms without having to consider the full evolution of the spacetime. However, the particular form in which Eq. (6.14) is expressed leads to numerical difficulties since a second time derivative appears. A way to circumvent this problem is to eliminate all time derivatives using the equations of motion. Following Blanchet et al. (1990) one can arrive to an expression for $\ddot{Q}_{kl}$ with no explicit appearance of time derivatives. This is the so-called stress formula

$$\ddot{Q}_{ij} \approx {\rm STF}\left\{2\int d^3\boldsymbol{x}\sqrt{\hat{\gamma}}D^*\left(\hat{\gamma}_{ik}\,\hat{\gamma}_{jl}\,v^k v^l + x^k\,\hat{\gamma}_{ki}\,\hat{\nabla}_j U\right)\right\} \tag{6.15}$$

where STF means symmetric and traceless part. This formula has proved to be numerically more accurate than the original formula (Finn 1989) and hence, we use it in this thesis to numerically extract gravitational waveforms.

In the case of a magnetized fluid in the ideal MHD case, the gravitational wave is also affected by the energy content of the magnetic field. Kotake et al. (2004b) have derived an extension of the quadrupole formula for such case. In a similar way, it is possible to calculate the corresponding stress formula (Obergaulinger et al. 2005) which reads

$$\ddot{Q}_{ij} \approx {\rm STF}\left\{2\int d^3\boldsymbol{x}\sqrt{\hat{\gamma}}\left[D^*\left(\hat{\gamma}_{ik}\,\hat{\gamma}_{jl}\,v^k v^l + x^k\,\hat{\gamma}_{ki}\,\hat{\nabla}_j U\right) - \hat{\gamma}_{ik}\hat{\gamma}_{jl}b^k b^l\right]\right\}. \tag{6.16}$$

Note that in the limit of weak magnetic fields the original stress formula is recovered. We use this formula in the magnetized core collapse simulations of Chapter 10 to numerically calculate the contribution of the magnetic field to the waveforms.

6.4 Near-zone far-zone link for gravitational waves

It is now possible to investigate the asymptotic behavior of $h_{ij}^{\rm 2PN}$ in a similar way as we did for the intermediate potentials. The computation does not present any particular subtleties in contrast to that of the full field variable dominant contribution. The operator $\hat{\gamma}_{ij}^{{\rm TT}kl}$ commutes with the Poisson integral so that $\mathcal{M}(\hat{\Delta}^{-1}\hat{\gamma}_{ij}^{{\rm TT}kl}F_{kl}) = \hat{\gamma}_{ij}^{{\rm TT}kl}\mathcal{M}(\hat{\Delta}^{-1}F_{kl}) = \hat{\gamma}_{ij}^{{\rm TT}kl}(M_{kl}/r)+\mathcal{O}(1/r^2)$. The action of the transverse trace-free projector is computed with the help of Eq. (B.3), which gives

$$\begin{aligned} h_{ij}^{\rm 2PN}(\boldsymbol{x},t) = \Bigg[&\frac{3}{16}\hat{\gamma}_{(ij}\hat{\gamma}^{kl)} + \frac{3}{4}\delta^k_{(i}\hat{\gamma}_{j)p}n^l n^p \\ &+ \frac{3}{16}\hat{\gamma}_{ip}\hat{\gamma}_{jq}n^p n^q n^k n^l \\ &- \frac{5}{16}\left(\hat{\gamma}_{ij}n^k n^l + \hat{\gamma}^{kl}\hat{\gamma}_{ip}\hat{\gamma}_{jq}n^p n^q\right)\Bigg] \\ &\times \frac{M_{kl}(t)}{r} + \mathcal{O}\left(\frac{1}{r^2}\right), \end{aligned} \tag{6.17}$$

with $M_{<ij>} = 2G\ddot{Q}_{ij}/c^4$. By applying the operator $P_{ij}^{{\rm TT}kl}$ on both sides of Eq. (6.17), we find that $P_{ij}^{{\rm TT}kl}h_{kl}^{\rm 2PN} = P_{ij}^{{\rm TT}kl}G\ddot{Q}_{kl}/(4rc^4)$. As a conclusion, comparing with the Newtonian quadrupole formula (6.14), we have

$$P_{ij}^{{\rm TT}kl}h_{kl}^{\rm 2PN}(\boldsymbol{x},t_{\rm ret}) \sim \frac{1}{8}h_{ij}^{\rm quad}(\boldsymbol{x},t), \tag{6.18}$$

or in components,

$$h_{+}^{\rm 2PN}(\boldsymbol{x},t_{\rm ret}) \sim \frac{1}{8}h_{+}^{\rm quad}(\boldsymbol{x},t), \tag{6.19}$$

$$h_{\times}^{\rm 2PN}(\boldsymbol{x},t_{\rm ret}) \sim \frac{1}{8}h_{\times}^{\rm quad}(\boldsymbol{x},t). \tag{6.20}$$

In spherical coordinates $h_{+}^{\rm 2PN}$ can be trivially calculated from the combination $h_{+} = (h_{\theta\theta}^{\rm TT} - h_{\varphi\varphi}^{\rm TT})/2$, whereas $h_{\times}^{\rm 2PN}$ is equal to $h_{\theta\varphi}^{\rm 2PN}$.

We see that the two polarizations extracted directly from $h_{ij}^{\rm 2PN}$ in the wave zone of the true waves differ from the quadrupole waveforms by (i) a factor 8

and (ii) the absence of retardation. The gravitational waveforms can thus be evaluated directly from $h_+^{\rm 2PN}$ and $h_\times^{\rm 2PN}$ even though there are no propagating gravitational waves in the CFC+ spacetime (which just means that there is no radiation back-reaction due to energy losses caused by gravitational waves). Furthermore, the wave amplitude can be deduced solely from $h_+^{\rm 2PN}$ in the axisymmetric case.

Part III

NUMERICAL METHODS

Chapter 7

Solving the magneto-hydrodynamics equations

The code used for the relativistic simulations presented in this thesis is an extension of the code described in Dimmelmeier et al. (2002a,b), and was discussed in Cerdá-Durán et al. (2005). We start by describing the magneto-hydrodynamical piece of the code. In this respect our code extends Dimmelmeier's code, which did not include any treatment of magnetic fields, through the incorporation of a number of new features:

- A general treatment for the metric appearing in the (magneto-) hydrodynamics equations, as the assumption of a diagonal three-metric is not hardwired in the code.
- An extension of the recovery algorithm for the primitive variables in order to include more general equations of state other than polytropes or ideal gas equations of state.
- Inclusion of an evolution equation to advect a second species (e.g. electron fraction) with the fluid.

- Incorporation of additional Riemann solvers (HLL) and high-order, symmetric schemes (KT).

- Inclusion of evolution equations for the magnetic field in the ideal GRMHD approximation.

The equations are implemented in the code using spherical polar coordinates $\{t, r, \theta, \varphi\}$, assuming axial symmetry with respect to the rotation axis and symmetry with respect to the equatorial plane at $\theta = \pi/2$. The computational grid to perform the simulations is composed of n_r radial zones and n_θ equidistant angular zones, whose specific values for the simulations depend on the particular application (see Part IV). For convenience the radial cell-spacing is chosen equidistant for evolutions of equilibrium neutron stars and logarithmically spaced when simulating core collapse. As in the original code (Dimmelmeier et al. 2002a) the part of the grid outside the star is filled with an artificial atmosphere as customary in finite difference codes similar to ours (see Font et al. 2002; Duez et al. 2002; Baiotti et al. 2005). This atmosphere obeys a polytropic equation of state and has a very low density such that its presence does not affect the dynamics of the star (see Dimmelmeier et al. 2002a, for details). Moreover, an extended grid containing no matter is used beyond the atmosphere for the CFC+ metric calculations, namely to properly capture the radial fall-off behavior of the metric potentials and to extract the gravitational radiation using components of $h_{ij}^{\rm TT}$ in the wave zone (see Sect. 9.3.2).

7.1 Hydrodynamics and magneto-hydrodynamics solver

The hydrodynamics and magneto-hydrodynamics solver performs the numerical integration of the corresponding system of conservation equations (3.11) using a high-resolution shock-capturing (HRSC) scheme. Since these schemes are described in a number of references (e.g. Leveque 1990; Toro 1999; Martí & Müller 2002; Font 2003), only the basic aspects of our implementation will be presented here. The interested reader is addressed to the existing literature for details. As the equations for the evolution of the magnetic field also require the fulfillment of the divergence constraint (3.45), the specific features of the

numerical solution of these equations are described in the next section, while this section is devoted to general issues having to do with numerical solution of systems of conservation laws.

HRSC methods ensure numerical conservation of physically conserved quantities and a correct treatment of discontinuities such as shocks. In such methods a local Riemann problem needs to be solved at each cell interface, as a result of the discretization process, which requires the reconstruction of the primitive variables $(\rho, v^i, \epsilon, B^j)$ at such interfaces.

In the purely hydrodynamical case we use the relativistic expression of the PPM method of Colella & Woodward (1984) for the reconstruction (see Martí & Müller 1996), which yields third order accuracy in space. The solution of the family of Riemann problems provides the so-called numerical fluxes at cell interfaces. In order to obtain this solution, the characteristic structure of the Jacobian matrices of the hydrodynamics equations is explicitly needed (Banyuls et al. 1997). We note that in contrast to CFC in the CFC+ approximation the metric has non-vanishing off-diagonal elements. Hence, we use the most general expression of the eigenvalues and eigenvectors of the general relativistic hydrodynamics equation as reported in Ibáñez et al. (1999). Once the spectral information is known, the numerical fluxes are computed by means of Marquina's approximate flux formula (Donat & Marquina 1996).

In the magneto-hydrodynamical case, following Antón et al. (2006), we use a linear reconstruction procedure with a *minmod* slope limiter, which yields second order accuracy in space. To calculate the numerical fluxes at cell interfaces, we use "incomplete" approximate Riemann solvers, i.e. solvers that do not need the full characteristic information of the system. This kind of solvers are particularly useful in GRMHD, where the full eigenspeeds of the flux-vector Jacobians are not known in a closed form (see Antón et al. 2006). We have implemented the HLL single-state solver of Harten et al. (1983) and the symmetric scheme of Kurganov & Tadmor (2000) (KT hereafter). Both solvers have proved to yield results with an accuracy comparable to complete Riemann solvers (with the full characteristic information) in simulations involving purely hydrodynamical special relativistic flows (Lucas-Serrano et al. 2004) and general relativistic flows in dynamical spacetimes (Shibata & Font 2005). Test of both solvers in general relativistic magnetohydrodynamics scenarios have been recently reported by Antón et al. (2006). To calculate the fluxes with the HLL or KT solver we need the eigenvalues of the system, in

particular the maximum and minimum value for the HLL scheme and only the maximum absolute value for the KT scheme. We note that as in the GRMHD simulations reported in this thesis we adopt the passive field approximation, the eigenvalues of the GRMHD system reduce to those of the hydrodynamics system (see Chapter 3). The numerical procedure to calculate the eigenvalues in the general case can be found in Antón et al. (2006).

The time update of the conserved vector $\boldsymbol{U}$ is done using the method of lines in combination with a Runge–Kutta method with second order accuracy in time. Once the conserved quantities $(D^*, S_i^*, \tau^*, B^{*j})$ are updated in time, the primitive variables need to be recovered. This is done through an iterative Newton–Raphson method, as these variables cannot be obtained in closed form from the conserved variables. This recovery scheme has been improved to handle general equations of state of the form $P = P(\rho, \epsilon, Y_a)$, where Y_a is the fraction of the fluid that belongs to the species a, advected with the fluid.

We note that the sources $\boldsymbol{Q}$ of the hydrodynamic equations have been implemented in the code using a general form for the metric, although they can be simplified for a metric with vanishing nondiagonal terms in the three-metric as, for example, in CFC.

7.2 Magnetic field evolution

The magnetic field evolution is given by the induction equation (3.46) and the divergence constraint (3.45). If we were to follow a naive approximation to solve the induction equation we could take the same approach as for the fluid variables, as the equations can be cast as conservations laws (3.11). Unfortunately, this leads to numerical schemes that do not preserve the divergence free condition for the magnetic flux. A possible explanation of this failure is that the conservation of the magnetic field inside a volume has no physical meaning. Instead, the main physical implication of the divergence constraint is that the magnetic flux through a closed surface is zero. Therefore, we can use this conservation law to build a numerical scheme which preserves the magnetic flux. Among the numerical schemes that fulfill this property (see Tóth (2000) for a review), the constrained transport (CT) scheme (Evans & Hawley 1988) is very appropriate to perform accurate simulations of magnetized flows.

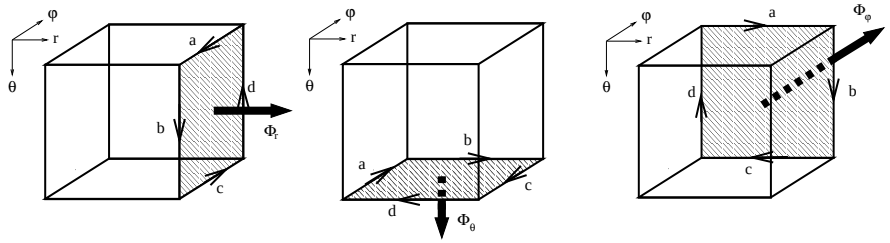

Figure 7.1: Schematic representation of the numerical cell. The time derivative of the magnetic fluxes Φ_i over the r interface (a), the θ interface (b) and the φ interface (c) can be written as line integrals along the corresponding closed path a-b-c-d.

7.2.1 The constrained transport scheme

In order to implement the CT scheme in our numerical code, in which we assume axisymmetry and use spherical polar coordinates (r, θ, φ), we have to analyze how the magnetic flux behaves at the surface of a numerical cell. Therefore, we apply Eq. (3.49) for the magnetic flux evolution to the interfaces in each of the directions of the coordinates (see Fig. 7.1). To do this we assume that B^{*i} is constant over each cell surface, and E_i^* is constant along each cell edge. In the r direction (Fig. 7.1 panel a) this yields

$$\frac{\partial \Phi_r}{\partial t} = \Delta \hat{S}_r \frac{\partial}{\partial t} B^{*r} = [E_\varphi^* \Delta \hat{l}_\varphi]_a - [E_\varphi^* \Delta \hat{l}_\varphi]_c, \tag{7.1}$$

keeping in mind that the axisymmetry condition imposes that $[E_\theta^* \Delta \hat{l}_\theta]_b = [E_\theta^* \Delta \hat{l}_\theta]_d$. We define $\Delta \hat{A}_i \equiv \int d\hat{A}_i$ as the surface of the cell interface perpendicular to the i direction and $\Delta \hat{l}_i \equiv \int d\hat{l}_i$ the length of the cell edge in the i direction.

In the θ direction (Fig. 7.1 panel b) the variation of the magnetic flux is given by

$$\frac{\partial \Phi_\theta}{\partial t} = \Delta \hat{A}_\theta \frac{\partial}{\partial t} B^{*\theta} = [E_\varphi^* \Delta \hat{l}_\varphi]_c - [E_\varphi^* \Delta \hat{l}_\varphi]_a, \tag{7.2}$$

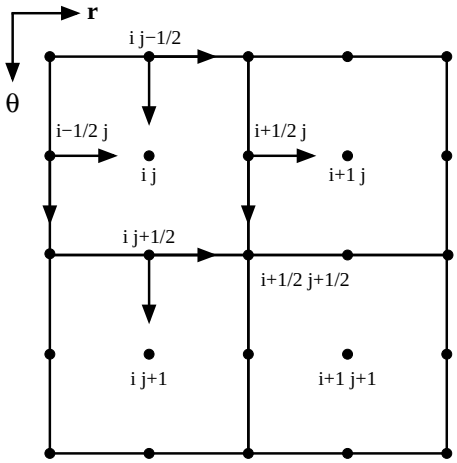

Figure 7.2: Schematic representation of the grid, where $(i\ j)$ denote cell centers, $(i + 1/2\ j)$ radial cell interfaces, $(i\ j + 1/2)$ angular cell interfaces and $(i + 1/2\ j + 1/2)$ edges in the φ direction (which is suppressed in the plot).

where axisymmetry implies that $[E_r^* \Delta \hat{l}_r]_b = [E_r^* \Delta \hat{l}_r]_d$. Finally, in the φ direction (Fig. 7.1 panel c)

$$\frac{\partial \Phi_\varphi}{\partial t} = \Delta \hat{A}_\varphi \frac{\partial}{\partial t} B^{*\varphi} = [E_r^* \Delta \hat{l}_r]_c - [E_r^* \Delta \hat{l}_r]_a + [E_\theta^* \Delta \hat{l}_\theta]_d - [E_\theta^* \Delta \hat{l}_\theta]_b. \tag{7.3}$$

We represent all these quantities in the numerical grid (Fig. 7.2), in which the radial direction is discretized in n_r zones and the angular (θ) direction in n_θ zones , giving a total number of $n_r \times n_\theta$ points (cell centers) labelled $(i\ j)$, with $i = 1 \ldots n_r$ and $j = 1 \ldots n_\theta$. Cell interfaces between neighbouring cells are denoted as $(i + 1/2\ j)$ for the radial ones and $(i\ j + 1/2)$ for the angular ones. The indices $(i + 1/2\ j + 1/2)$ hence denote cell edges in the φ direction. In order to implement the CT scheme we do not define the poloidal magnetic field cell-centered but at the interfaces, i.e $B^{*r}_{i+1/2\ j}$ and $B^{*\theta}_{ij+1/2}$. As we assume axisymmetry we work with a cell-centered toroidal field $B^{*\varphi}_{ij}$ because this component does not play any role in the CT scheme (see below). With such considerations the above equations for the magnetic flux time evolution lead to equations for the magnetic field evolution (CT scheme). The poloidal

components yield:

$$\left.\frac{\partial B^{*\,r}}{\partial t}\right|_{i+1/2\;\,j} = \frac{\left[E^*_\varphi\;\Delta\hat{l}_\varphi\right]_{i+1/2\;\,j-1/2} - \left[E^*_\varphi\;\Delta\hat{l}_\varphi\right]_{i+1/2\;\,j+1/2}}{\Delta A_{r\;\,i+1/2\;\,j}}, \tag{7.4}$$

$$\left.\frac{\partial B^{*\,\theta}}{\partial t}\right|_{i\;\,j+1/2} = \frac{\left[E^*_\varphi\;\Delta\hat{l}_\varphi\right]_{i+1/2\;\,j+1/2} - \left[E^*_\varphi\;\Delta\hat{l}_\varphi\right]_{i-1/2\;\,j+1/2}}{\Delta A_{\theta\;\,i\;\,j+1/2}}, \tag{7.5}$$

while the toroidal component yields

$$\left.\frac{\partial B^{*\,\varphi}}{\partial t}\right|_{i\;\,j} = \frac{1}{\Delta A_{r\;\,i\;\,j}}\left\{\left[E^*_r\;\Delta\hat{l}_r\right]_{i\;\,j+1/2} - \left[E^*_r\;\Delta\hat{l}_r\right]_{i\;\,j-1/2} + \left[E^*_\theta\;\Delta\hat{l}_\theta\right]_{i-1/2\;\,j} - \left[E^*_\theta\;\Delta\hat{l}_\theta\right]_{i+1/2\;\,j}\right\}. \tag{7.6}$$

The total magnetic flux through the cell interfaces is given by

$$\Phi_{\mathrm{T\;i\;j}} = \Phi_{r\;\,i+1/2\;\,j} - \Phi_{r\;\,i-1/2\;\,j} + \Phi_{\theta\;\,i\;\,j+1/2} - \Phi_{\theta\;\,i\;\,j-1/2}, \tag{7.7}$$

where we have taken into account that the total flux in the φ direction is zero owing to the axisymmetry condition. The time evolution of the total magnetic flux evolved with the CT scheme satisfies by construction that

$$\left.\frac{\partial \Phi_{\mathrm{T}}}{\partial t}\right|_{i\;\,j} = 0, \tag{7.8}$$

and therefore every numerical scheme constructed on the basis of the CT scheme will conserve magnetic flux up to machine accuracy. If we are able to generate initial conditions which satisfies the divergence constraint, i.e. with $\Phi_{\mathrm{T}} = 0$ at each numerical cell, then, the constraint will be preserved during the numerical evolution. The way of constructing such initial data is explained in Chapter 10.

The next step is to choose a discretization of the integrals by making explicit

the values of the interface surfaces and the edge lengths. The latter read

$$\Delta\hat{l}_{r\ i\ j+1/2} = \int dr \Big|_{i\ j+1/2} = \Delta r_i, \tag{7.9}$$

$$\Delta\hat{l}_{\theta\ i+1/2\ j} = \int r\, d\theta \Big|_{i+1/2\ j} = r_{i+1/2}\Delta\theta_j, \tag{7.10}$$

$$\Delta\hat{l}_{\varphi\ i+1/2\ j+1/2} = \int r\sin\theta\, d\varphi \Big|_{i+1/2\ j+1/2} = r_{i+1/2}\sin\theta_{j+1/2}\Delta\varphi, \tag{7.11}$$

where $\Delta r_i \equiv r_{i+1/2} - r_{i-1/2}$, $\Delta\theta_j \equiv \theta_{j+1/2} - \theta_{j-1/2}$ and $\Delta\varphi$ is arbitrary as we have axisymmetry and the cell size on the φ direction does not play any role in the numerical scheme. Correspondingly, the interface surfaces read:

$$\Delta A_{r\ i+1/2\ j} = \int r^2\sin\theta\, d\theta\, d\varphi \Big|_{i+1/2\ j} = -r^2_{i+1/2}\ \Delta(\cos\theta)_j\ \Delta\varphi, \tag{7.12}$$

$$\Delta A_{\theta\ i\ j+1/2} = \int r\sin\theta\, dr\, d\varphi \Big|_{i\ j+1/2} = \frac{1}{2}\sin\theta_{j+1/2}\ \Delta r_i^2\ \Delta\varphi, \tag{7.13}$$

$$\Delta A_{\varphi\ i\ j} = \int r\, dr\, d\theta \Big|_{ij} = \frac{1}{2}\ \Delta r_i^2\ \Delta\theta_j, \tag{7.14}$$

where $\Delta r_i^2 \equiv r^2_{i+1/2} - r^2_{i-1/2}$ and $\Delta(\cos\theta)_j \equiv \cos\theta_{j+1/2} - \cos\theta_{j-1/2}$. Taking the above expressions into account, the evolution equations for the magnetic field read

$$\left.\frac{\partial B^{*\,r}}{\partial t}\right|_{i+1/2\ j} = \frac{\sin\theta_{j+1/2}\ E^*_{\varphi\ i+1/2\ j+1/2} - \sin\theta_{j-1/2}\ E^*_{\varphi\ i+1/2\ j-1/2}}{r_{i+1/2\ j}\ \Delta(\cos\theta)_j}, \tag{7.15}$$

$$\left.\frac{\partial B^{*\,\theta}}{\partial t}\right|_{i\ j+1/2} = 2\ \frac{r_{i+1/2}\ E^*_{\varphi\ i+1/2\ j+1/2} - r_{i-1/2}\ E^*_{\varphi\ i-1/2\ j+1/2}}{\Delta r_i^2}, \tag{7.16}$$

$$\begin{aligned}\left.\frac{\partial B^{*\,\varphi}}{\partial t}\right|_{i\ j} &= \frac{2\Delta r_i}{\Delta\theta_j\Delta r_i^2}\left[E^*_{r\ i\ j+1/2} - E^*_{r\ i\ j-1/2}\right] \\ &\quad - \frac{2}{\Delta r_i^2}\left[r_{i+1/2}\ E^*_{\theta\ i+1/2\ j} - r_{i-1/2}\ E^*_{\theta\ i-1/2\ j}\right].\end{aligned} \tag{7.17}$$

These expressions are used in the numerical code to evolve in time the magnetic field. The only remaining aspect is to give an explicit expression for the value

of E_i^*. The time discretization of the equations is performed in the same way that for the fluid evolution equations.

7.2.2 The numerical fluxes

So far, no characteristic information of the Jacobian matrices of the system has been used to numerically solve the magnetic field evolution equations. However it is important to include this information since discontinuities can also appear in the magnetic field. The missing link comes through the electric field. The electric field can be calculated from Eq. (3.38) and is related to the numerical fluxes,Eqs. (3.61), for the magnetic field. For the r and θ direction, their components simply read

$$E^*_{r\ i\ j+1/2} = -\left[v^{*\theta}B^{*\varphi} - v^{*\varphi}B^{*\theta}\right]_{i\ j+1/2} = (\boldsymbol{F}^{\theta})^{\varphi}_{i\ j+1/2}, \tag{7.18}$$

$$E^*_{\theta\ i+1/2\ j} = -\left[v^{*\varphi}B^{*r} - v^{*r}B^{*\varphi}\right]_{i+1/2\ j} = -(\boldsymbol{F}^{r})^{\varphi}_{i+1/2\ j}, \tag{7.19}$$

where $(\boldsymbol{F}^k)^l$ denotes the numerical flux in the k direction that appears in the equation for B^{*l}. As all quantities are evaluated at cell interfaces, the numerical fluxes can be calculated by solving the Riemann problem at the interfaces. In fact, as E_r^* and E_θ^* only appear in the evolution of the φ component of the magnetic field, this equation can be solved in the usual way that is done for conservation laws using HRSC schemes. On the other hand, the value of E_φ^* reads

$$E^*_{\varphi\ i+1/2\ j+1/2} = -\left[v^{*r}B^{*\theta} - v^{*\theta}B^{*r}\right]_{i+1/2\ j+1/2}, \tag{7.20}$$

which needs to be evaluated at cell edges, where the numerical fluxes are not defined. A practical way to calculate E_φ^* from the numerical fluxes in the adjacent interfaces (Balsara & Spicer (1999)) is

$$\begin{aligned} E^*_{\varphi\ i+1/2\ j+1/2} = -\frac{1}{4}\Big[&(\boldsymbol{F}^{r})^{\theta}_{i\ j+1/2} + (\boldsymbol{F}^{r})^{\theta}_{i+1\ j+1/2} \\ &-(\boldsymbol{F}^{\theta})^{r}_{i+1/2\ j} - (\boldsymbol{F}^{\theta})^{r}_{i+1/2\ j+1}\Big], \end{aligned} \tag{7.21}$$

where the fluxes are obtained in the usual way by solving the Riemann problem at the interfaces. The combination of the CT scheme and this way of calculating the electric field is called the flux-CT scheme.This scheme is what we

will use in all numerical simulations reported in this thesis involving magnetic fields.

Chapter 8

Solving the metric equations

The starting point to solve the metric equations has been the general relativistic code developed by Dimmelmeier et al. (2002a,b) in the CFC approximation. In this thesis we have improved the metric calculation to account for the additional metric potentials of the CFC+ approximation (Cerdá-Durán et al. (2005)).

As described in Chapters 4 and 5, the main feature of the approximations we are using for the metric (CFC and CFC+) is that only elliptic equations have to be solved to update the metric at each time step. In our approximate scheme we solve the equations hierarchically (see Section 5.5). First, a solution of the Poisson equation (5.24) for U is obtained. Then we solve the equations (5.42–5.46) for the intermediate potentials $\mathcal{S}$, $\mathcal{S}_i$, $\mathcal{T}_i$, $\mathcal{R}_i$, and $\mathcal{S}_{ij}$, which we need to calculate $h_{ij}^{\rm TT}$ in Eq. (5.47). Finally, we use $h_{ij}^{\rm TT}$ to solve the modified CFC equations for ϕ, β^i, and α, Eqs. (4.17, 4.19, 5.38). For each step we use different methods according to the mathematical character of each equation.

8.1 Poisson solver

The equation for the Newtonian potential U is a linear Poisson equation with compact support sources. Hence, standard methods for such equations, like integral solvers, can be used to obtain a numerical solution. For an equation of the form

$$\hat{\Delta} u(\boldsymbol{x}) = f(\boldsymbol{x}), \tag{8.1}$$

the solution for the potential u can be expanded in axisymmetry as

$$\begin{aligned} u(\boldsymbol{x}) &= -\frac{1}{4\pi} \int \mathrm{d}^3\boldsymbol{x}' \, \sqrt{\hat{\gamma}} \, \frac{f(\boldsymbol{x})}{|\boldsymbol{x} - \boldsymbol{x}'|} \\ &= -\frac{1}{2} \sum_{l=0}^{\infty} P_l(\mu) \left(u_{\mathrm{in}}^{(l)}(\boldsymbol{x}) + u_{\mathrm{out}}^{(l)}(\boldsymbol{x}) \right), \end{aligned} \tag{8.2}$$

where

$$u_{\mathrm{in}}^{(l)}(\boldsymbol{x}) = \frac{1}{r^{l+1}} \int_{|\boldsymbol{x}'|<R} \mathrm{d}r' \, \mathrm{d}\mu' \, f(\boldsymbol{x}') r'^{l+2} P_l(\mu'), \tag{8.3}$$

$$u_{\mathrm{out}}^{(l)}(\boldsymbol{x}) = r^l \int_{|\boldsymbol{x}'|>R} \mathrm{d}r' \, \mathrm{d}\mu' \, f(\boldsymbol{x}') \frac{1}{r'^{l-1}} P_l(\mu'). \tag{8.4}$$

Here P_l are the Legendre polynomials, and $\mu = \cos\theta$. We numerically integrate Eqs. (8.3, 8.4) by assuming $f(\boldsymbol{x}')$ to be constant inside each computational cell, integrating over r' and θ' analytically within each cell, and then adding up the partial integrals to obtain the solution at every grid point of the computational domain. This method has been described and tested in Müller & Steinmetz (1995) and Zwerger (1995), and successfully used by Zwerger & Müller (1997) to calculate the Newtonian potential in axisymmetric core collapse simulations.

8.2 h_{ij}^{TT} metric solver

The equations (5.42–5.46) for the intermediate potentials, which are needed to compute the second post-Newtonian corrections to CFC, can in general be solved separately as a scalar Poisson equation for $\mathcal{S}$, three vector Poisson equations for $\mathcal{S}_i$, $\mathcal{T}_i$, and $\mathcal{R}_i$, and a tensor Poisson equation for $\mathcal{S}_{ij}$. In the

axisymmetric case we can take advantage of some additional simplifications: The φ-component of the vector-Poisson equations decouples from the r- and θ-components, and the $r\varphi$- and $\theta\varphi$-components of the tensor-Poisson equation decouple from all other components, even though e.g. $\hat{\Delta}\mathcal{S}_i \neq (\hat{\Delta}\mathcal{S})_i$ (similar for the other vectors and tensor), which means that the various components in general couple to each other. Therefore, the equations can be grouped into 9 sets of linear elliptic equations: four sets of one equation, four sets of two equations, and one set of four equations, with coupling only within the respective set.

The discretization of each of the equations on the $\{r,\theta\}$-grid leads to 9 sparse linear matrix equations of the type

$$\boldsymbol{\mathcal{A}}\boldsymbol{u} = \boldsymbol{f}, \tag{8.5}$$

where $\boldsymbol{u} = u_{ij}^k$ is the vector of unknowns with i,j labeling the grid points and k ranging from 1 to 1, 2, or 4 depending on the number of coupled components. The vector of sources is respectively denoted as $\boldsymbol{f} = f_{ij}^k$, and $\boldsymbol{\mathcal{A}}$ is a matrix which does not depend on $\boldsymbol{u}$, as the original system is linear. The linearity of the equations allows us to avoid an iteration scheme and to use instead the LU decomposition method to invert $\boldsymbol{\mathcal{A}}$. The main advantage of the LU method is that the decomposition itself (which is the most time consuming step) only has to be done once at the beginning. Then it can be used to calculate the solution for different source vectors $\boldsymbol{f}$ during the metric computations, which is computationally very fast and efficient. The LU decomposition is performed using standard LAPACK libraries for banded matrices. We use the monopole solution of Eqs. (5.61–5.65) as explicit outer boundary condition for the intermediate potentials. This procedure is only accurate far from the sources, and the matching of the metric to a monopole solution deteriorates if it is performed too close to a strongly gravitating nonspherical star. As a consequence when calculating the components of the spacetime metric we use a grid which extends well beyond both the boundary of the star and also the atmosphere, and apply the boundary condition at the outer boundary of this extended vacuum grid. An example of the influence of the location where the boundary condition is applied on the accuracy of the metric solution is presented in Sect. 9.2.1. Although the nonlinear metric equations for ϕ, α, and β^i have source terms with noncompact support, the location of the outer grid

boundary has much less influence on the accuracy of the numerical solution (see Dimmelmeier et al. 2005b).

8.3 CFC metric solver

At this stage we have a numerical solution for $h_{ij}^{\rm TT}$ and are ready to solve the CFC+ metric equations for the conformal factor ϕ, the shift vector β^i, and the lapse function α, Eqs. (4.17, 4.19, and 5.38). For the comparison between CFC and CFC+ presented in Sects. 9.2 and 9.3, we also need to solve the CFC metric equations, which, we recall, are equivalent to the CFC+ equations up to corrections in the metric equation for α (4.18). As both systems of equations are 5 nonlinear elliptic coupled Poisson-like equations, we can apply the same methods to solve them. In either case, we can write them in compact form as

$$\hat{\Delta}\boldsymbol{u}(\boldsymbol{x}) = \boldsymbol{f}(\boldsymbol{x};\boldsymbol{u}(\boldsymbol{x})), \tag{8.6}$$

where $\boldsymbol{u} = u^k = (\phi, \alpha\phi, \beta^j)$, and $\boldsymbol{f} = f^k$ is the vector of the respective sources. These five scalar equations for each component of $\boldsymbol{u}$ couple to each other via the source terms that in general depend on the various components of $\boldsymbol{u}$.

We use a fix-point iteration scheme in combination with the linear Poisson solver (8.2) described above to solve these equations. The value of $\boldsymbol{u}$ at each iteration s, denoted by $\boldsymbol{u}^s$, is set constant in the sources $\boldsymbol{f}$ to calculate a new value $\boldsymbol{u}^{s+1}$,

$$\boldsymbol{u}^{s+1}(\boldsymbol{x}) = \hat{\Delta}^{-1}\boldsymbol{f}\,(\boldsymbol{x};\boldsymbol{u}^s(\boldsymbol{x}))\,. \tag{8.7}$$

As a result the 5 previously coupled nonlinear equations reduce to a decoupled set of 5 linear scalar Poisson equations. The solution vector $\boldsymbol{u}^{s+1}$ at each iteration step is obtained by solving the associated 5 Poisson equations of the type (8.1) separately. After the computation of $\boldsymbol{u}^{s+1}$, the right-hand side of Eq. (8.7) is updated by replacing $\boldsymbol{u}^s \to \boldsymbol{u}^{s+1}$, which is used as a new starting value for the next iteration. Convergence to the desired numerical solution $\boldsymbol{u}$ is achieved when the relative variation $|\boldsymbol{u}^{s+1}/\boldsymbol{u}^s - 1|$ of the numerical solution of $\boldsymbol{u}$ between two successive iterations is smaller than a certain threshold, which we set to 10^{-6}. In the simulations reported here the metric solver successfully converges when using the flat metric as initial guess in each metric computation. However, to accelerate convergence, during the hydrodynamic evolution

we take the metric from the previous metric computation as starting value for the subsequent one. Furthermore, we cut the Legendre polynomial expansion in Eq. (8.2) at $l = 10$. For the CFC metric equations in axisymmetry the above method was recently discussed in detail in Dimmelmeier et al. (2005b).

Part IV

RESULTS

Chapter 9

CFC+: Core collapse dynamics and gravitational waveforms

In this chapter we present the results of numerical simulations of neutron star evolution and core collapse to neutron star in the CFC+ approximation to the general relativistic Einstein's field equations. We compare the improved CFC+ dynamics and gravitational waveforms with the CFC approximation and with previous general relativistic simulations. These results have been published in Cerdá-Durán et al. (2005).

9.1 Initial models

As initial models for describing either rotating neutron stars or rotating stellar cores at the onset of gravitational collapse, we construct uniformly or differentially rotating relativistic polytropes in equilibrium. These are obtained using Hachisu's self-consistent field (HSCF) method as described in Komatsu et al. (1989a,b), which solves the general relativistic hydrostatic equations for self-gravitating rotating matter distributions, whose pressure obeys the polytropic

relation

$$P = K\rho^{\gamma}, \tag{9.1}$$

where K is the polytropic constant and γ the adiabatic index. The gauge used in the HSCF method is maximal slicing with quasi-isotropic coordinates (MSQI). The most general metric to describe these objects in the MSQI gauge is

$$ds^2 = -e^{2\tilde{\nu}}d\tilde{t}^2 + e^{2\tilde{\alpha}}(d\tilde{r}^2 + \tilde{r}^2 d\tilde{\theta}^2) + e^{2\tilde{\beta}}\tilde{r}^2 \sin\tilde{\theta}^2(d\tilde{\varphi} - \tilde{\omega}d\tilde{t})^2, \tag{9.2}$$

where $\{\tilde{t}, \tilde{r}, \tilde{\theta}, \tilde{\varphi}\}$ are the coordinates in the MSQI gauge, and $\tilde{\nu}$, $\tilde{\alpha}$, $\tilde{\beta}$, and $\tilde{\omega}$ are metric potentials. Throughout this chapter quantities with a tilde are in the MSQI gauge, and all other quantities are in the ADM gauge. The hydrostatic equilibrium equations can be numerically integrated by prescribing a value for the central density $\rho_{\rm c}$ and the rotation rate (selected by setting a ratio of polar radius $r_{\rm p}$ to equatorial radius $r_{\rm e}$), and by choosing a rotation law. As it is usual practice we use a rotation law given by

$$\Omega = \Omega_{\rm c}\frac{A^2}{A^2 + \varpi^2}, \tag{9.3}$$

where Ω is the angular velocity of the fluid as measured from infinity, $\Omega_{\rm c}$ its value at the center, and $\varpi = r\sin\theta$ the distance to the rotation axis. The positive constant A parametrizes the rate of differential rotation, with $A \to \infty$ for a rigid rotator and $A \lesssim r_{\rm e}$ for differentially rotating stars. The interested reader is addressed to Stergioulas (2003) for a comprehensive review on rotating relativistic stars.

For the study of rotating neutron stars, we choose the polytropic EOS (9.1) with $K = 1.456 \times 10^5$ (in cgs units) and $\gamma = 2$. We construct a sequence of uniformly rotating models with a central density $\rho_{\rm c} = 7.95 \times 10^{14}$ g cm^{-3}, and a ratio $r_{\rm p}/r_{\rm e}$ of polar to equatorial coordinate radius ranging from 1.00 (spherical model; labeled RNS0) to 0.65 (rapidly rotating model near the mass-shedding limit; labeled RNS5). A summary of important quantities specifying these models is given in Table 9.1. Note also that models with this choice of parameters are of widespread use in the literature (see e.g. Font et al. 2002 or Dimmelmeier et al. 2005b and references therein) and will be used in this work for comparison with previous results obtained with independent codes.

Table 9.1: Equatorial radius r_e, axis ratio r_p/r_e, angular velocity Ω, and ADM mass M_{ADM} for a sequence of uniformly rotating neutron stars used in this work. Along the sequence the rotation rate increases from the spherical model RNS0 to the most rapidly rotating model RNS5, which rotates near the mass shedding limit at $\Omega_K = 5.363$ kHz.

Model	r_e [km]	r_p/r_e	Ω/Ω_K	M_{ADM} $[M_\odot]$
RNS0	14.1	1.00	0.00	1.40
RNS1	16.2	0.95	0.42	1.44
RNS2	17.3	0.85	0.70	1.51
RNS3	18.7	0.75	0.87	1.59
RNS4	19.6	0.70	0.93	1.63
RNS5	20.7	0.65	0.98	1.67

On the other hand, to model a stellar iron core as initial model for simulating rotational stellar core collapse to a neutron star we again utilize the HSCF method with the EOS parameters $K = 4.897 \times 10^{14}$ (in cgs units) and $\gamma = 4/3$, chosen to approximate the pressure profile in a degenerate electron gas. The initial central density is set to $\rho_{c\,ini} = 10^{10}$ g cm^{-3}. Again each initial model is further determined by its rotation profile parameter A and the rotation rate, which is specified by the axis ratio r_p/r_e or equivalently by the ratio of rotational energy and gravitational potential energy, $\beta = T/|W|$.

Following Dimmelmeier et al. (2002a) we use a hybrid EOS in the core collapse simulations. This EOS consists of a polytropic part $P_p = K\rho^\gamma$ plus a thermal part $P_{th} = (\gamma_{th} - 1)\epsilon_{th}$, where $\gamma_{th} = 1.5$ and $\epsilon_{th} = \epsilon - \epsilon_p$. The thermal contribution is chosen to take into account the rise of thermal energy due to shock heating. Gravitational collapse is initiated by slightly decreasing γ from its initial value to $\gamma_1 < 4/3$. As ρ reaches nuclear matter density $\rho_{nuc} = 2.0 \times 10^{14}$ g cm^{-3}, we raise γ to $\gamma_2 = 2.5$ and adjust K accordingly to maintain monotonicity of the pressure. Due to this stiffening of the EOS the core undergoes a bounce. In Table 9.2 we present the main properties of models A1B3G3, A1B3G5, A2B4G5, and A4B5G5 used in this work to study core collapse. These models are identical to those with the same labels in the comprehensive core collapse study performed by Dimmelmeier et al. (2002b).

Table 9.2: Parameters used in the core collapse simulations. The initial models are differentially rotating stellar cores specified by the parameter A controling the degree of differential rotation (cf. Eq. (9.3)) and the ratio of rotational to potential energy, $\beta = T/|W|$. The collapse is initiated by reducing γ from its initial value 4/3 to γ_1. Additionally, the values for the initial equatorial radius r_e and the initial ADM mass $M_{\rm ADM}$ are given. The label AxByGz of each model is a combination of the initial rotation parameters A and β (AxBy) and the value of γ_1 during collapse (Gz).

Model	A [10^3 km]	β [%]	r_e [km]	$M_{\rm ADM}$ [$M_\odot$]	γ_1
A1B3G3	50.0	0.89	2247	1.46	1.31
A1B3G5	50.0	0.89	2247	1.46	1.28
A2B4G1	1.0	1.81	1739	1.50	1.325
A4B5G5	0.5	4.03	1249	1.61	1.28

We note that when evolving the initial models constructed on the basis of the HSCF method (which uses the MSQI gauge) with the CFC+ evolution code (which uses the ADM gauge), we have to consider that in general the two gauges differ. This could potentially lead to an unsuitable matching of the data describing the initial models when evolved with the numerical code. Let us consider the most general metric in a generic dynamic scenario,

$$\gamma_{ij} = \phi^4 \hat{\gamma}_{ij} + h_{ij}^{\rm TT} \qquad \text{(ADM gauge)}, \tag{9.4}$$

$$\tilde{\gamma}_{ij} = \tilde{\phi}^4 \hat{\gamma}_{ij} + \tilde{\gamma}_{<ij>} \qquad \text{(MSQI gauge)}, \tag{9.5}$$

In general $\tilde{\gamma}_{<ij>}$ is not transverse, so that the ADM gauge and the MSQI gauge differ. To quantify the differences between both gauges it is relevant to compare the traceless part of the 3-metric $\gamma_{<ij>}$ and the trace $\hat{\gamma}^{ij}\gamma_{ij} = 3\phi^4$ itself. For an equilibrium stellar model constructed within the MSQI gauge one obtains

$$\tilde{\gamma}_{<ij>} = (\tilde{\gamma}_{rr} - \tilde{\gamma}_{\varphi\varphi}) \, {\rm diag}\left(\frac{1}{3}, \frac{1}{3}, -\frac{2}{3}\right). \tag{9.6}$$

In Fig. 9.1 we plot equatorial profiles of $|\tilde{\gamma}_{rr} - \tilde{\gamma}_{\varphi\varphi}|/(\hat{\gamma}^{ij}\tilde{\gamma}_{ij})$ for (i) the equilibrium model A1B3 used as initial data for core collapse simulations (lower

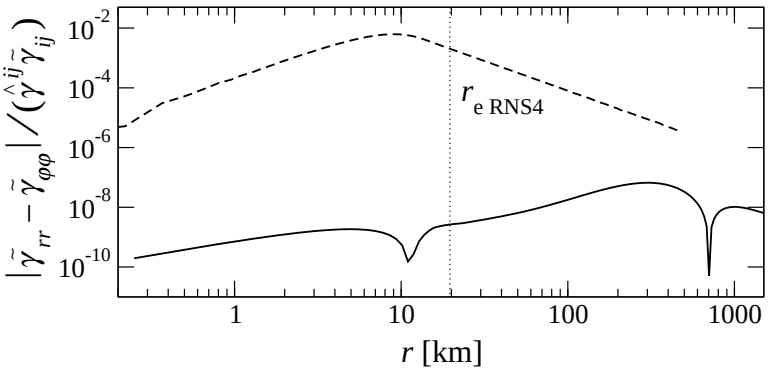

Figure 9.1: Deviation from conformal flatness along the equatorial plane for a typical rotating stellar core initial model (model A1B3; solid line), and for a typical rotating neutron star in equilibrium with axis ratio $r_{\rm p}/r_{\rm e} = 0.7$ (model RNS4; dashed line). The vertical dotted line indicates the equatorial stellar radius for the neutron star.

curve; cf. Table 9.2), and for (ii) the equilibrium rotating neutron star model RNS4 (upper curve; cf. Table 9.1). In both cases, but especially in the (only weakly relativistic) collapse initial model, we observe that deviations from conformal flatness are negligible, which makes the initial models built with the HSCF method suitable for time evolution in the CFC approximation. It also shows that the differences between both gauges are very small, namely of the same order of magnitude as $\tilde{\gamma}_{<ij>}$. Consequently, the use of initial models computed in the MSQI gauge for evolutions using the ADM gauge is entirely justified since the differences are negligible and only appear at the second post-Newtonian order.

9.2 Rotating neutron stars

9.2.1 Effects of the boundary on the metric solution

As mentioned in Chapter 8 the location where the boundary conditions for the CFC+ intermediate potentials are imposed can have a significant impact on the accuracy of the metric solution. Additionally, the extension of the

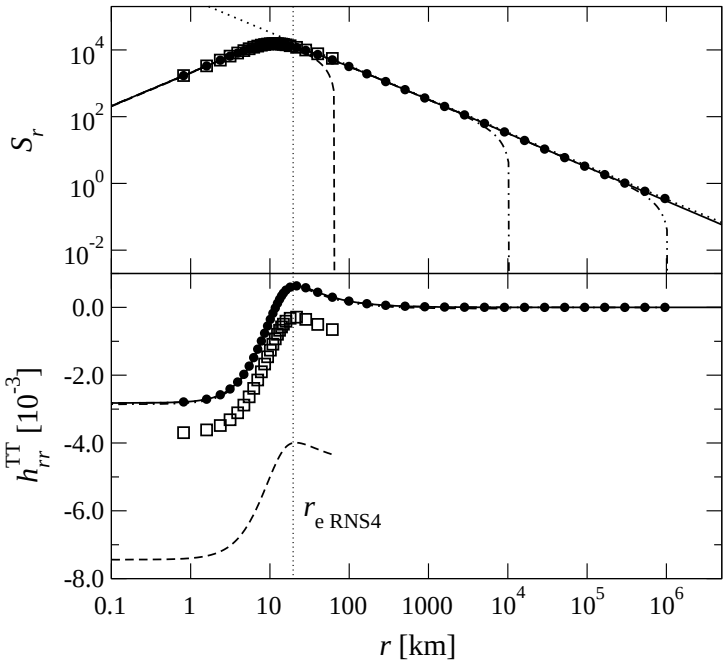

Figure 9.2: Effects of the outer boundary conditions on the equatorial radial profile of the intermediate potential $\mathcal{S}_r$ (top panel) and the metric component $h_{rr}^{\rm TT}$ (bottom panel) for the rotating neutron star model RNS4. Zero-value boundary conditions are imposed at 62 km (dashed line), at 10^4 km (dashed-dotted line), at 10^6 km (dashed-dot-dotted line), and at 10^{11} km (solid line). Alternatively, monopole boundary conditions are imposed at 62 km (open boxes) and at 10^6 km (filled circles). Overplotted to $\mathcal{S}_r$ is the monopole behavior (dotted line).

numerical grid is also of paramount importance for numerically solving the CFC equations to obtain the conformal factor, the shift vector, and the lapse function. As the sources of these equations have non-compact support, it is necessary to integrate out far enough in radius to obtain the desired accuracy for the numerical solution.

To accomplish this we use an extended (vacuum) grid going far beyond

the actual stellar boundary. Monopole behavior at the outer boundary of this vacuum domain has been checked by comparison with calculations done imposing zero values for the potentials as outer boundary conditions at extremely large distances (see Fig. 9.2). Convergence tests with different parameters for the outer grid (number of cells, distance of the outer boundary, amplification factor of the grid) were performed. The conclusion of these tests is that for simulations of rotating neutron stars we need to use a numerical grid consisting of $n_\theta = 30$ angular cells and $n_r = 250$ radial cells (of which 100 are equally spaced inside the neutron star and 150 are logarithmically spaced for the atmosphere) to correctly capture the conformally flat part of the metric. In order to impose outer boundary conditions for the CFC+ metric potentials, an extra grid of 70 radial cells extending out to 10^6 km needs to be added.

9.2.2 CFC+ corrections to the 3-metric

We now turn to measure the magnitude of the CFC+ corrections to the metric of our sample of rotating neutron star models (cf. Table 9.1). First, from the distribution of the hydrodynamic variables in the equilibrium models provided by the HSCF method we recompute the CFC+ metric components. For equilibrium configurations, i.e. in an axisymmetric stationary spacetime, the components $h^{\rm TT}_{r\varphi}$ and $h^{\rm TT}_{\theta\varphi}$ vanish. All other components are shown in Fig. 9.3 for different models with increasing rotation rate. Note that as discussed in Sect. 9.1 the ADM gauge is not quasi-isotropic in the CFC+ approach, because $h^{\rm TT}_{r\theta} \neq 0$ and $h^{\rm TT}_{rr} \neq h^{\rm TT}_{\theta\theta}$. Therefore, a direct comparison with the full general relativistic metric calculated in the MSQI gauge is not possible. As expected, $h^{\rm TT}_{ij}$ vanishes for the spherical case RNS0, in which both CFC and CFC+ agree exactly with general relativity, and their metrics have no traceless and transverse part. As we increase the rotation rate from RNS1 to RNS5, the value of $h^{\rm TT}_{ij}$ increases, resulting in a departure of the metric from conformal flatness. As $h^{\rm TT}_{ij}$ is a correction to the conformally flat 3-metric (which is of order unity, $\phi \sim 1$), it can be shown that even in our most extreme case RNS5, which is very near to the mass shedding limit, the values of $h^{\rm TT}_{ij}$ amount to a correction of only about 1%. Therefore, qualitative differences with respect to the CFC approximation are not expected in the dynamics of such objects.

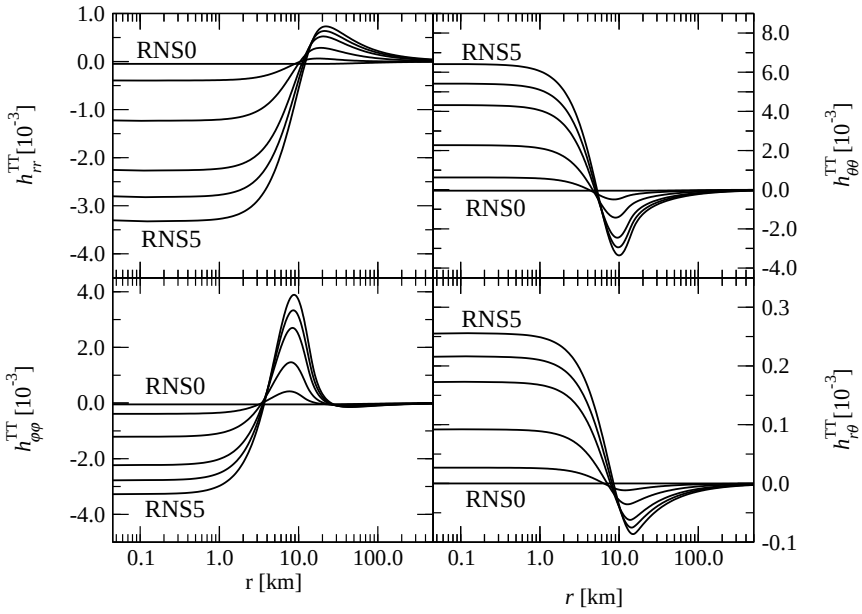

Figure 9.3: Radial profiles at the equator of the non-vanishing components of $h_{ij}^{\rm TT}$ for the sequence of models RNS0 to RNS5. The strength of the correction $h_{ij}^{\rm TT}$ increases with the rotation rate. The equatorial radius of each model is given in Table 9.1.

9.2.3 Oscillations of rotating neutron stars

A further test of the new approximation for the metric is provided by studying pulsations of rotating neutron stars. To this aim we perturb the neutron star models described in Sect. 9.1 with a density perturbation of the form $\rho_{\rm pert} = \rho\,[1 + a\cos(\pi r/(2r_{\rm e}))]$, where a is an arbitrary parameter controlling the strength of the perturbation. The perturbed models are evolved in time in two different ways, either considering *coupled* evolutions for the hydrodynamics and the metric, or evolving *only* the hydrodynamics in a fixed background metric corresponding to the metric provided by the elliptic solvers at the first time step (an approximation commonly referred to in the literature as the Cowling approximation). Both metric approximations, CFC and CFC+, are

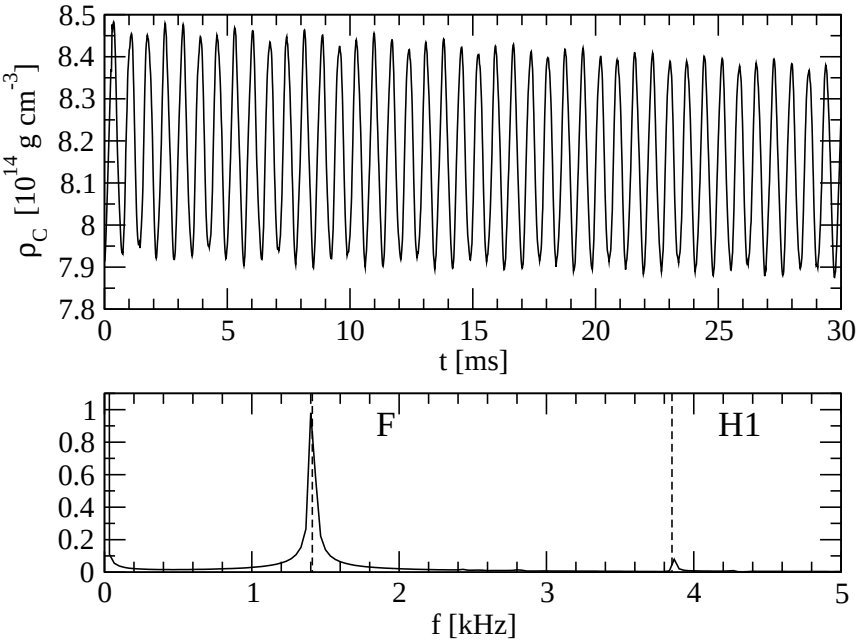

Figure 9.4: Time evolution of the central density ρ_c (upper panel) and its Fourier transform (lower panel) for model RNS1 in the CFC+ approximation with coupled evolution of spacetime and hydrodynamics.The amplitude of the Fourier transform is normalized to the F mode amplitude.

used to compare the respective results.

The oscillations of the stars can be observed in various hydrodynamic and metric quantities. In particular we monitor the central density ρ_c (see upper panel of Fig. 9.4), the radial velocity v_r at half the stellar radius, and the gravitational wave amplitudes A_{20}^{E2} extracted with the standard quadrupole formula. When Fourier transforming the time evolution of these quantities, distinctive peaks appear at the same (discrete) frequencies for any of these variables (see lower panel of Fig. 9.4). Those frequencies can be identified with the quasi-normal modes of pulsation of the star, as described in Font

Table 9.3: Frequencies of small-amplitude quasi-radial pulsations for model RNS4. We compare the frequencies obtained from simulations with the present code (using either the CFC or the CFC+ approximation) with those obtained independently from a 3D full general relativistic code (GR). The results are extracted from time evolutions where the spacetime metric is kept fixed (Cowling approximation). The relative differences between the CFC+ and the GR code are shown in the last column.

Mode	$f^{\rm CFC}$ [kHz]	$f^{\rm CFC+}$ [kHz]	$f^{\rm GR}$ [kHz]	Rel. diff. [%]
F	2.48	2.48	2.468	0.5
H1	4.39	4.39	4.344	1.1
H2	6.30	6.30	6.250	0.8

et al. (2000). To further validate our approach we present the quasi-normal modes calculated in the CFC and CFC+ approximation in comparison with those reported by Font et al. (2002), which are calculated with a 3D code in full general relativity (without any approximation).

Table 9.3 shows the mode-frequencies for the fundamental mode (F), as well as for the first (H1) and second (H2) harmonics obtained in evolutions of model RNS4 in which the spacetime metric is kept fixed (Cowling approximation). The accuracy in the frequency values depends on the total time of the evolution, increasing as the evolution is extended. We evolved all models for 30 ms, finding no significant deviations in the hydrodynamic profiles with respect to the original profiles of the equilibrium models (see fig. 9.5).

For such an evolution time the FFT yields a maximum frequency resolution of 0.03 kHz. Table 9.3 shows that no differences can be observed between the mode-frequencies computed with CFC and CFC+, and that, in addition, there is very good agreement with the general relativistic results, since the reported values are within the affordable resolution in frequency.

The corresponding results for the case of coupled evolutions of the spacetime metric and the hydrodynamics are shown in Tables 9.4 and 9.5 for the fundamental mode and the first harmonic, respectively. In these simulations, for the sake of computational efficiency and without affecting the dynamics, the metric is calculated every 100th hydrodynamic time step and extrapolated

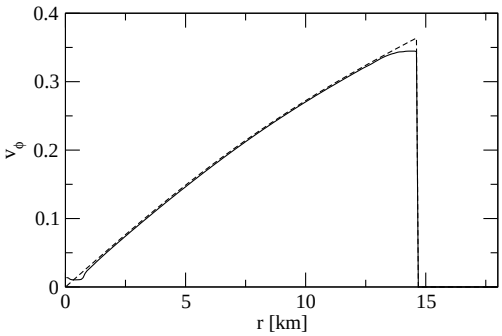

Figure 9.5: Radial profiles of v_φ at the equator for model RNS4 in the CFC+ approximation with coupled evolution of spacetime and hydrodynamics. The curves correspond to the initial time (dashed line) and the final time of the evolution, $t = 30$ ms (solid line).

in between, as explained in Dimmelmeier et al. (2002a). As in the Cowling simulations, all models are evolved for 30 ms. Even for the more rapidly rotating models, no differences in the frequencies from the CFC and CFC+ simulations can be found. This result can again be explained by the smallness of the components of $h_{ij}^{\rm TT}$, which does not modify the dynamics considerably.

Table 9.4: Fundamental mode frequency $f_{\rm F}$ of small-amplitude quasi-radial pulsations for a sequence of rotating polytropes with increasing ratio of polar to equatorial radius $r_{\rm p}/r_{\rm e}$. We compare the frequencies obtained from simulations with the present code using either the CFC or the CFC+ approximation with those obtained independently from a 3D full general relativistic code (GR). The results are extracted from coupled spacetime metric and hydrodynamic time evolutions. The relative differences between the CFC+ and the GR code are shown in the last column.

Model	$r_{\rm p}/r_{\rm e}$	$f_{\rm F}^{\rm CFC}$ [kHz]	$f_{\rm F}^{\rm CFC+}$ [kHz]	$f_{\rm F}^{\rm GR}$ [kHz]	Rel. diff. [%]
RNS0	1.00	1.43	1.43	1.450	1.4
RNS1	0.95	1.40	1.40	1.411	0.8
RNS2	0.85	1.34	1.34	1.350	0.7
RNS3	0.75	1.27	1.27	1.265	0.4
RNS4	0.70	1.24	1.24	1.247	0.6
RNS5	0.65	1.21	1.21	1.195	1.0

Table 9.5: Same as Table 9.4 but for the frequency $f_{\rm H1}$ of the first harmonic mode. In the model RNS5 this harmonic was not sufficiently excited by the perturbation chosen for a clear identification of its frequency.

Model	$r_{\rm p}/r_{\rm e}$	$f_{\rm H1}^{\rm CFC}$ [kHz]	$f_{\rm H1}^{\rm CFC+}$ [kHz]	$f_{\rm H1}^{\rm GR}$ [kHz]	Rel. diff. [%]
RNS0	1.00	3.97	3.97	3.958	0.3
RNS1	0.95	3.87	3.87	3.852	0.5
RNS2	0.85	3.95	3.95	3.867	2.0
RNS3	0.75	3.98	3.98	4.031	1.3
RNS4	0.70	4.02	4.02	3.887	2.0
RNS5	0.65	—	—	3.717	—

Furthermore, the results agree to high precision with the GR results of Font et al. (2002) within the limits set by the temporal and spatial resolution (see Dimmelmeier et al. (2005) for a recent study of mode-frequencies of rotating stars in CFC).

We emphasize that, for accurately extracting the oscillation mode frequencies, the code has to maintain the initial equilibrium configuration in a hydrodynamical evolution for many rotation periods (usually several tens of periods). Irrespectively of the approximation assumed for the metric (either CFC or CFC+) and the (small) gauge mismatch, we tested that our code is able to perform that task successfully.

9.3 Rotational core collapse to neutron star

We now present results of simulations of rotational core collapse to neutron stars. The core collapse models we have selected (see Table 9.2) are representative of the different types of collapse dynamics and gravitational radiation waveforms observed in the CFC simulations of Dimmelmeier et al. (2002a): A1B3G5 as type I (regular collapse), A2B4G5 as type II (multiple bounce collapse), A1B3G5 as type III (rapid collapse), and A4B5G5 as a case with extreme rotation, i.e. a strongly and highly differentially rotating core with

an initial torus-like structure which is strongly enhanced during collapse. We use a numerical grid consisting of $n_\theta = 30$ equally spaced angular cells and $n_r = 300$ logarithmically spaced radial cells covering the star. In order to calculate $h_{ij}^{\rm TT}$ and extract waveforms, an extra grid of 300 radial cells extending out to 10^{11} km needs to be added (600 cells for model A2B4G1).

9.3.1 Collapse dynamics

In Figs. 9.6 to 9.9 we compare the time evolution of selected matter and metric quantities for all four collapse models considered using both the CFC and the CFC+ approximation. We show the time evolution of the central density $\rho_{\rm c}$, which is a representative quantity of the hydrodynamic evolution. We present $\rho_{\rm c}$ for all models except model A4B5G5 for which the time evolution of the maximum density $\rho_{\rm max}$ is used instead. In this model the density maximum is not attained at the center due to the strong differential rotation. The evolution of the central density in models A1B3G3 and A1B3G5 (see Figs. 9.6 and 9.7) shows a distinctive rise during collapse until $\rho_{\rm c}$ reaches its maximum at the time of bounce $t_{\rm b}$ (at $t_{\rm b} \sim 49$ ms and $t_{\rm b} \sim 30$ ms, respectively). Later on, the density oscillates around the new equilibrium value of the compact remnant (which can be identified with the new-born proto-neutron star). These oscillations are highly damped due to the presence of an extended stellar envelope surrounding the proto-neutron star. Note that in models A2B4G1 and A4B5G5 (see Fig. 9.8 and 9.9), the collapse is stopped by rotation before nuclear matter density is reached, as strong centrifugal forces build up during the collapse. As a result, the evolution of model A2B4G1 is characterized by consecutive multiple bounces, while the centrifugal hang-up in model A4B5G5 causes a single bounce below nuclear matter density, leaving a low density proto-neutron star behind.

The top panels of Figs. 9.6 to 9.9 also show the central lapse function $\alpha_{\rm c}$ (dashed line; labels on the right vertical axis). In the CFC+ approach the new $h_{ij}^{\rm TT}$ terms couple directly to the metric equation (5.38) for α, while they couple indirectly to the metric equations for ϕ and β^i through α itself. The evolution of the lapse closely mirrors that of the density, decreasing while the density increases, i.e. while the star contracts, and vice-versa.

For the four collapse models considered here, there is no direct visual evidence of discrepancies between the CFC and CFC+ results. The corresponding

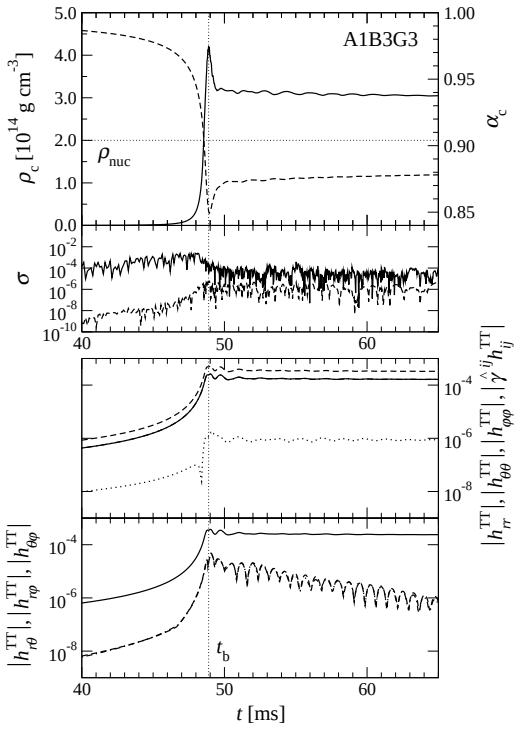

Figure 9.6: Time evolution of hydrodynamic and metric quantities for the regular collapse model A1B3G3. The top panel shows the central density ρ_c (solid line) and lapse function α_c (dashed line). Both the CFC and the CFC+ results overlap. Nuclear matter density ρ_{nuc} is indicated by the horizontal dotted line. The second panel from the top displays the relative difference σ of ρ_c (solid line) and α_c (dashed line) between the simulation using CFC and CFC+. In the third panel the CFC+ evolution of the absolute values of h^{TT}_{rr} (solid line), $h^{TT}_{\theta\theta}$ (dashed line), $h^{TT}_{\varphi\varphi}$ (dashed-dotted line), as well as the trace of h^{TT}_{ij} (dotted line) are shown, all measured at the center of the star. Note that h^{TT}_{rr} and $h^{TT}_{\varphi\varphi}$ cannot be discerned, as they practically overlap. The bottom panel depict the evolution of the maximum absolute values of $h^{TT}_{r\theta}$ (solid line), $h^{TT}_{r\varphi}$ (dashed line), and $h^{TT}_{\theta\varphi}$ (dashed-dotted line), respectively. Again the latter two quantities closely coincide. The vertical dotted line in all panels marks the time of bounce t_b.

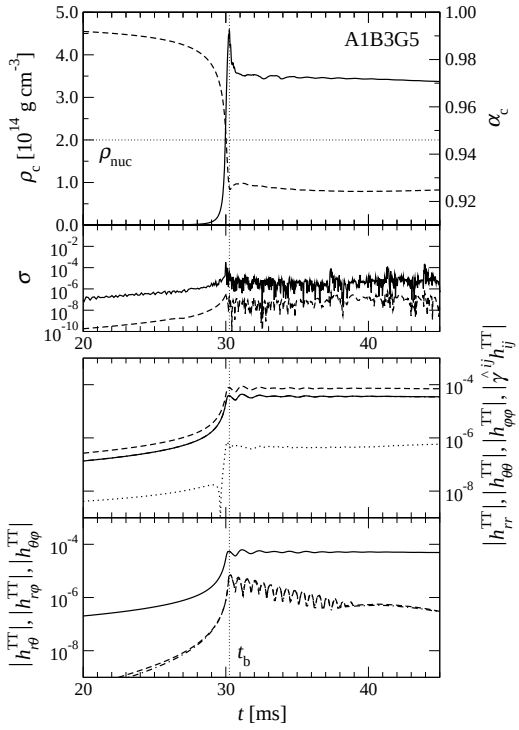

Figure 9.7: Same as Fig. 9.6 for the rapid collapse model A1B3G5.

curves for CFC and CFC+ in the top panels of Figs. 9.6 to 9.9 coincide perfectly in the case of both the lapse function and the density. Therefore, as no appreciable differences are visible, we plot the relative differences σ of these two quantities between CFC and CFC+ in the second panels (from the top) of these figures. Maximum differences of the order of $\sim 1\%$ are found in the density evolution (solid line) for the strongly differentially rotating models A2B4G1 and A4B5G5 (see Fig. 9.8 and 9.9). In the two other models the differences are two orders of magnitude smaller. The lapse function (dashed line) shows even smaller differences between CFC and CFC+, the maximum

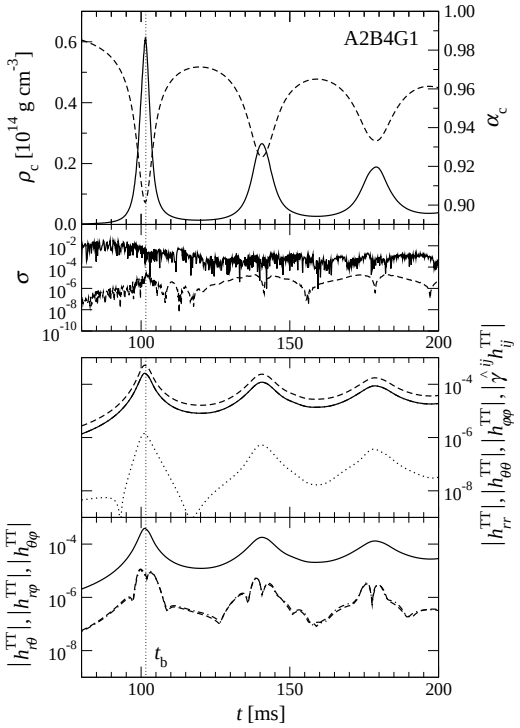

Figure 9.8: Same as Fig. 9.6 for the multiple bounce collapse model A2B4G1. This model centrifugally bounce before reaching $\rho_{\rm nuc}$.

values of σ being smaller than 0.1% even for the rapidly rotating models. This is simply due to the fact that $h_{ij}^{\rm TT}$ arises at the 2PN order in the 3-metric while it appears with a pre-factor $1/c^6$ in the source of α. In fact, the relative difference roughly coincides with the one expected naively from the post-Newtonian approximation level, i.e., $h_{ij}^{\rm TT} \sim (U/c^2)$. By contrast, for slowly rotating collapses described by models A1B3G3 and A1B3G5 , the non-conformally flat contribution is one order of magnitude smaller than (U/c^2). The factor 1/10 may be interpreted as coming from the proximity of spherical symmetry.

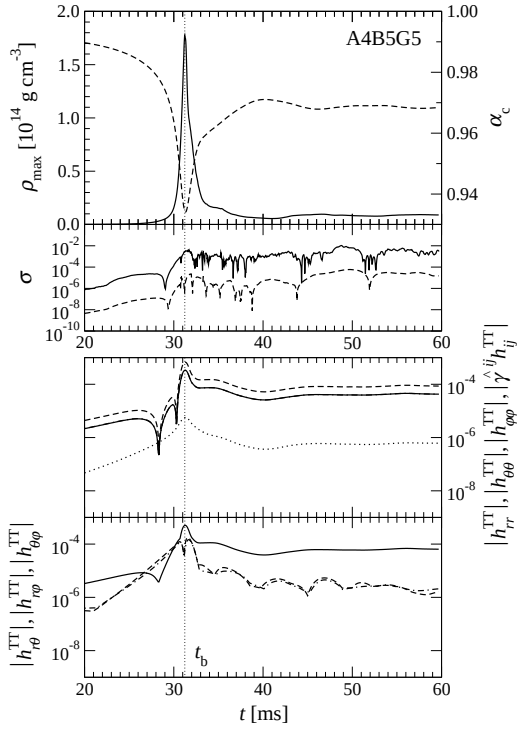

Figure 9.9: Same as Fig. 9.6 for the extremely rotating collapse model A4B5G5. This model centrifugally bounce before reaching $\rho_{\rm nuc}$. Note that we plot the maximum density $\rho_{\rm max}$ instead of $\rho_{\rm c}$, as this model has a toroidal density configuration.

The time evolution of the diagonal components of $h_{ij}^{\rm TT}$ at the center ($r = 0$) are also plotted in Figs. 9.6 to 9.9 (third panels from the top), along with the trace of $h_{ij}^{\rm TT}$. Correspondingly, the maximum absolute values of the off-diagonal terms of $h_{ij}^{\rm TT}$ are displayed in the panels at the bottom. As expected, the various components of $h_{ij}^{\rm TT}$ appear and increase with deviations from sphericity. The profiles show that in all collapse simulations, $h_{ij}^{\rm TT}$ is quite small in comparison to the isotropic part which is of order unity. It can be

Table 9.6: Summary of various quantities that characterize the different core collapse models. The table shows the time of bounce $t_{\rm b}$, the maximum density at bounce $\rho_{\rm b}$, the maximum density reached after the bounce $\rho_{\rm f}$, the gravitational wave amplitude at bounce $\left|A_{20}^{\rm E2}\right|_{\rm b}$ as measured using the quadrupole formula, the dominant frequency $f_{\rm max}$ of proto-neutron star oscillations, the radius $r_{\rm ef}$ of the star after bounce and ringdown (defined as the radial location along the equator where the density first falls below 10% of the maximum density), the size of the near zone $\lambda/(2\pi)$, and the distance $r_{\rm ex}$ at which gravitational waves are extracted from $h_{ij}^{\rm TT}$.

Model	$t_{\rm b}$	$\rho_{\rm b}$ $\times 10^{14}$	$\rho_{\rm f}$ $\times 10^{14}$	$\left\|A_{20}^{\rm E2}\right\|_{\rm b}$	$f_{\rm max}$	$r_{\rm ef}$	$\frac{\lambda}{2\pi}$	$r_{\rm ex}$ $\times 10^3$
	[ms]	$[\frac{g}{cm^3}]$	$[\frac{g}{cm^3}]$	[cm]	[Hz]	[km]	[km]	[km]
A1B3G3	48.89	4.23	3.22	1223	674	13	71	2.6
A1B3G5	30.25	4.65	3.53	131	890	9	52	2.6
A2B4G1	101.60	0.60	0.27	936	54	34	884	40.0
A4B5G5	31.23	1.78	0.096	3757	142	60	334	20.0

seen that models with strong gravity but small asphericities (such as model A1B3G3) and models with weaker gravity but more apparent deviations from sphericity (such as models A2B4G1 or A4B5G5) all reach values for $h_{ij}^{\rm TT}$ of similar magnitude. Note that the components $h_{r\varphi}^{\rm TT}$ and $h_{\theta\varphi}^{\rm TT}$ rapidly decrease after the bounce, because a quasi-equilibrium configuration is reached in the new-born proto-neutron star. In all cases considered the trace of $h_{ij}^{\rm TT}$ is much smaller than the $h_{ij}^{\rm TT}$ components themselves, i.e. numerically $h_{ij}^{\rm TT}$ is traceless to high accuracy and also remains traceless during the entire evolution. In addition, we checked the transverse character of $h_{ij}^{\rm TT}$, i.e. $\nabla^i h_{ij}^{\rm TT} = 0$. The latter expression is found to be compatible with zero, as the dimensionless quantity $r\,\nabla^i h_{ij}^{\rm TT}$ is much smaller than $h_{ij}^{\rm TT}$.

The radial profiles of $h_{ij}^{\rm TT}$ are very similar for all collapse models we have analyzed except for model A4B5G5 that collapses off-center with a torus-like structure. In Fig. 9.10 we compare this model to a model in which the maximum density is reached at the center (A1B3G3). The profiles are depicted at the instant of maximum density ($t_{\rm b} = 48.9$ ms for model A1B3G3 and

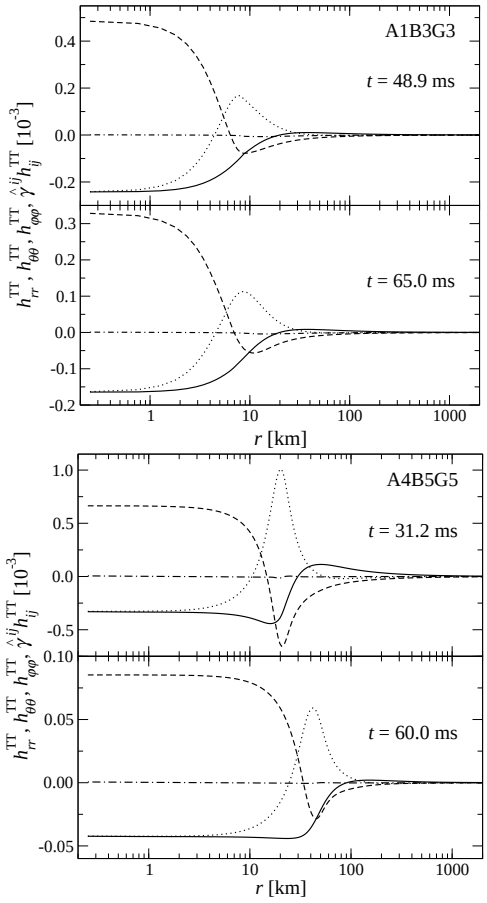

Figure 9.10: Radial profiles of $h_{ij}^{\rm TT}$ at the equator for model A1B3G3 (left) and model A4B5G5 (right) at the time of maximum density (upper panels) and at the final time of the simulation (lower panels). The curves plotted correspond to $h_{rr}^{\rm TT}$ (solid line), $h_{\theta\theta}^{\rm TT}$ (dashed line), $h_{\varphi\varphi}^{\rm TT}$ (dotted line), and the trace of $h_{ij}^{\rm TT}$ (dashed-dotted line), respectively.

$t_b = 31.2$ ms for model A4B5G5) and at the end of the simulation, when the system has reached equilibrium. For the spheroidal model A1B3G3, the maximum values of h_{ij}^{TT} are reached at the center, and the components $h_{\theta\theta}^{TT}$ and $h_{\varphi\varphi}^{TT}$ have local maxima inside the star. However, in the toroidal model A4B5G5 the maximum values are off-centered, while the three components exhibit their peak value inside the torus. Note that the strong deviations from sphericity in model A4B5G5 generate larger values of h_{ij}^{TT} as compared to model A1B3G3 at the time of bounce, but once the torus collapses to the final oblate star, the values become smaller than for the regular collapse model.

Table 9.6 summarizes the results of all collapse simulations, including relevant information to calculate the size of the near zone $\lambda/(2\pi)$ needed for the gravitational wave extraction we discuss next.

9.3.2 Gravitational radiation waveforms

Gravitational waves from the collapse simulations discussed in the preceding section were calculated for both the CFC and the CFC+ approximation of the field equations, using the quadrupole formula. In addition, in the case of CFC+ they were also extracted directly from h_{ij}^{TT} evaluated in the wave zone. The radial extension of the near zone $\lambda/(2\pi)$ can be calculated from the approximate size of the source r_e and the typical timescale of gravitational wave emission $1/f_{max}$. Results for each collapse model are listed in Table 9.6, which also gives the distance r_{ex} at which the waveforms are actually extracted from h_{ij}^{TT}. In our simulations we extract the waveforms at a distance $r \sim 50\lambda/(2\pi)$ in the equatorial plane. This ensures that we are indeed in the wave zone of the true waves where the Newtonian quadrupole formula applies. We checked that $h_+^{2PN} \propto \sin^2\theta/r$ there, so that the gravitational wave amplitude A_{20}^{E2} is approximately constant independent of the radius r or angle θ (except near the rotation axis where h_+^{2PN} vanishes). Due to the smallness of h_+^{2PN} for $r \gg \lambda/(2\pi)$, some numerical error appears because of the cancellations of the different terms in Eq. (5.39). That yields an offset in the gravitational wave signal that can be corrected as follows:

$$h_+^{2PN\,corrected} = h_+^{2PN} - a\,\hat{\gamma}^{ij} h_{ij}^{2PN}. \tag{9.7}$$

Although the term $\hat{\gamma}^{ij} h_{ij}^{2PN}$ should be zero in principle, it is numerically comparable to h_{ij}^{2PN} in the wave zone; the parameter a corrects the offset in the

waveforms.

The gravitational waveforms are displayed in the top panels of Figs. 9.11 and 9.12. The waveforms extracted using the quadrupole formula (solid lines) are very similar for CFC and CFC+ and would not be discernible in the figures. Thus, only the CFC+ waveforms are plotted, along with the absolute differences $\sigma_{\rm abs}$ with respect to CFC (shown in the bottom panels of each figure). For all collapse models considered the differences are smaller than 0.1% of the signal maximum. This is expected from the fact that the quadrupole formula involves an integral of hydrodynamic quantities, and from the observation that the modifications in the collapse dynamics between CFC and CFC+ are not significant, as mentioned in Sect. 9.3.1.

Concerning the waveforms extracted directly from $h_{ij}^{\rm TT}$ (dashed and dotted lines in Figs. 9.11 and 9.12), it can be seen that when directly using Eq. (6.19) to calculate the wave amplitude $A_{20}^{\rm E2}$, the resulting signals are larger at bounce for all models. After bounce these signals show an offset for the models with stronger gravity (A1B3G3 and A1B3G5, see Fig. 9.11), where the waveform amplitude should actually approach zero, because the pulsations of the newborn proto-neutron star are rapidly damped and the star tends towards a state of equilibrium. If the signals are corrected by means of Eq. (9.7), the offset disappears and the gravitational wave amplitude agrees remarkably well with the waveforms calculated with the quadrupole amplitude. Although the extraction methods are not really independent, the agreement found between the two ways of calculating waveforms in the CFC+ approach is a consistency check for the calculation of the $h_{ij}^{\rm TT}$, because the asymptotic behavior given by Eq. (6.19) can be assessed numerically this way.

The agreement holds for all cases except for model A2B4G1, where the amplitudes obtained by the quadrupole formula and from the $h_{ij}^{\rm TT}$ differ by about 50% both at the main bounce and at the subsequent bounces even after the offset correction is applied. For this particular model the size of the near zone is very large, $\lambda/(2\pi) = 884$ km; therefore, an accurate extraction of the waveforms can only be performed at a radius very far away from the star. We thus set the extraction radius $r_{\rm ex} = 4 \times 10^4$ km. As a consequence the extended grid needs to be covered with at least 600 radial zones in order to avoid too extreme logarithmic cell spacing, which would be the source of numerical inaccuracies in the fall-off behavior when solving the elliptic equations with finite difference methods.

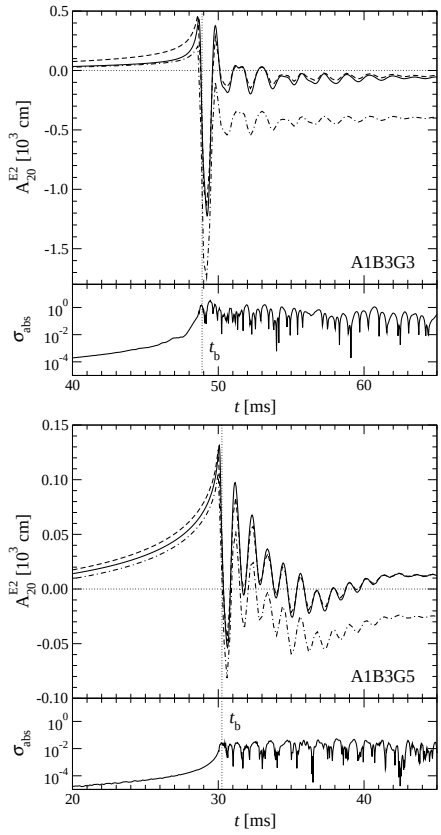

Figure 9.11: Gravitational wave amplitude A_{20}^{E2} computed with the CFC+ approximation of the spacetime metric for the regular collapse model A1B3G3 (left) and the rapid collapse model A1B3G5 (right). Depicted in the top panels are the waveforms extracted using the quadrupole formula (solid line) and extracted directly from h_{ij}^{TT} with (dashed line) or without (dashed-dotted line) corrections for the offset after core bounce. The lower panels show the absolute difference σ_{abs} of the quadrupole waveforms obtained using the CFC+ and CFC approximation of the spacetime metric. The vertical dotted line marks the time of bounce t_{b}.

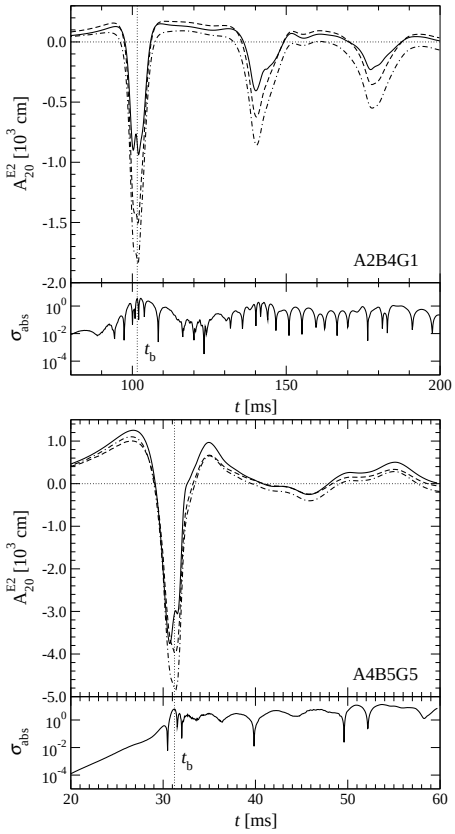

Figure 9.12: Same as Fig. 9.11 for the multiple bounce model A2B4G1 (left) and the extremely rotating collapse model A4B5G5 (right).

9.4 Collapse of cores with extreme rotation

The last issue in this Chapter is the study of the collapse of an extremely rotating core, very near to the mass-shedding limit, and which also has a high degree of differential rotation. The goal of this simulation is to compare

the CFC and the CFC+ approaches in a highly nonspherical scenario, as the CFC+ corrections to the CFC metric take into account the deviations from sphericity. We note that this is likely an academic model, as the rotation rates considered are hardly justified, as state-of-the-art stellar evolution calculations predict much smaller values (Heger et al. 2005). However, in some scenarios those values could be realistic, as in accretion induced collapse (see Fryer & New 2003, and references therein), high rotation rates could be achieved as the NS accretes matter from a companion star and spins up.

Therefore, we extend the parametric study of Dimmelmeier et al. (2002a,b) with a new rotating initial model, labeled A4B6G5. In this model the parameters are the same as for the A4 and G5 models but the rotation rate is such that $r_{\rm p}/r_{\rm e} = 0.4$. The resulting star has an initial equatorial radius of $r_e = 1306$ km, a mass $M = 1.846 M_\odot$, and $\beta = 7.2\%$, and its initial structure is almost toroidal. To correctly simulate the evolution of the star we use a resolution of $n_r = 400$ and $n_\theta = 50$.

The time evolution of the maximum density, $\rho_{\rm max}$, the lapse function at the center, α, and the $h_{ij}^{\rm TT}$ components of the CFC+ metric are plotted in Fig. 9.13, in comparison with the results in the CFC approximation. The relative differences between both approximations, as well as the values for $h_{ij}^{\rm TT}$, are, despite of the more extreme rotation rates involved in the present model, of the same order than for the previous collapse models. In fact they are very similar to those for model A4B5G5. This is due to the fact that, although this model is much more aspherical than the other ones, the densities at bounce are much smaller, $\rho_{\rm max} \sim 6 \times 10^{13}$ g cm^{-3}. The gravitational waveform (see Fig. 9.14) is also similar to that of model A4B5G5, with similar amplitude.

As the rotation rate is very extreme, the collapse proceeds slower, $t_{\rm b} = 40.5$ ms, than for all other models of the G5 series, with $t_{\rm b} \sim 30$ ms. The region near the axis has very low density. Indeed, most of this "funnel" is treated by the code as atmosphere as its density is below the atmosphere threshold. The bounce of the torus is produced by centrifugal forces, but before the maximum density is reached, at $t \sim 37$ ms, the compression of the torus produces a shock at the inner edge, travelling inwards. Due to the restriction of axisymmetry, the shock reflects at the center ($r = 0$) and thereafter follows a natural path to leave the system, that where it finds less obstacles to progress, along the axis where the matter density is the lowest (see Fig. 9.15). In addition the density and pressure gradients in this region are very steep which helps to

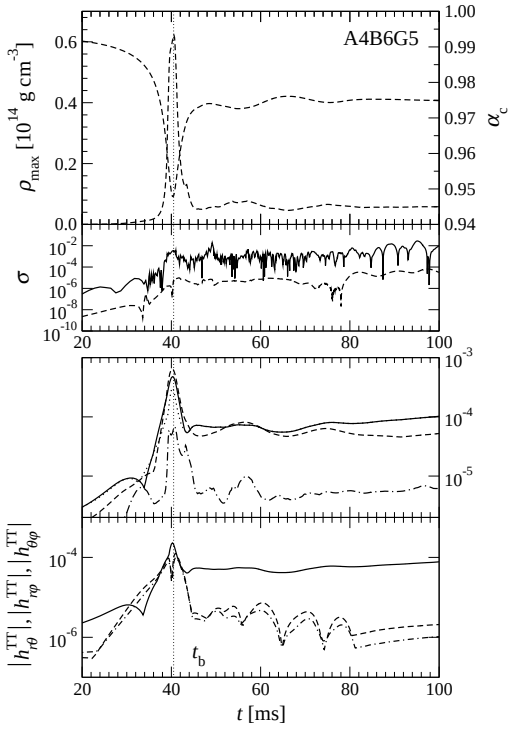

Figure 9.13: Same as Fig. 9.6 for the extremely rotating collapse model A4B6G5. We plot the maximum density $\rho_{\rm max}$ instead of $\rho_{\rm c}$, as this model has a toroidal density configuration.

accelerate the shock. We call this the "toothpaste" effect. As the axis is a low density region surrounded by higher densities, the shock is collimated through a sequence of reflections in the funnel and the axis, reaching easily the surface of the star in about 5 ms, where it rapidly expands into some kind of fireball (see the accompanying movies on the CD). The velocities of this jet are an important fraction of the speed of light, with a Lorentz factor of about $W \sim 1.5$ in the funnel, which accelerates in the exterior to $W \sim 2.4$ before leaving the computational domain. At the same time, at $t_{\rm b} = 40.5$ ms, the

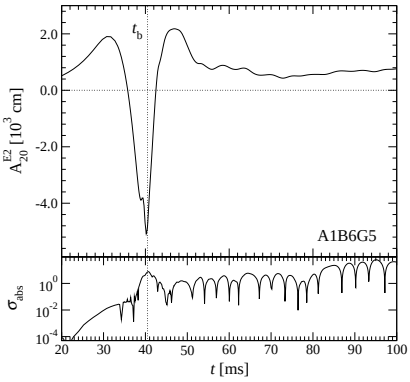

Figure 9.14: Gravitational wave amplitude A_{20}^{E2} computed with the CFC+ approximation of the spacetime metric for the extremely rotating collapse model A4B6G5. Depicted in the top panel is the waveform extracted using the quadrupole formula. The lower panels show the absolute difference σ_{abs} of the quadrupole waveform obtained using the CFC+ and CFC approximation of the spacetime metric. The vertical dotted line marks the time of bounce t_{b}.

maximum density is reached and the torus bounces back forming the usual shock travelling outwards. This shock has a very aspherical shape, as it is mostly concentrated at the equator, and its velocity is much smaller than that of the jet. The remaining torus oscillates several times producing small shocks propagating alternatively outwards and inwards. The latter ones produce by the end of the simulation a flow along the funnel with small velocities and densities.

Although this scenario is not itself a jet formation mechanism, such toothpaste effect could play a role in jet formation scenarios. In such an scenario, the combined collimation effects of a high magnetic field and of the neutrino emission at the funnel, can enhance this effect, powering a highly relativistic continuous jet. On the other hand, the high rotation rates present in the model could lead to three-dimensional instabilities that break axisymmetry, hence affecting at some degree the toothpaste effect.

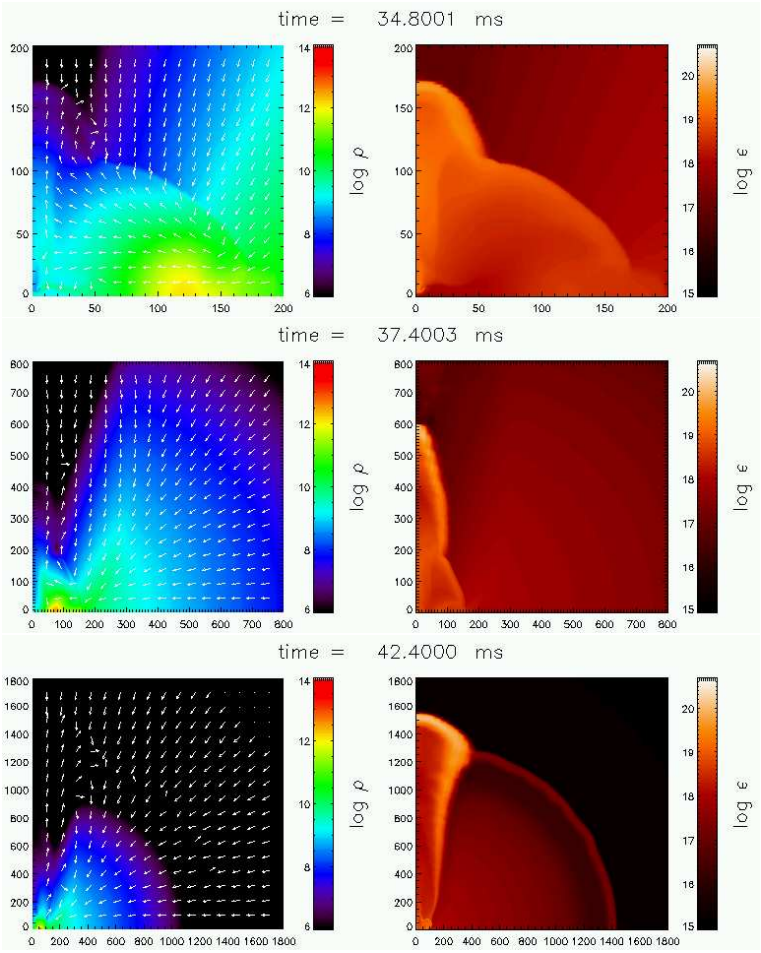

Figure 9.15: Formation of a mildly relativistic jet in model A4B6G5. The left panels show the logarithm of the density, in g cm^{-3}, and the right panels the logarithm of the specific internal energy, in erg. The velocities, normalized to the maximum value at each time (white arrows), are shown in the left panels. The upper panels correspond to time $t = 34.8$ ms, the middle panels to $t = 37.4$ ms, and the lower panels to $t = 42.4$ ms. All axes are in km.

Chapter 10

Magnetorotational core collapse

10.1 Initial data

The magnetic field structure and strength of the core-collapse progenitors, needed as initial conditions for our numerical simulations, is still an open question in astrophysics. Models from stellar evolution predict that magnetic field strengths in iron cores probably do not exceed 10^9 G and that the toroidal field component is expected to be much stronger than the poloidal one (Heger et al. 2005). Therefore, for such weak fields ($P_{\rm mag} \ll P$), the passive field approximation (see Chapter 3) is sufficient to perform core collapse simulations, as the magnetic fields are not going to affect the fluid evolution for the time scales involved. We note however, that, as mentioned in the introduction of this thesis, there could be various amplification mechanisms operating during core collapse (e.g. the so-called magneto-rotational instability (Balbus & Hawley 1991)), which might increase the amplitude of the magnetic field to values were the passive field approximation is no longer valid. The results presented in this chapter have to be considered, hence, as part of a broader program aimed at simulating relativistic, magnetized core collapse with no approximations in the dynamics. Those simulations will be presented elsewhere.

10.1.1 Stationary models

In order to perform numerical simulations of magnetized core collapse, we have to build initial conditions for the magnetized initial cores. Keeping in mind that our ultimate goal is to calculate the gravitational radiation from such events, it is interesting to come up with a parametrized sample of models, spanning the relevant range of variation of significant quantities, such as rotation rate, and magnetic field distribution. Therefore, we proceed in a similar way that we did in Chapter 9 with unmagnetized models. The main problem of such an approach however is that if one tries to impose similar symmetries to the magnetized case, one finds that restrictions on the magnetic field structure immediately arise. If one imposes that no meridional flux is allowed in the equilibrium model and the flow is isentropic, then the magnetic field has to be purely poloidal, i.e. with no toroidal component (see Bekenstein & Oron 1979). The reason is that, otherwise, the circularity condition is violated (Carter 1979). Stationary models of magnetized stars have been computed under these assumptions by Bocquet et al. (1995). In the general case in which meridional circulation is allowed, a toroidal component of the magnetic field may exist, but the method to calculate stationary models is far more complicated (Gourgoulhon & Bonazzola 1993; Ioka & Sasaki 2003, 2004). When one considers ideal MHD, the condition is relaxed, and also purely toroidal magnetic fields maintain the circularity condition (Oron 2002), and therefore it is possible to generate stationary models without meridional components. Finally, in the case that magnetic pressure does not exceed the hydrostatic pressure, Oron (2002) has shown that stationary models with mixed toroidal and poloidal component approximately accomplish the circularity condition.

The last case matches with our adopted passive field approximation. As the energy-momentum content of the magnetic field is set to zero in comparison with the fluid component, no magnetic field components appear in the equilibrium equations. Hence, the method described in Section 9.1 can be used unaltered to generate equilibrium models for the fluid variables. The only additional aspect to consider in our equilibrium models is to generate a magnetic field that preserves the divergence-free constraint, and remains constant in time (in the passive field approximation).

If we consider a rotating axisymmetric configuration with no meridional

flows the components of the velocity field can be written as

$$\begin{aligned} v^{*r} &= 0, \\ v^{*\theta} &= 0, \\ v^{*\varphi} &= r\,\Omega^* \sin\theta, \end{aligned} \tag{10.1}$$

where $\Omega^* = \Omega^*(r,\theta)$ is the rotation law. In axisymmetry and using spherical coordinates the induction equation (3.46) reads, under the above conditions

$$\frac{\partial B^{*r}}{\partial t} = 0, \tag{10.2}$$

$$\frac{\partial B^{*\theta}}{\partial t} = 0, \tag{10.3}$$

$$\frac{\partial B^{*\varphi}}{\partial t} = \frac{1}{r}\frac{\partial}{\partial r}(r^2 \sin\theta\,\Omega^* B^{*r}) + \frac{1}{r}\frac{\partial}{\partial \theta}(r \sin\theta\,\Omega^* B^{*\theta}). \tag{10.4}$$

The equation for the evolution of the φ component can be expanded as

$$\begin{aligned} \frac{\partial B^{*\varphi}}{\partial t} &= \Omega^* r \sin\theta \left[\frac{1}{r^2}\frac{\partial (r B^{*r})}{\partial r} + \frac{1}{r\sin\theta}\frac{\partial (\sin\theta B^{*\theta})}{\partial \theta}\right] \\ &\quad + r\sin\theta \left[B^{*r}\frac{\partial \Omega^*}{\partial r} + B^{*\theta}\frac{1}{r}\frac{\partial \Omega^*}{\partial \theta}\right], \end{aligned} \tag{10.5}$$

where the first term vanishes by means of the divergence constraint (3.45) yielding

$$\frac{\partial B^{*\varphi}}{\partial t} = r\sin\theta\,\vec{B}^* \cdot \vec{\tilde{\nabla}}\Omega^*. \tag{10.6}$$

By integrating this equation one shows that, in the passive field approximation, the toroidal magnetic field component increases linearly with time as

$$B^{*\varphi}(t) = B^{*\varphi}(t=0) + t\; r\sin\theta\,\vec{B}^* \cdot \vec{\tilde{\nabla}}\Omega^*. \tag{10.7}$$

This amplification mechanism of the toroidal magnetic field is the so-called Ω-dynamo (Meier et al. 1976). If meridional flows are also considered, i.e. non vanishing v^{*r} and $v^{*\theta}$, the toroidal magnetic field can be transformed back into the poloidal component via the α-Ω-dynamo, which is a full three-dimensional process not allowed in axisymmetry.

Eq. (10.6) shows that an equilibrium solution can be found in three cases: (i) a purely toroidal magnetic field, i.e. $B^{*r} = B^{*\theta} = 0$, (ii) a rigid rotator i.e. $\hat{\vec{\nabla}}\Omega^* = 0$ and therefore $\Omega^* = \text{const.}$, and (iii) the special case in which $\vec{B}^* \perp \hat{\vec{\nabla}}\Omega^*$. Note that the rotation law given by Eq. (9.3), as well as any rotation law given by $\Omega = \Omega(\varpi)$ (ϖ being the distance to axis), fulfills condition (iii) if the magnetic field is parallel to the axis. Using these properties we can construct stationary models with non-evolving magnetic fields. This is of the great interest in order to design numerical tests of the code (see Section 10.2) and to build initial models in equilibrium (see below).

10.1.2 Magnetic field configurations

Aiming to generate parametrized magnetic field configurations we have first to design a method to build divergence-free configurations in general relativity. The particularity of curved spacetimes is that the condition (3.39) in the magnetic field B^i involves the covariant derivative, and hence the metric appears in this condition. A way to overcome this problem is to work with the "starred" magnetic field B^{*i}, for which flat-metric operators apply (3.46). Once we have a divergence-free magnetic field B^{*i} we can easily calculate the physical one B^i using the metric. To ensure the divergence constraint we work with a vector potential $\vec{A}^*$, such that the magnetic field generated by it

$$\vec{B}^* = \hat{\nabla} \times \vec{A}^*, \tag{10.8}$$

is divergence-free by construction. As we assume axisymmetry, the toroidal component of the magnetic field does not affect the divergence constraint, because φ derivatives vanish, and therefore we do not need to construct the $B^{*\varphi}$ component from the vector potential. In spherical coordinates and axisymmetry the above condition for the poloidal field reads

$$B^{*\,r} = \frac{1}{r\sin\theta}\frac{\partial}{\partial\theta}\left(\sin\theta A^*_\varphi\right), \tag{10.9}$$

$$B^{*\,\theta} = -\frac{1}{r}\frac{\partial}{\partial r}\left(rA^*_\varphi\right). \tag{10.10}$$

Given a value for the vector potential A^*_φ, we have designed a numerical method well suited to our numerical description of the divergence-free equation. The

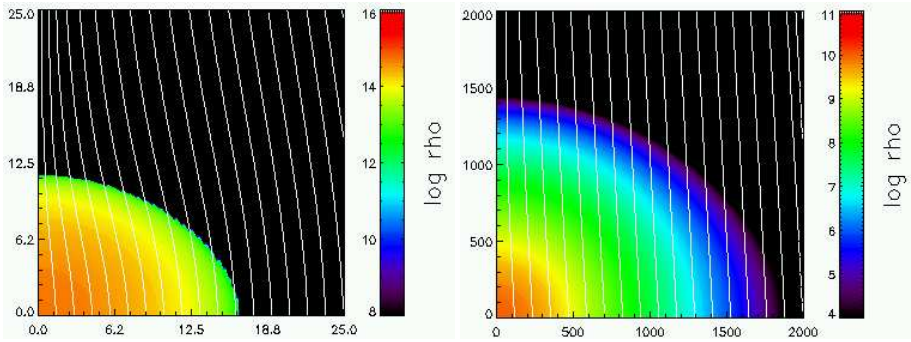

Figure 10.1: Logarithm of the rest mas density ($\log \rho$, color coded) and magnetic field (B^i) lines in a homogeneous B^{*i} field configuration, for a typical rotating neutron star of about $1.4 M_\odot$ (left panel) and a typical rotating iron core (model A1B3 in Table 9.2) used for the collapse simulations (right panel). The magnetic field lines have been calculated as isocontours of the vector potential. The axis scale is in km and the density in c.g.s. units.

components of the magnetic field at the interfaces can be discretized as

$$B^{*r}_{i+1/2\ j} = -\frac{1}{r_{i+1/2}} \frac{\sin\theta_{j+1/2}\ A^*_{\varphi\ i+1/2\ j+1/2} - \sin\theta_{j-1/2}\ A^*_{\varphi\ i+1/2\ j-1/2}}{\Delta(\cos\theta)_j}, \quad (10.11)$$

$$B^{*\theta}_{i\ j+1/2} = -2\frac{r_{i+1/2}\ A^*_{\varphi\ i+1/2\ j+1/2} - r_{i-1/2}\ A^*_{\varphi\ i-1/2\ j+1/2}}{\Delta r_i^2}. \quad (10.12)$$

With this prescription and the surface elements given by Eqs. (7.14), the total numerical flux $\Phi_{\rm T}$ over a cell is zero (up to round off error) as

$$\begin{aligned}\Phi_{\rm T} =& B^{*r}_{i+1/2\ j}\ \Delta\hat{S}_{r\ i+1/2\ j} - B^{*r}_{i-1/2\ j}\ \Delta\hat{S}_{r\ i-1/2\ j} \\ &+ B^{*\theta}_{i\ j+1/2}\ \Delta\hat{S}_{\theta\ i\ j+1/2} - B^{*\theta}_{i\ j-1/2}\ \Delta\hat{S}_{\theta\ i\ j-1/2} = 0, \end{aligned} \quad (10.13)$$

and will remain zero during a numerical evolution using CT schemes (see Chapter 7).

Throughout this chapter we use the following three magnetic field configurations:

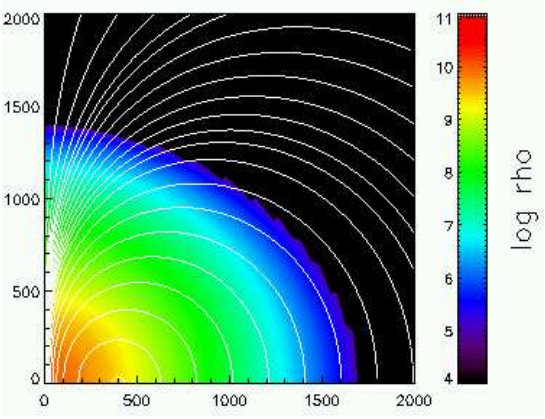

Figure 10.2: Same as Fig. 10.2 but for a rotating iron core (model A1B3 in Table 9.2) with the magnetic field generated by a circular loop current in the equatorial plane of radius $r_{\rm mag} = 400km$.

- **Homogeneous** "starred" magnetic field ($B^{*\,i}$) of the form

$$\begin{aligned} B^{*\,r} &= B_0^* \cos\theta, \\ B^{*\,\theta} &= B_0^* \sin\theta, \end{aligned} \tag{10.14}$$

where B_0^* is the magnetic field at the center ($r = 0$). Note that this configuration describes a homogeneous B^{*i} field, but not a homogeneous physical magnetic field B^i, as metric components are involved in the relation (3.41) between both. In fact, a homogeneous B^i field only is possible in the limit of Newtonian gravity where the three-metric is flat. Fig. 10.1 shows how such magnetic field looks like as we increase the compactness of the star and hence the curvature of the spacetime.

- Magnetic field generated by a **circular current loop** of radius $r_{\rm mag}$ in the equatorial plane (Jackson (1962)), that can be calculated from the only non-vanishing component of the vector potential A_φ^* as

$$A_\varphi^* = \frac{r_{\rm mag}^2 B_0^*}{2} \sum_{n=0}^{\infty} \frac{(-1)^n (2n-1)!!}{2^n (n+1)!} \frac{r_<^{2n+1}}{r_>^{2n+2}} P_{2n+1}^1(\cos\theta), \tag{10.15}$$

where $r_< = \min(r, r_{\rm mag})$, $r_> = \max(r, r_{\rm mag})$, and B_0^* is the magnetic field at the center. The resulting magnetic field (see Fig. 10.2) does not

have a toroidal component. In the limiting case of $r \ll r_{\rm mag}$ or $\theta \ll 1$ the magnetic field is homogeneous and parallel to the axis

$$\begin{aligned} B^{*\,r} &\approx B_0^* \cos\theta, \\ B^{*\,\theta} &\approx B_0^* \sin\theta, \end{aligned} \tag{10.16}$$

while in the limiting case of $r \gg r_{\rm mag}$ the magnetic field is dipolar

$$\begin{aligned} B^{*\,r} &\approx 2B_0^* \frac{\cos\theta}{r^3}, \\ B^{*\,\theta} &\approx B_0^* \frac{\sin\theta}{r^3}. \end{aligned} \tag{10.17}$$

- **Toroidal** magnetic field of the form

$$B^{*\varphi} = B_0^* \frac{r_{\rm mag}^2}{r_{\rm mag}^2 - \varpi^2}, \tag{10.18}$$

where B_0^* is the central magnetic field, and its maximum value is reached at $\varpi = r_{\rm mag}$.

10.1.3 Summary of initial models

As the magnetic field is not going to affect the equilibrium models, we choose as initial models for the core collapse simulations suitable combinations of the models given in Table 9.2 with the magnetic field configurations of the previous section. Aiming at comparing our results with the recent numerical simulations performed by Obergaulinger et al. (2005) in Newtonian gravity, a subset of our models (those with purely poloidal magnetic field) have been selected as general relativistic counterparts of their models. Our initial data are described in Table 10.1. Note that the models of Obergaulinger et al. (2005) are not stationary in the sense of Section 10.1.1. Only models labeled A1 are approximately stationary since they are almost rigidly rotating. All models with purely toroidal field (labeled T) are stationary.

Table 10.1: Initial models used in the magnetized core collapse simulations. The magnetic field configuration can be the poloidal field generated by a circular loop (CL) or the purely toroidal field (T) given by Eq. (10.18). In all cases $r_{\rm mag} = 400$ km. The models are labeled following the notation of Obergaulinger et al. (2005) with "T" instead of "D" for the toroidal configurations. The label "M0" indicates that we use the passive field approximation. The specific parameters corresponding to the hydro model can be found in Table 10.1. Last column gives information of the stability of the magnetic field configuration (see text for details).

Model	Hydro model	magnetic field	stationary
A1B3G3-D3M0	A1B3G3	CL	approx.
A1B3G5-D3M0	A1B3G5	CL	approx.
A4B5G5-D3M0	A1B3G5	CL	no
A1B3G3-T3M0	A1B3G3	T	yes
A1B3G5-T3M0	A1B3G5	T	yes

10.2 Tests

We have designed several tests in order to check the accuracy of our numerical code when solving the induction equation with the numerical methods described in Chapter 7. The "toroidal test" is designed to assess the ability of the code to maintain equilibrium magnetic field configurations (TTA and TTB) and to correctly calculate the amplification of the toroidal magnetic field as it is wound up by a rotating fluid (TTC). On the other hand, the poloidal test (PT) is designed to check whether the code can correctly compute the compression of the poloidal magnetic field in a spherical collapse, and its ability to handle the presence of radial shocks.

10.2.1 Toroidal test

In a stationary case, in which the fluid does not evolve in time, and only an azimuthal component of the velocity is allowed, i.e. $v^{*r} = 0$, $v^{*\theta} = 0$ and $v^{*\varphi} \neq 0$, the analytic solution in the passive field approximation is known. It is given by Eq. (10.6) for the toroidal magnetic field, while the poloidal

component does not change with time. In order to test whether the numerical code is able to recover this solution, we investigate three particular cases of this solution. For the three tests, we consider a non evolving fluid of constant density $\rho = 10^{14}$ g cm^{-3} filling the computational domain, and an equally-spaced grid in both the angular and radial direction. The radial boundary is located at 20 km. We consider a static background spacetime with a flat metric. The tests performed are the following:

- Toroidal test A (TTA): In this test we consider the purely poloidal magnetic field generated by a circular current loop given by Eq. (10.15), with $r_{\rm mag} = 6$ km. The fluid rotates rigidly, $\Omega^* = \Omega_0^*$, in such a way that the velocity at the numerical boundary is $0.1\,c$. With this configuration the toroidal magnetic field should remain zero. We evolve the magnetic field only, keeping fixed the fluid and spacetime evolution, during a total time of 1 ms (10 rotations for the chosen Ω_0^*),at which time we calculate the global error with respect to the analytic solution ($B^\varphi_{\rm (th)}(t) = 0$) as

$$\sigma(B^\varphi) = \sqrt{\sum_{ij} \sigma_{i\,j}}, \qquad \sigma_{i\,j} \equiv B^\varphi - B^\varphi_{\rm (th)} \tag{10.19}$$

  where $\sigma_{i\,j}$ is the local error at a given cell and the sum extended over all cells of the numerical grid.

- Toroidal test B (TTB): In this test we consider the second nontrivial configuration for a stationary magnetic field according to Eq. (10.6). We use a purely poloidal field, homogeneous and parallel to the rotation axis, as given by Eq. (10.14), in combination with a rotation law depending only on the distance to the axis ϖ. In particular we use for $\Omega^*(\varpi)$ the law given by Eq. (9.3), with the same value for Ω_c^* as in TTA, and $A = 6$ km. For a total time evolution of 1 ms, the fluid rotates ten times at the center, and only once at the outer boundary, while the magnetic field should not evolve. We calculate the error at the final time, $\sigma(B^\varphi)$, in the same way as in the TTA case.

- Toroidal test C (TTC): In the last test, we do not consider a stationary configuration, but an evolving one. We choose the homogeneous poloidal

field of case TTB, and the rotation law given by

$$\Omega^* = \frac{A^2 \Omega_c^*}{A^2 + r^2}, \tag{10.20}$$

where A is a parameter controlling the degree of differential rotation. Note that this rotation law does not depend on the distance to the axis ϖ, but on the distance to the center r. The same values for A and Ω_c^* as in TTB are also adopted in this test. Acording to Eq. (10.6) the toroidal magnetic field is given by the analytic expression

$$B^{*\varphi}_{(\mathrm{th})}(t) = -B_0^* \Omega_c^* \frac{A^2 r^2 \, t}{(A^2 + r^2)^2} \, \sin 2\theta. \tag{10.21}$$

We calculate the error after a total evolution time of 1 ms, $\sigma(B^{\varphi})$, in the same way as in the TTA case.

For numerical scheme of order N the numerical representation $f_{\mathrm{num}}(r, \theta)$ of a given function $f(r, \theta)$ differs by σ with respect to the true value of the function

$$f(r, \theta) = f_{\mathrm{num}}(r, \theta) + \sigma \left(\Delta r^{\, p}, \Delta \theta^{\, q} \right), \qquad p + q = N, \tag{10.22}$$

where σ depends linearly on $\Delta r^{\, p}$ and $\Delta \theta^{\, q}$. The test simulations are performed with equidistant grids in both r and θ,

$$\Delta r = \frac{R}{n_r}, \quad \Delta \theta = \frac{\pi}{2 n_\theta}, \tag{10.23}$$

where R is the outer radius of the numerical domain. If we consider a reference (low resolution) grid $n_{r\mathrm{ref}} \times n_{\theta\mathrm{ref}}$ with an error σ_{ref}, and a subsequent grid with a factor f higher resolution, i.e. $n_r = f n_{r\mathrm{ref}}$ and $n_\theta = f n_{\theta\mathrm{ref}}$, then the error on the new grid, σ_f, is related to the error on the reference grid as

$$\sigma_f = \sigma_{\mathrm{ref}} \left(\frac{1}{f} \right)^N. \tag{10.24}$$

By fitting the values of σ_f as a function of $1/f$ we can easily calculate the convergence order N. For our test simulations we consider a reference grid of

Test	Reconst.	N	$\sigma_{320\times40}$
TTA	*minmod*	2.35	$1.20\,10^{-6}$
TTA	MC	2.16	$2.37\,10^{-6}$
TTA	PPM	2.24	$2.33\,10^{-6}$
TTB	*minmod*	2.64	$7.66\,10^{-6}$
TTB	MC	2.53	$1.19\,10^{-5}$
TTB	PPM	2.55	$1.20\,10^{-5}$
TTC	*minmod*	1.54	$7.99\,10^{-5}$
TTC	MC	1.48	$7.03\,10^{-5}$
TTC	PPM	1.46	$6.39\,10^{-5}$

Table 10.2: Convergence order N for the three tests performed (TTA, TTB and TTC) and for different reconstruction procedures (*minmod*, MC and PPM). The error $\sigma_{320\times40}$ on the higher resolution grid is also given.

80×10 cells ($f = 1$) , and higher resolution grids of 160×20 ($f = 2$) and 320×40 ($f = 4$) cells respectively. Figures 10.3 and 10.4 show the resulting σ_f for the three tests versus $1/f$. The convergence orders, N, resulting of the fit of these data to a power law, as well as the errors for the finest grid are given at Table 10.2.

Our results show that (i) the orders of convergence and the errors are almost independent of the reconstruction scheme, (ii) the order for the TTC test is smaller than for the TTA and TTB tests, and (iii) the order for cases TTA and TTB is $N > 2$, and hence higher than the theoretical expectation (second order, since limited by the time discretization, a second order Runge-Kutta method of lines).

In all tests we obtain similar results for the linear reconstruction (*minmod* and MC) and for the PPM reconstrution, as the order of the scheme is limited by the second order discretization in time. In fact, linear reconstruction with *minmod* slope limiter yields the most accurate results. The main difference between the case TTC and the cases TTA and TTB, is that in the first case there is a component of the magnetic field, $B^{*\varphi}$, evolving in time (growing linearly), while in the other cases this component does not evolve. The results for the latter cases are more accurate due to exact cancellations in the numerical scheme used in these particular tests. Their high order can be explained if we calculate the local convergence order, i.e. the convergence order obtained when computing the errors of each numerical cell, σ_{ij}, instead of the global error σ. To do that, we average the errors in the high resolution grids, $f = 2$

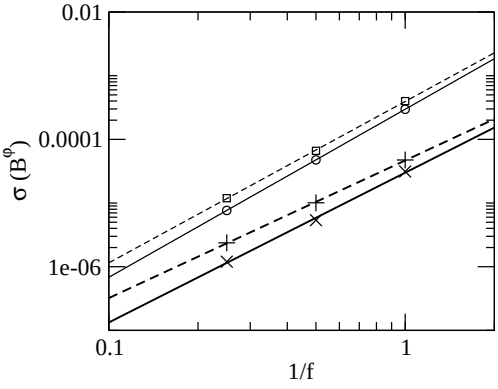

Figure 10.3: Global error in the toroidal magnetic field, $\sigma(B^\varphi)$, after 1 ms time evolution of test TTA (+ for *minmod* and × for MC) and TTB (circles for *minmod* and squares for MC), as a function of $1/f$ for a sequence of models with grid resolution: 80×10 ($f = 1$), 160×20 ($f = 2$) and 320×40 ($f = 4$). Thin and thick lines represent the best fit of the test TTA and TTB, respectively, to Eq (10.24) (solid for *minmod* and dashed for MC).

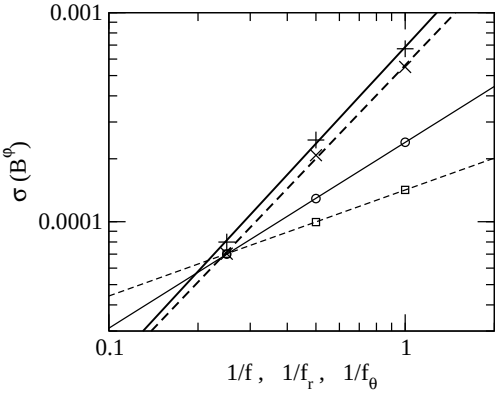

Figure 10.4: Global error in the toroidal magnetic field, $\sigma(B^\varphi)$, after 1 ms time evolution of test TTC as a function of $1/f$ and its best fit, for both *minmod* (+ and solid line) and MC (× and dashed line). Also plotted are the global errors for high angular (radial) resolution grids with increasing radial (angular) resolution as a function of $1/f_r$ ($1/f_\theta$) with circles (squares), and its fits to Eq (10.24) with solid (dashed) lines.

and $f = 4$, to the 80×10 reference grid, and then we calculate the order of convergence at each cell. The results for the three tests and the three reconstructions used are displayed in Figs. 10.5, 10.6, and 10.7. It can be seen, that at some particular locations the order of convergence is larger than two, while at most locations of the grid it remains around two. These scattered points cause the high global order of convergence, but in general the second order convergence of the code is well achieved. It can also be noted that the order drops at the outer boundary, where boundary conditions are imposed, and in some cases near the center ($r = 0$), where symmetries are imposed.

Additionally, if we consider a reference grid with high resolution in the angular direction, we can set $\Delta\theta_{n_{\theta\mathrm{ref}}} \to 0$, and thus $\sigma \approx \sigma(\Delta r^N)$. For a grid with a factor f_r times higher radial resolution, i.e. with grid resolution $n_r = f_r n_{r\mathrm{ref}}$ and $n_\theta = n_{\theta\mathrm{ref}}$, the error is related to the error in the reference grid with high angular resolution ($\sigma_{\mathrm{ref}\ r}$) according to

$$\sigma_{f_r} = \sigma_{\mathrm{ref}\ r} \left(\frac{1}{f_r}\right)^{N_r}, \tag{10.25}$$

where N_r represents the order of convergence when increasing the radial resolution at fixed high angular resolution, which can be calculated fitting data to the above equation. In an equivalent way, we can also define a convergence order for the angular direction N_θ, if we consider a reference grid with high resolution in the radial direction.

We have calculated both the radial convergence order N_r and the angular one N_θ for the TTC case with MC linear reconstruction. To compute N_r we take a grid with high angular resolution (80×40) as reference ($f_r = 1$), and then we increase the radial resolution by taking 160×40 ($f_r = 2$) and 320×40 ($f_r = 4$) zones. If we then fit the errors (see Fig. 10.3) to Eq. (10.25) we can calculate N_r. In a similar way we calculate N_θ, from the sequence of grids 320×10 (f_θ=1), 320×20 (f_θ=2) and 320×40 (f_θ=4). The resulting values are $N_r = 0.89$ and $N_\theta = 0.51$. In both cases the values obtained are smaller than the order of convergence obtained in the case of increasing both the radial and the angular resolution ($N = 1.48$). As $N_r > N_\theta$, the solution will converge faster if we increase the radial resolution than if we increase the angular resolution. As a result, in order to obtain more accurate results under the (practical) constraint that we can not afford to increase

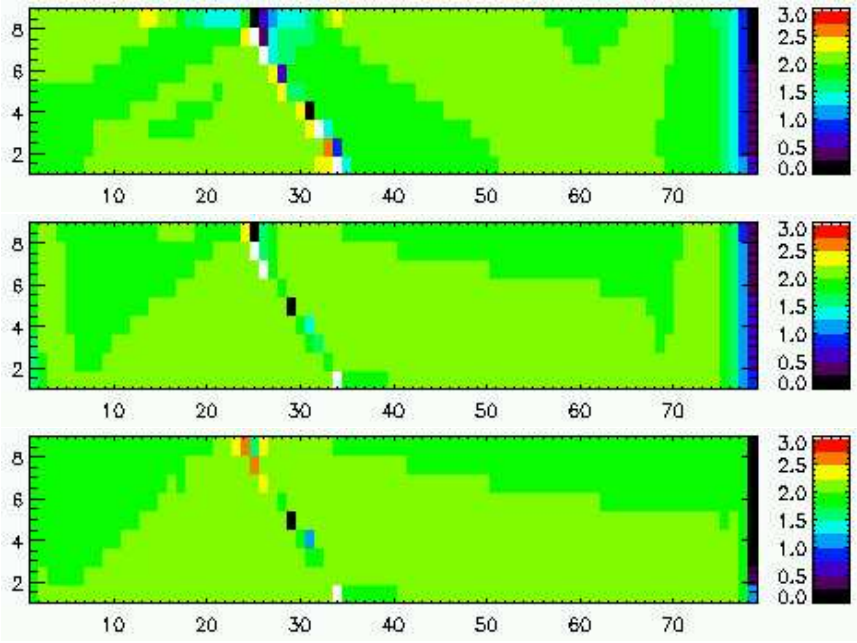

Figure 10.5: Local order of convergence (color coded) in the TTA test after a total time evolution of 1 ms, for three different reconstruction schemes: linear reconstruction with *minmod* slope limiter (upper panel), MC slope limiter (middle panel), and PPM reconstruction (lower panel). White color is used for values bigger or equal than 3.0. The axes represent the number of cells of the reference grid in the radial and angular direction.

the resolution in both directions, it is more efficient from a computational point of view, to increase the radial resolution than the angular resolution. Therefore, although the angular resolution plays a crucial role in order to correctly evolve the magnetic field, we should also take into account the radial resolution. Using this information we will design the grids for the magnetized core collapse simulations (see below), in such a way that they have sufficient radial resolution, especially the inner regions where the proto-neutron star will

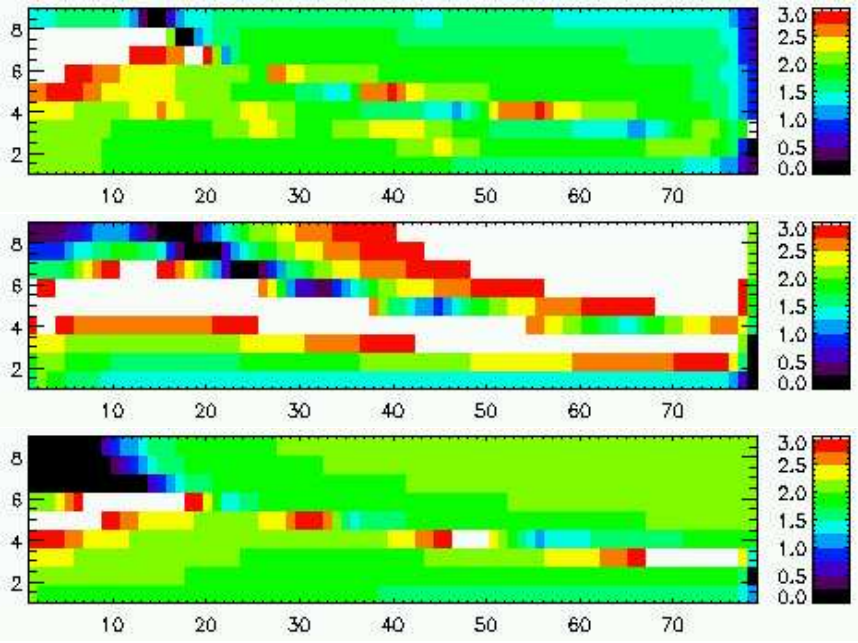

Figure 10.6: Same as Fig. 10.5 but for the case TTB.

form.

10.2.2 Poloidal test

We consider now a test in which only radial velocities of the fluid are allowed, i.e. $v^{*r} \neq 0$, $v^{*\theta} = 0$ and $v^{*\varphi} = 0$. We also consider initially a purely poloidal magnetic field. In this case, it can be easily shown from the induction equation (3.46) and the continuity equation (3.11) that the following equivalence holds in the equatorial plane

$$\frac{\partial}{\partial t}\left(\frac{D^*}{B^{*\theta}}\right) = -v^{*r}\,\frac{1}{r}\frac{\partial}{\partial r}\left(r\frac{D^*}{B^{*\theta}}\right), \tag{10.26}$$

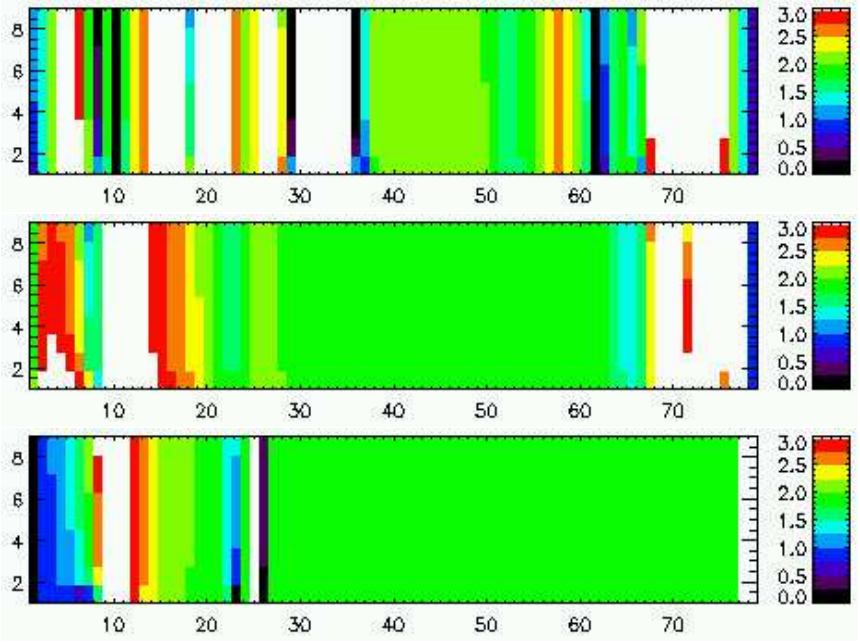

Figure 10.7: Same as Fig. 10.5 but for the case TTC.

which is an advection equation for $D^*/B^{*\theta}$ with velocity v^{*r} at the equator. Since only radial velocities are allowed, it is possible to define a Lagrangian coordinate system, in which the value $D^*/B^{\theta *}$ does not change with time. The easiest way of checking this condition is to calculate $\left[D^*/B^{\theta *}\right](m)$, i.e. as a function of the mass enclosed within a radius r defined as

$$m(r) \equiv 4\pi \int_0^r r'^2 dr' D^*(r'). \tag{10.27}$$

If the magnetic field is correctly evolved with our numerical code, this quantity should remain constant in time.

We perform simulations of spherical collapse in which the above conditions are satisfied. The initial magnetic field is homogeneous as described in Sec-

tion 10.1. The initial equilibrium model for the fluid variables consists of a spherical 4/3-polytrope with central density $\rho_c = 10^{10}$ g cm^{-3}. We induce the collapse by reducing the initial adiabatic index from $\gamma = 4/3$ to $\gamma_1 = 1.28$. As the equation of state stiffens at nuclear matter density (see Chapter 9), the star bounces, a shock forms and travels outward. We calculate the error σ in the collapse phase by applying Eq. (10.19) to the quantity $\left[D^*/B^{\theta *}\right](m)$, assuming that the theoretical value is the initial one. In Fig. 10.8 we show the evolution of the error during the collapse for different linear reconstructions (*minmod* and MC) and for different (r, θ)-grid resolutions (80×10, 300×30, and 400×60). The resulting errors for the MC slope limiter are slightly better than for *minmod*, decreasing in both cases with resolution. In any case the errors are below 1% even for the coarsest grid.

The resolutions employed are the same that will be used in the magnetized core collapse simulations. The cells are equally-spaced in the angular direction, while they are logarithmically spaced in the radial direction, except for the inner 100 radial grid points (in the 300×30, and 400×60 cases), which are equally-spaced. This guaranties sufficient resolution in the region where the proto-neutron star forms. After the shock forms the deviations from the initial profile increase as the order of reconstruction decreases locally to one.

In order to check our numerical code we plot $\left[D^*/B^{\theta *}\right](m)$ in Fig. 10.9, at time $t = 35$ ms, for three different grid resolutions and the *minmod* slope limiter. The initial profile given by the dotted curve. The effect of the travelling shock is seen as a small spike, that becomes narrower as the resolution is increased. On the other hand, deviations from the initial profile occur near the proto-neutron star boundary (where the density exceeds nuclear matter density). We interpret this small effect as a numerical error, as it is reduced when increasing the resolution. This feature also tends to disappear when using the MC slope limiter or the PPM reconstruction. However, we do not include these (still preliminary) results for two reasons: first, Antón et al. (2006), whose numerical scheme we use, performed an extended set of tests for the case of linear reconstruction with *minmod* slope limiter. Since no tests have yet been done for the MC slope limiter, nor with higher order reconstructions, we defer the use of such numerical schemes to a future investigation. Second, we have observed that the use of the MC slope limiter and PPM introduces point to point errors (high frequency noise) close to the center of the proto-neutron star after the bounce, while *minmod* does not. This feature appears even in the

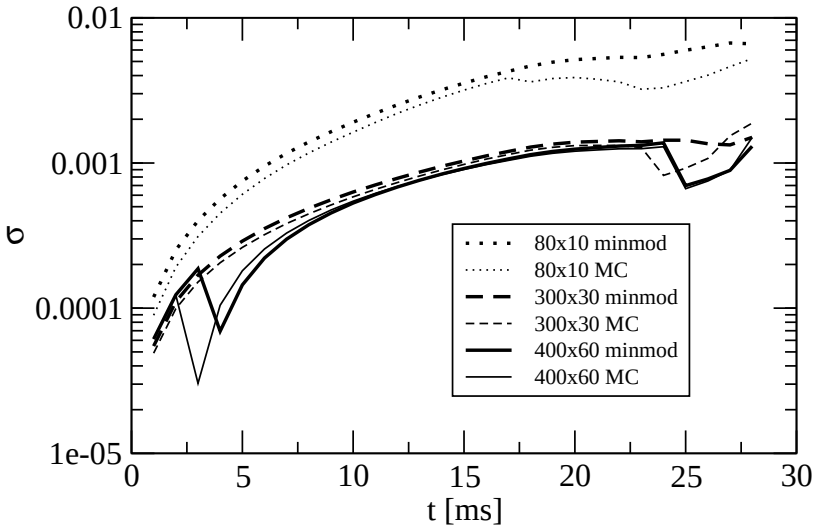

Figure 10.8: Error in the poloidal test (PT) as a function of time, for three different grid resolutions and two different linear reconstructions. Only the infall phase has been considered.

non-magnetized case but tends to dissapear with increasing resolution. In the magnetized case such point to point oscillations translate through the velocities to the magnetic field, which is very sensitive to this kind of noise, i.e. a small error in the velocities is magnified in the magnetic field by the induction equation. Although these effects have to be studied in detail in the future, to try to develop higher order schemes without this pathology, for the present work we have taken the practical decision of using the same approach as Antón et al. (2006) did, namely linear reconstruction with *minmod* slope limiter.

We have performed tests using both the HLL approximate Riemann solver and the KT symmetric scheme, finding almost identical results (in agreement with Lucas-Serrano et al. 2004; Shibata & Font 2005; Antón et al. 2006). As KT gives slightly better results (concerning the point to point error at the center for MC and PPM), we choose this Riemann solver for all our magnetized core collapse simulations discussed next.

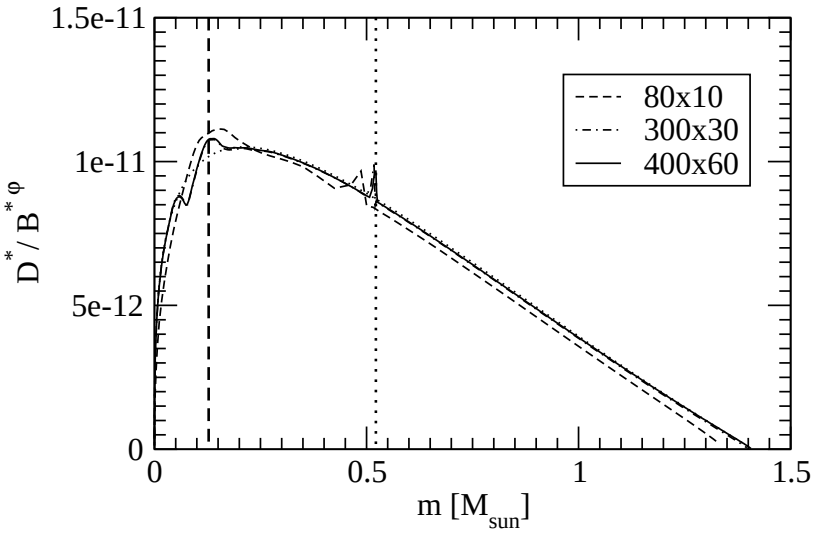

Figure 10.9: The quantity $D^*/B^{\theta *}$ versus m at $t = 35$ ms for the poloidal test (PT). Three different resolutions are plotted, in comparison with the initial value (dotted curve). The location of the proto-neutron star boundary (dashed vertical line) and location of the shock (dotted vertical line) for the highest resolution model are also shown.

10.3 Magnetized core collapse

We present in this section results from simulations of rotational magnetized core collapse to neutron stars. The dynamics of the models we have selected (see Table 10.1) is identical to the dynamics of the non-magnetized ones, since the passive field approximation is used. Therefore, we will not describe once again the morphological features of the hydrodynamics (see Chapter 9). We pay more attention instead to the magnetic field evolution. In all our simulations an initial magnetic field strength of $B_0^* = 10^{10}$ G is considered. As we adopt the passive field approximation, all results given for this magnetic field strength can be rescaled to other values of B_0^* by using the adequate factors. Note however that such rescaling is only valid in the passive approxi-

mation regime, as for strong enough magnetic fields (not considered here), the dynamics of the system wold be affected by magnetic effects.

We perform simulations of both, models labeled D3M0 and T3M0. For the former case the simulations are carried out in two resolutions ($n_r \times n_\theta$): regular resolution with 300×30 zones and high resolution (400×60 zones). In both cases the radial grid is equally spaced for the first 100 points, the first radial cell center being located at 50 m from the origin ($r = 0$). The remaining radial zones are logarithmically spaced to cover the outer parts of the star and the exterior atmosphere. We have checked that regular resolution is sufficient to correctly compute the evolution of the hydrodynamical quantities and of the magnetic field when this has toroidal topology. However, high resolution is needed to achieve similar accuracy in the evolution of the magnetic field with a poloidal component. Since models T3M0 do not have poloidal magnetic field components, we perform simulations only with the regular resolution grid for this case. Unless otherwise mentioned, the results presented belong to simulations with the highest resolution available.

10.3.1 D3M0 models

Fig. 10.10 shows the evolution of the energy parameters for the magnetic field, $\beta_{\rm mag}$, and for the rotational kinetic energy, $\beta_{\rm rot}$. They are defined as the ratio of magnetic energy, $E_{\rm mag}$, and the rotational kinetic energy, $E_{\rm rot}$, to the potential energy, respectively, $E_{\rm pot}$. Each of these energies are calculated in general relativity as:

$$E_{\rm mag} = \int d^3\mathbf{x}\ \frac{W\, b^2}{2}, \tag{10.28}$$

$$E_{\rm rot} = \int d^3\mathbf{x}\ \frac{\alpha\ \hat{v}^\varphi\ S^*_\varphi}{2}, \tag{10.29}$$

$$E_{\rm pot} = M_{\rm grav} - M_{\rm proper} - E_{\rm rot} - E_{\rm mag}, \tag{10.30}$$

where $M_{\rm grav}$ is the gravitational mass, and $M_{\rm proper}$ the proper mass.

The evolution of $\beta_{\rm rot}$ and $\beta_{\rm mag}$ allows us to quantify the amount by which rotation and magnetic fields would affect the dynamics of the system. Effects due to high $\beta_{\rm rot}$ are discussed later in the thesis, in Chapter 12. As the magnetic fields considered are weak enough not to affect the dynamics, the

resulting $\beta_{\rm mag}$ is much less than unity. In order to analyze the growth of the magnetic field, we separate the effect of the different components of the magnetic field into β_φ, for the toroidal component, and $\beta_{\rm polo} = \beta_{\rm mag} - \beta_\varphi$, for the poloidal component. As the collapse proceeds, the magnetic field grows by at least two reasons [1]. First, the radial flow compresses the magnetic field lines, amplifying the existing poloidal and toroidal magnetic field components. We call this effect *radial compression*, hereafter. Second, during the collapse of a rotating star differential rotation is produced, even for rigidly rotating initial models (as A1B3G3-D3M0 or A1B3G5-D3M0). Hence, if a seed poloidal field exists, the Ω-dynamo process acts (see Section 10.1) winding up poloidal field lines into the toroidal component. This amplification process generates a toroidal magnetic field component, even from purely poloidal initial configurations. We note, however, that the conversion of toroidal magnetic field lines back into poloidal components by means of the α-Ω-dynamo (Spruit 1999) is not possible in our simulations, since this is a three-dimensional effect and our simulations are axisymmetric. The toroidal component of the magnetic field is affected by the two effects, namely by the radial compression and the by Ω-dynamo, while the poloidal field is only amplified by the first effect. Thus, even if the initial magnetic field configuration is purely poloidal, the toroidal component dominates after some dynamical time. This effect can be seen in Fig. 10.10 as β_φ (dashed line) grows much faster than $\beta_{\rm polo}$ before the time of bounce.

The general features of the amplification of the magnetic field during the collapse and its posterior evolution are described next. As nuclear matter density is reached, the star bounces back forming a shock wave propagating outwards, and leaving the newly formed proto-neutron star behind. At this time, the radial compression of the magnetic field lines stops, and the Ω-dynamo process dominates the amplification of the magnetic field. Hence, $\beta_{\rm polo}$ almost stops growing, only a small growth can be seen due to the accretion of material onto the central regions. In model A4B5G5-D3M0 (Fig. 10.10, lower panel), $\beta_{\rm polo}$ decreases after the bounce, becoming nearly constant thereafter due to a small re-expansion of the star prior to reach a final quasi-equilibrium state. On the other hand β_φ keeps growing after bounce because the Ω-dynamo contin-

[1] See, however, Section 10.3.4 for a discussion of the possible influence of the magneto-rotational instability in the magnetic field amplification process.

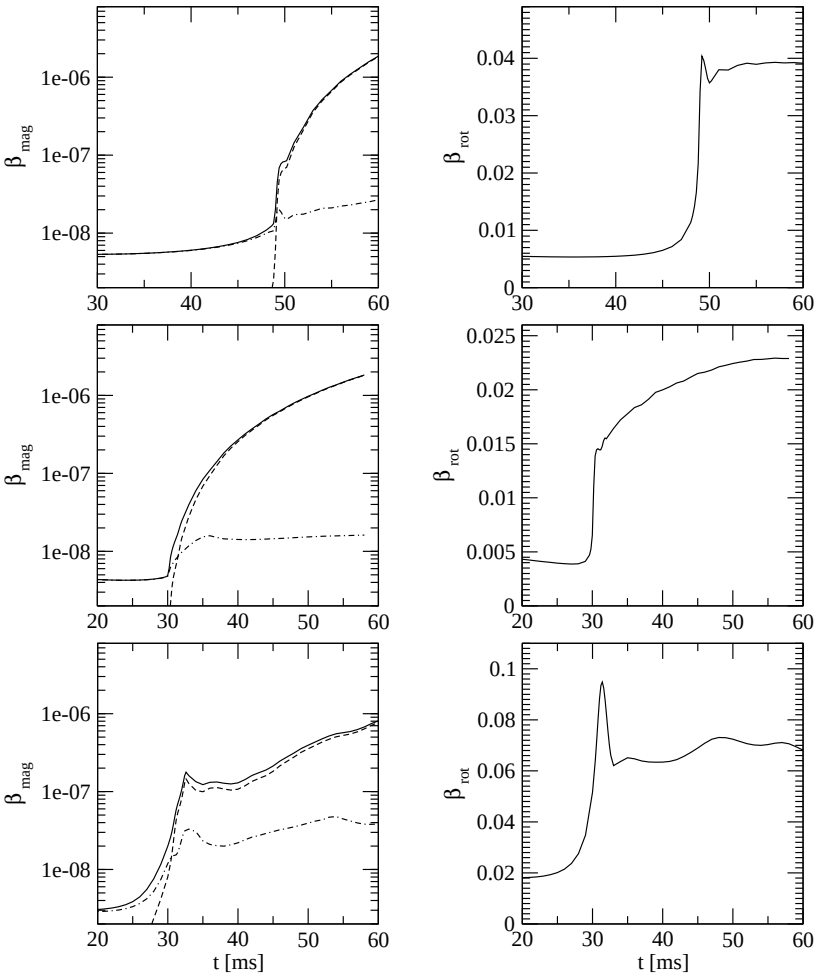

Figure 10.10: Time evolution of the energy parameters for models A1B3G3-D3M0 (upper panels) and A1B3G5-D3M0 (lower panels). The left panels show the evolution of the magnetic energy parameters $\beta_{\rm mag}$ (solid line), β_{φ} (dashed line), and $\beta_{\rm polo}$ (doted-dashed line), and the right panels show the evolution of the rotational energy parameter $\beta_{\rm rot}$.

Table 10.3: Values of the poloidal magnetic field component, $|B|_{\rm polo}$, the toroidal component, $|B|_\varphi$, and the energy parameters, $\beta_{\rm rot}$, $\beta_{\rm mag}$ and β_φ, at the time of bounce, $t_{\rm b}$, for all models studied.

Model	$\lvert B\rvert^{\rm b}_{\rm polo}$ (10^{10} G)	$\lvert B\rvert^{\rm b}_{\varphi}$ (10^{10} G)	$\beta^{\rm b}_{\rm rot}$ (10^{-2})	$\beta^{\rm b}_{\rm mag}$ (10^{-8})	$\beta^{\rm b}_{\varphi}$ (10^{-8})
A1B3G3-D3M0	1727	4878	4.0	3.2	1.8
A1B3G5-D3M0	1259	1328	1.4	0.83	0.21
A4B5G5-D3M0	1244	3488	9.5	6.9	5.3
A1B3G3-T3M0	0	1597	4.0	0.36	0.36
A1B3G5-T3M0	0	1411	1.4	0.6	0.6

ues winding up the existing poloidal magnetic field, becoming the dominating amplification process of the magnetic field in the star. To simplify the interpretation of the results we proceed first to describe the time evolution of the different models in the equatorial plane, and describe the more complex morphology of the magnetic field in the r-θ plane afterwards. Animations of all simulations performed can be found on the CD.

Models A1B3G3-D3M0 and A1B3G5-D3M0 have identical initial data for the hydrodynamics and magnetic field, differing only in the value of γ_1. Therefore, significant differences occur in the collapse. Model A1B3G3-D3M0 collapses slower (bounce at $t = 49.04$ ms) than model A1B3G5-D3M0, bouncing at $t = 30.24$. In the first model, the Ω-dynamo acts for a longer time and hence, the toroidal magnetic field component at the time of bounce is about an order of magnitude larger at the equator ($\sim 4 \times 10^{13}$ G at maximum) than in the rapidly collapsing one (thick-dashed lines in the upper panels of Figs. 10.11 and 10.12). As the poloidal component of the magnetic field is amplified only by the compression of the magnetic field lines, similar values of this component are found at the time of bounce in both models (thin-dashed lines), because similar maximum densities are reached in the collapse. Detailed values for these quantities at bounce can be found in Table 10.3. The distribution of the magnetic field in the equatorial plane is also similar for both models. While most of the poloidal component of the magnetic field is confined to the inner region, inside the radius at which the shock is formed, the toroidal field

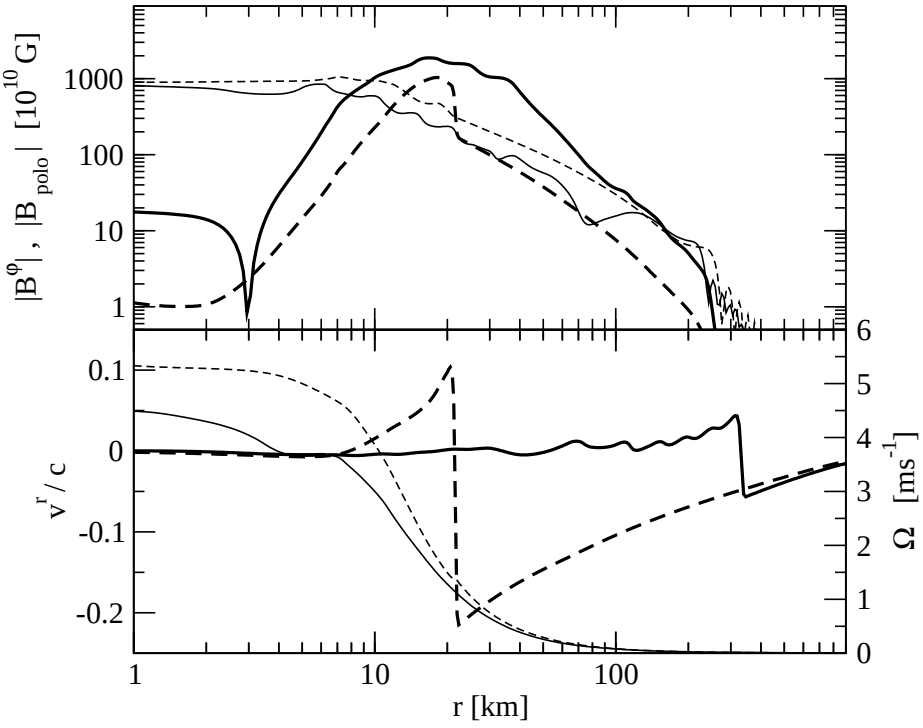

Figure 10.11: Radial profiles along the equator for model A1B3G3-D3M0. Depicted are the poloidal magnetic field, $|B_{\rm polo}|$ (thin lines in the upper panel), the toroidal component, $|B^{\varphi}|$ (thick lines in upper panel), the radial velocity, v^r (thick lines in lower panel), and the angular velocity, Ω, (thin lines in lower panel). The dashed lines represent these quantities at the time of bounce, $t_{\rm b} = 49$ ms, and the solid lines at the end of the simulation, $t = 60$ ms.

reaches its largest value in the region where the angular velocity gradients are larger, i.e. where the shock forms. This structure is crucial for the posterior amplification of the toroidal field via the Ω-dynamo. Due to Eq. (10.7), the amplification is more effective where the Ω gradients and the poloidal field are stronger, i.e. at the outer layers of the newly formed proto-neutron star (thick

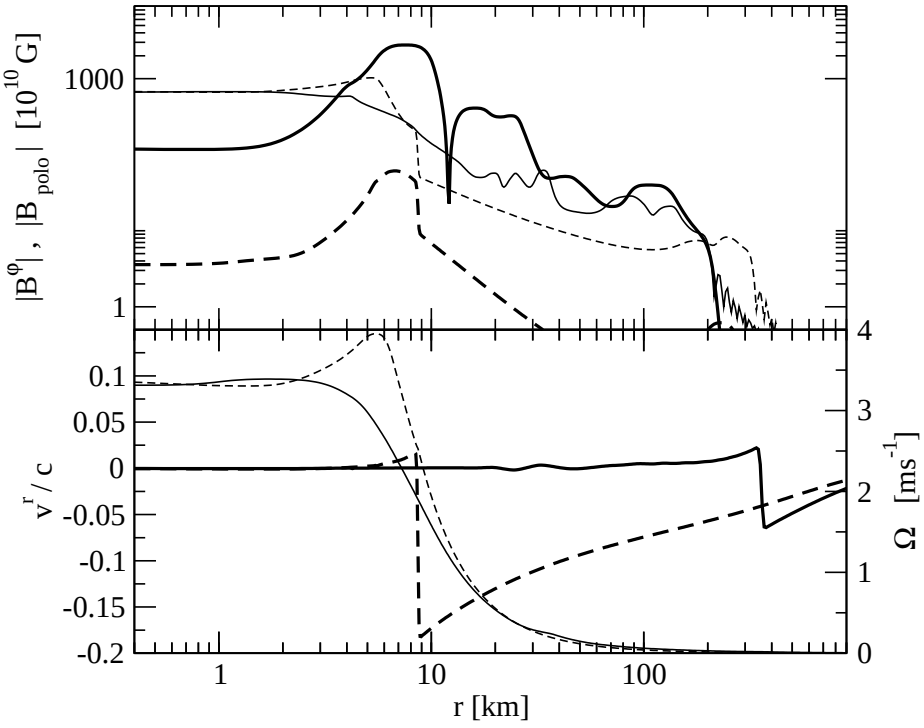

Figure 10.12: Same as Fig. 10.11 but for model A1B3G5-D3M0.

solid lines) extending from the location of the shock formation ($r \approx 10$ km), to the outer edge of the PNS ($r \approx 50$ km). Outside this region the poloidal field is too weak to generate strong toroidal fields. In the inner ~ 10 km, the angular velocity is approximately constant, and the amplification becomes slower.

The full structure of the magnetic field for models A1B3G3-D3M0 and A1B3G5-D3M0 can be seen in Figs 10.13-10.18. The general trends already discussed for the equatorial plane profiles are also followed in the r-θ plane. At the time of bounce, the initial poloidal configuration of the magnetic field (see Fig. 10.2) is highly distorted by the radial compression of the magnetic field

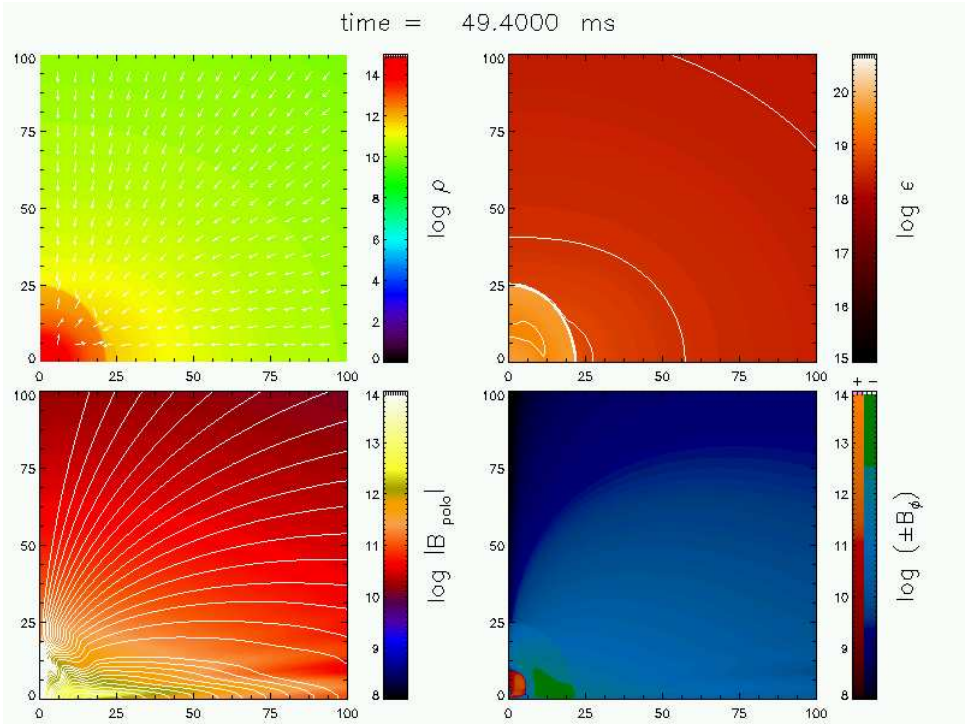

Figure 10.13: Configuration of the inner region of the star near the time of bounce, $t = 49.4$ ms, for model A1B3G3-D3M0. The upper left panel shows the logarithm of density, $\log \rho$, in g cm^{-3} (color coded), and the distribution of the velocity field, v^i (white arrows). The upper right panel shows the logarithm of the specific internal energy, $\log \epsilon$, in erg (color coded and contours). The lower left panel shows the logarithm of the poloidal component of the magnetic field, $\log |B_{\rm polo}|$, in G (color coded), and the magnetic field lines in the r-θ plane (lines). The lower right panel shows the logarithm of the toroidal component of the magnetic field, $\log |B^\varphi|$, in G (color coded). All axes are given in km.

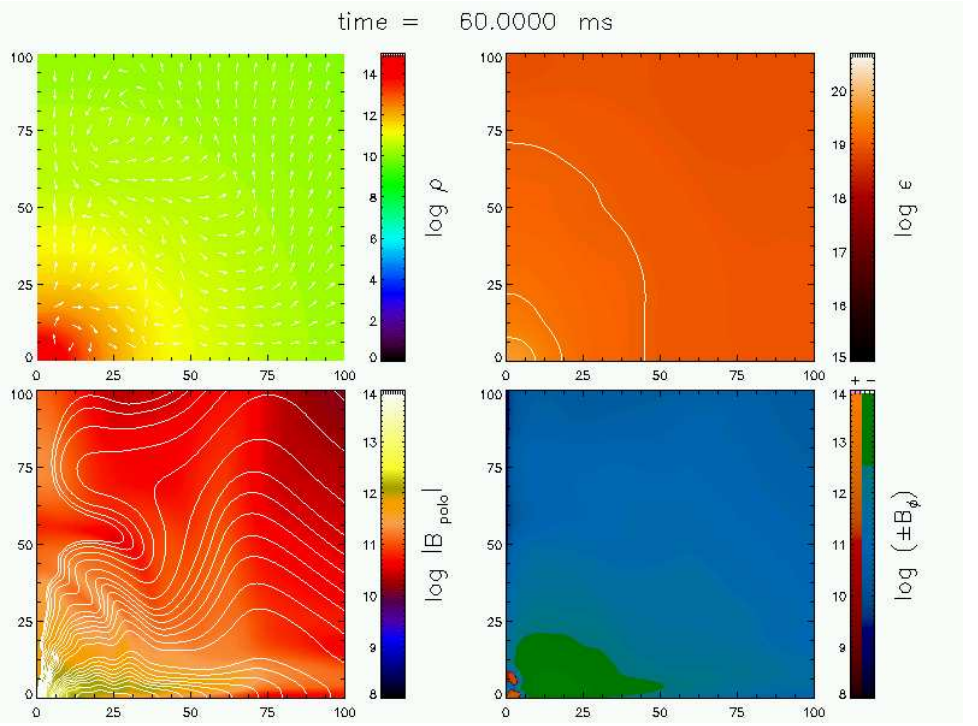

Figure 10.14: Same as Fig 10.13 but for model A1B3G3-D3M0 at the end of the simulation, $t = 60$ ms.

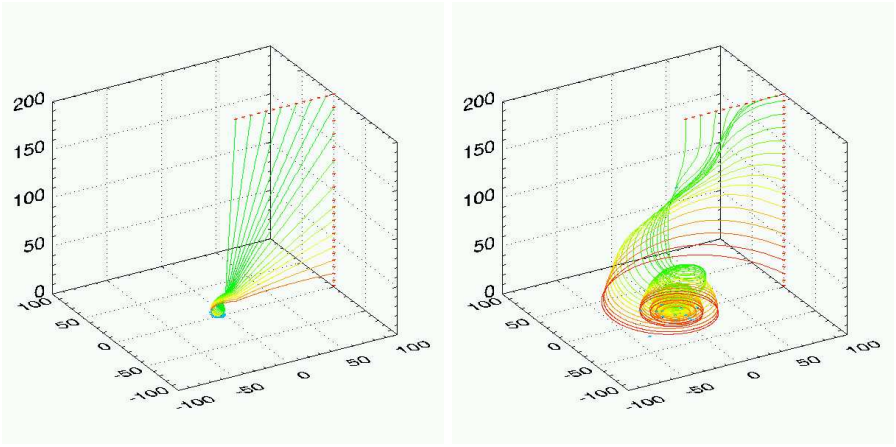

Figure 10.15: Magnetic field lines for model A1B3G3-D3M0 near the time of bounce, $t = 49$ ms (left panel), and at the end of the simulation, $t = 60$ ms (right panel). The box represents the region above the equatorial plane, and the axes are in km.

lines (see Figs. 10.13 and 10.16), while a toroidal component has been formed surrounding the inner core. The shock wave travelling otwards can be seen in the hydrodynamical quantities and in the magnetic field components. Until the end of the simulation (see Figs. 10.14 and 10.17) the toroidal component of the magnetic field is mostly confined to the outer layers of the PNS, while the inner region is dominated by the poloidal component. In model A1B3G5-D3M0 the configuration of the toroidal field is more compact than in model A1B3G3-D3M0, as inferred from the color coding. The distribution of the velocity field shows that convective motions occur outside the innermost regions and near the pole. These meridional flows are responsible for the winding of the poloidal magnetic field in the r-θ plane, especially in model A1B3G5-D3M0. As a consequence, the drastic change of direction of the poloidal field in this region makes the product $\vec{B}^* \cdot \hat{\nabla}\Omega^*$ in Eq. (10.7) to change its sign. Hence, for model A1B3G5-D3M0, the Ω-dynamo produces a change in the sign of the toroidal magnetic field in this thin shell, $B^\varphi > 0$, surrounded by toroidal field in the usual direction, $B^\varphi < 0$. Until the end of the simulation ($t = 60$

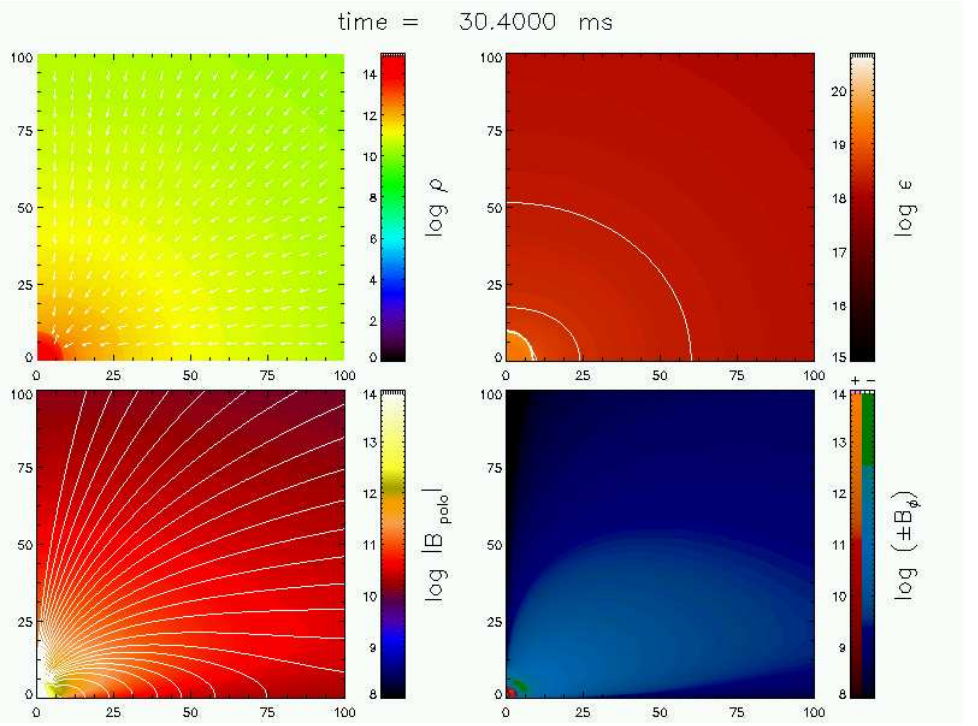

Figure 10.16: Same as Fig 10.13 but for model A1B3G5-D3M0 near the time of the bounce, $t = 30.4$ ms.

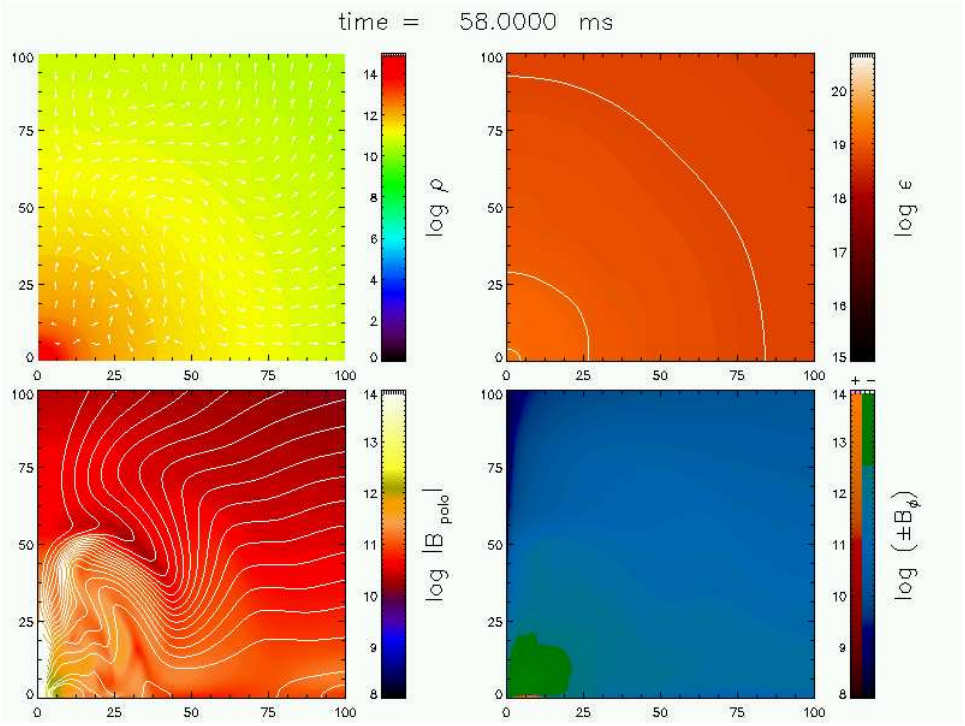

Figure 10.17: Same as Fig 10.13 but for model A1B3G5-D3M0 at the end of the simulation, $t = 58$ ms.

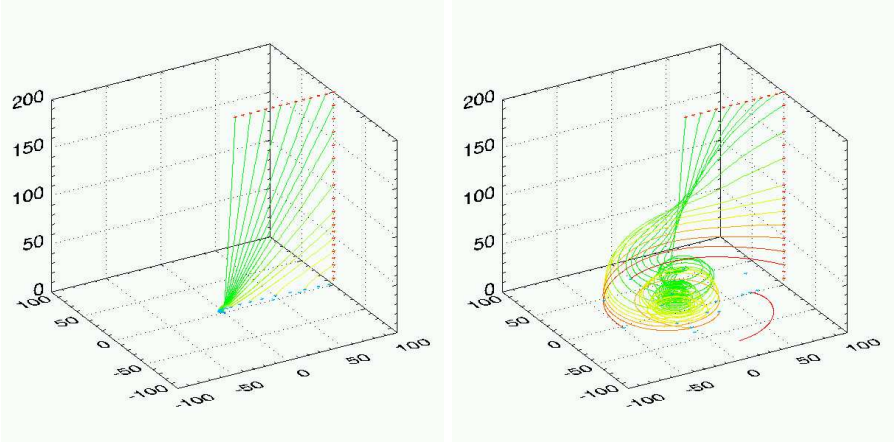

Figure 10.18: Same as Fig. 10.15, but for model A1B3G5-D3M0 near the time of bounce, $t = 30.4$ ms (left panel), and at the end of the simulation, $t = 58$ ms (right panel).

ms), this configuration is maintained, resulting in a linear amplification of the toroidal magnetic field in this region. The three-dimensional structure of the magnetic field lines has been computed and is shown in Figs. 10.15 and 10.18. The magnetic field lines have been calculated by integrating the equation

$$\frac{d\vec{x}}{d\lambda} = \frac{\vec{B}}{|\vec{B}|}, \tag{10.31}$$

where $\vec{x}(\lambda)$ is the equation of the line as a function of the parameter λ. In spherical coordinates this equation reads,

$$\frac{dr}{d\lambda} = \frac{B^r}{|\vec{B}|}, \qquad \frac{d\theta}{d\lambda} = \frac{1}{r}\frac{B^\theta}{|\vec{B}|}, \qquad \frac{d\varphi}{d\lambda} = \frac{1}{r\sin\theta}\frac{B^\varphi}{|\vec{B}|}. \tag{10.32}$$

We first select the domain in which we want to calculate the lines (box in Figs. 10.15 and 10.18), and then we integrate the equations from the outer limits of the box at $\varphi = 0$ (red dots in CD animations), to the points at

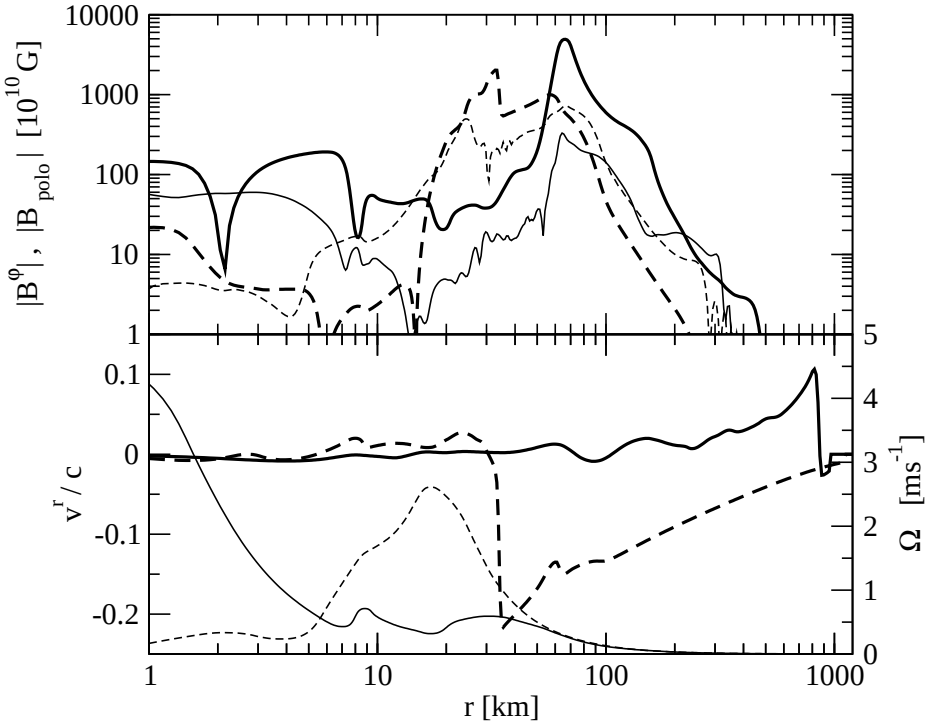

Figure 10.19: Same as Fig. 10.11 but for model A4B5G5-D3M0.

which lines leave the box (blue dots). It can be seen that outside the PNS the magnetic field is approximately poloidal while a shell of entwined toroidal field lines forms formed around the inner core of the PNS. The poloidal structure of the innermost region can not be seen in these figures because the shell hides the interior. Simulations covering a longer time interval are needed to establish whether this configuration is stable, or whether it is a transient.

Model A4B5G5-D3M0 rotates faster initially than the models previously described, and is also differentially rotating initially. Therefore, the Ω-dynamo is stronger, and, for a similar collapsing time as model A1B3G5-D3M0, the re-

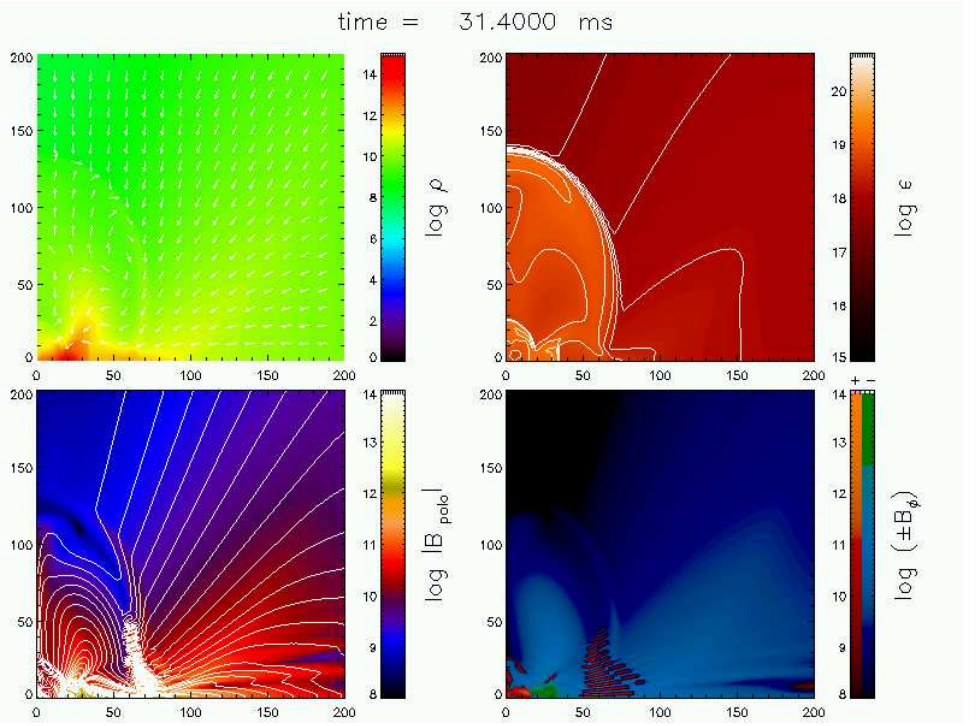

Figure 10.20: Same as Fig 10.13 but for model A4B5G5-D3M0 near the time of the bounce, $t = 31.4$ ms.

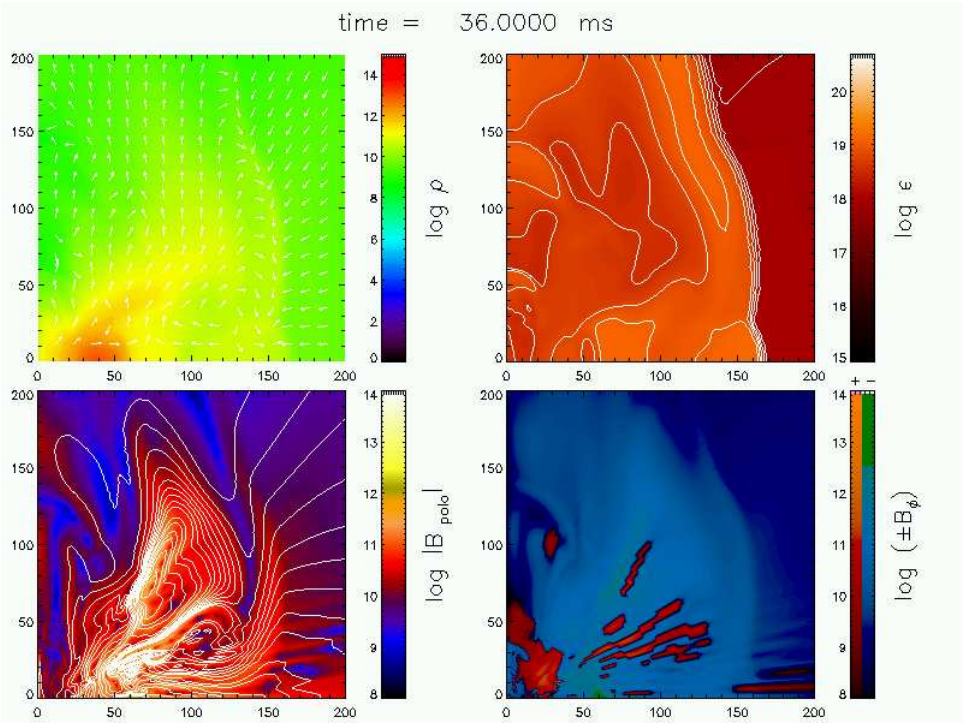

Figure 10.21: Same as Fig 10.13 but for model A4B5G5-D3M0 at time $t = 36$ ms.

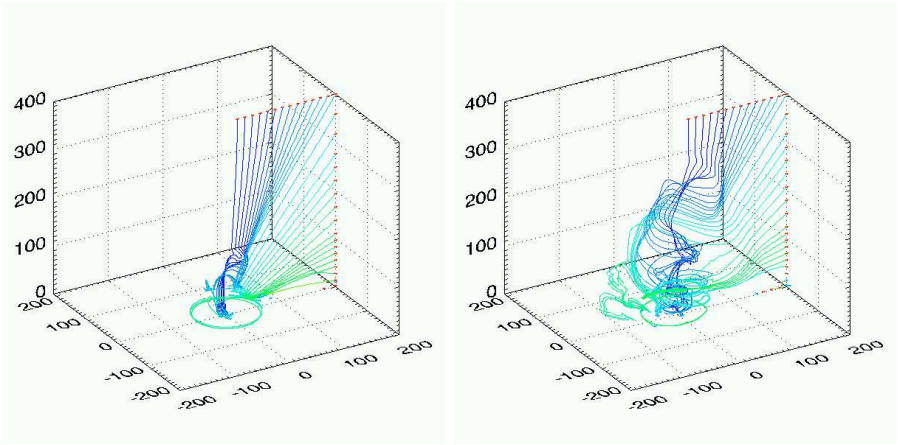

Figure 10.22: Same as Fig. 10.15, but for model A4B5G5-D3M0 near the time of bounce, $t = 31.4$ ms (left panel), and at time $t = 36$ ms (right panel).

sulting toroidal component of the magnetic field is about an order of magnitude larger at the equator (see the thick-dashed line in the upper panel of Fig. 10.19), even though the radial compression effect is weaker in this case, since the collapse is stopped at densities below nuclear matter density. The distribution of the magnetic field in the equatorial plane (see Fig 10.19) is completely different to the distribution of models A1B3G3-D3M0 and A1B3G5-D3M0. In model A4B5G5-D3M0 the matter distribution at the time of bounce reaches its maximum off center, due to the strong centrifugal forces acting on it. Both, the poloidal and toroidal magnetic field components at the time of bounce are not confined inside the shock location, at a distance of about 30 km from the center, but they extend outside to more than 100 km. As the shock travels outwards, the magnetic field is transported with the shock spreading it. In the inner "hole" of the toroidal-like configuration of the star (the innermost 10 km at the time of bounce) the magnetic field is very weak, since no matter flows have transported any magnetic field lines into this region and the Ω-dynamo does not act efficiently in such low-poloidal field regions. After the shock formation, the quasi-toroidal star re-expands and settles down in a quasi sta-

tionary equilibrium the maximum density being located at about 45 km. This state is reached after a couple of bounces which are strongly damped by the surrounding material. Angular momentum and magnetic field are transported in the innermost region during bounce, producing a region with high angular velocity (see the thin-solid line in the lower panel of Fig. 10.19). This leads finally to an amplification of the poloidal magnetic field via the Ω-dynamo in the inner region and in the outer layers of the star. As the final maximum densities reached for this model are smaller than in models A1B3G3-D3M0 and A1B3G5-D3M0, the final rotation rates are also smaller producing a smaller amplification.

The structure of model A4B5G5-D3M0 in the r-θ plane (see Figs. 10.20 and 10.21) is far more complicated than in the previous cases. The strongest magnetic field is reached outside the shock location at the time of bounce (see Fig 10.20), the shock dragging the magnetic field along its path. Near the rotation axis, the matter falls nearly parallel to the axis, while off the axis, the post-shock flow is in almost perpendicular direction, i.e. away from the axis (see the upper left panel of Fig 10.20). This flow twists the field lines in the r-θ plane in a similar way as convection does in model A1B3G5-D3M0. As a consequence similar regions with positive toroidal magnetic field are formed (see Fig 10.21). The three-dimensional structure of magnetic field lines is shown in Fig. 10.22. It consists of a series of windings and twists of the magnetic field lines by the action of the Ω-dynamo and the meridional flows, respectively. Note that in these regions, the magnetic field has large variations in small scales, and therefore finite conductivity effects such as field line reconnection colud be necessary, since the magnetic diffusion term in the evolution equation for the magnetic field is proportional to $\nabla^2 \vec{B}$. Close to the equatorial plane there exist regions where the magnetic field is almost purely toroidal, and hence circular closed lines can be found.

The models of this series, A1B3G3-D3M0, A1B3G5-D3M0 and A4B5G5-D3M0, can be compared with models A1B3G3-D3M10, A1B3G5-D3M10 and A4B5G5-D3M10, respectively, of Obergaulinger et al. (2005) who have recently performed a comprehensive parameter study of magnetized rotational core collapse in Newtonian gravity and MHD. Since we use the passive approximation, the comparison can only be done with the low magnetic field models of Obergaulinger et al. (2005), namely their "M10" models. In general, both sets of models show similar qualitative behavior, although some differences are

Table 10.4: Values of the energy parameter for the magnetic field, $\beta_{\rm mag}^{\rm N}$, at the time t reported in table D.1 of Obergaulinger et al. (2005), compared with the corresponding values for CFC, $\beta_{\rm mag}^{\rm CFC}$ at the same time.

Model	t (ms)	$\beta_{\rm mag}^{\rm N}$ (10^{-6})	$\beta_{\rm mag}^{\rm CFC}$ (10^{-6})
A1B3G3-D3M10	66.16	20.0	4.0
A1B3G5-D3M10	48.33	1.8	0.8
A4B5G5-D3M10	64.00	3.3	1.0

found. As shown by Dimmelmeier et al. (2002b) in purely hydrodynamical core collapse simulations, the main difference between using CFC and Newtonian gravity is that higher densities are reached in the former case and thus, higher rotation rates. Our magneto-rotational collapse simulations show that the magnetic field structure is very similar, although the values reached for $\beta_{\rm mag}$ are smaller for the CFC case (compare Fig. 10.10 with Fig. 3 in Obergaulinger et al. (2005)). In Table 10.4 we compare the values of $\beta_{\rm mag}$ at the time t reported in Table D.1 of the Newtonian simulations of Obergaulinger et al. (2005) with our results in the CFC approximation. Note that for models A1B3G3-D3M10 and A4B3G5-D3M10 we have no data for that time, and the values correspond to an extrapolation using the fit of Section 10.3.5. Very recently Obergaulinger et al. (2006) have performed numerical simulations of the same models but using a modified Newtonian potential which mimics general relativistic effects (TOV models hereafter). From all our performed simulations only model A1B3G3-D3M0 has its correspondence in TOV gravity (A1B3G3-D3M10-T). Their result for the energy parameter of the magnetic field at $t = 85.1$ ms is $\beta_{\rm mag}^{\rm TOV} = 10^{-4}$ (extracted from Obergaulinger et al. (2006)) while our result for the same time (extrapolated) is $\beta_{\rm mag}^{\rm CFC} = 1.68 \times 10^{-5}$. Since our comparison is restricted to a single model further investigation is needed to asses whether the smaller values attained for $\beta_{\rm mag}$ in CFC compared with TOV and Newtonian gravity is a general trend.

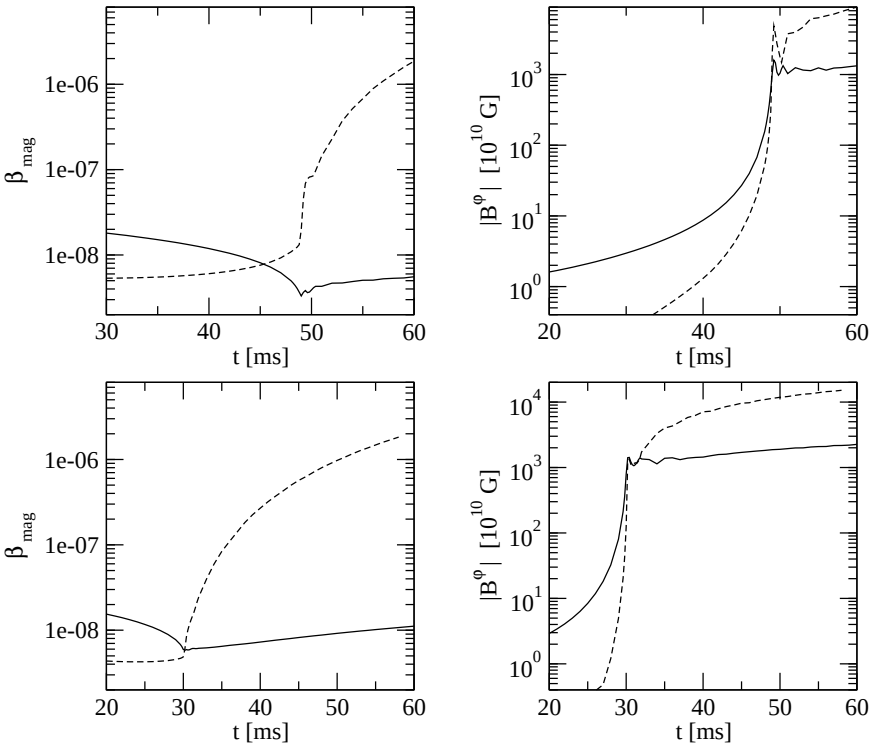

Figure 10.23: Time evolution of $\beta_{\rm mag}$ (left panels) and of the maximum poloidal magnetic field, $|B^{\varphi}|$ (right panels), for models A1B3G3-T3M0 (upper panels) and A1B3G5-T3M0 (lower panels). These graphics are depicted in solid lines. Overplotted with dashed lines are the corresponding values for models A1B3G3-D3M0 (upper panels) and A1B3G5-D3M0 (lower panels).

10.3.2 T3M0 models

The time evolution of $\beta_{\rm mag}$ for models A1B3G3-T3M0 and A1B3G5-T3M0 is presented in Fig. 10.23. In order to get a better understanding of the evolution of the magnetic field in these models, the evolution of the maximum value for

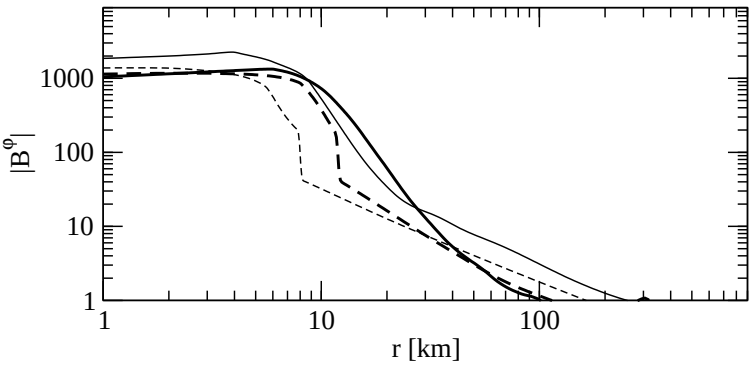

Figure 10.24: Radial profiles of the toroidal magnetic field, $|B^{\varphi}|$ for models A1B3G3-T3M0 (thin lines) and A1B3G5-T3M0 (thick lines). Dashed lines depict those quantities near the time of bounce while solid lines correspond to the end of the simulation.

the magnetic field is also presented. To this end we compare these models, which initially have a purely toroidal magnetic field, with their counterparts with initial poloidal magnetic fields (A1B3G3-D3M0 and A1B3G5-D3M0). As no poloidal field is present in the T3M0 models, toroidal fields can not be amplified via the Ω-dynamo. Furthermore, since we impose axisymmetry, no poloidal field can be formed along the evolution, and thus the toroidal component of the magnetic field is the only one evolving. The only amplification process in the collapse is the radial compression of the field lines. This mechanism is much slower than the Ω-dynamo and thus, the toroidal magnetic field at the time of bounce is larger in the D3M0 models than in the T3M0 models, despite the fact that D3M0 models do not have a toroidal component initially. The fraction of magnetic energy in models T3M0 decreases during the collapse as the magnetic energy grows slower than the potential energy. As a consequence, although the magnetic field grows, the final PNS is "less magnetized" than its progenitor, i.e. the effects of the magnetic field on the dynamics become smaller in a collapse if the only amplification mechanism is the radial compression.

At the time of bounce most of the toroidal field is confined to the inner region, inside the shock location (see Fig. 10.24). This is very similar to

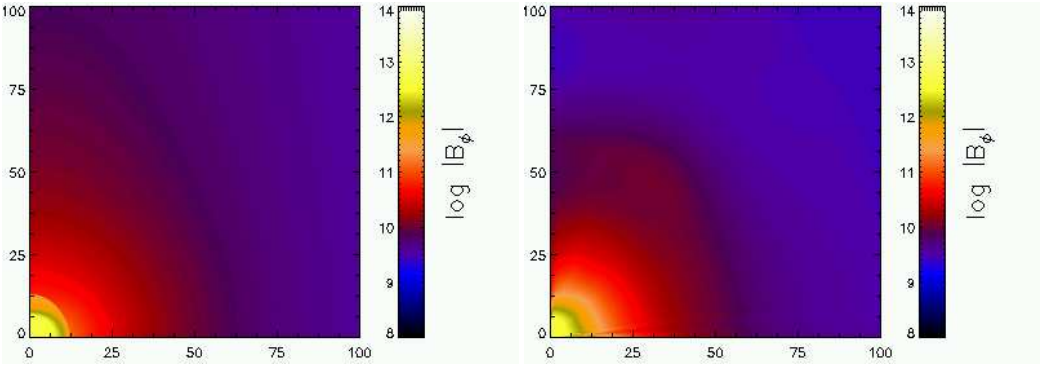

Figure 10.25: Logarithm of the toroidal magnetic field for model A1B3G3-T3M0 near the time of bounce, $t = 49.4$ ms (left panel), and at the end of the simulation, $t = 60$ ms (right panel).

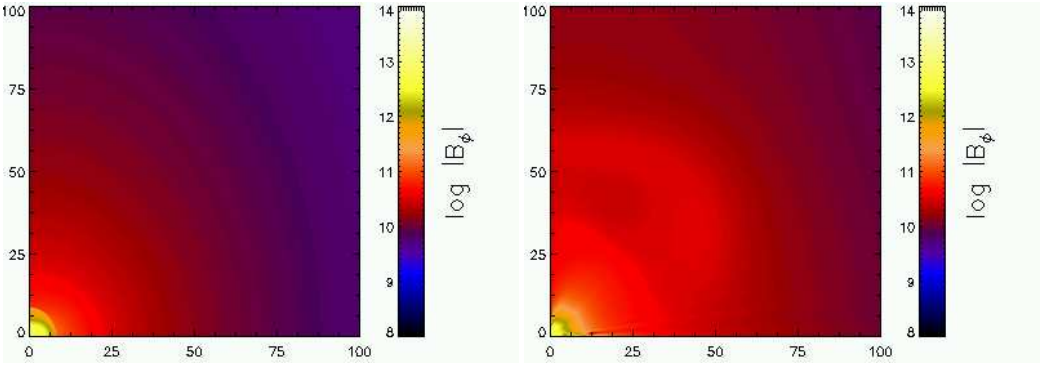

Figure 10.26: Logarithm of the toroidal magnetic field for model A1B3G5-T3M0 near the time of bounce, $t = 30.4$ ms (left panel), and at the end of the simulation, $t = 58$ ms (right panel).

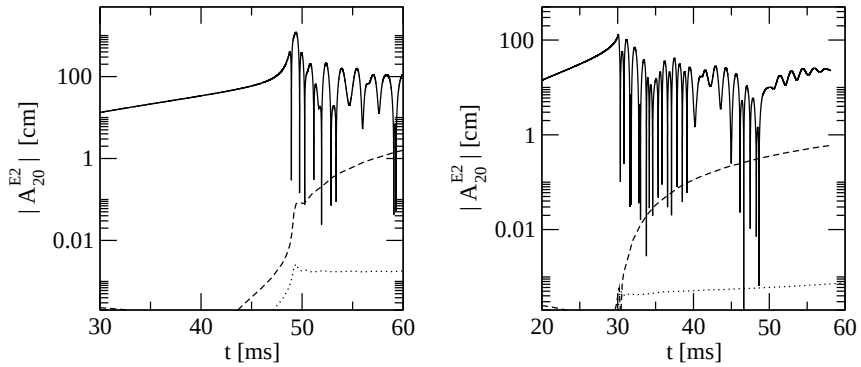

Figure 10.27: Absolute value of the gravitational wave amplitude A_{20}^{E2} (solid line) for models A1B3G3-D3M0/T3M0 (left panel) and A1B3G5-D3M0/T3M0 (right panel). For the low magnetic field strengths considered, the magnetic contribution in the waveform is negligible, and the signals of both series D3M0 and T3M0 coincide with the pure hydrodynamical waveform. For clarity, the magnetic component of the waveform, $A_{20\,\mathrm{mag}}^{\mathrm{E2}}$, is also plotted for models A1B3G3-D3M0 (left panel, dashed line), A1B3G3-T3M0 (left panel, dotted line), A1B3G5-D3M0 (right panel, dashed line), and A1B3G5-T3M0 (right panel, dotted line).

what happens for the poloidal field in models D3M0, as in both cases the only amplification process at work (in the passive approximation) is the radial compression. As the shock propagates outward, the toroidal field remains in the inner core, yielding the final quasi-equilibrium state. Only a small growth of the magnetic field can be seen, as the accreting material transports magnetic field onto the proto-neutron star. As the potential energy does not grow in the quasi-equilibrium, the growth of the magnetic field leads to a slow growth of β_{mag}. Figs. 10.25 and 10.26 display the strength of the toroidal magnetic field, $|B^{\varphi}|$ in the r-θ plane for both T3M0. At the time the shock forms, a jump in the magnetic field appears (left panels) which propagates outwards. The final state (right panels) is almost stationary, most of the magnetic field being concentrated in the innermost region of the star.

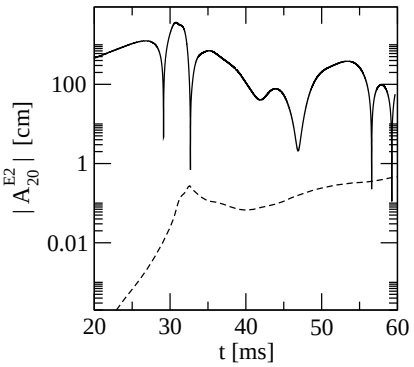

Figure 10.28: Absolute value of the gravitational wave amplitude $A^{\rm E2}_{20}$ (solid line) for model A4B5G5-D3M0, and the corresponding magnetic component of the waveform, $A^{\rm E2}_{20\,\rm mag}$ (dashed line).

10.3.3 Gravitational waves

We calculate the gravitational wave output from our CFC magnetized core collapse simulations using the Newtonian quadrupole formula given in Eq. (6.16) which includes the magnetic terms. In order to understand how the magnetic field affects the waveforms, we have also computed the component corresponding to the magnetic field, $A^{E2}_{20\,\rm mag}$, separately. The resulting waveforms can be found in Figs. 10.27 and 10.28. As the magnetic field is very low, $b^2 \ll \rho$, therefore the magnetic component of the gravitational wave is several orders of magnitude smaller than the total one.

After bounce, the star reaches a quasi-equilibrium state, and thus, the hydrodynamic component of the waveform decreases. At the same time, for models D3M0, the magnetic field increases linearly with time. Such behaviour in the magnetic field produces a signal that grows with time. However, at the end of the simulation, the magnetic field component of the waveform is still negligible in comparison with the hydrodynamical component. It is expected that at later times, as the amplification of the magnetic field reaches saturation, the effects on the waveform become significant, due to the changes in the dynamics and due to the effect of the magnetic field itself [2]. For models T3M0, on the other hand, the magnetic field component of the waveform is even

[2] We note that the effect of the MRI, discussed in the next section, may lead to noticeable changes in the waveforms, as it is the most efficient mechanism to amplify the magnetic field.

smaller than for the D3M0 models. This is due to the inefficient amplification of the magnetic field via the radial compression. After bounce, the magnetic component of the waveforms in models T3M0 does not grow, and hence it is not expected to dominate the waveform later in the evolution, unless other processes amplificating the magnetic field are present.

10.3.4 Magneto-rotational instability

The magneto-rotational instability (MRI) is a shear instability that generates turbulence and an amplification of the magnetic field in rotating magnetized plasma (Balbus & Hawley 1991, 1992), transporting angular momentum in the star. In this section we analyze whether the magnetized collapse models studied in this thesis are susceptible of developing such an instability. If one neglects buoyancy effects, *and* the magnetic field strength is very low, as in our case, then the condition for the instability to occur, in the Newtonian limit, is (Balbus & Hawley 1991):

$$\frac{d\Omega^2}{d\ln\varpi} < 0. \tag{10.33}$$

If this condition is fulfilled, *and* the magnetic field has a poloidal component, the instability grows exponentially in time. The time-scale of the fastest growing unstable mode is

$$\tau_{\rm MRI} = 4\pi \left| \frac{d\Omega}{d\ln\varpi} \right|^{-1}, \tag{10.34}$$

which is independent of the magnetic field configuration and strength. The instability saturates when the magnetic field energy is of the order of the rotational energy (Akiyama et al. 2003), i.e. at similar saturation value, $B^{\varphi}_{\rm sat}$, as for the Ω-dynamo (see below).

As the MRI needs a back reaction of the magnetic field onto the dynamics, we cannot study this effect in our simulations within the passive field approximation. Nevertheless, in order to estimate how this effect could change our results if it were taken into account, we have determined the regions where the condition (10.33) if fulfilled. Inside these regions we calculate the timescale of the fastest growing mode. In Fig. 10.29 we show the results for the D3M0 models. During the collapse, there appear regions near the rotation axis where the MRI is possible, but as the timescales are much larger (> 10 s) than the

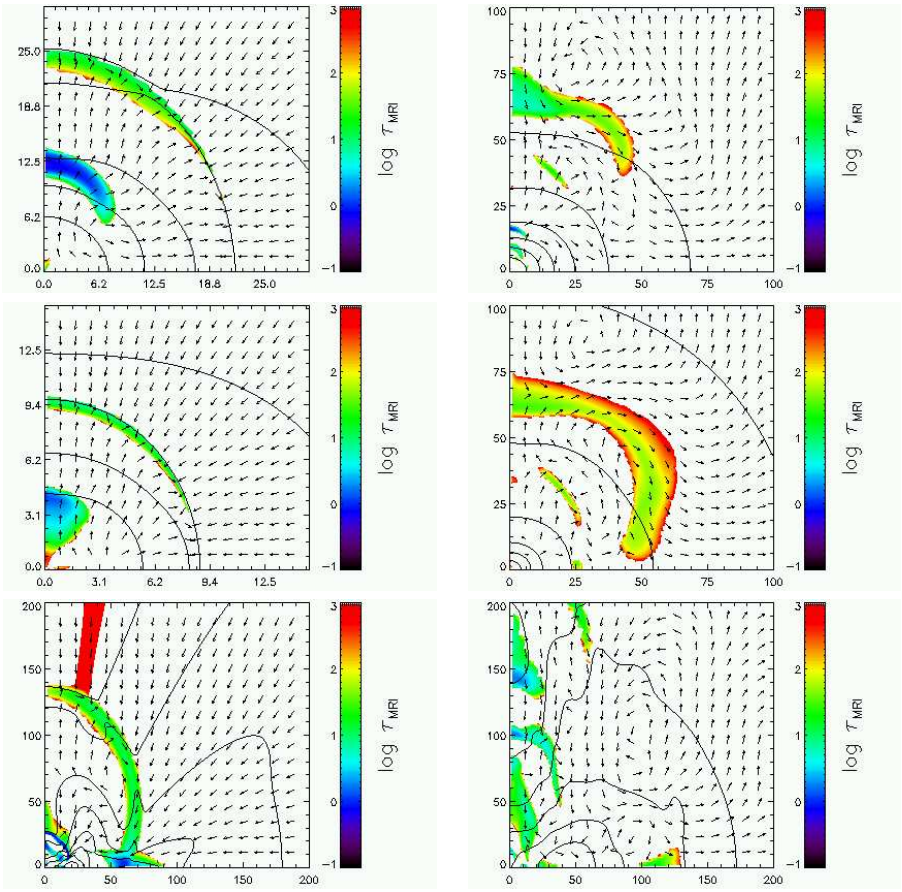

Figure 10.29: Magneto-rotational instability in models A1B3G3-D3M0 (upper panels), A1B3G5-D3M0 (middle panels) and A4B5G5-D3M0 (lower panels), near the time of bounce (t = 49.4 ms, t = 30.4 ms and t = 31.4 ms respectively; left panels), and at the end of the simulation (t = 60.0 ms, t = 58.0 ms and t = 60.0 ms respectively; right panels). Color coded is the logarithm of $\tau_{\rm MRI}$, the time scale of the fastest growing mode, in ms. Depicted in white are the regions where the MRI condition is not fulfilled or $\tau_{\rm MRI} > 1$ s. Arrows indicate the velocity field, and the contours the rest-mass density. All axes are in km.

duration of the collapse itself, the instability cannot affect the dynamics nor the magnetic field strength in that phase. After core bounce, the region below the shock becomes unstable with $\tau_{\rm MRI} \sim 10$ ms, and as it propagates outward, the timescale of the MRI grows, reaching values of $\tau_{\rm MRI} \sim 1$ s at the end of the simulation. At the same time, regions inside the PNS become unstable with $\tau_{\rm MRI} \sim 1$ ms, affecting both the inner core of the PNS and the surrounding material. At the end of the simulation for models A1B3G3-D3M0 and A1B3G5-D3M0, the region surrounding the PNS, at about 100 km, remains unstable with $\tau_{\rm MRI} \sim 10$ ms. Therefore, a significant fraction of the newly-formed PNS, as well as the region behind the shock at the moment of its formation are going to be affected by the MRI. As a result, the magnetic field is going to grow exponentially on dynamical timescales and will reach saturation in those regions, becoming important for the dynamics. In these regions the passive field approximation is not a valid approximation, and the full magnetic field treatment is needed. We conclude that, although the MRI does not affect the collapse dynamics (i.e. during the infall phase), the evolution after core bounce will be dominated by this instability. Therefore, the conclusions extracted in this chapter are likely to be modified once the effects of the MRI are accounted for the dynamics. Such simulations will be presented elsewhere.

On the other hand, in models T3M0 the instability cannot appear since the poloidal component of the magnetic field is not present. Therefore, the results from these models in axisymmetry, despite the assumption of the passive field approximation, are completely valid. However, in a real collapse the axisymmetry condition is not exactly satisfied, and the toroidal field can be transformed easily into poloidal field via the α-Ω-dynamo. In this case the MRI can act, and the results for the T3M0 models could be subject to important changes.

10.3.5 Long-term evolution of the magnetic field.

The long-term evolution of the newly formed proto-neutron star highly depends on the final magnetic field configuration, and on the rotation profiles. A detailed study of this issue is out of the scope of the work reported in this thesis, but, nevertheless, we can still provide here some estimates. We note that in Chapter 11 details about the long-term evolution of non-magnetized

proto-neutron stars are given.

We can divide our simulations into three groups depending on the final state. First, in models A1B3G3-D3M0 and A1B3G5-D3M0, the PNS has a compact inner core of nuclear matter with stable magnetic fields, surrounded by a shell where the toroidal magnetic field is amplified via the Ω-dynamo process. The final quasi-stationary structure of these two models can be found in Figs. 10.30 and 10.31. Second, in model A4B5G5-D3M0, nuclear matter density is not reached, and both the magnetic field and the density have a extended structure. The Ω-dynamo mechanism acts in some regions near the equatorial plane, outside the star. Third, in models A1B3G3-T3M0 and A1B3G5-T3M0, no poloidal magnetic field is generated, and therefore the Ω-dynamo does not act. Hence, these two models will not be considered in the following analysis.

If no other processes other than the Ω-dynamo were acting to amplify the magnetic field strength, the poloidal component should become steady for the quasi-stationary state of the star. This configuration of the magnetic field would prevail as long as the passive field approximation were valid, but it would break up when the toroidal component became too strong for the approximation to be valid. During this steady phase one can assume fixed angular profiles and poloidal magnetic field distribution, and from Eq. (10.7) the toroidal field has to grow linearly with time,

$$B^{\varphi}(t) = B^{\varphi}(t_0)\left(1 + \frac{t - t_0}{\tau_\Omega}\right), \tag{10.35}$$

where t_0 is the time at which the quasi-equilibrium configuration is reached, and τ_Ω is the typical timescale of the growth of the toroidal magnetic field via the Ω-dynamo mechanism. Therefore, $\beta_{\rm mag}$ has to grow roughly as

$$\beta_{\rm mag}(t) \approx \beta_{\rm mag}(t_0)\left(1 + \frac{t - t_0}{\tau_\Omega}\right)^2. \tag{10.36}$$

We fit the values of $\beta_{\rm mag}$ obtained in our simulations after core bounce (see Fig. 10.32) to calculate τ_Ω in models A1B3G3-D3M0 ($t_0 = 50$ ms), A1B3G5-D3M0 ($t_0 = 35$ ms), and A4B5G5-D3M0 ($t_0 = 40$ ms). The resulting values are given in Table 10.5. For models reaching nuclear matter density we also calculate the rotational and magnetic energy contained in the region where

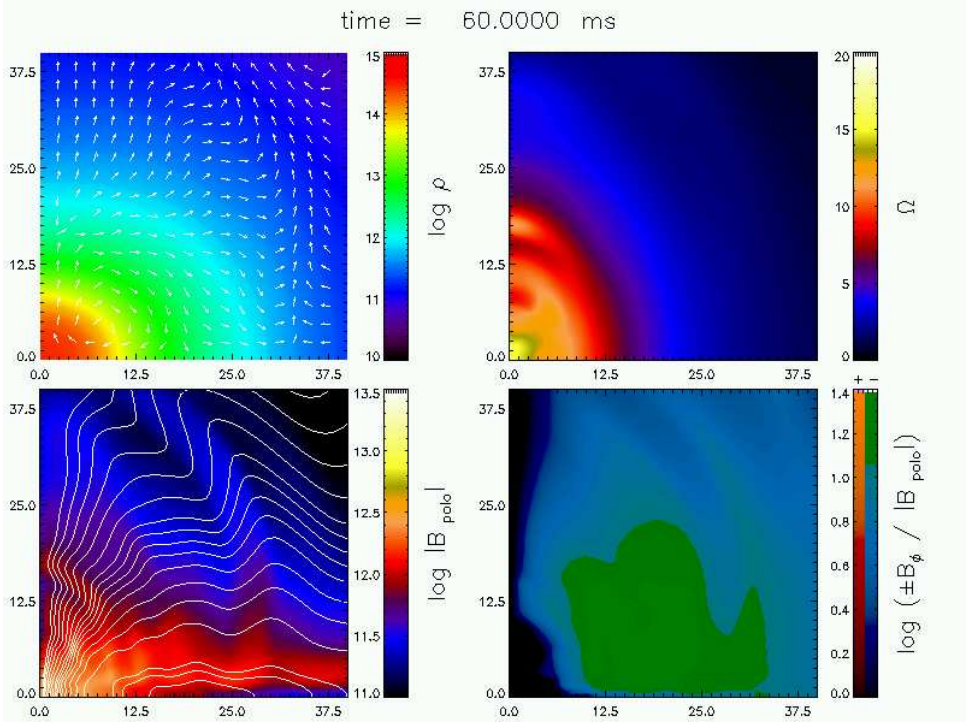

Figure 10.30: Details of the inner region of the star at the end of the simulation, $t = 60$ ms, for model A1B3G3-D3M0. The upper left panel shows the logarithm of density, $\log \rho$, in g cm^{-3} (color coded), and the direction of the velocity field, v^i, (white arrows). The upper right panel shows the angular velocity, Ω (color coded). The lower left panel shows the logarithm of the poloidal component of the magnetic field, $\log |B|_{\rm polo}$, in G (color coded), and the magnetic field lines in the r-θ plane (lines). Finally, the lower right panel shows , $\log B^\varphi / |B_{\rm polo}|$ (color coded). All axes are in km.

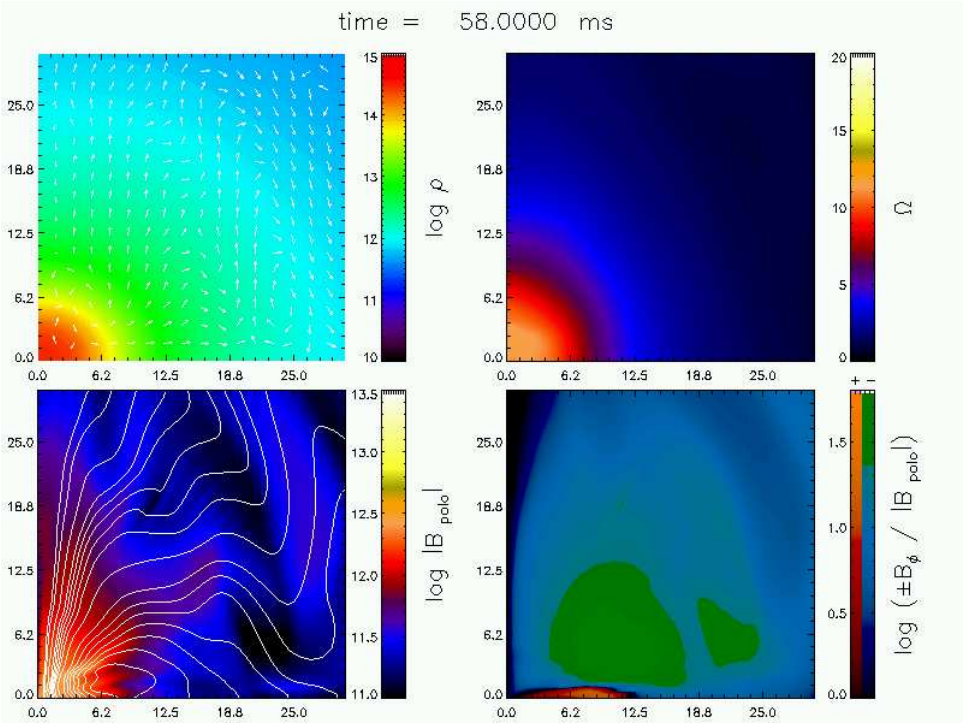

Figure 10.31: Same as Fig. 10.30 but for model A1B3G5-D3M0 at the end of the simulation, $t = 58$ ms.

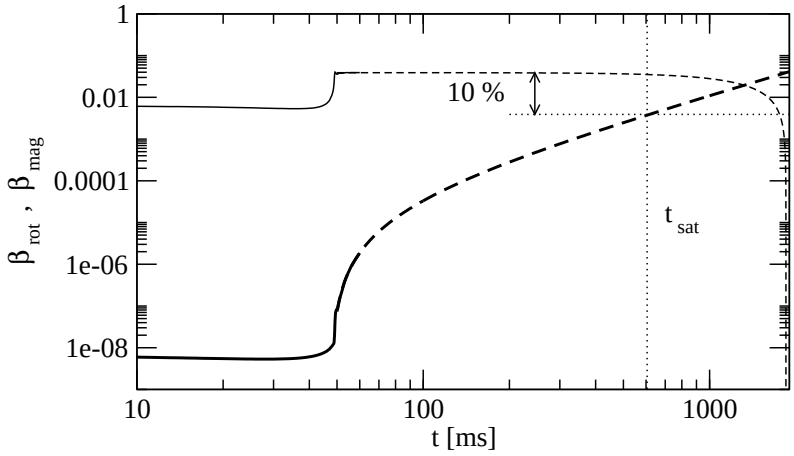

Figure 10.32: Evolution of $\beta_{\rm rot}$ (solid thin line), and $\beta_{\rm mag}$ (solid thick line) for model A1B3G3-D3M0. Dashed lines represent an extrapolation of the computed values assuming that a quasi equilibrium state has been reached at the end of the simulation: $\beta_{\rm rot} + \beta_{\rm mag}$ is assumed to remain constant (dashed thin line) and $\beta_{\rm mag}$ to grow as Eq. (10.36) (dashed thick line). We calculate the saturation time, $t_{\rm sat}$, as the time at which $\beta_{\rm mag}$ reaches a value of a 10% of $\beta_{\rm rot}$ (dotted line).

$\rho > \rho_{\rm nuc}$. We define $\beta^{\rm n}_{\rm rot}$ and $\beta^{\rm n}_{\rm mag}$ as the corresponding energy fractions with respect to the total potential energy.

The Ω-dynamo mechanism works by transforming rotational energy into magnetic energy. As the toroidal magnetic field is amplified the energy in the magnetic field grows, becoming at a certain time comparable to the rotational energy (it is actually sufficient to reach about a 10% (Obergaulinger et al. 2005)). At this point, the effects of the magnetic field on the dynamics become important and thus, the passive field approximation breaks down. While the PNS rotates gradually slower, owing to $\beta_{\rm rot} \to 0$ (see Fig. 10.32), the magnetic field saturates, because the Ω-dynamo can not extract more energy from rotation. This effect can drive the PNS to a complete halting, and even to exchange its sense of rotation (retrograde rotation). In the final state, the exchange of rotational and magnetic energy can make the PNS behave as a

Table 10.5: Fitted parameters for the long-term evolution of the star under the assumption that the Ω-dynamo mechanism is the only amplification process at work. Values for supra-nuclear density regions (labeled with superscripts n) are also reported for completeness. From left to right the columns report: timescales of the Ω-dynamo (τ_Ω and $\tau_\Omega^{\rm n}$), rotational energy parameters at the end of the simulation ($\beta_{\rm rot}$ and $\beta_{\rm rot}^{\rm n}$), saturation times of the amplification process ($t_{\rm sat}$ and $t_{\rm sat}^{\rm n}$), and value of the magnetic field at saturation ($B_{\rm sat}^{\varphi}$ and $B_{\rm sat}^{\varphi\,{\rm n}}$). * In model A1B3G5-D3M0 the fit for the inner region gives values for $\tau_\Omega^{\rm n}$ between 17 ms and 137 ms, since the slope of its evolution is very small. The resulting $t_{\rm sat}^{\rm n}$ can be affected in a similar way.

Model	τ_Ω	$\tau_\Omega^{\rm n}$	$\beta_{\rm rot}$	$\beta_{\rm rot}^{\rm n}$	$t_{\rm sat}$	$t_{\rm sat}^{\rm n}$	$B_{\rm sat}^{\varphi}$	$B_{\rm sat}^{\varphi\,{\rm n}}$
			$\times 10^{-2}$	$\times 10^{-3}$			$\times 10^{15}$	$\times 10^{15}$
	[ms]	[ms]			[s]	[s]	[G]	[G]
A1B3G3-D3M0	2.48	77*	3.9	4.0	0.6	66*	1.15	0.001
A1B3G5-D3M0	17.3	5.3	2.2	1.0	2.2	2.6	0.3	0.29
A4B5G5-D3M0	12.6	-	7.0	-	3.6	-	2.5	-

torsion pendulum. We calculate the time of saturation, $t_{\rm sat}$, and the magnetic field at this time, $B_{\rm sat}^{\varphi}$, by imposing $\beta_{\rm mag}(t_{\rm sat}) = 0.1\,\beta_{\rm rot}$, in Eq. (10.36). The results are given in Table 10.5. In addition, we calculate the corresponding values, $\tau_\Omega^{\rm n}$ and $t_{\rm sat}^{\rm n}$ for the nuclear matter region.

In order to rescale all these quantities for other values of the initial magnetic field, i.e. for other B_0^*, we need the following expressions:

$$B^i = B_{10}^i \left(\frac{B_0^*}{10^{10}G}\right), \tag{10.37}$$

$$\beta_{\rm mag} = \beta_{\rm mag\,10} \left(\frac{B_0^*}{10^{10}G}\right)^2, \tag{10.38}$$

$$\tau_\Omega = \tau_{\Omega\,10}, \tag{10.39}$$

$$t_{\rm sat} \approx t_{\rm sat\,10} \left(\frac{10^{10}G}{B_0^*}\right), \tag{10.40}$$

where quantities with subindex "10" are the corresponding quantities for $B_0^* = 10^{10}G$. Note that the typical growth time of the Ω-dynamo mechanism, τ_Ω, is independent of the strength of the magnetic field provided this is low enough to fulfill the passive field condition. Expression (10.40) is an approximation only valid if $t_{\rm sat} \gg \tau_\Omega$.

The results of this section rely heavily on the condition (unlikely) that the Ω-dynamo is the only amplification process at work on the system. Unfortunately, other processes can amplify the field in shorter timescales, and this condition is probably not fulfilled at all if the passive field approximation is relaxed. As discussed in the previous section, the MRI is probably going to amplify the magnetic field in a few ms, to values of the order of 10^{14}-10^{15} G, acting on the overall dynamics by transporting angular momentum outwards. Additional processes not considered here can affect both the dynamics and the magnetic field structure as well: the α-Ω-dynamo mechanism is going to transform toroidal magnetic field into poloidal one, the diffusion of the magnetic field also needs to be considered in the long term evolution, and the cooling of the PNS as it transforms into a cold and compact NS (see Chapter 11). Therefore, the timescales reported in this section cannot be taken as realistic values of the amplification of the magnetic field of the PNS, but as an estimation of the amplification via the Ω-dynamo only. The comparison with other amplification mechanisms shows that it is slower, which stresses the necessity of relaxing the passive field condition to be able to account for other processes such as MRI.

Chapter 11

Evolutionary sequences of rotating proto-neutron stars

Protoneutron stars are born following core collapse supernovae. Initially hot and rich in leptons, they become neutrino–free, cold, and more compact standard neutron stars in less than one minute. In this Chapter we study the evolution of rigidly and differentially rotating protoneutron stars by calculating evolutionary sequences of stationary axisymmetric configurations in general relativity. The knowledge of the evolution of these configurations, obtained by solving Einstein's equations coupled to a finite temperature, relativistic equation of state, allows us to discuss the possible appearance of dynamical instabilities, which are possible sources of gravitational waves, and that are discussed later in Chapter 12. The material discussed in this Chapter has been published in Villain et al. (2004).

11.1 Introduction

During the first minute of their life, non-rotating protoneutron stars (PNS), remnants of successful core collapse supernovae, evolve from initial hot, lepton rich objects to cold ($T < 10^{10}$ K) catalyzed neutron stars. This process, studied in detail in the last two decades (Burrows & Lattimer 1986; Keil & Janka 1995; Pons 1999), can be summarized in three main stages: i) *mantle contraction* with fast cooling of the outer regions in about 0.5 s, and probably significant accretion; ii) *deleptonization* and consequently heating of the internal core as energetic neutrinos diffuse out leaving most of their chemical energy on the way out; and iii) *cooling* by means of diffusion of (mostly) thermal neutrinos, resulting in a decrease of temperature from about 40-50 MeV to below 2-4 MeV, point at which the star becomes transparent to neutrinos.

Little is known about the early evolution of rapidly rotating PNSs, since a fully consistent study requires solving the neutrino transport equations in at least 2-dimensions, coupled to general relativistic hydrodynamics that describes the fluid motion in rotating relativistic stars. Moreover, the microphysics would also have to be treated carefully: internal consistency between the equation of state (EOS) and the neutrino opacities describing the interaction between neutrinos and matter is needed to achieve reliable results (Pons 1999).

A few attempts to treat this problem in simplified ways exist (e.g. Goussard et al. 1997, 1998; Strobel et al. 1999) based on the study of temporal sequences of quasi-equilibrium models that mimic the temporal evolution. The quasi–static approximation is well justified, since the hydrodynamical timescale (10^{-3} s) is much smaller than the timescale in which substantial thermodynamical changes occur (diffusion timescale ≈ 1 s). In all previous studies, constant temperature, entropy and/or neutrino fraction profiles were used. Hence, without doing a complete study, the previous works can be improved in several aspects. First, instead of isentropic or isothermal models, we use realistic profiles, which come from 1D diffusion simulations, rescaling temperature and chemical profiles as functions of density; second, we do not restrict ourselves to the rigid rotation case, including differential rotation in the analysis; last but not least, we checked whether fixing the baryonic mass and the angular momentum along the evolution results in some reasonable time dependence of the integrated relevant physical quantities such as the gravitational mass, which has to agree

with the loss of energy due to neutrino luminosity. A more detailed description of the results presented here can be found in Villain et al. (2004).

11.2 Numerical solution of Einstein's equations for stationary axisymmetric spacetimes

In the quasi–stationary approximation the evolution consists of a collection of stationary and asymptotically flat snapshots, each one being a solution of Einstein's equations, but with a different stress-energy tensor. More explicitly, the fluid is described by non-trivial thermodynamical profiles rescaled from 1-D simulations (Pons 1999), while the spacetime is solved employing a fully relativistic spectral code (Bonazzola et al. 1993). This code uses the same formalism as the code used in Section 9.1 to calculate initial models for the core collapse and for neutron stars, but has some improvements such as a compactification of the grid outside the star or the use of spectral methods to increase the spatial accuracy. We describe next some of the features of this code.

The $3+1$ formulation of general relativity is used, in MSQI coordinates, with the assumption that matter is free of convective motions. This hypothesis implies the circularity of the stationary axisymmetric spacetime (Carter 1979) which greatly simplifies the calculations. Under these approximations, the metric is written (cf. Eq. (9.2))

$$\begin{aligned} \mathrm{d}s^2 &\equiv -\left(\alpha^2 - \beta_\varphi\,\beta^\varphi\right)\mathrm{d}t^2 - 2\,\beta_\varphi\,\mathrm{d}t\,\mathrm{d}\varphi \\ &+ \frac{\mathcal{A}^4}{\mathcal{B}^2}\left(\mathrm{d}r^2 + r^2\,\mathrm{d}\theta^2 + \mathcal{B}^4\,r^2\,\sin^2\theta\,\mathrm{d}\varphi^2\right), \end{aligned} \tag{11.1}$$

where the functions $\mathcal{A}$ and $\mathcal{B}$ depend only on r and θ.

The version of the code that we use is based on the C++ library LORENE[1], a software package for numerical relativity freely available under GNU license. This code solves the system of elliptic partial differential equations for the metric, plus the algebraic equation resulting from the conservation of the energy-momentum tensor. Indeed, the conditions for the existence of stationary solutions of Einstein's equations in the presence of a rotating perfect fluid make

[1] http://www.lorene.obspm.fr

the relativistic Euler equations, derived from the conservation of the energy-momentum tensor projected into a space-like three-surface, to be reduced in the case of stationary rotating motion to

$$\frac{1}{e+P}\frac{\partial P}{\partial x^i} + \frac{\partial}{\partial x^i}\left[\ln\left(\frac{\alpha}{W}\right)\right] = -F\frac{\partial \Omega}{\partial x^i}, \tag{11.2}$$

where $e \equiv \rho(1+\epsilon)$ is the total energy density as measured in the comoving frame, $\Omega \equiv u^\varphi/u^t$ the angular velocity, and $F \equiv u_\varphi\, u^t$.

In general, Eq. (11.2) does not admit a first integral for arbitrary thermodynamics or rotation profiles $\Omega(r,\theta)$, but it does in some simple cases. Concerning rotation, the right hand side of Eq. (11.2) is an exact derivative if either Ω is constant in space (rigid rotation), or the function F can be locally written as $F = F(\Omega)$. The latter leads to a relation between Ω and the coefficients of the metric, which allows the determination of the profile of angular velocity. For differential rotation, we adopt the law proposed by Komatsu et al. (1989b)

$$F(\Omega) \;=\; A^2\,(\Omega_c \;-\; \Omega)\,, \tag{11.3}$$

where Ω_c is the limit of Ω on the rotation axis and A is a parameter with the dimension of length. In the next section we verify that, despite its simplicity, this law gives reasonable rotation profiles qualitatively similar to those obtained from core collapse simulations.

Concerning the EOS, it can be shown that isentropic or isothermal profiles are sufficient conditions for Eq. (11.2) to be integrable. Yet another less restrictive possibility exists: assuming that the total energy density e can be written as an *effective* function of the pressure $e = e(P)$. Indeed, in this case, even if the actual EOS is not barotropic, assuming that the EOS is a one–parameter function ensures the existence of the first integral

$$\int \frac{\mathrm{d}P}{e(P)\,+\,P} \;+\; \ln\left(\frac{\alpha}{W}\right) \;+\; \int F(\Omega)\,\mathrm{d}\Omega \;=\; \text{const.}\,, \tag{11.4}$$

with suitable boundary conditions. Hence, at each evolutionary time, we use the results from 1D diffusion calculations to obtain the temperature and composition profiles as functions of the baryon density n_B only. In this way, the EOS is *effectively* barotropic.

11.3 Choice of the initial models

One of the first issues that must be addressed to study the early evolution of neutron stars is the initial model. In Pons (1999) it was shown that for spherical models the overall evolution is not very sensitive to modifications of the initial thermodynamical profiles, while the total mass of the star is the parameter that affects mostly the subsequent evolution. It seems therefore natural to choose a canonical star with a baryon mass of 1.6 $M_\odot$, that corresponds to a gravitational mass of the old, cold configuration of about 1.44 $M_\odot$. For completeness, we have also studied a model with a baryonic mass of 1.2 $M_\odot$. Notice that one cannot use the effective barotropes obtained for a PNSs with a given mass in the calculations of sequences with a different mass, because the thermodynamic properties are different.

More difficult is to guess the particular rotation properties of a newly born neutron star. Newly born neutron stars are expected to rotate differentially, as opposed to old neutron stars where various viscous mechanisms had sufficient time to turn it into a rigid rotator. Even in the case that the iron core of the supernova progenitor was rigidly rotating (a quite reasonable assumption, since it is an old massive star), the process of collapse would generate a significant amount of differential rotation. Indeed, recent calculations of stellar evolution indicate that the iron core of a massive star is rotating almost rigidly (Heger et al. 2000, 2004), and this approximation is used in most recent simulations of rotational core collapse (Müller et al. 2004). Based on these works, we have decided to study a few models from Dimmelmeier et al. (2002b) (DFM hereafter), and to run some more simulations of similar models of stellar core collapse varying the total initial angular momentum. Our models correspond to those labeled by A1 in DFM, *i.e.*, the iron core of the progenitor is almost rigidly rotating. In Figure 11.1, we show profiles of the angular velocity (left panel) and density (right panel) of the inner 150 km, as a function of the equatorial radius, immediately after the PNS is formed. The different lines correspond to models with a different amount of initial angular momentum, the ratio of rotational and gravitational potential energy ($|T/W|$) being of 0.9% (models B3 in DFM), 0.5% (B2), 0.25% (B1) and 0.05%, respectively. We include the last lower value because it is more realistic (Heger et al. 2004; Müller et al. 2004) than those studied in DFM. In the figure we also show, with dotted curves, simple fits to the rotation law Eq. (9.3), which corresponds to

the Newtonian limit of Ω consistent with Eq. (11.3). From this limiting case we infer that A is the value of the radius at which, in the equatorial plane ($\vartheta \equiv \pi/2$), the angular velocity is half its limiting central value, Ω_c. Although this fact is only strictly valid in the Newtonian case, it approximately holds for relativistic stars, too. For all four models we set $A^2 = 50$ km^2, with Ω_c equal 4500, 3500, 2600, and 1300 rad/s, from top to bottom. The agreement between the simple law (9.3) and the results from simulations is quite acceptable. In all the models the spatial scale of variation of the angular velocity (A) is the same, because the density profiles are very similar (see Figure 11.1, right panel). Varying the EOS might lead to a different density distribution: One should expect a smaller A for softer EOSs (more compact PNS), and a larger A for stiffer EOSs. We note again that our assumption of stationary axisymmetric configurations implies that the function F on the r.h.s. of the equation of stationary motion (11.2) is only a function of the angular velocity. In the Newtonian case, this is equivalent to say that the angular velocity depends only on the distance to the axis ($r \sin\theta$). In the relativistic case, there are small corrections but the overall distribution of the angular velocity is nearly cylindrical, as can be seen in Fig. 11.2.

In reality, immediately after core collapse and bounce, there is no reason to expect that the distribution of angular velocity corresponds to that of stationary equilibrium, and it may take several rotation periods for the star to relax to some stationary solution. A more detailed analysis of all these issues requires a parametric study of rotating core collapse simulations. However, for the purpose of this chapter, which is to understand which range of parameters one should expect when using Eq. (11.3), the conclusion is that a reasonable realistic model with differential rotation should be consistent with A being of the order of 10 km. Considering that there might be a number of processes that could lead to rigid rotation on a dynamical timescale, such as shear or magneto-rotational instabilities, we study both cases, with substantial differential rotation and with rigid rotation. Notice that previous works (Goussard et al. 1997, 1998) on differentially rotating PNSs have focused on the parameter space region corresponding to $A \approx 1$ km, which seems to be too low according to our results.

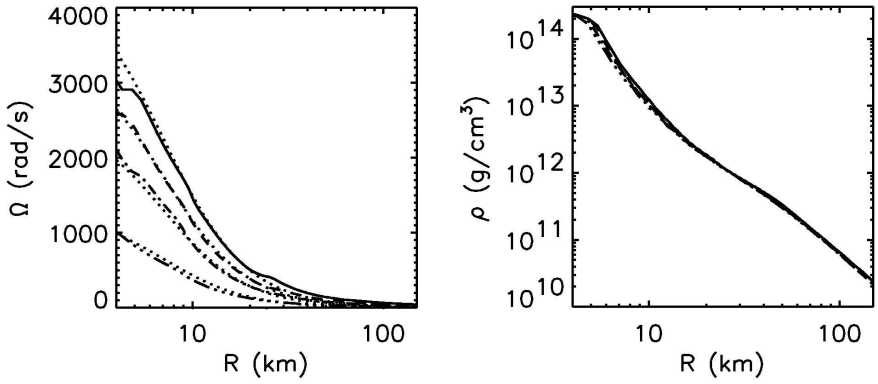

Figure 11.1: Equatorial profiles of angular velocity (left panel), and density (right panel) of PNSs from axisymmetric simulations of stellar core collapse (DFM). The four models correspond to a different amount of angular momentum of the iron core, namely, $|T/W| = 0.9\%$ (solid), 0.5% (dashed), 0.25% (dashed-dotted), and 0.05% (dashed-3 dotted). The dotted lines in the left panel are fits to the simple law (9.3) with $A^2 = 50$ km^2.

11.4 Time evolution of rotating PNS

In our analysis, different thermodynamical profiles corresponding to different epochs of the early evolution of PNSs are used. We also cover situations from rigid rotation to quite strong but realistic differential rotation in agreement with core collapse simulations, i.e., A is in the range from 10 km (significant differential rotation) to 50 km (almost rigid rotation).

A first and already known effect of differential rotation (Baumgarte et al. 2000; Yoshida et al. 2002) that we have verified is the fact that for a given EOS, differential rotation enables a star to contain more angular momentum and to reach higher values of the ratio of rotational and gravitational potential energy $\beta \equiv |T/W|$. Thus, we find that the central angular velocity can be up to a factor of 5 to 10 larger in the case of differential rotation, but the maximum angular momentum is only about fifty percent larger than for rigid rotation. More important is the variation of the maximum of $|T/W|$. While for rigidly

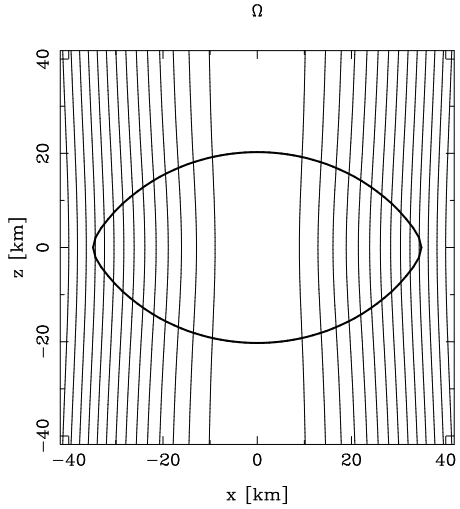

Figure 11.2: Surfaces of constant angular velocity (projected in a transversal plane) of a differentially rotating star with $A = 100$ km, for $t = 1$ s, and rotating with $\Omega = 354$ rad/s. ($\Omega/\Omega_K = 0.995$). The surface is marked by the thick solid line. Because of relativistic effects, the stationary solution does not show exact cylindrical symmetry.

rotating stars $\beta \sim 0.1$, in PNSs with a large degree of differential rotation it can be as high as 0.2. The latter value, however, does not exceed the dynamical instability threshold (≈ 0.27), but it is sufficiently large to allow the growth of either the secular, gravitational wave driven, instability (CFS, Chandrasekhar (1970); Friedman & Schutz (1978)) that happens between $0.07 - 0.14$, the lower value being for more compact stars (Stergioulas & Friedman 1998), or the recently proposed low $|T/W|$ dynamical instabilities (see Shibata et al. 2002, and Chapter 12).

Since the initial angular momentum of a PNS is not well-known, the occurrence of these instabilities is still questionable. Indeed, recent stellar evolution calculations suggest that the specific angular momentum of the inner 1.7 $M_\odot$ of a 15 $M_\odot$ star can be as high as 3×10^{16} cm^2/s if magnetic braking is neglected, or 10^{15} cm^2/s if magnetic torques are included in the evolution (Heger

et al. 2004). This corresponds to J/M in the range $J/M = (0.2 - 6)\ GM_\odot/c$.

To illustrate the influence of the rotation profile on the fate of an evolving newly born PNS, we shall now look at the time evolution of a star with given angular momentum ($J = 1.5\ GM_\odot^2/c$), and fixed baryonic mass $1.6M_\odot$. This value of the angular momentum is considerably smaller than the maximum value predicted by stellar evolution calculations, but as can be seen in the left panel of Fig. 11.3, a rigidly rotating PNS with such an angular momentum would contract and spin up to the point where its angular velocity reaches the mass shedding limit Ω_K, where the star starts to eject matter at the equator. Notice that, in this case, $|T/W|$ stays always below the threshold values for secular instability (above 0.1, because the star is still not very relativistic) and far below the limit of dynamical instability (~ 0.27). Instabilities could arise if neutrino transport cannot redistribute and remove a substantial fraction of the initial angular momentum. Whether this can happen is unclear and needs multidimensional transport simulations for clarification. In general, it is assumed that the angular momentum is approximately constant during this era of a PNS's life, and that it only varies on timescales longer than the diffusion timescale. If this were the case, PNSs born with a large angular momentum could not loose it via neutrino diffusion with the same efficiency as the binding energy, and this may result in a significant mass loss after reaching the mass shedding limit even for PNSs that are not born maximally rotating (as in the chosen case).

To see the influence of the rotation profile, we consider the same model (same total baryonic mass and initial angular momentum) but for differentially rotating PNSs with $A = 10$ or 20 km. The right panel of Fig. 11.3 shows the temporal evolution of the central angular velocity (top) and of $|T/W|$ (bottom). As in the case of rigid rotation, $|T/W|$ increases as the star contracts and loses its binding energy in a neutrino diffusion timescale of about 10 s. Yet, the mass shedding limit is not reached while higher values of $|T/W|$ are. Thus, if there are no significant losses of angular momentum, the various types of dynamical instabilities associated to critical values of the rotation parameter may again not be encountered at the very beginning, but several seconds after formation. Moreover, only at this moment the star is compact enough to apply relativistic criteria (lower thresholds for instability), which makes the star more unstable.

Hence, we expect that if the angular momentum at the birth of a PNS

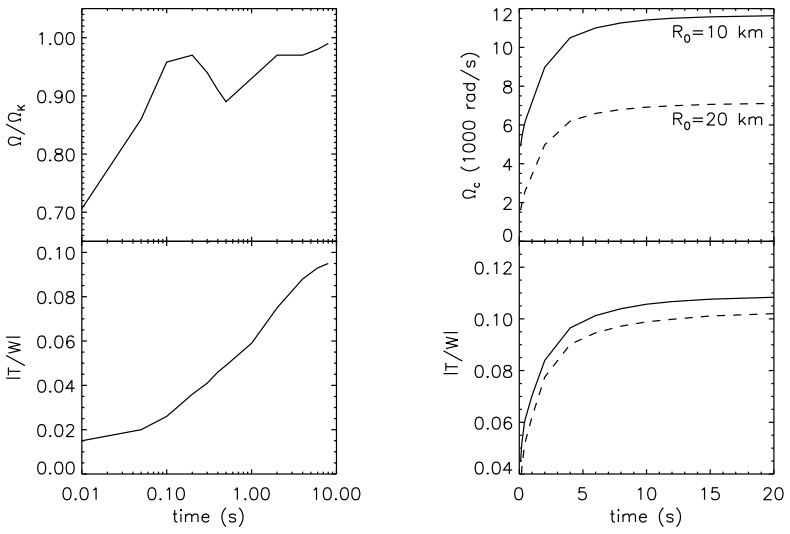

Figure 11.3: Left panel: Time evolution of the angular velocity Ω/Ω_K and the rotation parameter $|T/W|$ for rigidly rotating PNSs. Right panel: Time evolution of the central angular velocity Ω_c and the rotation parameter $|T/W|$ for differentially rotating PNSs with $A = 10$ km (solid line) and 20 km (dashed line). In both cases the total angular momentum is $1.5\, GM_\odot^2/c$ and the baryonic mass $M_{\rm B} = 1.6\, M_\odot$.

happens to be such that $J/M > 2$, centrifugal forces would stop the collapse before the PNS is formed, while intermediate values ($J/M = 1$) may result in the formation of a rapidly rotating PNS that becomes unstable several seconds after birth. An observational evidence of this scenario would be the detection, with a delay of a few seconds, of a neutrino burst and a gravitational wave burst, in the event of a galactic supernova. Ultimately, if magnetic braking is very efficient during the evolution of a massive star, $J/M < 0.5$, the PNS will be formed after collapse without reaching extreme values of $|T/W|$.

Finally, let us mention that as a consistency check of our assumptions and simplifications, we made a simple estimate of the neutrino luminosity consid-

ering that the variation in the gravitational mass of the PNS is equal to the neutrino luminosity. We found that within our approach, both the order of magnitude and the exponential decay of the luminosity during 10 seconds are consistent with the results of detailed simulations with neutrino transport in spherical symmetry (Pons 1999). Therefore, imposing conservation of angular momentum and baryonic mass, and building a sequence with fixed A is not violating conservation of energy, and therefore provides a reasonable qualitative approach to the real case.

Chapter 12

Bar mode instabilities

It has been recently argued through numerical work that rotating stars with a high degree of differential rotation are dynamically unstable against bar-mode deformation, even for values of the ratio of rotational kinetic energy to gravitational potential energy as low as $\mathcal{O}(0.01)$. This may have implications for gravitational wave astronomy in high-frequency sources such as core collapse supernovae. In this Chapter we present high-resolution simulations, performed with an adaptive mesh refinement hydrodynamics code, of such low $T/|W|$ bar-mode instability. The complex morphological features involved in the nonlinear dynamics of the instability are revealed in our simulations, which show that the excitation of Kelvin-Helmholtz-like fluid modes outside the corotation radius of the star leads to the saturation of the bar-mode deformation. While the overall trends reported in an earlier investigation are confirmed by our work, we also find that numerical resolution plays an important role during the long-term, nonlinear behaviour of the instability, which has implications on the dynamics of rotating stars and on the attainable amplitudes of the associated gravitational wave signals. The work presented in this chapter has been submitted for publication (Cerdá-Durán et al. 2006).

12.1 Introduction

Neutron stars following a core collapse supernova are rotating at birth and can be subject to various nonaxisymmetric instabilities (see e.g. Stergioulas 2003, for a review). Among those, if the rotation rate is high enough so that the ratio of rotational kinetic energy T to gravitational potential energy W, $\beta \equiv T/|W|$, exceeds the critical value $\beta_{\rm d} \sim 0.27$, inferred from studies with incompressible Maclaurin spheroids, the star is subject to a *dynamical* bar-mode ($l = m = 2$ f-mode) instability driven by hydrodynamics and gravity. Its study is highly motivated nowadays as such an instability bears important implications in the prospects of detection of gravitational radiation from newly-born rapidly rotating neutron stars.

Simulations of the dynamical bar-mode instability are available in the literature, both using simplified models based on equilibrium stellar configurations perturbed with suitable eigenfunctions (Tohline et al. 1985; Houser et al. 1994; New et al. 2000; Shibata et al. 2000), and more involved models for the core collapse scenario (Rampp et al. 1998a; Shibata & Sekiguchi 2005; Saijo 2005; Ott et al. 2005), and in either case both in Newtonian gravity and general relativity. Due to its superior simplicity the former approach has received much more attention, notwithstanding that the conclusions drawn from perturbed stellar models may not be straightforwardly extended to the collapse scenario.

Newtonian simulations of triaxial instabilities following core collapse were first performed by Rampp et al. (1998a). These showed that the bar-mode instability sets in when $\beta \gg 0.27$ and when the progenitor rotates rapidly and highly differentially. Such conditions are met when the (artificial) depletion of internal energy to trigger the collapse is large enough to produce a very compact core for which a significant spun-up can be achieved. More recently, three-dimensional simulations of the core collapse of rotating polytropes in general relativity have been performed by Shibata & Sekiguchi (2005). These authors studied the evolution of the bar-mode instability starting with axisymmetric core collapse initial models which reached values of $\beta \sim 0.27$ during the infall phase. These simulations showed that the maximum value of β achieved during collapse and bounce depends strongly on the velocity profile, the total mass of the initial core, and on the equation of state. In agreement with the findings from the Newtonian simulations of Rampp et al. (1998a), the bar-mode instability sets in if the progenitor rotates rapidly ($0.01 \leq \beta \leq 0.02$) and

has a high degree of differential rotation. In addition, the artificial depletion of pressure and internal energy to trigger the collapse, leading to a compact core which subsequently spins up, also plays a key role in general relativity for a noticeable growth of the bar-mode instability.

Whether the requirements inferred from numerical simulations are at all met by the collapse progenitors remains unclear. As shown by Spruit & Phinney (1998) magnetic torques can spin down the core of the progenitor, which leads to slowly rotating neutron stars at birth ($\sim 10-15$ms). The most recent, state-of-the-art computations of the evolution of massive stars, which include angular momentum redistribution by magnetic torques and spin estimates of neutron stars at birth (Heger et al. 2005; Ott et al. 2006), lead to core collapse progenitors which do not seem to rotate fast enough to guarantee the unambiguous growth of the canonical bar-mode instability. Rapidly-rotating cores might be produced by an appropriate mixture of high progenitor mass ($M > 25M_{\odot}$) and low metallicity (N. Stergioulas, private communication; Woosley & Janka 2005). In such case the progenitor could by-pass the Red Supergiant phase in which the differential rotation of the core produces a magnetic field by dynamo action which couples the core to the outer layers of the star, transporting angular momentum outwards and spinning down the core. According to Woosley & Heger (2006) about 1% of all stars with $M > 10M_{\odot}$ will produce rapidly-rotating cores.

On the other hand, Newtonian simulations of the bar-mode instability from perturbed equilibrium models of rotating stars have shown that $\beta_{\rm d} \sim 0.27$ independent of the stiffness of the equation of state provided the star is not strongly differentially rotating. The relativistic simulations of Shibata et al. (2000) yielded a value of $\beta \sim 0.24-0.25$ for the onset of the instability, while the dynamics of the process closely resembles that found in Newtonian theory, i.e. unstable models with large enough β develop spiral arms following the formation of bars, ejecting mass and redistributing the angular momentum. As the degree of differential rotation becomes higher Newtonian simulations have also shown that $\beta_{\rm d}$ can be as low as 0.14 (Centrella et al. 2001). More recently Shibata et al. (2002, 2003) have reported that rotating stars with an *extreme* degree of differential rotation are dynamically unstable against bar-mode deformation even for values of β of $\mathcal{O}(0.01)$.

Given its recent discovery and its potential astrophysical implications for post-bounce core collapse dynamics and gravitational wave astronomy, we

present in this chapter high resolution simulations of such low $T/|W|$ bar-mode instabilities. This work is further motivated in the light of the few numerical simulations available in the literature. Our main goal is to revisit the simulations by Shibata et al. (2002) on the low $T/|W|$ bar-mode instability, and particularly to check how sensitive the onset and development of the instability is to numerical issues such as grid resolution. To this aim we perform Newtonian hydrodynamical simulations of a subset of models analyzed by Shibata et al. (2002) using an adaptive mesh refinement (AMR) code (Quilis 2004) which allows us to perform such three dimensional simulations with the highest resolution ever used. Our simulations reveal the complex morphological features involved in the nonlinear dynamics of the instability, where the excitation of Kelvin-Helmholtz-like fluid modes influences the saturation of the bar-mode deformation. We advance that while the overall trends found by Shibata et al. (2002) are confirmed by our work, the resolution employed in the simulations does play a key role for the long-term behaviour of the instability and for the nonlinear dynamics of rotating stars, which has implications on the attainable amplitudes of the associated gravitational wave signals. We note that we plan to upgrade the existing AMR code to account for the effects of magnetic fields in order to attempt the current study in a more realistic setup. The present work is a step towards that goal.

As the framework of this chapter differs from the rest of the thesis, because Newtonian gravity is used, we briefly describe the theoretical formalism and the numerical schemes used, before presenting the results of the performed simulations.

12.2 Mathematical framework

The evolution of a self-gravitating ideal fluid in the Newtonian limit is described by the hydrodynamics equations and Poisson's equation:

$$\frac{\partial \rho}{\partial t} + \nabla \cdot (\rho \mathbf{v}) = 0 \tag{12.1}$$

$$\frac{\partial \mathbf{v}}{\partial t} + (\mathbf{v} \cdot \nabla)\mathbf{v} = -\frac{1}{\rho}\nabla p - \nabla \phi \tag{12.2}$$

$$\frac{\partial E}{\partial t} + \nabla \cdot [(E+p)\mathbf{v}] = -\rho \mathbf{v} \nabla \phi \tag{12.3}$$

$$\nabla^2 \phi = 4\pi G \rho \tag{12.4}$$

where $\mathbf{x}$, $\mathbf{v} = \frac{d\mathbf{x}}{dt} = (v_x, v_y, v_z)$, and $\phi(t, \mathbf{x})$ are, respectively, the Eulerian coordinates, the velocity, and the Newtonian gravitational potential. The total energy density, $E = \rho\epsilon + \frac{1}{2}\rho v^2$, is defined as the sum of the thermal energy, $\rho\epsilon$, where ρ is the mass density and ϵ is the specific internal energy, and the kinetic energy (where $v^2 = v_x^2 + v_y^2 + v_z^2$). Pressure gradients and gravitational forces are the responsible for the evolution. An equation of state $p = p(\rho, \epsilon)$ closes the system. We use an ideal gas equation of state $p = (\Gamma - 1)\rho\epsilon$ with $\Gamma = 2$.

The hydrodynamics equations, Eqs. (12.1–12.3), can be rewritten in flux-conservative form:

$$\frac{\partial \mathbf{u}}{\partial t} + \frac{\partial \mathbf{f}(\mathbf{u})}{\partial x} + \frac{\partial \mathbf{g}(\mathbf{u})}{\partial y} + \frac{\partial \mathbf{h}(\mathbf{u})}{\partial z} = \mathbf{s}(\mathbf{u}) \tag{12.5}$$

where $\mathbf{u}$ is the vector of *unknowns* (conserved variables):

$$\mathbf{u} = [\rho, \rho v_x, \rho v_y, \rho v_z, E] \quad . \tag{12.6}$$

The three *flux* functions $\mathbf{F}^\alpha \equiv \{\mathbf{f}, \mathbf{g}, \mathbf{h}\}$ in the spatial directions x, y, z, respectively, are defined by

$$\mathbf{f}(\mathbf{u}) = \left[\rho v_x, \rho v_x^2 + p, \rho v_x v_y, \rho v_x v_z, (E+p)v_x\right] \tag{12.7}$$

$$\mathbf{g}(\mathbf{u}) = \left[\rho v_y, \rho v_x v_y, \rho v_y^2 + p, \rho v_y v_z, (E+p)v_y\right] \tag{12.8}$$

$$\mathbf{h}(\mathbf{u}) = \left[\rho v_z, \rho v_x v_z, \rho v_y v_z, \rho v_z^2 + p, (E+p)v_z\right] \tag{12.9}$$

and the *source terms* $\mathbf{s}$ are given by

$$\begin{aligned} \mathbf{s}(\mathbf{u}) &= \left[0, -\rho\frac{\partial \phi}{\partial x}, -\rho\frac{\partial \phi}{\partial y}, -\rho\frac{\partial \phi}{\partial z},\right. \\ &- \left. \rho v_x \frac{\partial \phi}{\partial x} - \rho v_y \frac{\partial \phi}{\partial y} - \rho v_z \frac{\partial \phi}{\partial z}\right] . \end{aligned} \tag{12.10}$$

System (12.5) is a three-dimensional hyperbolic system of conservation laws with sources $\mathbf{s}(\mathbf{u})$.

Table 12.1: Overview of the initial models and results of the simulations. The rows report the name of the model, the ratio of equatorial-to-polar radii (r_e/r_p), the degree of differential rotation ($\hat{A}$), the ratio of kinetic to potential energy ($T/|W|$), the size of the computational grid (L) and the location of the corotation radius (r_c) for the two resolutions used: high (AMR H) and low (AMR L). In models R1H and R2H the corotation radius lies outside the star. The real (frequency) and imaginary (growth rate) parts of the bar-mode σ_2 are shown, for the low and high resolution simulation in comparison with the numerical results and linear analysis by Shibata et al. (2002). Note that for model D3 no linear analysis results are available.

Model		D1	D2	D3	R1	R2
r_e/r_p		0.805	0.605	0.305	0.305	0.255
$\hat{A}$		0.3	0.3	0.3	1.0	1.0
$T/\|W\|$		0.039	0.085	0.149	0.253	0.275
L/r_e		4.06	3.73	3.21	4.25	4.03
r_c/r_e	AMR L	0.38	0.47	0.58		
	AMR H	0.36	0.48	0.56	-	-
$\mathrm{Re}(\sigma_2)/\Omega_0$	AMR L	0.76	0.58	0.41		
	AMR H	0.81	0.55	0.43	-	0.82
	Shibata	0.80	0.60	0.45	0.92	0.75
	linear	0.80	0.58	-	0.92	0.75
$\mathrm{Im}(\sigma_2)/\Omega_0$	AMR L	0.0042	0.0154	0.0200		
	AMR H	0.0089	0.0190	0.0240	0.0005	0.1960
	Shibata	0.009-0.013	0.019-0.021	0.013	$<$0.002	0.23
	linear	0.015	0.021	-	$<$0.002	0.20

12.3 Numerical approach

For our study of the low $T/|W|$ bar-mode instability we perform high-resolution simulations of rotating neutron stars using a Newtonian AMR hydrodynamics code called `MASCLET` (Quilis 2004). The implementation of the AMR technique in the code follows the procedure developed by Berger & Colella (1989). The hydrodynamics equations are solved using a high-resolution shock-capturing scheme based upon Roe's Riemann solver and second-order cell reconstruction procedures, while Poisson's equation for the gravitational field is solved using multigrid techniques. The accuracy and performance of the `MASCLET` code has been assessed in a number of tests (Quilis 2004). We note that the code was originally designed for cosmological applications, and here it is applied to simulations of self-gravitating stellar objects for the first time.

The simulations are performed with two different grid resolutions. The low resolution grid consists of a box of size L with 128^3 zones, yielding a fixed resolution of $L/128$. We note that the effective resolution of our coarse grid is comparable to that used by Shibata et al. (2002). Correspondingly, the high resolution grid consists of a base coarse grid of 128^3 cells, and one level of refinement composed of patches with maximum size of 64^3 cells (32^3 coarse cells). This yields a grid resolution on the finest grid of $L/256$. This resolution is enough to resolve the structures simulated, and hence no deeper refinement levels are needed. The patches are dynamically allocated covering those regions of the star where the highest resolution is required (highest densities). Typically only one patch is needed for spheroidal models, and 4-8 in models with toroidal topology. The use of AMR techniques in our high resolution simulations, allows us to save about a factor 4 in CPU time and memory with respect to a unigrid simulation with 256^3 cells. No symmetries are imposed in the simulations. To the best of our knowledge, in the investigations of the bar-mode instability performed by previous groups, grid resolutions as high as the ones we use here were never employed.

As customary in grid-based codes the vacuum surrounding the star is filled with a tenuous numerical atmosphere with density $\rho/\rho_{\max} \approx 10^{-12}$ and zero velocities, $\rho_{\max}$ being the maximun density. Every grid cell with $\rho/\rho_{\max} < 10^{-6}$ is reset to the atmosphere values. A correct treatment of the atmosphere is essential for an accurate description of the stellar dynamics and correct computation of the growth rates of unstable modes. We have checked that

values for the atmosphere higher than those we chose or a free evolution of the atmosphere altogether, lead to remarkable changes in the mode behaviour, growth rates, and frequencies.

12.4 Results

12.4.1 Initial data

Differentially rotating stellar models in equilibrium are built according to the method of Eriguchi & Müller (1984), and used as initial data for the AMR evolution code. The stars obey a polytropic equation of state $P = K\rho^{\Gamma}$ with index $\Gamma = 2$. As Shibata et al. (2002) the profile of the angular velocity Ω is given by

$$\Omega = \frac{\Omega_0 \hat{A}^2}{(\varpi/r_e)^2 + \hat{A}^2}, \tag{12.11}$$

where r_e is the equatorial radius of the star, Ω_0 is the central angular velocity, ϖ is the distance to the rotation axis, and $\hat{A}$ parametrizes the degree of differential rotation, from $\hat{A} \ll 1$ for highly differentially rotating stars to $\hat{A} \to \infty$ for rigidly rotating stars. For comparison purposes these parameters are chosen as in some of the models of Shibata et al. (2002), and are summarized in Table 12.1. Models labelled D rotate with a high degree of differential rotation, as $\hat{A} = 0.3$, and may therefore be subject to the low $T/|W|$ bar-mode instability. We also consider models almost rigidly rotating, labelled R, prone to experience the "classical" bar-mode instability. Labels L and H in the models refer to low and high resolution respectively.

Following Shibata et al. (2002) we perturb the initial density profile $\rho^{(0)}$ according to

$$\rho = \rho^{(0)} \left(1 + \delta \frac{x^2 - y^2}{r_e^2}\right), \tag{12.12}$$

the perturbation of the pressure given by the equation of state accordingly. A perturbation amplitude $\delta = 0.1$ is used in all our simulations. As we show below this form of the perturbation excites the $l = m = 2$ bar-mode. In

addition, grid discretization can leak small amounts of energy to all other possible modes, which could in principle grow provided they were unstable and the simulations were carried on for sufficiently long times.

12.4.2 Stability analysis

To compare with Shibata et al. (2002) we calculate the distortion parameters η_+ and $\eta_\times$ (and $\eta = (\eta_+^2 + \eta_\times^2)^{1/2}$) defined as

$$\eta_+ \equiv \frac{I_{xx} - I_{yy}}{I_{xx} + I_{yy}}, \qquad \eta_\times \equiv \frac{2I_{xy}}{I_{xx} + I_{yy}}, \tag{12.13}$$

where $I_{ij}(i,j = x,y,z)$ is the mass-quadrupole moment

$$I_{ij} = \int d\mathbf{x}^3 \rho\, x^i x^j. \tag{12.14}$$

For the study of the growth rate and interaction of the different angular modes within the star is useful to calculate the global quantity

$$A_m = \int d\mathbf{x}^3 \rho(\mathbf{x})\, e^{-im\varphi}, \tag{12.15}$$

and $\mathcal{A}_m \equiv A_m/A_0$. We follow the time evolution of modes with m ranging from 1 to 8. Since our initial equilibrium models are axisymmetric and have equatorial plane symmetry, all $\mathcal{A}_m$ are zero initially, but once perturbed all initial models exhibit a dominant $m = 2$ component. Assuming that the modes behave as $e^{-i(\sigma_m t - m\varphi)}$, the real part of σ_m can be obtained by Fourier transforming $\mathcal{A}_m$. In particular $\mathrm{Re}(\sigma_2)$, the bar-mode frequency, can be extracted from either $\mathcal{A}_2$ or η as both represent the same mode. This is the dominant mode in all our simulations and its frequency and growth rate are given in Table 12.1. The latter corresponds to the imaginary part of σ_2, which is calculated fitting an exponential to the peak values of η in the growing phase of the evolution until the modes saturate. Other modes are also identified in the simulations for values of $\mathcal{A}_m$ with lower amplitudes. We have checked that these modes are harmonics of the $l = m = 2$ mode so that they follow to good accuracy the relation $\sigma_m = m\sigma_p$, σ_p being the pattern frequency, calculated as $\sigma_p = \sigma_2/2$. This is shown for model D3H in Fig. 12.1 which displays the

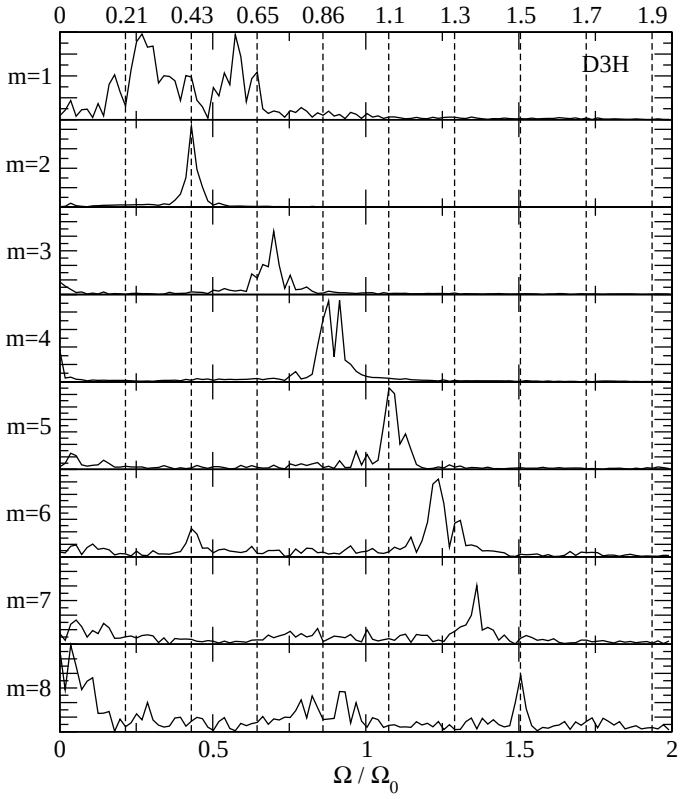

Figure 12.1: Power spectra of $\mathcal{A}_m$ from $m = 1$ to $m = 8$ for model D3H.

spectrum of $\mathcal{A}_m$ from $m = 1$ to $m = 8$ (in arbitrary units). The vertical dashed lines in this figure indicate the location of the integer multiples of the pattern frequency σ_p, their values indicated on the axis at the top of the figure. Each spectrum for each mode is normalized to its own maximum for plotting purposes. Note that the lower the mode amplitude the noisier the spectrum and the less accurate the relation $\sigma_m = m\sigma_p$.

For the models of our sample subject to the "clasical" bar-mode deforma-

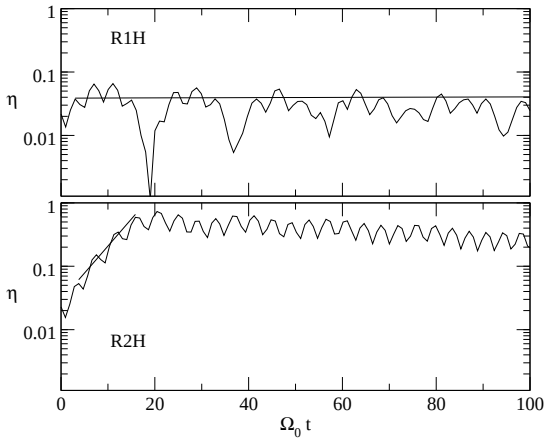

Figure 12.2: Evolution of η for models R1H (upper panel) and R2H (lower panel). Exponential fits to the peaks in the growing phase are overplotted as solid lines.

tion (R1H and R2H), our simulations yield a value of β between 0.253 and 0.275, in good agreement with the critical value for the onset of the dynamical bar-mode instability. Model R1H is stable and model R2H is unstable. The growth rates and frequencies reported in Table 12.1 agree with those of Shibata et al. (2002). Note that for model R1H, which is stable, the frequency for the $m = 2$ mode cannot be computed. The time evolution of η for these two models is displayed in Fig. 12.2. For the unstable model R2H, our simulations show the formation of a bar (See Fig. 12.3) which saturates for values of η_+ and $\eta_\times$ close to 1, i. e. in the full nonlinear regime.

Fig. 12.4 shows the time evolution of η for models D in our sample, prone to suffer the low $T/|W|$ bar-mode instability. Solid lines correspond to high resolution simulations and dashed lines to low resolution. For all three models the pattern frequencies σ_p are such that there exists a corotation radius inside the star, i.e. a radius at which the bar-mode rotates with the same angular velocity as the fluid. The location of the corotation radius for all models of our sample is reported in Table 12.1. As recently discussed by Watts et al. (2005) the existence of such corotation radius is a potential requirement for the ocurrence of the instability. As becomes clear from Fig. 12.4, all models are unstable but grid resolution has an important effect on the saturation of the instability once the nonlinear phase has been reached, as well as in the

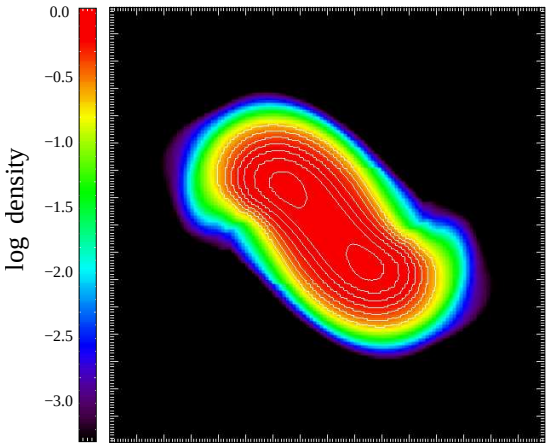

Figure 12.3: Logarithm of density normalized to maximum density (color coded and contours) for model R2H at time $\Omega_0 t = 18.0$.

long-term dynamics of the stars.

In the linear phase of models D1H and D2H, the growth rates and frequencies agree with the results of Shibata et al. (2002) in both, the numerical simulations and the linear analysis (see Table 12.1). In the linear phase of model D3H, our frequencies are similar to the numerical results of Shibata et al. (2002), although our growth rates are about a factor two larger. We emphasize that no results are reported in the linear analysis for this model in the work of Shibata et al. (2002), and therefore this discrepancy can be an effect of the resolution used or of the characteristics of each numerical code. Increasing resolution leads to similar results in the frequencies but to higher growth rates.

In the nonlinear phase, models D1 and D3 behave similarly for the two resolutions used (see Fig. 12.4), and also similarly to the results by Shibata et al. (2002) (compare with Fig. 3 of that paper). For model D2 we observe a radical change of behavior in the nonlinear phase of the mode evolution depending on the grid resolution. This has implications on the long-term dynamics of the star and, in particular, on the attainable amplitudes of the gravitational radiation emitted, as we discuss below.

It is worth mentioning the possibility that the unstable mode at the start of model D2H might excite some other mode in the corotation band, which could

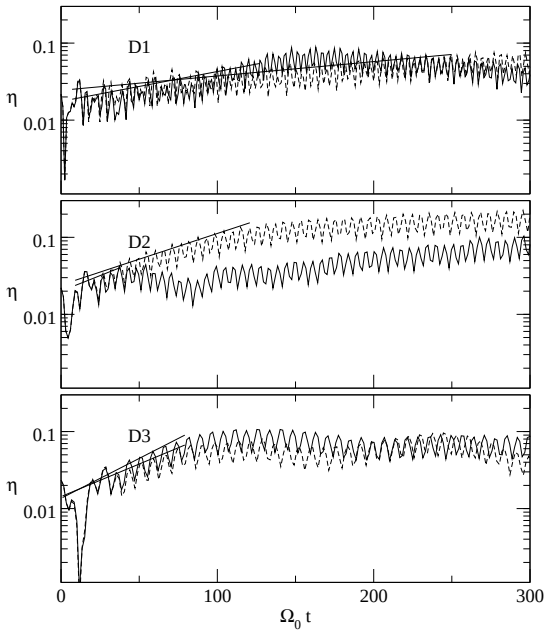

Figure 12.4: Evolution of η for models D1 (upper panel), D2 (central panel) and D3 (lower panel). Dashed lines correspond to low resolution and solid lines to high resolution. Exponential fits to the peaks in the growing phase are overplotted as solid lines.

not otherwise be excited for lower grid resolution. As discussed by Watts et al. (2003, 2004) in their study of differentially rotating shells, there are many zero-step modes in the band, so that the whole continuous spectrum could potentially be excited. In such case these modes would have very slow power-law growth.

For all our models we have checked mass conservation along the evolution. The worst results are obtained for model D3H, for which mass is conserved within 2.5% error when the instability saturates. At the end of the simulation (after 48 orbital periods and 25000 iterations in the coarsest grid) the error has grown to only 6%. For all other models mass conservation is even more accurate. Note that these errors are within the round-off error of the code, and it is not related to the conservation properties of the numerical scheme itself. For a regular grid with 128^3 cells and a simulation employing 25000 iterations, the accumulated round-off error (binomial distribution) using single-precision

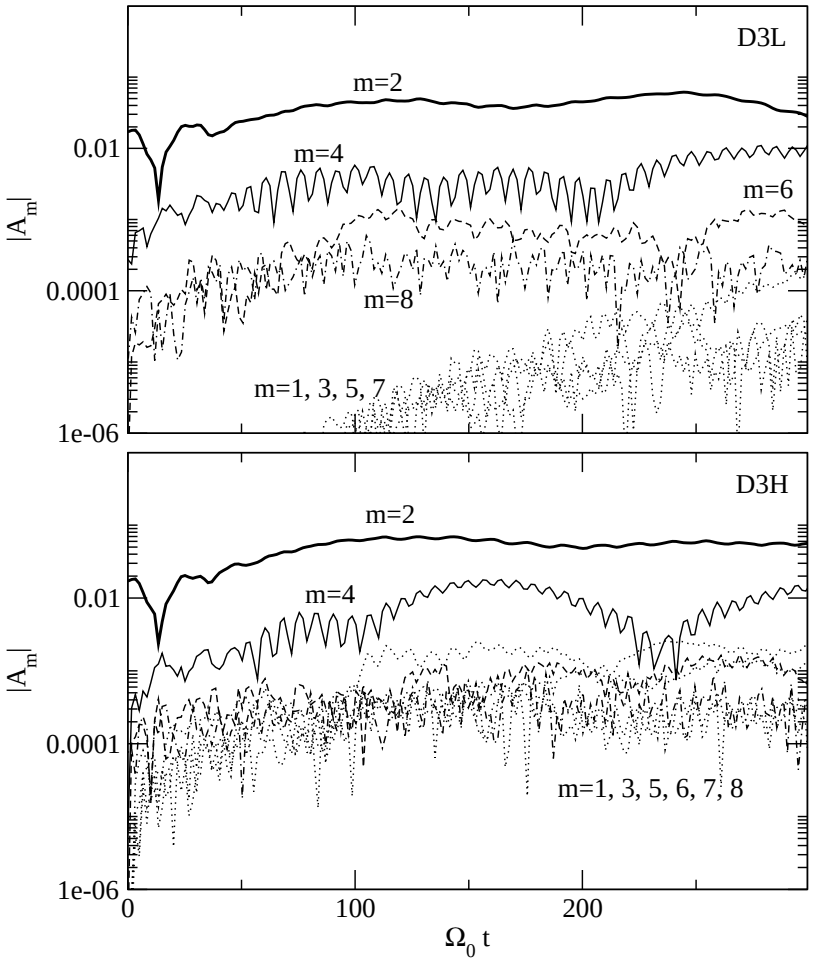

Figure 12.5: Evolution of $|\mathcal{A}_m|$ for model D3 with low resolution (top) and high resolution (bottom). The $m = 2$ mode is represented with thick solid line, $m = 4$ with thin solid line, $m = 6$ with dashed line, $m = 8$ with dot-dashed line, and all other odd m with dotted lines.

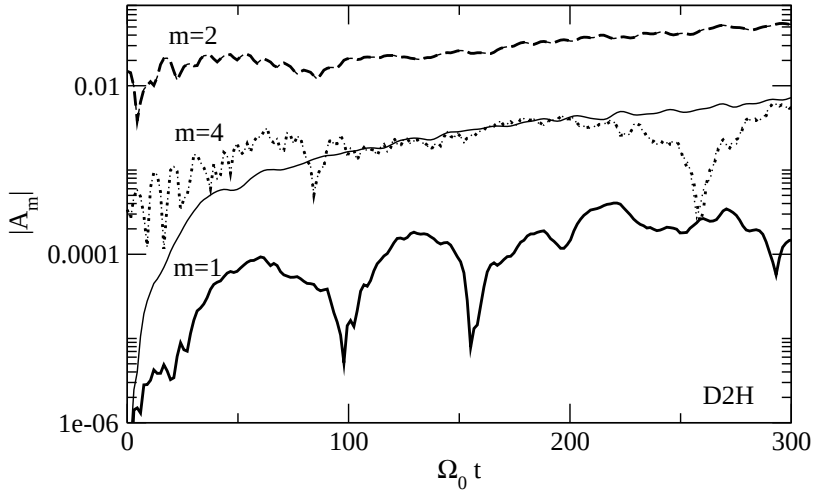

Figure 12.6: Effects of the artificial displacement of the center of mass (of only one numerical cell) on the time evolution of $|\mathcal{A}_1|$ for model D2H. The thin solid line shows a fictitiuos evolution resulting from the numerical artifact originated by the center of mass displacement.

arithmetics, is about $\sqrt{128^3 \times 25000} \times 10^{-8} = 0.0023 = 0.23\%$. Correspondingly, for a 256^3 grid (with twice the number of iterations for the simulation) the error is about 0.9%. Taking into account that this error affects the nonlinear evolution of the system, it is not surprising to have an error at the level of a few percent by the end of our high resolution simulations, for all conserved quantities.

Figure 12.5 shows the evolution of $\mathcal{A}_m$ for model D3 and for m ranging from 1 to 8 for our two resolutions. According to this figure, the only two modes relevant for the dynamics of the star are $m = 2$ and $m = 4$. All other modes have smaller amplitudes and play no role in the dynamics. Note that for odd m modes, the value of the integrated quantity $\mathcal{A}_m$, if close to zero, is extremely sensitive to very small numerical asymmetries, which are induced by the patch creation scheme of our AMR code. This explains the resolution

differences in the initial values for odd m modes in Fig. 12.5 (at $t = 0$ they start off at 10^{-8} level for the low resolution simulation), although they saturate at the same value irrespective of the resolution.

An important diagnosis for the accuracy of the results is the location of the center of mass during an evolution. The round-off error of the numerical code imposes controlled errors in mass and linear momentum, which results in tiny displacements of the center of mass. However small (one numerical cell in our runs) this unphysical displacement may hinder the correct analysis of the mode growth rates. For this reason all integrated quantities shown in Fig. 12.5 are computed after correcting for the displacement of the center of mass, $\mathbf{x}_{\rm new} = \mathbf{x}_{\rm old} - \mathbf{x}_{\rm CM}$, in a post-processing stage of the data analysis. Were this not done, a one-armed $m = 1$ mode would grow much faster than it should to bring up fictitious features in the plots. This is shown for model D2H in Fig. 12.6. The thick solid line in this figure corresponds to the evolution of the $m = 1$ mode taking into account the correction for the center of mass displacement, while the thin solid line is the corresponding evolution of this mode without the correction.

12.4.3 Gravitational waves

The growth and saturation of the instability is also imprinted on the gravitational waves emitted. The gravitational waveforms h_+ and $h_\times$ for models D1, D2, and D3, computed using the standard quadrupole formula, are shown in Fig. 12.7. For a source of mass M located at a distance R those waveforms can be calculated from the dimensionless waveform amplitudes a_+ and $a_\times$ as

$$h_{+,\times} = a_{+,\times} \frac{\sin^2\theta}{R} \frac{M^2}{r_e}, \tag{12.16}$$

using $G = c = 1$ units. The resulting chirp-like signal in all the models, particularly apparent for model D2L, indicates the presence of a bipolar distribution of mass within the star (see Sec. 12.4.4).

As mentioned before, the effects of grid resolution on the evolution of the nonlinear phase of the bar-mode are imprinted on the gravitational waveforms. Thick solid lines in Fig. 12.7 are the waveforms which correspond to the low-resolution models, and thin solid lines to the high-resolution counterparts. The

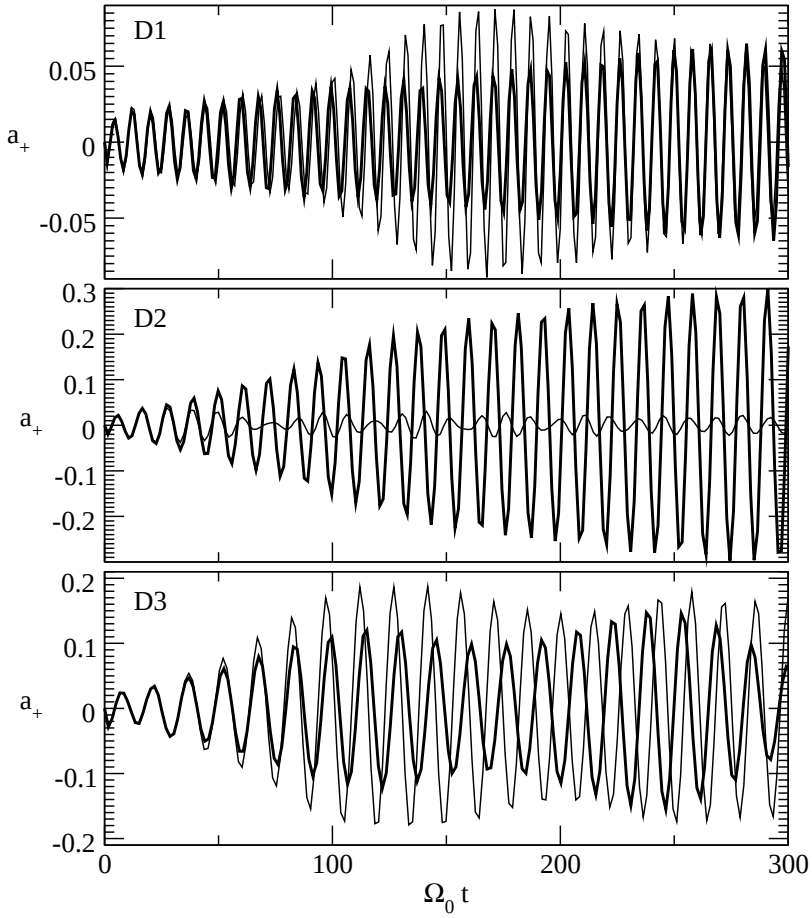

Figure 12.7: Gravitational waves for models D1 to D3 extracted using the standard quadrupole formula. Thick (thin) solid lines correspond to low (high) resolution. Only the dimensionless waveform amplitude a_+ is plotted.

evolution of η for model D3, displayed in Fig. 12.4, shows little deviations with grid resolution, and this translates into very similar gravitational wave patterns (bottom panel of Fig. 12.7), the differences becoming more noticeable in the nonlinear phase following saturation ($\Omega_0 t \geq 75$). For model D1 (top panel), the differences also become more apparent at later times during the evolution, in good agreement with the dissimilar behaviour of the matter dynamics in this model, as encoded in the evolution of η in Fig. 12.4. As happens for model D3 the first few cycles of the gravitational waveform, when the mode is still in the linear phase, are accurately captured for both resolutions.

The major dependence of the waveform on the grid resolution is found for model D2. Again, the linear phase for the growth of the bar deformation is accurately captured irrespective of the resolution (and agrees with the perturbative results of Shibata et al. 2002). This is signalled in the perfect overlapping of both gravitational waveforms during the first three cycles (see the middle panel of Fig. 12.7). However, the different nonlinear dynamics of the bar-mode deformation for this model, shown in the middle panel of Fig. 12.4, is severely imprinted on the gravitational waveform. Model D2H emits gravitational waves which have roughly one order of magnitude smaller amplitude than those computed for the corresponding low resolution model.

12.4.4 Morphology

We next describe the morphological features encountered during the evolution of some representative models. Fig. 12.8 shows three snaphsots of the evolution of model D3H for the density (top), the azimuthal component of the vorticity, $\vec{w}^{\varphi} = (\nabla \times \vec{v})^{\varphi}$ (middle), and the specific angular momentum, $\vec{l} = \vec{r} \times \vec{v}$ (bottom). From left to right the snapshots correspond to the initial time ($\Omega_0 t = 0$), a time when the bar-mode instability is growing ($\Omega_0 t = 33.6$), and the time when the instability saturates ($\Omega_0 t = 70.4$). Only the equatorial plane of the stars is shown in all these plots. Animations of all simulations performed can be found on the CD. We note that our AMR code is able to dynamically place patches (e. g. between 4 and 8 in the D3H model) and evolves the system with continuous matching between patches, as exemplified in Fig. 12.8.

The evolution of model D3H shows that as the $m = 2$ mode grows the star develops an ellipsoidal shape which remains spinning beyond saturation. Since the low β $m = 2$ mode saturates at lower values ($\eta \sim 0.1$) than the

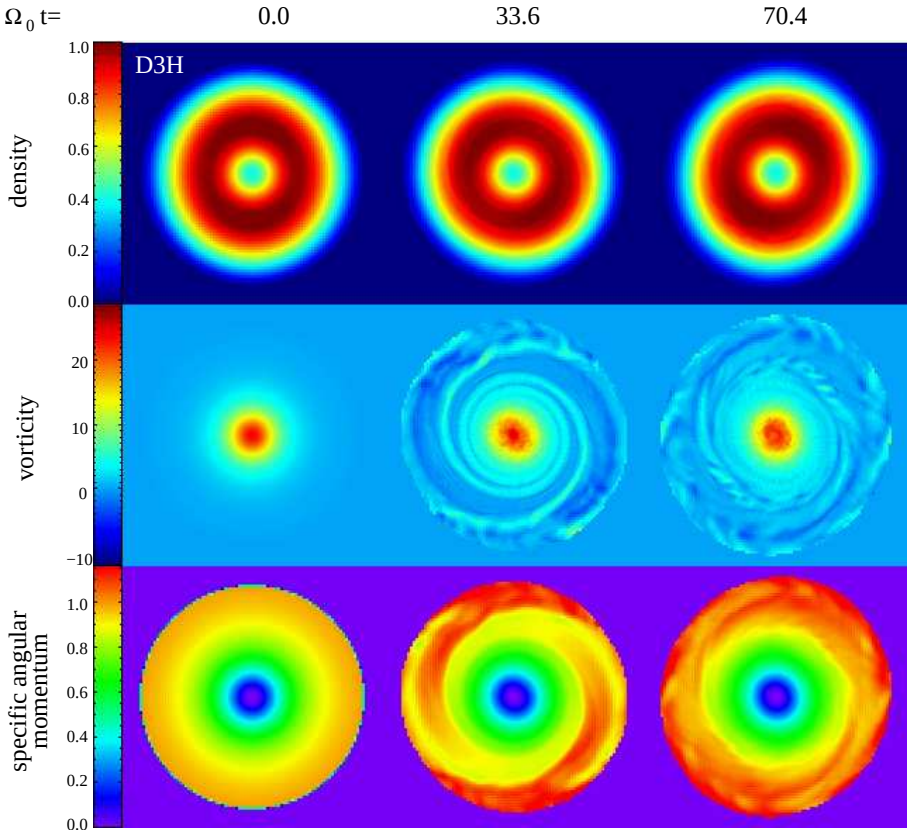

Figure 12.8: Snapshots of the density, vorticity, and specific angular momentum, for model D3H, at three representative instants of the evolution. All snapshots show slices of the stars in the equatorial plane. Quantities are normalized as follows: $\rho/\rho^{(0)}_{\rm max}$, $r_e w^\varphi / v_s^{(0)}$, and $l^\varphi/(r_e v_s^{(0)})$, where $v_s^{(0)}$ is the initial velocity at the surface of the star.

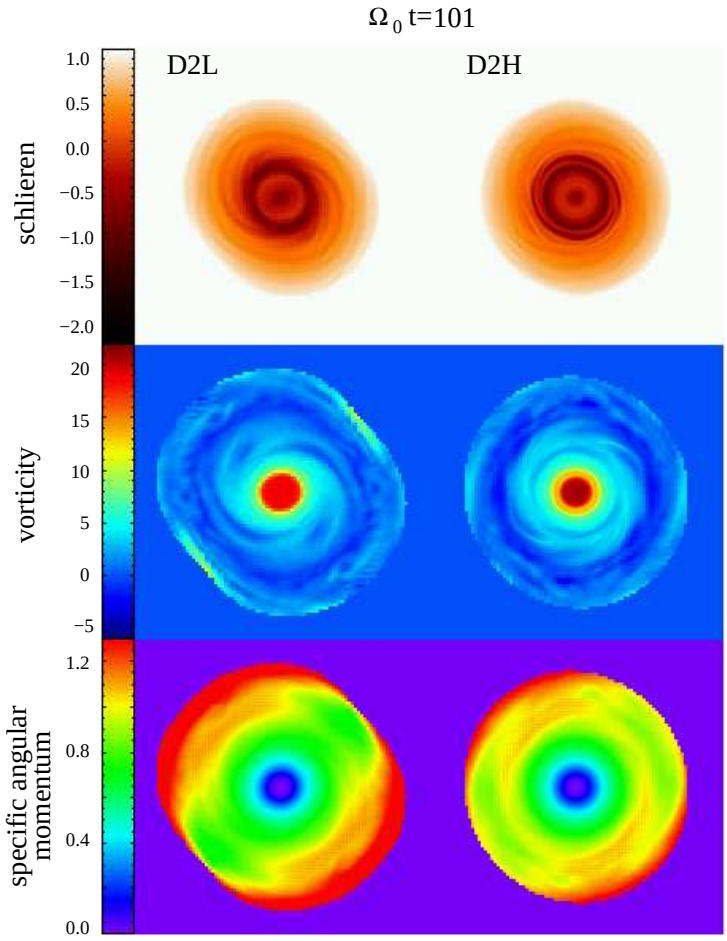

Figure 12.9: Resolution comparison between models D2L and D2H once the instability has saturated. Only slices of the stars in the equatorial plane are shown.

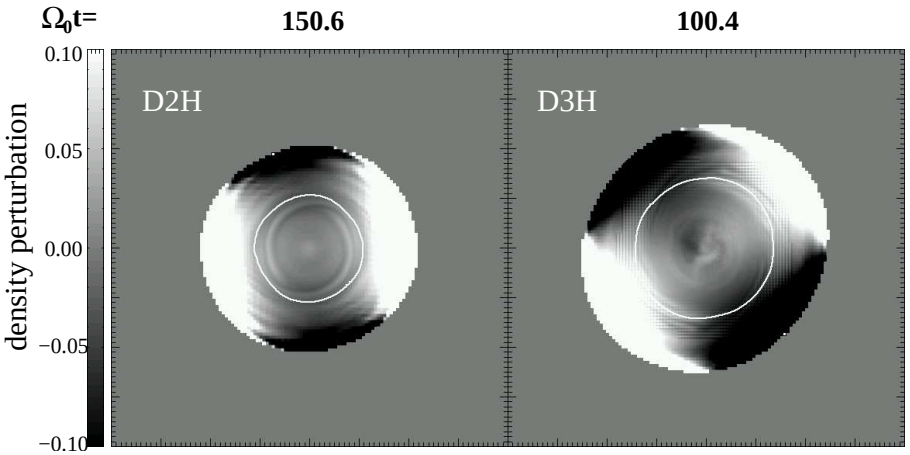

Figure 12.10: Snapshots of the density perturbation at the equatorial plane for models D2H and D3H. The white solid curves indicate the location of the corotation radius.

classical bar-mode instability ($\eta \sim 1$), no clear bars are visible in the density plot. At late times ($\Omega_0 t > 100$) a "boxy" structure becomes apparent as the $m = 4$ mode has grown to almost similar amplitude as the $m = 2$ mode (see animations and Fig. 12.5). No other global features can be seen, consistent with the fact that $|\mathcal{A}_m| \ll 1$ for all modes other than $m = 2$ and 4. The vorticity plot shows that the $m = 2$ mode at $\Omega_0 t = 33.6$ adopts the form of a two-armed spiral winding up around the central parts of the star. As the mode begins to saturate ($\Omega_0 t = 70.4$) the spirals break apart into the outer layers in a turbulent flow reminiscent of the (shear) Kelvin-Helmholtz instability, and shock as they reach the atmosphere. These trends are also visible in the specific angular momentum plot.

The presence of a corotation radius, at $r/r_e = 0.56$ for model D3H, seems to play a role in the growth and saturation of the instability, in agreement with the recent findings of Saijo & Yoshida (2005). As the bar-mode grows, pressure waves carry angular momentum outside the corotation radius, which

is deposited in the outer layers of the star. This excites Kelvin-Helmholtz-like instabilities in the fluid that break the mode outside the corotation radius. When this happens the $m = 2$ instability stops growing and no more angular momentum is extracted. Figure 12.10 shows late-time snapshots of the equatorial plane distribution of the density perturbation, i.e. $(\rho - \rho^{(0)})/\rho^{(0)}_{\rm max}$, for models D2H and D3H. The times are chosen well inside the nonlinear and saturation phase of the instability. This figure helps to interpret the mode dynamics and its saturation along the lines mentioned before: During the evolution the density perturbations are shed in waves from the center towards the outer layers of the star. At late times, when the instability saturates, such shedding stops, and the density perturbation reaches the largest values outside the corotation radius (depicted with white solid lines in Fig. 12.10), for either model.

We note in passing that the corotation radius in all our high resolution models lies well inside the outer boundary of the finest box set up by the AMR refinement pattern. This rules out the possibility of a numerical artifact resulting from the patch creation scheme of our AMR code being the cause for the different long-term evolution between low and high resolution models, particularly noticeable for model D2 in Fig. 12.4.

Finally, Fig. 12.9 shows a comparison between models D2L and D2H at $\Omega_0 t = 101$ (i.e. well within the nonlinear phase), to highlight the effects of the numerical resolution on the morphology. From top to bottom this panel shows a schlieren plot ($|\nabla \log \rho|$) , $\vec{w}^{\varphi}$, and $\vec{l}$. The resolution differences in the evolution of model D2 become apparent from this figure. In particular, the "boxy" structure becomes much more clearly visible in the low resolution simulation (D2L), indicating an excessive growth rate of the $m = 4$ mode. The presence of pressure waves is emphasized in the schlieren plot, very accurately captured in model D2H. Those waves, once the flow is driven to turbulence past the corotation radius, redistribute the angular momentum in the outer layers of model D2L in a much more pronounced way than for model D2H.

Part V

SUMMARY AND OUTLOOK

Chapter 13

Summary and outlook

The final chapter summarizes the results presented in this thesis for the different scenarios that have been studied: core collapse, evolution of proto-neutron stars, and bar-mode instabilities of neutron stars. Where applicable we mention possible extensions of the work presented to be carried out in the future.

13.1 Core collapse simulations

We have presented results for the collapse of rotating stellar cores incorporating two main improvements with respect to previous studies: the CFC+ approximation to the Einstein's field equations, and the evolution of 'test' magnetic fields in dynamical spacetimes. We summarize next our main results on these two issues, and we provide an outlook on future work on core collapse.

13.1.1 CFC+: improved dynamics and waveforms

In Chapters 5 and 9 we have presented a new approximation for the Einstein's field equations, which we call CFC+. We tested its suitability for simulations of rotating neutron star spacetimes, both for equilibrium models and for configurations formed after gravitational core collapse. This approach is based on second order post-Newtonian corrections to conformal flatness, i.e. CFC+

represents an extension of the CFC (or Isenberg–Wilson–Mathews) approximation. The derivation of the extended system of equations has been presented in great detail, as well as the boundary conditions to apply when numerically solving them. All CFC+ field equations are elliptic, since at second post-Newtonian order the hyperbolic character of Einstein's equations disappears. This is a consequence of the fact that the time derivatives of $h_{ij}^{\rm TT}$ appear first at the 2.5th post-Newtonian order.

We note in passing that solving elliptic equations ensures numerical stability of the solution and avoids numerical problems sometimes encountered in long-term evolutions of strongly gravitating systems when using the $3+1$ formulation of general relativity. On the other hand, the price to pay for using this approximation is that gravitational radiation reaction on the dynamics, caused by gravitational waves carrying away energy and angular momentum from the system, is absent. However, in the case of models where a comparison of our results to fully general relativistic results is possible, we checked that the absence of gravitational back-reaction does not significantly affect the results. In scenarios such as the merging of compact binaries (not investigated here), this effect would indeed be important, but only at late times. Hence, CFC+ should also be a good approximation for modeling phenomena occurring on dynamical timescales, such as the final stages of the plunge and merger.

We compared the new CFC+ approximation with the CFC approach used by Dimmelmeier et al. (2002a,b) in two different scenarios, oscillating relativistic stars and core collapse to a neutron star. In the case of pulsating neutron stars, we find that there are no differences in the calculation of the quasi-radial normal mode frequencies of those objects, even in the most extreme situations considered when the star is rotating at the maximum allowed rate (i.e. at the mass-shedding limit). It has been possible to compare our results directly with fully general relativistic computations and, again, a very close agreement is found. Furthermore, our simulations of stellar core collapse to neutron stars covered the basic morphology and dynamics of core collapse types studied by Dimmelmeier et al. (2002b), including the extreme case of a core with strong differential rotation and torus-like structure. Once more, no significant differences between the two approximations are observed. Therefore, we can conclude that second post-Newtonian corrections to CFC do not significantly improve the results when simulating the dynamics of core collapse to a neutron star as well as when investigating the evolution of neutron stars

in equilibrium.

Regarding the gravitational wave extraction we also did not observe any substantial differences between CFC and CFC+ either. The comparison has been carried out using the quadrupole formula, commonly employed in the literature to extract gravitational waveforms. In addition we also calculated the gravitational waves directly from the $h_{ij}^{\rm TT}$ components, which permits a straightforward use of the spacetime metric to study the gravitational wave generation mechanism from the near zone to the wave zone. Although the waveforms computed with the latter approach cannot be regarded as an independent way of calculating gravitational wave signals, it nevertheless provides a good consistency check of the CFC+ approximation that has served to validate the numerical scheme we use to calculate $h_{ij}^{\rm TT}$.

The main conclusion of Chapter 9 is the assessment of the CFC approximation as a highly suitable alternative to the full Einstein's equations in axisymmetric scenarios, involving rotating neutron stars in equilibrium and as end states of core collapse. These findings are supported by two facts: First, we demonstrated that second post-Newtonian corrections do not play an important role in either the dynamics or the gravitational radiation waveforms of core collapse. This suggests that higher order post-Newtonian corrections will be completely insignificant at least on dynamic timescales. Second, the direct comparison of the CFC approach with exact fully general relativistic simulations of pulsating neutron stars yields normal-mode frequencies in excellent agreement. Furthermore, comparisons of the CFC approach with fully general relativistic simulations were also reported recently by Shibata & Sekiguchi (2004) in the context of axisymmetric core collapse simulations. Again, the differences found in both the dynamics and the waveforms are minute, which highlights the suitability of CFC (and CFC+) for performing accurate simulations of those scenarios without the need for solving the full system of the Einstein equations.

13.1.2 Magnetized core collapse

In Chapter 10 we have presented simulations of the collapse of rotating magnetized stellar cores, as well as tests assessing our numerical approach to solving the ideal general relativistic magneto-hydrodynamics equations.

We have designed a method for calculating stationary configurations of

weakly magnetized stars in general relativity, with either toroidal or poloidal (or both) magnetic field components. As a first step we have used the "test" passive field approximation for these initial models, for which the magnetic pressure in all cases considered is several orders of magnitude smaller than the fluid pressure.

We have performed tests to check the accuracy and convergence properties for the GRMHD extension of our code. We have found an order of convergence larger than one in the magnetic field in all of the performed tests. In the stationary cases (TTA, TTB) the order of convergence obtained is higher than two. These results are consistent with the second-order accuracy, in space and time, of our numerical scheme, only reduced to first order at shocks. The resolution needed to correctly evolve the magnetic field in a core collapse simulation has been established. The errors in all of the cases in which the theoretical solution is known are below 0.1%, except at shocks, which are correctly captured within a couple of numerical cells due to the use of HRSC schemes.

Regarding simulations of magnetized core collapse in the CFC approximation, we have considered cases with initially purely poloidal magnetic field (series D3M0) and with initially purely toroidal magnetic field (series T3M0), in the passive field approximation. The D3M0 models are a general relativistic extension of a subset of the cases considered by Obergaulinger et al. (2005) in Newtonian gravity and MHD. Our aim has been to compare the dynamics and gravitational waveforms with those previous results. No qualitative differences have been found in the models studied, although the strength of the magnetic field at bounce and after the collapse is consistently smaller ($50-80\%$) in the CFC case than in the Newtonian case.

In each series of models the amplification of the magnetic field proceeds in a very different way. While in the D3M0 models the winding up of the poloidal magnetic lines into toroidal magnetic field lines due to differential rotation (Ω-dynamo) is the main amplification mechanism in the collapse, in the T3M0 models the magnetic field is amplified only due to the radial compression, as poloidal magnetic fields are absent in the evolution. We have found that, for our particular models, the Ω-dynamo is much more efficient in amplifying the magnetic field than radial compression. Therefore, the final toroidal magnetic field in the T3M0 models is weaker than in the D3M0 models, in which no toroidal component was present initially.

At the end of our simulations the fluid variables reach a quasi-equilibrium state. For the D3M0 models the formed proto-neutron star has a core/shell structure. Inside the core, where nuclear matter density is reached, the dominant magnetic field is poloidal and the rotation profiles are almost flat, i.e. the PNS core rotates rigidly. On the other hand, the surrounding shell rotates differentially and, hence, toroidal magnetic fields dominate this region due to the Ω-dynamo mechanism. This effect produces a sustained linear growth of the toroidal component after the bounce. If no other processes act, the magnetic field is expected to saturate after $\sim$ 1 s with values of about $B^{\varphi} \sim 10^{15}$ G. For the models T3M0 the Ω-dynamo is not active, since no poloidal magnetic field is present. Therefore, when the PNS reaches a quasi-equilibrium state, the magnetic field remains stationary.

Other amplification mechanisms can act if no passive magnetic field approximation is considered or if the axisymmetry condition is removed. We have estimated the effect of the amplification mechanism that is more likely to dominate, that is, the magneto-rotational instability. We have found that during the collapse, the typical timescale of the fastest growing mode of the MRI is about 1 s, and hence it will not affect our results in the infall phase. However, after the bounce two regions are susceptible to develop MRI, the region behind the shock wave and the convective region surrounding the PNS. In both regions the estimated timescale, $\sim$ 1 ms, is of the order of the dynamical timescale. In simulations without the passive field approximation and with sufficiently high resolution, the MRI is expected to develop in these regions, and to dominate their dynamics within a few ms.

13.1.3 Going further

Our results show that a numerical code based on CFC is a very useful tool for investigating core collapse to neutron stars in general relativity. Hence, the CFC approach (as well as CFC+) is suitable to form the basis of a future core collapse supernova code which can be gradually extended in various directions to incorporate additional physics such as realistic equations of state, magnetic fields fully acting on the dynamics, and eventually neutrino transport. In the near future we plan to further validate the CFC+ equations in other scenarios where higher densities are present (e.g. collapse to a black hole), as well as in the fully three-dimensional case (namely to investigate the merging of neutron

stars). Such scenarios are in principle beyond the range of applicability of the CFC approximation, but can possibly still be handled in a satisfactory way with the new CFC+ approach presented in this thesis. Some of the immediate extensions we are working on are briefly described next.

GRMHD: active field

The passive approximation for the magnetic field has shown to be very useful in the study of the evolution of weakly magnetized objects as core collapse progenitors. However, the absence of a reaction of the magnetic field on the matter dynamics prevents some instabilities to develop, such as the MRI, which amplifies the magnetic field exponentially in time from arbitrarily weak magnetic fields. The study of this effect on the post-bounce dynamics is of crucial importance, as it is going to affect a number of processes: (i) the amplification of the magnetic field can change the structure of the PNS, in particular its rotation profiles, which could become constant, preventing the development of three-dimensional instabilities (e.g. bar-mode instabilities), which are strong sources of gravitational waves. (ii) The turbulence generated in the dynamics could lead to detectable gravitational wave signals in a similar way as the convective unstable regions described by Müller et al. (2004). (iii) The amplification of the magnetic field behind the shock can enhance the effect of the neutrinos to power the delayed explosion of the supernova.

Furthermore, in other gravitational collapse scenarios such as jet-like explosions or the collapsar model for GRBs, strong magnetic fields could play an important role in the collimation of the matter flows leaving the system along the axis.

With all those scenarios in mind we have already extended the GRMHD code reported in this thesis to the general case without the passive field approximation. To this end we have taken advantage of the numerical schemes developed in Antón et al. (2006) and Antón (2006) to build a robust code with the capability of solving the ideal GRMHD equations within a dynamical spacetime in the CFC/CFC+ approximation. A version of this code is just finished, although some tests still have to be done.

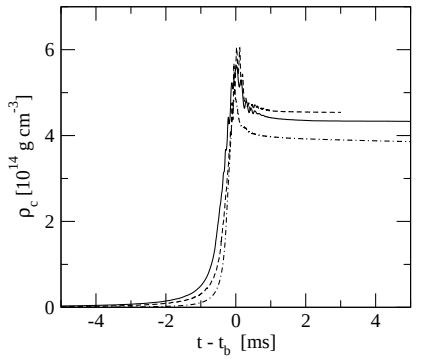

Figure 13.1: Time evolution of the central density in a spherical core collapse using the LS EOS (see text) with realistic initial models (solid line) and adapted polytropes as initial models (dashed line). For comparison we have plotted the evolution for the case of the hybrid EOS with similar initial models.

Realistic equation of state

We are currently working towards the inclusion in the collapse modelling of more realistic equations of state than the one used in this thesis. We have obtained preliminary results for spherical core collapse using the equation of state of Lattimer & Swesty (1991) (LS hereafter). Although the initial models are spherically symmetric, we do not impose this restriction in the simulation in order to test if the 2D code is able to handle the collapse. To choose the initial models we follow two approaches. First, we collapse the inner iron core of a realistic model from stellar evolution (Heger et al. 2000). A reduction of the internal energy of the model is necessary in order to begin the collapse. The second approach consists in generating an initial model with a polytropic equation of state such that the density and the specific internal energy distributions are as close as possible to those of realistic models. The initial electron fraction is selected to be constant and with values near the realistic models. Our future plan is to generate in a systematic and consistent way, initial models based on polytropes but with similar features (same central density and pressure, and same electron fraction and temperature profiles) as the realistic models from stellar evolution. This will allow us to perform parametric studies for the more general case of rotating core collapse, possibily including a simplified treatment for neutrino transport.

As an example, in Fig 13.1, we show preliminary results for spherical core collapse with the LS equation of state compared with the collapse with the

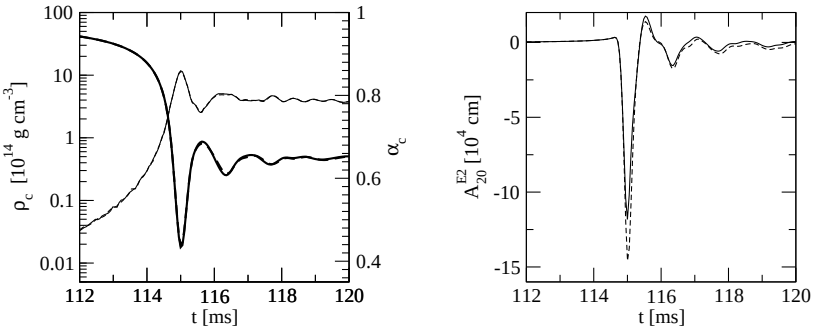

Figure 13.2: Time evolution of the central density (left panel, thin lines), the lapse function (left panel, thick lines), and the gravitational wave amplitude (right panel) for the collapse model M7c5 using the CFC approximation (solid lines) and the CFC+ approximation (dashed lines). In the left panel both curves almost coincide.

hybrid equation of state used in this thesis. The time of bounce in the three cases is different since the way of triggereing the collapse is in all cases arbitrary. In the case of the LS EOS with realistic initial models $t_b = 213$ ms, in the case of polytropic initial models with the LS EOS for the evolution $t_b = 86.4$ ms, and in the case of hybrid EOS $t_b = 30$ ms.

Rotational core collapse to a black hole

In order to validate the CFC/CFC+ approximation in scenarios involving higher densities, we plan to study the case of black hole formation, where the differences between CFC and CFC+ should become more visible. Direct comparisons with full general relativistic simulations using the `CACTUS/WHISKY` code will help us to establish which is the limit of applicability of the CFC and CFC+ approximations, and if they are adequate at all to study the rotational collapse to black holes.

Following this line of research we have performed simulations of the collapse of massive stellar cores to either neutron stars or black holes. Those simulations comprise a subset of the axisymmetric simulations performed by Shibata & Sekiguchi (2005). Our results in the CFC and CFC+ approxima-

tion are very similar to those of Shibata & Sekiguchi (2005) with differences in the evolution of the maximum density of about 2%, with the exception of the extreme model M8c4 where the differences are $\sim 30\%$. In all cases we obtain the same final object as Shibata & Sekiguchi (2005), i.e. a neutron star, a black hole, or a neutron star that undergoes delayed black hole formation after a certain time. Fig 13.2 shows the evolution of model M7c5 of Shibata & Sekiguchi (2005) which forms a neutron star as end product. The evolution of the central density, ρ_c, and central lapse function, α_c, are shown for both the CFC and the CFC+ approximation. Although the differences in these quantities are small, the resulting waveforms display visible differences in the maximum amplitude. More details about these simulations are reported in Dimmelmeier et al. (2005a).

In the near future we plan to perform simulations of the collapse of neutron stars to black holes with detailed comparisons of the different approaches used: CFC, CFC+ and full general relativity (withint the BSSN framework). We also plan to include an apparent horizon finder for the black hole formation, and eventually to implement a BH excision algorithm in the numerical code. The final goal is to study scenarios including black holes and magnetic fields such as thick accretion disks and tori, jet formation, and the collapsar model of GRB, which are of great interest for astrophysics in general, and in the detection of gravitational waves in particular.

Post-Newtonian quadrupole formula

The Newtonian quadrupole formula (NQF) is nowadays the usual way of calculating the gravitational waves from core collapse simulations (the only exception is the work of Siebel et al. (2003)). The validity of this formula for the compact objects involved in the collapse is still unclear. It has been shown in general relativistic simulations (Dimmelmeier et al. 2002a,b) that the dynamics of the sources differs from the Newtonian case, and hence, the waveforms calculated with the NQF also differ. In order to be consistent with the dynamics, general relativistic effects have also to be taken into account in the quadrupole formula itself.

When considering the NQF to extract the GWs from core collapse simulations there is a usual ambiguity related with the definition of the quadrupole moment of a general relativistic object. In the Newtonian limit the mass

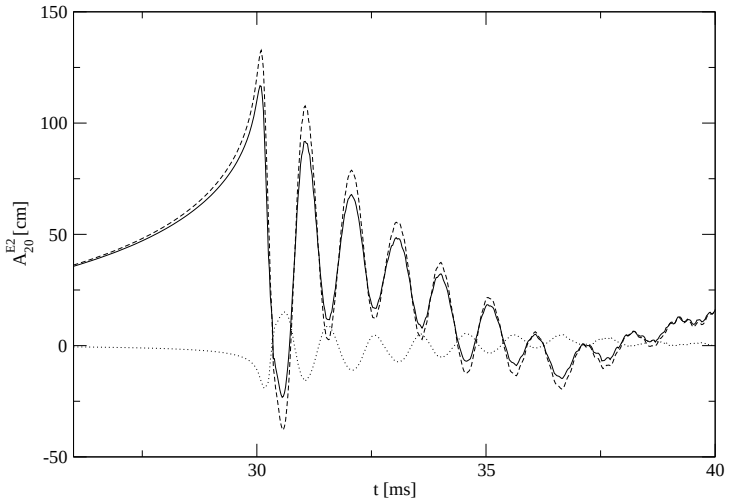

Figure 13.3: Gravitational wave amplitude calculated with the Newtonian quadrupole formula (dashed line) and the 1PN quadrupole formula (solid line). The contribution of the 1PN correction is also plotted (dotted line).

quadrupole is used, i.e. the integrand involves the density ρ, but in general relativity the magnitude appearing in the integrand of the quadrupole moment depends on the particular variables used in the post-Newtonian expansion of the sources. Usually ρ or D^* are used but more complicated forms including metric factors and energy terms are in some cases included (Nagar et al. 2005). Each of these choices is in principle valid and all forms of the NQF should give the same result *in the range of validity of the NQF*. The results from numerical simulations of rotating core collapse show that the waveform extracted with the NQF can differ within a few 10% when using different forms of the NQF. This fact strongly suggests that core collapse dynamics may be out of the range of validity of the NQF (slow motion), and that post-Newtonian corrections should be included.

We are currently working on a 1PN quadrupole formula, which includes terms of first post-Newtonian order in the expansion of the sources. To this end we are adapting the formalism of Faye & Schäfer (2003) to design a method

which allows us to calculate the 1PN correction to the mass quadrupole, in a way well adapted to numerical simulations. In Fig. 13.3 we present preliminary results of the corrected waveforms in a rotational core collapse, namely model A1B3G5. These preliminary data show that the 1PN correction (solid line) is about 20% of the signal extracted with the NQF. The 1PN correction also introduces a phase shift in the signal in some cases.

13.2 Evolutionary sequences of rotating PNS

In Chapter 11 we have addressed the problem of the evolution of rotating proto-neutron stars by constructing evolutionary sequences of axisymmetric, stationary configurations in General Relativity. The thermodynamical structure and evolution have been extrapolated from simulations in spherical symmetry that included neutrino transport. Although this is a crude simplification, it already gives an interesting insight about how the different relevant quantities can evolve as the rotating PNS loses its lepton content and its excess binding energy, and contracts. Moreover, we have found that the luminosity estimates are not very different from what one expects.

A special effort has been made to understand where in the parameter space a realistic case should be located. The biggest uncertainty concerns the rotation law that PNS have at birth. By analyzing results from simplified core collapse simulations, it seems that a typical scale for variations of the angular velocity is about 10 km, and that conservation of angular momentum during the collapse of a stellar core (initially rigidly rotating) does not seem to allow for angular velocities varying on a length–scale shorter than a few km. Less is known about the angular distribution, except that most recent simulations show the presence of important meridional currents and some turbulent motion. For simplicity, we restricted ourselves to the stationary case. Stationarity implies a quasi-cylindrical distribution (with deviations due to relativistic corrections) of the angular velocity. This stage can only be reached after several dynamical and rotation periods, after the PNS had time to relax. Therefore, one must be aware that the first 0.5 s are probably far from stationarity, but after that evolution proceeds in a quasi-stationary way, except for low velocity convective motions. From our study of quasi-stationary sequences we can draw a few interesting qualitative results.

i) For each instant in the evolution, stars with strong differential rotation can have 5 to 10 times larger central angular velocities, and accommodate about a 50% more angular momentum. The maximum specific angular momentum J/M varies between $(1-2)\,GM_\odot/c \approx (0.5-1)\times 10^{16}$ cm^2/s, depending on the degree of differential rotation.

ii) The maximum value of $|T/W|$ obtained in the case of differential rotation is about 0.2, while for rigid rotation it is ≈ 0.11. Thus, differentially rotating PNSs might undergo the CFS instability, which arises at ≈ 0.14 and, in any case, the recently discussed low $|T/W|$ instability (Shibata et al. 2002, 2003; Watts et al. 2003) is plausible to happen.

iii) More interestingly, we found several situations in which, even if the initial model is well below the critical value of $|T/W|$, as the star contracts on a neutrino diffusion timescale of 5-10 s, it speeds up entering the window of instability. An observational evidence of this effect could be a few seconds delay between the neutrino luminosity peak and a gravitational wave burst in the event of a galactic supernova. Ultimately, this depends on the initial amount of angular momentum, which is approximately equal to the angular momentum of the iron core of the progenitor. Recent stellar evolution calculations suggest that the specific angular momentum of the inner 1.7 $M_\odot$ of a 15 $M_\odot$ star can be as high as 3×10^{16} cm^2/s if magnetic braking is neglected, or 10^{15} cm^2/s if magnetic torques are included in the evolution (Heger et al. 2004). This corresponds to $J/M = (0.2 - 6)\ GM_\odot/c$. If the angular momentum happens to be large ($J/M > 2$), centrifugal forces would stop the collapse before the PNS is formed. Intermediate values ($J/M = 1$) may result in the formation of a rapidly rotating PNS that enters the instability region several seconds after the birth. If magnetic braking is very effective during the evolution of a massive star, $J/M < 0.5$, and the PNS will be formed after collapse without reaching extreme values of the angular velocities and $|T/W|$.

The next natural step to improve this work is to include possible mechanisms to transport angular momentum between the different layers of the star, that may involve neutrino transport, turbulent transport, magnetic fields, neutrino viscosity, convective motion, and/or angular momentum losses by gravitational wave emission. Unless the star is born with almost maximum angular velocity, some or all of these dissipative mechanisms can modify our current vision of PNS evolution.

13.3 Low $T/|W|$ bar-mode instability of neutron stars

In Chapter 12 we have presented AMR high-resolution simulations of the low $T/|W|$ bar-mode instability of extremely differentially rotating neutron stars. Our main motivation has been to revisit the simulations by Shibata et al. (2002), assessing how sensitive the onset and development of the instability is to numerical issues such as grid resolution. We have addressed the importance of a correct treatment of delicate numerical aspects which may spoil three-dimensional simulations in (Cartesian) grid-based codes, always hampered by insufficient resolution, namely the handling of the low-density atmosphere surrounding the star, the correction for the center of mass displacement, and the mass and momentum conservation properties of the numerical scheme. Our simulations have revealed the complex morphological features involved in the nonlinear dynamics of the instability. We have found that in the nonlinear phase of the evolution, the excitation of Kelvin-Helmholtz-like fluid modes outside the corotation radii of the stellar models leads to the saturation of the bar-mode deformation. While the overall trends reported in the investigation of Shibata et al. (2002) are confirmed by our work, the resolution used to perform the simulations may play a key role on the long-term behaviour of the instability and on the nonlinear dynamics of rotating stars, which has only become apparent for one specific model of our sample (namely model D2). This, in turn, has implications on the attainable amplitudes of the associated gravitational wave signals.

The work reported in this chapter is a first step in our ongoing efforts of studying the dynamical bar-mode instability within the magnetized core collapse scenario.

Appendices

Appendix A

Flat operators in spherical coordinates

In Chapter 5 we presented a new approach to the metric, the CFC+ approximation, that is briefly described in Section 5.5. However, to implement the resulting formalism in our numerical code, one has to express all equations in spherical coordinates. We present here all the possible contractions appearing in the Eqs. (5.42-5.46) for the intermediate potentials, and Eq. (5.47) for the value of $h_{ij}^{\rm TT}$ in CFC+, needed for the implementation of the CFC+ approximation in a numerical code:

- $W_i \equiv \hat{\nabla}_i S$

$$W_r = \partial_r S \tag{A.1}$$

$$W_\theta = \frac{1}{r}\partial_\theta S \tag{A.2}$$

$$W_\varphi = \frac{1}{r\sin\theta}\partial_\varphi S \tag{A.3}$$

- $W_{ij} \equiv x^k x^l \hat{\nabla}_i \hat{\nabla}_j S_{kl}$

$$
\begin{aligned}
W_{rr} =& r^2\, \partial_{rr} S_{rr} && \text{(A.4)}\\
W_{\theta\theta} =& -2\, S_{rr} + 2\, S_{\theta\theta} - 4\, \partial_\theta S_{r\theta} + \partial_{\theta\theta} S_{rr} + r\, \partial_r S_{rr} && \text{(A.5)}\\
W_{\varphi\varphi} =& 2\, S_{\varphi\varphi} - 2\, S_{rr} - 4 \csc\theta\, \partial_\varphi S_{r\varphi} + \csc^2\theta\, \partial_{\varphi\varphi} S_{rr} \\
& + \cot\theta\, (-4\, S_{r\theta} + \partial_\theta S_{rr}) + r\, \partial_r S_{rr} && \text{(A.6)}\\
W_{r\theta} =& W_{\theta r} = 2\, S_{r\theta} - \partial_\theta S_{rr} - 2r\, \partial_r S_{r\theta} + r\, \partial_{r\theta} S_{rr} && \text{(A.7)}\\
W_{r\varphi} =& W_{\varphi r} = 2\, S_{r\varphi} - \csc\theta\, \partial_\varphi S_{rr} - 2r\, \partial_r S_{r\varphi} + r \csc\theta\, \partial_{r\varphi} S_{rr} && \text{(A.8)}\\
W_{\theta\varphi} =& W_{\varphi\theta} = 2\, \cot\theta\, S_{r\varphi} + 2\, S_{\theta\varphi} - 2\, \partial_\theta S_{r\varphi} \\
& + \csc\theta\, (-\cot\theta\, \partial_\varphi S_{rr} - 2\, \partial_\varphi S_{r\theta} + \partial_{\theta\varphi} S_{rr}) && \text{(A.9)}
\end{aligned}
$$

- $W_{ij} \equiv \hat{\nabla}_i S_j$

$$
\begin{aligned}
W_{rr} =& \partial_r S_r && \text{(A.10)}\\
W_{\theta\theta} =& \frac{1}{r}\, (\, S_r + \partial_\theta S_\theta) && \text{(A.11)}\\
W_{\varphi\varphi} =& \frac{1}{r}\, (\, S_r + \cot\theta\, S_\theta + \csc\theta\, \partial_\varphi S_\varphi) && \text{(A.12)}\\
W_{r\theta} =& \partial_r S_\theta && \text{(A.13)}\\
W_{\theta r} =& \frac{1}{r}\, (-\, S_\theta + \partial_\theta S_r) && \text{(A.14)}\\
W_{r\varphi} =& \partial_r S_\varphi && \text{(A.15)}\\
W_{\varphi r} =& \frac{1}{r}\, (-\, S_\varphi + \csc\theta\, \partial_\varphi S_r) && \text{(A.16)}\\
W_{\theta\varphi} =& \frac{1}{r}\, \partial_\theta S_\varphi && \text{(A.17)}\\
W_{\varphi\theta} =& \frac{1}{r}\, (-\cot\theta\, S_\varphi + \csc\theta\, \partial_\varphi S_\theta) && \text{(A.18)}
\end{aligned}
$$

- $W_{ij} \equiv x^k \hat{\nabla}_i \hat{\nabla}_j S_k$

$$W_{rr} = r\,\partial_{rr} S_r \tag{A.19}$$

$$W_{\theta\theta} = \frac{1}{r}\left(-S_r - 2\,\partial_\theta S_\theta + \partial_{\theta\theta} S_r + r\,\partial_r S_r\right) \tag{A.20}$$

$$W_{\varphi\varphi} = \frac{1}{r}\left(-S_r - 2\csc\theta\,\partial_\varphi S_\varphi + \csc^2\theta\,\partial_{\varphi\varphi} S_r + \cot\theta\,(-2\,S_\theta + \partial_\theta S_r) + r\,\partial_r S_r\right) \tag{A.21}$$

$$W_{r\theta} = W_{\theta r} = \frac{1}{r}\left(S_\theta - \partial_\theta S_r\right) - \partial_r S_\theta + \partial_{r\theta} S_r \tag{A.22}$$

$$W_{r\varphi} = W_{\varphi r} = \frac{1}{r}\left(S_\varphi - \csc\theta\,\partial_\varphi S_r - r\,\partial_r S_\varphi + r\csc\theta\,\partial_{r\varphi} S_r\right) \tag{A.23}$$

$$W_{\theta\varphi} = W_{\varphi\theta} = \frac{1}{r}\left(\cot\theta S_\varphi - \partial_\theta S_\varphi - \csc\theta\,(\cot\theta\,\partial_\varphi S_r + \partial_\varphi S_\theta - \partial_{\theta\varphi} S_r)\right) \tag{A.24}$$

- $W_{ij} \equiv \hat{\nabla}_i \hat{\nabla}_j S$

$$W_{rr} = \partial_{rr} S \tag{A.25}$$

$$W_{\theta\theta} = \frac{1}{r^2}\left(\partial_{\theta\theta} S + r\,\partial_r S\right) \tag{A.26}$$

$$W_{\varphi\varphi} = \frac{1}{r^2}\left(\csc^2\theta\,\partial_{\varphi\varphi} S + \cot\theta\,\partial_\theta S + r\,\partial_r S\right) \tag{A.27}$$

$$W_{r\theta} = W_{\theta r} = \frac{1}{r^2}\left(-\partial_\theta S + r\,\partial_{r\theta} S\right) \tag{A.28}$$

$$W_{r\varphi} = W_{\varphi r} = \frac{1}{r^2}\csc\theta\left(-\partial_\varphi S + r\,\partial_{r\varphi} S\right) \tag{A.29}$$

$$W_{\theta\varphi} = W_{\varphi\theta} = \frac{1}{r^2}\left(\csc\theta\left(-\cot\theta\,\partial_\varphi S + \partial_{\theta\varphi} S\right)\right) \tag{A.30}$$

- $W_{ij} \equiv x^k \hat{\nabla}_i S_{kj}$

$$
\begin{aligned}
W_{rr} =& r\,\partial_r S_{rr} && \text{(A.31)}\\
W_{\theta\theta} =& S_{rr} - S_{\theta\theta} + \partial_\theta S_{r\theta} && \text{(A.32)}\\
W_{\varphi\varphi} =& - S_{\varphi\varphi} + S_{rr} + \cot\theta\, S_{r\theta} + \csc\theta\,\partial_\varphi S_{r\varphi} && \text{(A.33)}\\
W_{r\theta} =& r\,\partial_r S_{r\theta} && \text{(A.34)}\\
W_{\theta r} =& - 2S_{r\theta} + \partial_\theta S_{rr} && \text{(A.35)}\\
W_{r\varphi} =& r\,\partial_r S_{r\varphi} && \text{(A.36)}\\
W_{\varphi r} =& - 2S_{r\varphi} + \csc\theta\,\partial_\varphi S_{rr} && \text{(A.37)}\\
W_{\theta\varphi} =& - S_{\theta\varphi} + \partial_\theta S_{r\varphi} && \text{(A.38)}\\
W_{\varphi\theta} =& - \cot\theta\, S_{r\varphi} - S_{\theta\varphi} + \csc\theta\,\partial_\varphi S_{r\theta} && \text{(A.39)}
\end{aligned}
$$

Appendix B

The Hadamard finite part regularization

It is beyond the scope of this appendix to review all properties of the Hadamard finite part regularization. However, as it is used intensively in Chapter 5, we recall its definition for completeness, as well as those features needed in our derivation of the CFC+ equation. When a function $f(\boldsymbol{x})$, $\boldsymbol{x} \in \mathbb{R}^3$, is smooth outside a finite number of singularities, locally integrable, but not integrable on $\mathbb{R}^3$, we can instead consider the new integrand $(|\boldsymbol{x}-\boldsymbol{x}_0|/r_0)^B f(\boldsymbol{x})$, where B is a complex number, r_0 a positive number, and where $|\boldsymbol{x}-\boldsymbol{x}_0|$ denotes the Euclidean norm of $\boldsymbol{x}-\boldsymbol{x}_0$, with $\boldsymbol{x}_0$ being an arbitrary vector of $\mathbb{R}^3$. The integral $\int_{|\boldsymbol{x}-\boldsymbol{x}_0|>r_0} \mathrm{d}^3\boldsymbol{x}\,(|\boldsymbol{x}-\boldsymbol{x}_0|/r_0)^B f(\boldsymbol{x})$, defined by means of the natural measure $\mathrm{d}^3\boldsymbol{x} = \mathrm{d}x^1\,\mathrm{d}x^2\,\mathrm{d}x^3$ in Cartesian coordinates, converges for B belonging to an appropriate domain D of the complex plane. It can be regarded as a holomorphic function on D. It is then possible to extend $I_f(B) = \int \mathrm{d}^3\boldsymbol{x}\,(|\boldsymbol{x}-\boldsymbol{x}_0|/r_0)^B f(\boldsymbol{x})$ by analytic continuation as close to the point $B=0$ as desired, and to obtain its Laurent expansion $\sum_{k\in\mathbb{Z}}(I_f)_k B^k$ there, as explained by Blanchet & Damour (1986). The zeroth order coefficient $(I_f)_0$ is often referred to as the finite part integral of $f(\boldsymbol{x})$, which in our

notation reads

$$\mathrm{FP}_{B=0} \int \mathrm{d}^3\boldsymbol{x}\, \sqrt{\hat{\gamma}} \left(\frac{|\boldsymbol{x}-\boldsymbol{x}_0|}{r_0} \right)^B f(\boldsymbol{x}) = (I_f)_0. \tag{B.1}$$

The finite part integral of f may depend on the arbitrary radius r_0; in fact, this will typically happen when the result contains logarithms. Nonetheless, as long as f is integrable, its finite part integral coincides with $\int \mathrm{d}^3\boldsymbol{x}\, f$ and does not show any dependence on r_0.

An important property of the Hadamard regularization is that the finite part Poisson integral of a smooth function always exists, whereas the simple Poisson integral may not. The covariant expression of this finite part reads

$$\mathrm{FP}\, \hat{\Delta}^{-1}_{\boldsymbol{x}_0} f = \mathrm{FP}_{B=0} \int \frac{\mathrm{d}^3\boldsymbol{x}'\, \sqrt{\hat{\gamma}}}{-4\pi} \left(\frac{|\boldsymbol{x}'-\boldsymbol{x}_0|}{r_0} \right)^B \frac{f(\boldsymbol{x}')}{|\boldsymbol{x}-\boldsymbol{x}'|}, \tag{B.2}$$

where the Euclidean volume element has been written as $\mathrm{d}^3\boldsymbol{x}\, \sqrt{\hat{\gamma}}$ in an arbitrary coordinate system. When $\hat{\Delta}^{-1} f$ exists, it satisfies $\mathrm{FP}\, \hat{\Delta}^{-1}_{\boldsymbol{x}_0} f = \hat{\Delta}^{-1} f$. In any case, the regularized Poisson integral is the particular solution of a Poisson equation of the type $\hat{\Delta} g = f$. Thus, the operator $\mathrm{FP}\, \hat{\Delta}^{-1}$ constitutes a genuine generalization of the ordinary Poisson operator $\hat{\Delta}^{-1}$ and will be denoted as $\hat{\Delta}^{-1}_{\boldsymbol{x}_0}$ henceforth. It has the important property that it commutes with the spatial derivatives $\hat{\nabla}_i$, which allows us to work on the form of the elementary (super-)potentials of Chapter 5 by applying simple and systematic rules.

An important formula related to the Hadamard regularization is the one giving the generalized Poisson integral of the distance to the field point $\boldsymbol{x}$,

$$\hat{\Delta}^{-1}_{\boldsymbol{x}} |\boldsymbol{x}-\boldsymbol{x}'|^A = \frac{|\boldsymbol{x}-\boldsymbol{x}'|^{A+2}}{(A+2)(A+3)}, \tag{B.3}$$

for an arbitrary complex exponent $A \neq -2, -3$. Notably, it can be used to evaluate the action of the operator $\hat{\Delta}^{-1}_{\boldsymbol{x}} = \mathrm{FP}_{C=0} \int \mathrm{d}^3\boldsymbol{x}''\, \sqrt{\hat{\gamma}}/(-4\pi r_0^C |\boldsymbol{x}-\boldsymbol{x}''|)$ on the "r^a"-potential $\mathrm{FP}_{B=0} \int \mathrm{d}^3\boldsymbol{x}'\, \sqrt{\hat{\gamma}} |\boldsymbol{x}-\boldsymbol{x}'|^{a+B} f/(-4\pi r_0^B)$ with $a \in \mathbb{Z}$. By permuting the two triple integrals, we obtain the relation

$$\begin{aligned} &\hat{\Delta}^{-1}_{\boldsymbol{x}}\, \mathrm{FP}_{B=0} \int \frac{\mathrm{d}^3\boldsymbol{x}'\, \sqrt{\hat{\gamma}}}{-4\pi r_0^B} |\boldsymbol{x}-\boldsymbol{x}'|^{a+B} f \\ &\quad = \mathrm{FP}_{B=0} \frac{\int \mathrm{d}^3\boldsymbol{x}'\, \sqrt{\hat{\gamma}} |\boldsymbol{x}-\boldsymbol{x}'|^{a+B+2} f}{-4\pi r_0^B (a+B+2)(a+B+3)}. \end{aligned} \tag{B.4}$$

The result has the same form as the source. If we make $\hat{\Delta}^{-1}$ act on it, we arrive at a quantity of the same type. This provides a straightforward procedure to determine the action of $\hat{\Delta}^{-p} = (\hat{\Delta}^{-1})^p$, $p \in \mathbb{N}$, on the original integral iteratively. In this way, we find:

$$\begin{aligned}
&\hat{\Delta}_{\boldsymbol{x}}^{-p}\,\mathrm{FP}_{B=0}\int \frac{\mathrm{d}^3\boldsymbol{x}'\,\sqrt{\hat{\gamma}}}{-4\pi r_0^B}|\boldsymbol{x}-\boldsymbol{x}'|^{a+B} f \\
&\quad = \mathrm{FP}_{B=0}\int \frac{\mathrm{d}^3\boldsymbol{x}'\,\sqrt{\hat{\gamma}}}{-4\pi r_0^B}(a+B+1+2p)^{-1} \\
&\qquad\qquad \times (a+B+2p)^{-1}\ldots(a+B+2)^{-1} \\
&\qquad\qquad \times |\boldsymbol{x}-\boldsymbol{x}'|^{a+B+2p} f. \qquad \text{(B.5)}
\end{aligned}$$

If the usual "r^a"-potential with source f exists, the pth iterated Poisson integral $\hat{\Delta}_{\boldsymbol{x}}^{-1}$ of its pth derivative also exists. It is equal to $\hat{\nabla}_{i_1}\ldots\hat{\nabla}_{i_p}$ applied to the right-hand side of Eq. (B.5). When we put all derivatives under the integration symbol, we end up with a convergent integral. At this stage, one no longer needs regularization, so we may take $B = 0$ if none of the terms $(a+2p+1)$, $(a+2p)$, $\ldots$, $(a+2)$ vanish. Finally, we pull the coefficients $(a+1+2p)^{-1}(a+2p)^{-1}\ldots(a+1+p)^{-1}$ out of the integration symbol and reintroduce the finite part. We have then proved the formula giving the explicit action of $\hat{\Delta}_{\mathbf{x}}^{-p}$ on arbitrary sources,

$$\begin{aligned}
&\hat{\Delta}_{\boldsymbol{x}}^{-p}\,\mathrm{FP}_{B=0}\int \frac{\mathrm{d}^3\boldsymbol{x}'\,\sqrt{\hat{\gamma}}}{-4\pi r_0^B}|\boldsymbol{x}-\boldsymbol{x}'|^{a+B}\hat{\nabla}_{i_1}\ldots\hat{\nabla}_{i_p} f \\
&\quad = \frac{\hat{\nabla}_{i_1}\ldots\hat{\nabla}_{i_p}\,\mathrm{FP}_{B=0}\int \frac{\mathrm{d}^3\boldsymbol{x}'\,\sqrt{\hat{\gamma}}}{-4\pi r_0^B}|\boldsymbol{x}-\boldsymbol{x}'|^{a+B+2p} f}{(a+1+2p)(a+2p)\ldots(a+2)}, \qquad \text{(B.6)}
\end{aligned}$$

to be valid for $a+2p+1 \notin \mathbb{N}$.

Bibliography

Abrahams, A., Bernstein, D., Hobill, D., Seidel, E., & Smarr, L. 1992, Phys. Rev. D, 45, 3544

Akiyama, S., Wheeler, J. C., Meier, D. L., & Lichtenstadt, I. 2003, ApJ, 584, 954

Alcubierre, M. 2005, in AIP Conf. Proc. 758: Gravitation and Cosmology, ed. A. Macias, C. Lämmerzahl, & D. Nunez, 193–207

Anile, A. M. 1989, *Relativistic Fluids and Magnetofluids* (Cambridge University Press, Cambridge, U.K.)

Antón, L. 2006, PhD thesis, Universidad de Valencia, Valencia, Spain

Antón, L., Zanotti, O., Miralles, J. A., et al. 2006, ApJ, 637, 296

Ardeljan, N. V., Bisnovatyi-Kogan, G. S., & Moiseenko, S. G. 2005, MNRAS, 359, 333

Arnett, W. D., Bahcall, J. N., Kirshner, R. P., & Woosley, S. E. 1989, ARA&A, 27, 629

Arnowitt, R., Deser, S., & Misner, C. W. 1962, in *Gravitation: An introduction to current research*, ed. L. Witten (New York, U.S.A.: Wiley), 227

Baiotti, L., Hawke, I., Montero, P. J., et al. 2005, Phys. Rev. D, 71, 024035

Balbus, S. A. & Hawley, J. F. 1991, ApJ, 376, 214

—. 1992, ApJ, 392, 662

—. 1998, Reviews of Modern Physics, 70, 1

Balsara, D. S. & Spicer, D. S. 1999, J. Comp. Phys., 149, 270

Banyuls, F., Font, J. A., Ibáñez, J. M., Martí, J. M., & Miralles, J. A. 1997, APJ, 476, 221

Baumgarte, T. W. & Shapiro, S. L. 1999, Phys. Rev. D, 59, 024007

Baumgarte, T. W., Shapiro, S. L., & Shibata, M. 2000, ApJ, 528, L29

Bekenstein, J. D. & Oron, E. 1979, Phys. Rev. D, 19, 2827

Berger, M. J. & Colella, P. 1989, J. Comp. Phys., 82, 64

Bethe, H. A. 1990, Reviews of Modern Physics, 62, 801

Bisnovatyi-Kogan, G. S., Popov, I. P., & Samokhin, A. A. 1976, Ap&SS, 41, 287

Blanchet, L. 1987, Proc. R. Soc. London A, 409, 383

—. 1998, Class. Quantum Grav., 15, 1971

—. 2002, Living Rev. Relativity, 5, 3, [Online article]: cited on 3rd July 2006, http://www.livingreviews.org/lrr-2002-3

Blanchet, L. & Damour, T. 1986, Philos. Trans. R. Soc. London A, 320, 379

Blanchet, L., Damour, T., & Schäfer, G. 1990, MNRAS, 242, 289

Blanchet, L. & Poujade, O. 2002, Phys. Rev. D, 65, 124020

Bocquet, M., Bonazzola, S., Gourgoulhon, E., & Novak, J. 1995, A&A, 301, 757

Bonazzola, S., Gourgoulhon, E., Grandclément, P., & Novak, J. 2004, Phys. Rev. D, 70, 104007

Bonazzola, S., Gourgoulhon, E., Salgado, M., & Marck, J. A. 1993, A&A, 278, 421

Bonazzola, S. & Marck, J. A. 1993, A&A, 267, 623

Bondi, H., van der Burg, M. G. J., & Metzner, A. W. 1962, Proc. R. Soc. London, Ser. A,, 269, 21

Burrows, A. & Lattimer, J. M. 1986, ApJ, 307, 178

Carter, B. 1979, J. Math. Phys., 10, 70

Centrella, J. M., New, K. C. B., Lowe, L. L., & Brown, J. D. 2001, ApJ, 550, L193

Cerdá-Durán, P., Faye, G., Dimmelmeier, H., et al. 2005, A&A, 439, 1033

Cerdá-Durán, P., Quilis, V., & Font, J. A. 2006, A&A, submitted

Chandrasekhar, S. 1970, Phys. Rev. Lett,, 24, 611

Choquet-Bruhat, Y. 1952, Acta Math., 88, 141

Colella, P. & Woodward, P. R. 1984, J. Comput. Phys., 54, 174

Dimmelmeier, H., Cerdá-Durán, P., Marek, A., & Faye, G. 2005a, in Proc. Einstein's Century International Conference, Paris (AIP Publishing, Melville, U.S.A.), submitted; astro-ph/0603760

Dimmelmeier, H., Font, J. A., & Müller, E. 2001, ApJ, 560, L163

—. 2002a, A&A, 388, 917

—. 2002b, A&A, 393, 523

Dimmelmeier, H., Novak, J., Font, J. A., Ibáñez, J. M., & Müller, E. 2005b, Phys. Rev. D, 71, 064023

Dimmelmeier, H., Stergioulas, N., & Font, J. A. 2005, ArXiv Astrophysics e-prints

Dirac, P. A. M. 1959, Phys. Rev., 114, 924

Donat, R. & Marquina, A. 1996, J. Comput. Phys., 125, 42

Duez, M. D., Baumgarte, T. B., Shapiro, S. L., Shibata, M., & Uryu, K. 2002, Phys. Rev. D, 65, 024016

Duncan, R. C. & Thompson, C. 1992, ApJ, L9, 392

Eriguchi, Y. & Müller, E. 1984, A&A, 147, 161

Evans, C. R. & Hawley, J. F. 1988, ApJ, 332, 659

Faye, G. & Schäfer, G. 2003, Phys. Rev. D, 68, 084001

Finn, L. S. 1989, in Frontiers in numerical relativity, ed. C. R. Evans, S. L. Finn, & D. W. Hobill (Cambridge, U.K.: Cambridge University Press), 126

Font, J. A. 2003, Living Rev. Relativity, 6, 4, [Online article]: cited on 3rd July 2006, http://www.livingreviews.org/lrr-2003-4

Font, J. A., Goodale, T., Iyer, S., et al. 2002, Phys. Rev. D, 65, 084024

Font, J. A., Stergioulas, N., & Kokkotas, K. D. 2000, MNRAS, 313, 678

Friedman, J. L. & Schutz, B. F. 1978, ApJ, 221, 937

Fryer, C. L., Holz, D. E., Hughes, S. A., & Warren, M. S. 2004, in *Stellar Collapse*, ed. C. L. Fryer, Astrophysics and Space Science Library (Amsterdam, Netherlands: Kluwer Academic), 373

Fryer, C. L. & New, K. C. B. 2003, Living Rev. Relativity, 6, 2, [Online article]: cited on 3rd July 2006, http://www.livingreviews.org/lrr-2003-2

Geroch, R. & Horowitz, G. T. 1978, Phys. Rev. Lett., 40, 203

Glendenning, N. K. 1997, *Compact Stars, Nuclear Physics, Particle Physics, and General Relativity* (Springer-Verlag, New York)

Gourgoulhon, E. & Bonazzola, S. 1993, Phys. Rev. D, 48, 2635

Goussard, J. O., Haensel, P., & Zdunik, J. L. 1997, A&A, 321, 822

—. 1998, A&A, 330, 1005

Harten, A., Lax, P. D., & van Leer, B. 1983, SIAM Review, 25, 35

Heger, A., Langer, N., & Woosley, S. E. 2000, ApJ, 528, 368

Heger, A., Woosley, S. E., Langer, N., & Spruit, H. C. 2004, in IAU Symposium, ed. A. Maeder & P. Eenens, 591

Heger, A., Woosley, S. E., & Spruit, H. C. 2005, ApJ, 626, 350

Houser, J. L., Centrella, J. M., & Smith, S. 1994, Phys. Rev. Lett., 72, 1314

Ibáñez, J. M., Aloy, M. A., Font, J. A., et al. 1999, arXiv:astro-ph/9911034

Ioka, K. & Sasaki, M. 2003, Phys. Rev. D, 67, 124026

—. 2004, ApJ, 600, 296

Isenberg, J. A. 1978, University of Maryland Preprint, unpublished

Jackson, J. D. 1962, *Classical electrodynamics* (Wiley, New York)

Janka, H.-T., Buras, R., Kitaura Joyanes, F. S., et al. 2005, Nuclear Physics A, 758, 19

Janka, H.-T., Zwerger, T., & Mönchmeyer, R. 1993, A&A, 268, 360

Keil, W. & Janka, H.-T. 1995, ApJ, 295, 146

Kley, W. & Schäfer, G. 1999, Phys. Rev. D, 60, 027501

Komatsu, H., Eriguchi, Y., & Hachisu, I. 1989a, MNRAS, 237, 355

—. 1989b, MNRAS, 239, 153

Kotake, K., Sato, K., & Takahashi, K. 2005a, arXiv:astro-ph/0509456

Kotake, K., Sawai, H., Yamada, S., & Sato, K. 2004a, ApJ, 608, 391

Kotake, K., Yamada, S., & Sato, K. 2005b, ApJ, 618, 474

Kotake, K., Yamada, S., Sato, K., et al. 2004b, Phys. Rev. D, 69, 124004

Kouveliotou, C., Strohmayer, T., & Hurley, K. e. a. 1999, ApJ, 510, L115

Kurganov, A. & Tadmor, E. 2000, J. Comp. Phys., 160, 214

Lattimer, J. M. & Swesty, F. D. 1991, Nucl. Phys. A, 535, 331

LeBlanc, J. M. & Wilson, J. R. 1970, ApJ, 161, 541

Leonard, D. C., Filippenko, A. V., Ardila, D. R., & Brotherton, M. S. 2001, ApJ, 553, 861

Leveque, R. J. 1990, *Numerical Methods for Conservation laws* (Birkhauser-Verlag, Basel)

Lichnerowicz, A. 1944, Journal de Math., 23, 3

Lucas-Serrano, A., Font, J. A., Ibáñez, J. M., & Martí, J. M. 2004, A&A, 428, 703

Martí, J. M. & Müller, E. 1996, J. Comput. Phys., 123, 1

—. 2002, Living Rev. Relativity, 6, 7, [Online article]: cited on 3rd July 2006, http://www.livingreviews.org/lrr-2003-7

Meier, D. L., Epstein, R. I., Arnett, W. D., & Schramm, D. N. 1976, ApJ, 204, 869

Misner, C. W., Thorne, K. S., & Wheeler, J. A. 1973, *Gravitation* (San Francisco: W. H. Freeman and Co., 1973)

Mönchmeyer, R., Schäfer, G., Müller, E., & Kates, R. E. 1991, A&A, 246, 417

Moncrief, V. 1974, Ann. Phys, 88, 323

Müller, E. 1982, A&A, 114, 53

Müller, E. 1998, Saas-Fee Advanced Course 27 (Springer, Berlin), 343

Müller, E. & Hillebrandt, W. 1979, A&A, 80, 147

Müller, E., Rampp, M., Buras, R., Janka, H.-T., & Shoemaker, D. H. 2004, ApJ, 603, 221

Müller, E. & Steinmetz, M. 1995, Comp. Phys. Comm., 89, 45

Nagar, A., Font, J. A., Zanotti, O., & Pietri, R. D. 2005, Phys. Rev. D, 72, 024007

New, K. C. B., Centrella, J. M., & Tohline, J. E. 2000, Phys. Rev. D, 62, 064019

Obergaulinger, M., Aloy, M. A., Dimmelmeier, H., & Müller, E. 2006, ArXiv Astrophysics e-prints

Obergaulinger, M., Aloy, M. A., & Müller, E. 2005, ArXiv Astrophysics e-prints

Ohnishi, T. 1983, Tech. Rep. Inst. Atom. Energy, 168

Oron, A. 2002, Phys. Rev. D, 66, 023006

Ott, C. D., Burrows, A., Livne, E., & Walder, R. 2004, ApJ, 600, 834

Ott, C. D., Burrows, A., Thompson, T. A., Livne, E., & Walder, R. 2006, ApJ, accepted

Ott, C. D., Ou, S., Tohline, J. E., & Burrows, A. 2005, ApJ, 625, L119

Pati, M. E. & Will, C. M. 2000, Phys. Rev. D, 62, 124015

Penrose, R. 1963, Phys. Rev. Lett., 10, 66

—. 1965, Proc. R. Soc. London, Ser. A, 284, 159

Pons, J. A. *et al.*. 1999, ApJ, 513, 780

Prakash, M., Lattimer, J. M., Pons, J. A., Steiner, A. W., & Reddy, S. 2001, LNP Vol. 578: *Physics of Neutron Star Interiors*, 578, 364

Quilis, V. 2004, MNRAS, 352, 1426

Rampp, M., Müller, E., & M., R. 1998a, A&A, 332, 969

Rampp, M., Müller, E., & Ruffert, M. 1998b, A&A, 332, 969

Regge, T. & Teitelboim, C. 1974, Ann. Phys., 88, 286

Regge, T. & Wheeler, J. A. 1957, Phys. Rev., 108, 1063

Reula, O. A. 1998, Living Rev. Relativity, 1, 3, [Online article]: cited on 3rd July 2006, http://www.livingreviews.org/lrr-1998-3

Roe, P. L. 1981, J. Comput. Phys., 43, 357

Sachs, R. 1962, Proc. R. Soc. London, Ser. A,, 270, 103

Saijo, M. 2005, Phys. Rev. D, 71, 104038

Saijo, M. & Yoshida, S. 2005, MNRAS

Sasaki, M. & Tagoshi, H. 2003, Living Rev. Relativity, 6, 6, [Online article]: cited on 3rd July 2006, http://www.livingreviews.org/lrr-2003-6

Sawai, H., Kotake, K., & Yamada, S. 2005, ApJ, 631, 446

Schäfer, G. 1985, Ann. Phys. N. Y., 81, 161

—. 1990, Astron. Nachr., 311, 213

Schäfer, G. & Gopakumar, A. 2004, Phys. Rev. D, 69, 021501

Schwinger, J. 1963, Phys. Rev., 130, 1253

Shapiro, S. L. 2005, ArXiv General Relativity and Quantum Cosmology e-prints

Shibata, M., Baumgarte, T. W., & Shapiro, S. L. 2000, ApJ, 542, 453

Shibata, M. & Font, J. A. 2005, Phys. Rev. D, 72, 047501

Shibata, M., Karino, S., & Eriguchi, Y. 2002, MNRAS, 334, L27

—. 2003, MNRAS, 343, 619

Shibata, M. & Nakamura, T. 1995, Phys. Rev. D, 52, 5428

Shibata, M. & Sekiguchi, Y. I. 2003, Phys. Rev. D, 68, 104020

—. 2004, Phys. Rev. D, 69, 084024

—. 2005, Phys. Rev. D, 71, 024014

Siebel, F., Font, J. A., Müller, E., & Papadopoulos, P. 2002, Phys. Rev. D, 65, 064038

Siebel, F., Font, J. A., Müller, E., & Papadopoulos, P. 2003, Phys. Rev. D, 67, 124018

Spruit, H. C. 1999, A&A, 349, 189

Spruit, H. C. & Phinney, E. S. 1998, Nature, 393, 139

Stergioulas, N. 2003, Living Rev. Relativity, 6, 3, [Online article]: cited on 3rd July 2006, http://www.livingreviews.org/lrr-2003-3

Stergioulas, N. & Friedman, J. L. 1998, ApJ, 492, 301

Strobel, K., Schaab, C., & Weigel, M. K. 1999, A&A, 350, 497

Symbalisty, E. M. D. 1984, ApJ, 285, 729

Takiwaki, T., Kotake, K., Nagataki, S., & Sato, K. 2004, ApJ, 616, 1086

Thompson, C. & Duncan, R. C. 1996, ApJ, 473, 332

Thorne, K. S. 1980, Reviews of Modern Physics, 52, 299

Tohline, J. E., Durisen, R. H., & McCollough, M. 1985, ApJ, 298, 220

Toro, E. F. 1999, *Riemann Solvers and Numerical Methods for Fluid Dynamics* (Springer Verlag)

Tóth. 2000, J. Comp. Phys., 161, 605

Villain, L., Pons, J. A., Cerdá-Durán, P., & Gourgoulhon, E. 2004, A&A, 418, 283

Wald, R. 1984, General relativity (University of Chicago Press, Chicago, U.S.A.)

Wang, L., Howell, D. A., Höflich, P., & Wheeler, J. C. 2001, ApJ, 550, 1030

Wang, L., Wheeler, J. C., Li, Z., & Clocchiatti, A. 1996, ApJ, 467, 435

Watts, A. L., Andersson, N., Beyer, H., & Schutz, B. F. 2003, MNRAS, 342, 1156

Watts, A. L., Andersson, N., & Jones, D. I. 2005, ApJ, 618, L37

Watts, A. L., Andersson, N., & Williams, R. L. 2004, MNRAS, 350, 927

Wheeler, J. C. & Akiyama, S. 2004, arXiv:astro-ph/0412382

Wheeler, J. C., Meier, D. L., & Wilson, J. R. 2002, ApJ, 568, 807

Wilson, J. R., Mathews, G. J., & Marronetti, P. 1996, Phys. Rev. D, 54, 1317

Winicour, J. 2005, Living Rev. Relativity, 8, 10, [Online article]: cited on 3rd July 2006, http://www.livingreviews.org/lrr-2005-10

Woosley, S. & Janka, T. 2005, Nature Physics, 1, 147

Woosley, S. E. & Heger, A. 2006, ApJ, 637, 914

Yamada, S. & Sawai, H. 2004, ApJ, 608, 907

Yoshida, S., Rezzolla, L., Karino, S., & Eriguchi, Y. 2002, ApJ, 568, L41

Zerilli, F. J. 1970, Phys. Rev. Lett, 24, 737

Zwerger, T. 1995, PhD thesis, Technische Universität München, München, Germany

Zwerger, T. & Müller, E. 1997, A&A, 320, 209